DUVAR KİTABEVİ

insac

ISBN: 978-625-7767-76-7

Research in Natural and Engineering Sciences

Editör
Doç. Dr. Mehmet Dalkılıç

Yazarlar

Chapter 1: Hatice Banu Keskinkaya, Cengiz Akköz,
Chapter 2: Ayşe Elif Ateş,
Chapter 3: Çağrı Deliceırmak,
Chapter 4: Çetin Gençer, Ramazan Alioğlu, Mustafa Yıldırım,
Chapter 5: Mustafa Koçer,
Chapter 6: Rahile Öztürk,
Chapter 7: Furkan Dinçer,
Chapter 8: Furkan Dinçer,
Chapter 9: Emir Haliki,
Chapter 10: Yeşim Dağlıoğlu, Betül Yılmaz Öztürk,

Research in Natural and Engineering Sciences

Editör
Doç. Dr. Mehmet Dalkılıç

Research in Natural and Engineering Sciences

Genel Yayın Yönetmeni: Berkan Balpetek
Kapak ve Sayfa Tasarımı: Duvar Design
Baskı: Eylül 2020
Yayıncı Sertifika No: 16122
ISBN: 978-625-7767-76-7

853 Sokak No:13 P.10 Kemeraltı-Konak/İzmir
Tel: 0 232 484 88 68

www.duvaryayinlari.com
duvarkitabevi@gmail.com

Baskı ve Cilt: Sonçağ Yayıncılık Matbaacılık Reklam San Ve Tic. Ltd.
İstanbul Cad. İstanbullu Çarşısı No:48/48-49
İskitler 06070 Ankara
Tel: 0 312 341 36 67
Sertifika No:47865

Research in Natural and Engineering Sciences

Editör
Mehmet Dalkılıç

Yazarlar
Chapter 1: Hatice Banu Keskinkaya, Cengiz Akköz,
Chapter 2: Ayşe Elif Ateş,
Chapter 3: Çağrı Deliceırmak,
Chapter 4: Çetin Gençer, Ramazan Alioğlu, Mustafa Yıldırım,
Chapter 5: Mustafa Koçer,
Chapter 6: Rahile Öztürk,
Chapter 7: Furkan Dinçer,
Chapter 8: Furkan Dinçer,
Chapter 9: Emir Haliki,
Chapter 10: Yeşim Dağlıoğlu, Betül Yılmaz Öztürk,

İletişim ve Çalışma Gönderim e-mail adresi:
insackongre@gmail.com

Editörün Notu

Bu kitapta yer alan bölümlerde kullanılan kaynakların, görüşlerin, bulguların, sonuçların, tablo, şekil, resim ve her türlü içeriğin sorumluluğu yazar veya yazarlarına ait olup ulusal ve uluslararası telif haklarına konu olabilecek mali ve hukuki sorumluluğu yazarlara aittir.

Contents

CHAPTER

1

RESEARCH IN NATURAL AND ENGINEERING SCIENCES

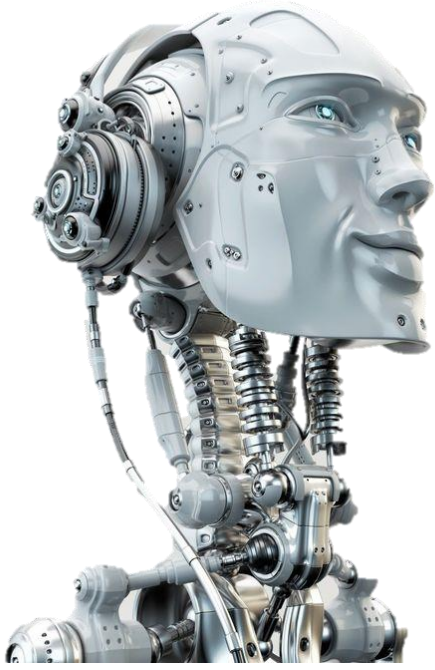

The Use of Nanoparticles Obtained by Green Synthesis by Algae in the Treatment of Antibiotic Resistant Bacterial Infections (Hatice Banu Keskinkaya, Cengiz Akköz)

The Use of Nanoparticles Obtained by Green Synthesis by Algae in the Treatment of Antibiotic Resistant Bacterial Infections

Hatice Banu Keskinkaya[1], Cengiz Akköz[1]
[1]*Selcuk University Faculty of Science Department of Biology:*
banu.keskinkaya@selcuk.edu.tr

1. Introduction

Since the term nanotechnology was first used in 1974, nanoparticle materials have become interesting for materials and product manufacturing processes. Since 1990, when their buildings can be manipulated, they are widely used in industrial terms. Although nanoscience is currently in its early stage, its effects have begun to be seen both in our daily life and in nature. For many different purposes, nanoparticles (NP), which have a very wide use purpose, show themselves in every aspect of our lives today. (Vilela et al.,2012)NPs are encountered in every field from medicine to textile, from cosmetics to high technology. In addition, the issue of the impact and accumulation of NPs on the environment has already started to be the subject of important researches.(Sharma et al.,2009). Due to the unique properties of nanoparticles and atomic arrays that can be changed according to the purpose, nanoparticle materials, which are extremely suitable for use both industrially and scientifically, have become a natural part of today's production technologies and therefore a scientific research subject that needs to be investigated in depth (Gao et al., 2011).

The physical and chemical properties of the particles in the nanoscale are different from those in larger sizes. This is due to the fact that although nanoscale particles consist of the same atoms as macro-sized particles, they have a different formation geometry. (Ali et al.,2011). The main reason why nanoparticle materials find a wide market for themselves in industry and scientific research is the changing catalytic, electrochemical, magnetic and optical properties with the reduction in size (Benn and Westerhoff, 2008).

1.1. What is a nanoparticle?

Nanoparticles are particles in sizes between 1-100 nm. Nano is derived from the Greek word Nanos, which means extremely small. It can be used as a prefix for any unit to mean one billionth of that unit (Fayaz et al.,2010). For example, nanoseconds (billionths of a second), nanometers (billionths of a meter), nanoliters (billionths of a liter). They consist of micro-molecular materials in which active ingredients (drug or biologically active material)

are dissolved, entrapped, encapsulated, adsorbed or added. Although there are different classifications according to different features, it can be classified as follows:

Carbon-based nanoparticles (fullerenes, multi-walled carbon nanotubes, etc.),

1. Metal-based nanoparticles (gold colloids, nanoshells, nanorods, superparamagnetic iron oxide nanoparticles, etc.),
2. Semiconductor based nanoparticles (quantum dots etc.).(Sharma et al.,2009).

1.2. Classification of Nanoparticles

In addition to the size of nanoparticles, features such as shape, surface load, presence of other materials in the environment are among the factors that affect their behavior. Nanoparticles can be classified into three subgroups;

1. Natural,
2. Anthropogenic (later emerging),
3. Designed

Natural nanoparticles consist of non-man-made, self-forming nanoparticles and come in a wide variety of materials (Ju-Nam and Lead, 2008).

Anthropogenic nanoparticles are nanoparticles created as a result of human activities, and the most typical example of these is the nanoscale "soot" resulting from cigarette and fossil fuel consumption. Engineered nanoparticles are nanoparticles specially designed and produced by human beings to serve the specified purposes (Isaeva et al.,2006).

1.2.1. Types of Nanoparticle

There are two different types of NP,

1. İnorganic NP
2. Organic NP

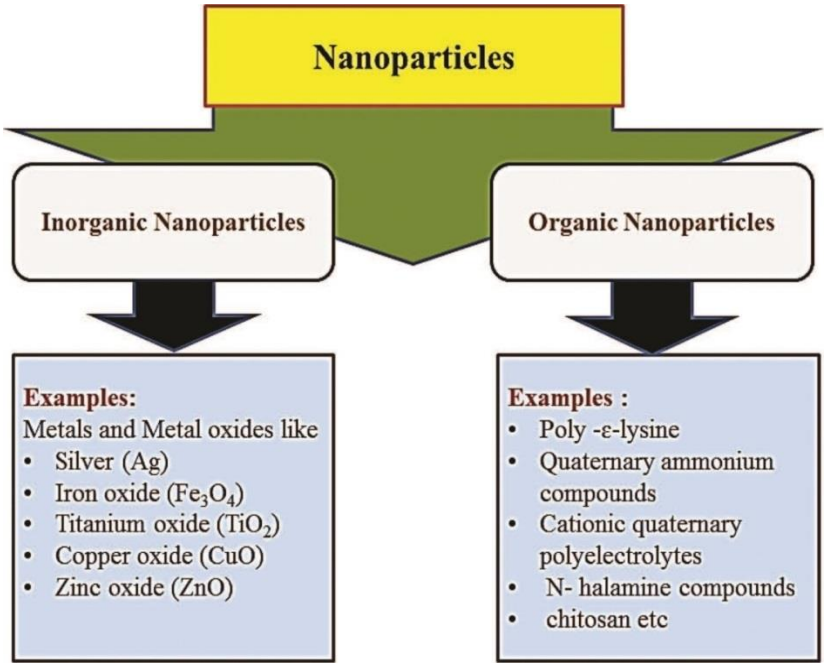

Figure 1. Type of nanoparticle and examples (Oskar et al.,2016).

Inorganic NPs contain metal and metal oxides that are powerful antibacterial agents. Metal oxide nanoparticles such as silver (Ag), iron oxide (Fe3O4), titanium oxide (TiO2), copper oxide (CuO), and zinc oxide (ZnO) are some examples of inorganic NPs. Organic nanoparticles are generally less stable at high temperatures. Therefore, inorganic nanoparticles are more preferred as antimicrobial polymers (Oskar et al., 2016).

1.3. Methods for the Synthesis of Nanoparticles

Algae are in a more important position in the green synthesis of NPs compared to other organisms such as fungi, yeasts and bacteria, because algae are economically and ecologically important photosynthetic organisms, because of their presence in a wide variety of regions such as seawater or moist rocks, and because of the large sample size. working opportunities are quite wide (Miri and Sarani,2018)

1.3.1. The Advantages of Green Synthesis over Chemical and Physical Method

a. It is environmentally friendly,

b. Low cost,

c. Can be used for large scale synthesis,

d. It does not require the use of high pressure, energy, temperature and toxic chemicals,

e. It has some advantages such as not needing any special culture preparation and isolation technique (De La Zerda et al., 2008).

Possible effects of nanoparticle materials on the environment and humans, for example, cleaning contaminated groundwater with NPs will allow more efficient aquatic organisms to grow. However, the possible effects of the use of Np on a living being are still uncertain. In this process, cellular extracts of living organisms such as bacteria, algae, fungi, actinomycetes and plants are used as green reaction media and capping agents (Choi and Hu, 2008).

Aqueous biological extracts have become a suitable environment for nanoparticles synthesis due to their non-toxic and non-volatile nature. Biological extracts are usually mixtures of different active biomolecules such as proteins, carbohydrates, vitamins, polymers and natural surfactants that provide high stability and improved dispersion to synthesized nanoparticles (Hall et al., 2007).

Important considerations in the production process of well-characterized nanoparticles are:

1. **Selection of the best and suitable organism:** To select the best example, researchers focused on growth rate, enzyme activities, and biochemical pathways

2. **Selection of biocatalyst status:** Organisms' enzymes (biocatalysts) appear to be major agents in nanoparticle biosynthesis.

3. **Optimal conditions for cell growth and enzyme activity:** Optimization of growing conditions is very important. Nutrients, inoculum size, pH, light, temperature and mixing speed should be optimized. Induction of the responsible enzymes is also very important.

4. **Optimal reaction conditions:** To use organisms for the production of nanoparticles on an industrial scale, yield and production rate are important issues to consider**.** Therefore, it is necessary to optimize the conditions of the bioreducers in the reaction mixture. (Mohanpuria et al., 2008).

2. Nanoparticle and Algae

Algae are an economically and ecologically important group of photosynthetic organisms. These are unicellular or multicellular organisms that live in different environments such as seawater or the surface of moist rocks (Thajuddin and Subramanian, 1992).

Algae are classified as microalgae (microscopic) and macroalgae (macroscopic) (Lewis-Oscar et al., 2014).

Until now, different groups of algae have been used for the biosynthesis of metallic NPs, such as Chlorophyceae, Phaeophyceae, Cyanophyceae, Rhodophyeae and others (diatoms and euglenoids) (Sharma et al., 2016).

2.1. The Importance of Algae in the Synthesis of Nanoparticles

The ability of algae to accumulate metals and reduce metal ions makes them a superior competitor for the biosynthesis of nanoparticles. In addition, algae are relatively comfortable and easy to use, allowing synthesis at low temperatures, less toxic to the environment, and the ability to complete the synthesis in a shorter time than other methods.

Among biological materials, algae are called bionano materials because both live and dead dried biomasses are used for the synthesis of metallic nanoparticles. Marine algae are rich in oil, vitamins and minerals and contain bioactive substances such as polysaccharides, proteins and polyps. On the other hand, their phytochemicals include hydroxyl (-OH), carboxyl (-COOH) and amino (-NH) functional groups that can provide NP synthesis in a single stage (Singaravelu et al., 2007).

2.1.1. Synthesis of Nanoparticles Using Algae

The synthesis of nanoparticles using algae can be carried out in 3 important stages,

(i) preparation of algae extract by heating or boiling for a certain period of time in water or in an organic solvent,

(ii) preparation of molar solutions of ionic metallic compounds and

(iii) incubation of algal solutions and molar solutions of ionic metallic compounds and monitoring under controlled conditions over a period of time without continuous stirring or stirring (Verbruggen et al.,2007).

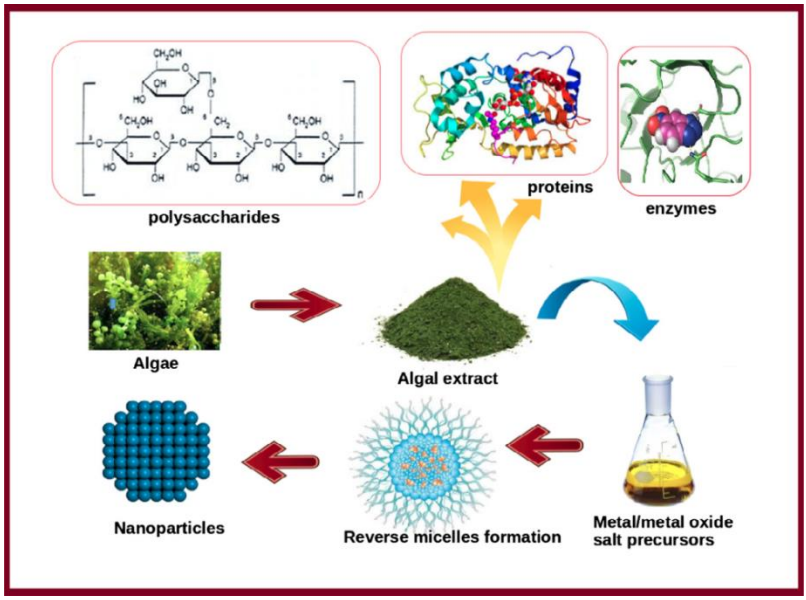

Figure 2. Biosynthesis mechanism of NPs using algae (Verbruggen et al.,2007).

The synthesis of NPs is dose dependent and also related to the algae used. There are various biomolecules responsible for the reduction of metals (Polysaccharides, peptides and pigments) in the reaction mixture. Stabilization of metal nanoparticles in aqueous solutions is done by proteins through amino (-NH) groups or cysteine (-SH) residues and sulphate polysaccharides. Unique properties such as large surface area, stability, exceptional mechanical strength and low melting points make NPs highly compatible for a variety of clinical applications such as drug delivery, cancer therapy, biofilm inhibition, and treatment of microbial infections. The ability of nanoparticles to hold both hydrophilic and hydrophobic materials makes them suitable drug carriers (Zuber et al.,2016).

2.2. Properties of Nanoparticles to Kill Bacteria

Nanotechnology has come up with an efficient solution to a serious problem of bacterial resistance to antibiotics. NPs can bind effectively to the bacterial surface and cause cell death by breaking down cell walls. It has been found that NPs smaller than 20 nm in size can penetrate the bacterial cell wall and block biochemical pathways by destroying cell organelles that ultimately lead to the death of bacteria (Stephen and Macnaughtont,1999).

Biogenic nanoparticles are suitably capped with natural flavonoids that inhibit the enzymatic activity that inhibit the synthesis of nucleic acids in various microorganisms (Rónavári et al., 2017).

NPs are known to produce reactive oxygen species (ROS) that cause mechanical damage to the bacterial cell membrane (Shahverdi et al.,2007). It is very difficult for bacteria to develop resistance to nanoparticles because nanoparticles target several cellular pathways at once. Therefore, NPs can replace traditional antibiotics to treat antibiotic-resistant bacterial infections (Singh et al.,2015).

2.2.1. How do antimicrobial nanoparticles work?

In microbial effects occurring in living things, antimicrobial Np's can cause the death of microbes by chemical or mechanical means.

So how does this happen;

1. Protein damage: Protein is essential for biological systems. Any damage to these components causes the living thing to die by disrupting its most basic needs such as energy production.

2. Membran **damage:** By disrupting the membrane structures of microbial organisms, it causes the organism to lose its structural integrity and consequently the life activities of the organism to cease.

3. Oxidative damage: Antimicrobials can cause an increase in reactive oxygen species that can damage the microbe's internal system.

4. DNA interference: It can prevent bacteria from reproducing by blocking the replication of genetic materials (Hassan et al.,2019).

2.3. Forms of Biogenic Nanoparticles and their Mechanism of Action

2.3.1. Mechanism of Action of Metal Np's and Metal Oxide Np's

The mechanism of action of metal and metal oxide nanoparticles against bacteria is still not very clear, and many studies are currently ongoing worldwide.

Researchers have shown that free metal nanoparticles exert toxic effects in dissolving the outer membrane of the bacterial surface. Oxidative stress induced by reactive oxygen species (ROS) is the fundamental mechanism in the case of metal oxide nanoparticles (Duguet et al.,2006).

Studies show that silver nanoparticals induce the formation of cavities and cavities on the membrane surface of bacteria by releasing ions that

further interact with the disulfide or sulfhydryl groups of the enzymes, resulting in interruption of the metabolic pathway and eventually bacterial cell death (Rónavári et al., 2017).

2.3.2. Effect of Biogenic Nanoparticles Under Aerobic and Anaerobic Conditions

The inhibitory and toxic effect of nanoparticles against bacterial strains depends on the ion flux released by the nanoparticles. The extent of this ion flow is directly proportional to the amount of oxygen present. Interestingly, AgNPs showed better toxicity against aerobic E. coli under adequate oxygen supply, the same nanoparticles showed lower toxicity to anaerobic bacteria with low oxygen supply. Thus, we can control the toxicity of nanoparticles by changing the accessibility of oxygen (Amro et al.,v2000).

2.3.3. Different Routes Targeted by Biogenic NPs

Biogenic nanoparticles take two different ways to demonstrate their antibacterial potency; either by generating ions (in the case of metallic NPs) or releasing reactive oxygen species (in the case of metallic oxide NPs). The released ions and ROS damage the cell wall, genetic material or membrane lipid through oxidation. During synthesis, biogenic nanoparticles are degraded by biologically active compounds such as vitamins, proteins, polyphenols, carbohydrates and polymers contained in the cellular extract. These molecules not only provide a high degree of stability to the synthesized nanoparticles, but also add different functional groups to the surface of the nanoparticals (Xie et al.,v2007).

These functional groups allow for the establishment of chemical bonds and provide active sites for the physical interaction between nanoparticles and the bacterial cell necessary for their inhibition. Accordingly, it has been noticed that biogenic nanoparticles show better antimicrobial properties than chemically synthesized ones (Rajasulochana et al.,v2010).

2.3.4. Effects of Biogenic NPs on Clinically Resistant Bacterial Strains

The development of resistance to antibiotics in bacterial strains has become a major concern. Therefore, many research studies are conducted in the field of nanobiotechnology to overcome this health problem.

It has been reported that biogenic silver nanoparticles can effectively inhibit the growth of clinically resistant P. aeruginosa strain isolated from the patient's wound site (MIC: 2.0mg / ml) (Singh et al., 2015). In another

notable approach, biogenic ZnO nanoparticles in combination with antibiotics were found to be able to effectively kill clinical isolates of methicillin-resistant S.aureus (MRSA) (MIK: 2000mg / mL, MBC: 2200mg / mL) (Zgoda and Porter, 2001).

Additionally, it has been reported that biogenic nanoparticles can overcome antibiotic resistance issues associated with bacterial biofilm formation (Zuber et al.,2016).

3. Conclusion and Suggestions

NPs interact with important cellular organelles and biomolecules such as DNA, enzymes, ribosomes, and lysosomes, which can affect cell membrane permeability, oxidative stress, gene expression, protein activation, and enzyme activation. Since NPs target more than one biomolecule at the same time; it becomes very difficult for bacteria to develop resistance against them.

Among the various reaction parameters, temperature, pH, and reaction time greatly influence the morphology (size and shape) of nanoparticles, their chemical properties, and the rate of synthesis by monitoring the formation of nucleation centers.

The antibacterial property of nanoparticles changes by changing the size, shape and oxidation state of the nanoparticles. However, many of these processes are costly and potentially dangerous to living organisms and the environment. Therefore, there is a need to develop an environmentally friendly and cost effective synthesis method. Recently, 'green synthesis' approaches have also attracted great attention at this point.

It has been shown that living organisms such as algae, bacteria, yeast, fungi, and plant cells can reduce inorganic metal ions by their cellular metabolites to metal NPs.

The yield and stability of biogenic NPs are highly satisfactory and it is thought that there may be viable and economical alternatives in the treatment of drug-resistant bacterial infections in the near future. The development of new and potent bactericidal agents is of great clinical importance, as over-the-counter and uncontrolled use of antibiotics leads to rapid development of antibiotic resistance in bacterial strains. Moreover, metallic nanoparticles (NP) have proven to be a promising alternative to antibiotics.

Recently, antibiotic resistance of bacteria has become one of the biggest concerns in human health. Metal nanoparticles are thought to be one of the best options for treating drug-resistant bacterial infections.

NPs of green synthesis can be synthesized both extracellularly and intracellularly. The extracellular method is preferred over the intracellular

method as it does not require any harvesting process (downstream process) to collect nanoparticles from organisms. Plant and algae assisted synthesis is cheaper than microbial agents and is more effective in obtaining higher nanoparticle yields.

References

Vilela, D., González, M. C. ve Escarpa, A., 2012. Sensing colorimetric approaches based on gold and silver nanoparticles aggregation: chemical creativity behind the assay. A review, *Analytica chimica acta*, 751, 24-43.

Sharma, V. K., Yngard, R. A. ve Lin, Y., 2009, Silver nanoparticles: green synthesis and their antimicrobial activities, *Advances in colloid and interface science*, 145 (1-2), 83-96.

Gao, C., Zhang, Q., Lu, Z. ve Yin, Y., 2011, Templated synthesis of metal nanorods in silica nanotubes, *Journal of the American Chemical Society*, 133 (49), 19706-19709.

Ali, D. M., Sasikala, M., Gunasekaran, M. ve Thajuddin, N., 2011, Biosynthesis and characterization of silver nanoparticles using marine cyanobacterium, Oscillatoria willei NTDM01, *Digest Journal of Nanomaterials and Biostructures*, 6 (2), 385-390.

Benn, T. M. ve Westerhoff, P., 2008, Nanoparticle silver released into water from commercially available sock fabrics, *Environmental science & technology*, 42 (11), 4133-4139.

Fayaz, A. M., Balaji, K., Girilal, M., Yadav, R., Kalaichelvan, P. T. ve Venketesan, R., 2010, Biogenic synthesis of silver nanoparticles and their synergistic effect with antibiotics: a study against gram-positive and gram-negative bacteria, *Nanomedicine: Nanotechnology, Biology and Medicine*, 6 (1), 103-109.

Ju-Nam, Y. ve Lead, J. R., 2008, Manufactured nanoparticles: an overview of their chemistry, interactions and potential environmental implications, *Science of the total environment*, 400 (1-3), 396-414.

Isaeva, E., Gorbunova, V., Sirotinkin, N., Shchukarev, A. ve Boitsova, T., 2006, Photochemical formation of silver nanoparticles in elastomer films, *Russian journal of general chemistry*, 76 (5), 687-693.

Oscar, F.L, Vismaya,S., Arunkumar,M., Thajuddin,N., Dhanasekaran,D., Chari Nithya,C.,2016. Algal Nanoparticles: Synthesis and Biotechnological Potentials.

Miri, A. ve Sarani, M., 2018, Biological studies of synthesized silver nanoparticles using Prosopis farcta, *Molecular biology reports*, 45 (6), 1621-1626.

De La Zerda, A., Zavaleta, C., Keren, S., Vaithilingam, S., Bodapati, S., Liu, Z., Levi, J., Smith, B. R., Ma, T.-J. ve Oralkan, O., 2008, Carbon nanotubes as photoacoustic molecular imaging agents in living mice, *Nature nanotechnology*, 3 (9), 557.

Choi, O. ve Hu, Z., 2008, Size dependent and reactive oxygen species related nanosilver toxicity to nitrifying bacteria, *Environmental science & technology*, 42 (12), 4583-4588.

Hall, J. B., Dobrovolskaia, M. A., Patri, A. K. and McNeil, S. E., 2007, Characterization of nanoparticles for therapeutics.

Mohanpuria, P., Rana, N. K. and Yadav, S. K., 2008, Biosynthesis of nanoparticles: technological concepts and future applications, *Journal of nanoparticle research*, 10 (3), 507-517.

Thajuddin, N. ve Subramanian, G., 1992, Survey of cyanobacterial flora of the southern east coast of India, *Botanica Marina*, 35 (4), 305-314.

LewisOscar, F., Vismaya, S., Arunkumar, M., Thajuddin, N., Dhanasekaran, D. ve Nithya, C., 2016, Algal nanoparticles: synthesis and biotechnological potentials, In: Algae-Organisms for Imminent Biotechnology, Eds: IntechOpen, p.

Sharma, A., Sharma, S., Sharma, K., Chetri, S. P., Vashishtha, A., Singh, P., Kumar, R., Rathi, B. ve Agrawal, V., 2016, Algae as crucial organisms in advancing nanotechnology: a systematic review, *Journal of applied phycology*, 28 (3), 1759-1774.

Singaravelu, G., Arockiamary, J., Kumar, V. G. ve Govindaraju, K., 2007, A novel extracellular synthesis of monodisperse gold nanoparticles using marine alga, Sargassum wightii Greville, *Colloids and surfaces B: biointerfaces*, 57 (1), 97-101.

Verbruggen, H., Leliaert, F., Maggs, C. A., Shimada, S., Schils, T., Provan, J., Booth, D., Murphy, S., De Clerck, O. ve Littler, D. S., 2007, Species boundaries and phylogenetic relationships within the green algal genus Codium (Bryopsidales) based on plastid DNA sequences, *Molecular phylogenetics and evolution*, 44 (1), 240-254.

Zuber, A., Purdey, M., Schartner, E., Forbes, C., van der Hoek, B., Giles, D., Abell, A., Monro, T. ve Ebendorff-Heidepriem, H., 2016, Detection of gold nanoparticles with different sizes using absorption and fluorescence based method, *Sensors and Actuators B: Chemical*, 227, 117-127.

Stephen, J. R. ve Macnaughtont, S. J., 1999, Developments in terrestrial bacterial remediation of metals, *Current opinion in biotechnology*, 10 (3), 230-233.

Rónavári, A., Kovács, D., Igaz, N., Vágvölgyi, C., Boros, I. M., Kónya, Z., Pfeiffer, I. ve Kiricsi, M., 2017, Biological activity of green-synthesized silver nanoparticles depends on the applied natural extracts: a comprehensive study, *International journal of nanomedicine*, 12, 871.

Shahverdi, A. R., Fakhimi, A., Shahverdi, H. R. ve Minaian, S., 2007, Synthesis and effect of silver nanoparticles on the antibacterial activity of different antibiotics against Staphylococcus aureus and Escherichia coli, *Nanomedicine: Nanotechnology, Biology and Medicine, 3 (2), 168-171.*

Singh, R., Shedbalkar, U. U., Wadhwani, S. A. ve Chopade, B. A., 2015, Bacteriagenic silver nanoparticles: synthesis, mechanism, and applications, *Applied microbiology and biotechnology*, 99 (11), 4579-4593.

Hassan, S. E.-D., Fouda, A., Radwan, A. A., Salem, S. S., Barghoth, M. G., Awad, M. A., Abdo, A. M. ve El-Gamal, M. S., 2019, Endophytic actinomycetes Streptomyces spp mediated biosynthesis of copper oxide nanoparticles as a promising tool for biotechnological applications, *JBIC Journal of Biological Inorganic Chemistry*, 1-17.

Duguet, E., Vasseur, S., Mornet, S. ve Devoisselle, J.-M., 2006, Magnetic nanoparticles and their applications in medicine.

Amro, N. A., Kotra, L. P., Wadu-Mesthrige, K., Bulychev, A., Mobashery, S. ve Liu, G.-y., 2000, High-resolution atomic force microscopy studies of the Escherichia coli outer membrane: structural basis for permeability, *Langmuir*, 16 (6), 2789-2796.

Xie, J., Lee, J. Y., Wang, D. I. ve Ting, Y. P., 2007, Silver nanoplates: from biological to biomimetic synthesis, *ACS nano*, 1 (5), 429-439.

Rajasulochana, P., Dhamotharan, R., Murugakoothan, P., Murugesan, S. ve Krishnamoorthy, P., 2010, Biosynthesis and characterization of gold nanoparticles using the alga Kappaphycus alvarezii, *International Journal of Nanoscience*, 9 (05), 511-516.

Zgoda, J. ve Porter, J., 2001, A convenient microdilution method for screening natural products against bacteria and fungi, *Pharmaceutical Biology*, 39 (3), 221-225.

CHAPTER

2

RESEARCH IN NATURAL AND ENGINEERING SCIENCES

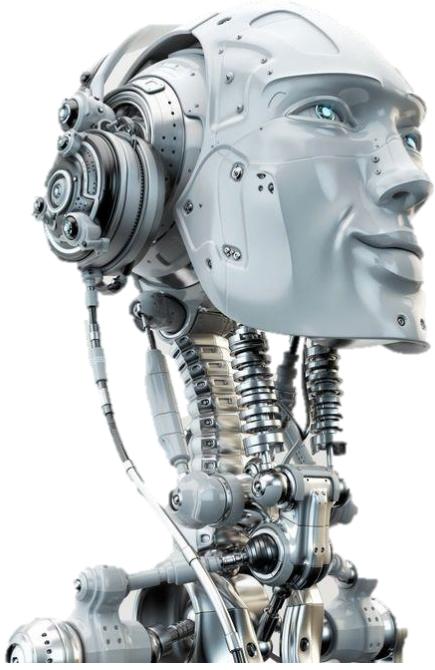

İç Ortam Havası Dezenfeksiyonunda Ultraviyole, Ozon ve Hidrojen Peroksit Kullanımı (Ayşe Elif Ateş)

İç Ortam Havası Dezenfeksiyonunda Ultraviyole, Ozon ve Hidrojen Peroksit Kullanımı

Ayşe Elif ATEŞ[1]
[1]*İstanbul Üniversitesi-Cerrahpaşa Mühendislik Fakültesi Çevre Mühendisliği Bölümü, E-mail: elifdenizler@istanbul.edu.tr*

1. Giriş

Patojenlerin bulaşmasında ortam havasının kirlenmesi ve kontamine yüzeylerin rolü daha net anlaşıldıkça ortam dezenfeksiyonun önemi artmıştır. Ancak yüzeyden bulaşma riski mikroorganizma türü, hasta hassasiyeti, kişisel hijyen gibi birçok faktöre bağlıdır. Yapılan çalışmalar araştırıldığında dezenfeksiyon sonrası kalan yüzey kontaminasyonu ile bulaş riski arasındaki ilişki ayrıntılı olarak çalışılmadığı görülmüştür. Bununla birlikte bulaş riskinin yüzey kontaminasyon seviyesiyle orantılı olduğuna dair sınırlı çalışma bulunmaktadır. Geleneksel temizlikte kullanılan deterjanlar kirlenmiş ortama insan operatör tarafından uygulandığı için ortam dezenfeksiyonun verimli şekilde gerçekleştirilmesinde dezenfektanların uygun kullanım yöntemlerinin seçilmesi ve ortam havasının yüzeylerle birlikte dezenfekte edilmesi oldukça önemlidir [1-4].

İç ortam havası dezenfeksiyonu özellikle hastanelerde, gıda sektöründe ve ambulanslarda uzun yıllardır sağlanmaktadır. Ancak gelişen teknoloji ve iklim şartlarına bağlı olarak hava dezenfeksiyonu konutlarda, alışveriş merkezlerinde, benzin istasyonlarında ve ortak kullanıma açık birçok alanda ön plana çıkmaktadır. Tarihte Sars ve Mers virüslerinin neden olduğu salgınlarda dünya üzerinde çok sayıda insan ölmüştür. Bu salgın hastalıkların havadaki aerosollerle bulaşması iç ortam havası dezenfeksiyonun daha da kritik noktaya taşımaktadır. Havadaki canlı mikrobiyal sayılarını azaltmak için kimyasal aerosolizasyon (hidrojen peroksit), ozonlama veya ultraviyole (UVC) ışınlama dahil olmak üzere farklı yaklaşımlar geliştirilmiştir. İlki, hidrojen peroksit çözeltisinin havada bir sis halinde dağılımından oluşur. Bu teknik hem havada taşınan hem de ulaşılması zor olabilecek yüzeylerdeki mikroorganizmaların sayısını azaltır. Aerosol hidrojen peroksit, hücre membranlarına, DNA'ya ve diğer hücre bileşenlerine saldırabilen hidroksil içermeyen radikallerin oluşumuna yol açan oksidatif etkisinden dolayı çoğu mikroorganizma için etkili bir dezenfektandır. Ozonlama, havadaki mikroorganizmaları etkisiz hale getirmek için alternatif bir yöntemdir. Bu uygun maliyetli ve çevre dostu işlem, gıda endüstrisi üretim ve depolama tesislerinde havadaki küflerin etkisiz hale getirmiştir. UVC lambalar yeni gelişen sistemlerle iç ortam dezenfeksiyonunda portatif ve sabit olarak kullanılmaya başlanmıştır. Dezenfektanların bakteriler üzerindeki germisidal

etkileri kullanım alanları, dozları ve bakteri türü gibi farklı parametrelere bağlıdır [5-9].

Çalışma kapsamında UVC, ozon ve hidrojen peroksitin farklı ortamda iç ortam hava dezenfeksiyonu çalışmaları özetlenecektir. Yöntemler karşılaştırılarak avantaj dezavantajları açıklanacaktır.

2. Hidrojen Peroksitle Dezenfeksiyon

Hidrojen peroksit uygulamaları aerosol ve buhar olmak üzere ikiye ayrılmaktadır. Yaygın kullanım şekli otomatik sistemlerdir. Operatörlere olan bağlılığı azaltmak ve insan hatası olasılığını en aza indirgemek için dezenfeksiyonun kritik olduğu alanlarda otomatik sistemler yaygın olarak kullanılmaktadır. Teknolojideki yeni gelişmelere rağmen otomatik sistemler yeni değildir. Kullanılacak olan alanlara ve istenen dezenfeksiyon verimine bağlı olarak seçilmesi gereken sistemler farklılık göstermektedir.

2.1. Buhar Hidrojen Peroksit

Buhar hidrojen peroksit (VHP) sistemlerinde buharlaştırılmış hidrojen peroksit ve çözeltileri kullanılmaktadır. Dezenfeksiyonda oksijen gazı ve klordioksit kullanımından kaynaklanan yüzeylerde kalıntı, korozyon, toksisite ve kanserojen olma gibi teknik sorunlara alternatif olarak görülmektedir. Araştırmacılar VHP sistemi spesifik mikrobiyal indirgemede kullanılabilecek umut vadeden teknik olarak görmektedir. VHP'nin avantajlarından biri kullanılabilecek cihaz farkı olmaksızın uygun sıcaklıkta buharlaştırılması sonucu dezenfeksiyon verimlerinin birbirine yakın olmasıdır. Fakat hidrojen peroksit hızlı bir şekilde su ve oksijene parçalandığı için ortamda bulunması gereken H_2O_2 konsantrasyonunun detaylı olarak hesaplanması gerekmektedir. Sıcaklık, basınç ve konsantrasyon gibi işletim parametrelerinin doğru ayarlanması durumunda su ve hidrojen peroksitin yoğunlaşması önlenebilmektedir [10-11].

H_2O_2 buhar dezenfeksiyon sistemleri sızdırmazlığı sağlanmış kapalı bir alanda homojen dağılım elde etmek için yüksek hızlı bir hava akımı yoluyla %30-35'lik sulu hidrojen peroksitin ısıtılarak buhar fazına geçirilmesidir. Mobil buhar hidrojen peroksit (VHP) dezenfeksiyon sistemlerinde H_2O_2 konsantrasyonunu, sıcaklığı ve bağıl nemi ölçen ekipmanlar bulunmaktadır. Sistemler çalıştıktan sonra dezenfeksiyon sonrası ortam havalandırması yaparak kalıntı oluşmasını önlemektedir. Dezenfeksiyon sonrası havalandırma yapılması ortamdaki konsantrasyonunun insan sağlığına zarar vermeyecek konsantrasyona (<1ppm) kısa süre içerisinde düşmesini sağlamaktadır. Otomatik VHP dezenfeksiyon cihazları insanların

maruziyetini sınırlandırmak amacıyla uzaktan kumandayla çalışmaktadır. Ortamdaki hava doygun hale gelene ve H_2O_2 yüzeyde yoğunlaşmaya başlayana kadar verilmektedir. Böylece hem ortam havası hem de yüzey dezenfeksiyonu sağlanmış olmaktadır. Ortam içinde, döngünün başlamasından önce ayarlanmış bir nem seviyesine ulaşmak için tasarlanmış entegre bir havalandırma ünitesi ve nemlendiriciye sahip bir jeneratöre sahiptir. Bu sistemler ameliyathanelerde, ambulanslarda, sızdırmazlığı sağlanmış ofislerde (insan yokken) kullanılmaktadır [12-17].

2.2. Aerosol Hidrojen Peroksit

Aerosol hidrojen peroksit (aHP) sistemleri ortama farkı boyutlarda (büyük boyut olarak 8-10 µm, küçük boyut olarak 0,5 µm) aerosol vermektedir. Bazı sistemler %35'lik hidrojen peroksit aerosolü kullanırken bazı sistemlerde gümüş içeren H_2O_2 çözeltisi kullanılmaktadır. Bu sistemler bazen "kuru sisli hidrojen peroksit" olarak bilinmektedir. Ortam dezenfeksiyonu çalışmalarında tipik olarak önerilen değer 6mL/m^3'dir. Ortama aHP sisteminde aerosol çoğu sistemde herhangi bir aktif havalandırma olmaksızın genellikle doğal olarak ayrışmaya bırakılır, ancak sürenin azaltılabilmesi için aktif havalandırma sistemi gerekmektedir [18-20].

aHP sisteminin kullanımı basittir. VHP ve UVC sistemlerine kıyasla nispeten daha ucuzdur. Ancak büyük alanları dekontamine etme kapasitesi sınırlı olduğu için birden fazla jeneratör gerekli olabilir. Dezenfeksiyon döngüleri sırasında ortamdan hiçbir sızıntının meydana gelmemesini sağlamak ve mahfaza içindeki hidrojen peroksit konsantrasyonunun sağlık ve güvenlik maruziyet sınırlarının altında olduğunu doğrulamak için kapılar ve havalandırma delikleri kapatılmalı ve güvenlik monitörleri kullanılmalıdır. Bildirilen döngü süreleri, birden çok döngü için 3–4 saat ve tek döngü için 2 saattir. Bununla birlikte, hidrojen peroksit konsantrasyonlarının odaya yeniden girmeden önce sağlık ve güvenlik sınırlarının altında olmasını sağlamak için el tipi sensörler kullanıldığında, tek kişilik odalar için döngü süreleri önemli ölçüde daha uzun olabilir. Birkaç çalışma, etken maddenin homojen dağılımının elde edilemediğini göstermektedir, bunun nedeni aerosol formunda hidrojen peroksitin tek yönlü şekilde ortama verilmesi ve parçacıkların yerçekiminden etkilenmesidir [21-23].

3. UV ile Dezenfeksiyon

UVC' lambaların kullanımı kolaydır. VHP sisteminde olduğu gibi kapı veya havalandırma deliklerinin kapatılmasını gerektirmez ve nispeten kısa bir çevrim süresine sahiptir. Bazı UVC sistemleri, döngüyü belirlemek için yansıyan doz ölçümüne dayandığından, UVC'yi yansıtmayan veya verimsiz

bir şekilde yansıtan (cam gibi) yüzeylerin varlığı, sıcaklık ve nemdeki değişiklikler ve ampullerin yaşını etkilemektedir. UV ışığının yoğunluğu, kaynağa olan mesafenin karesiyle birlikte dağılır, bu da tekli UVC cihazlarının tek odalarda daha büyük alanları dezenfekte etme kapasitesini sınırlar. UVC'nin yüzey malzemeleri üzerindeki uzun vadeli etkisi açıklanmamıştır. UVC, diğer ARD sistemlerine kıyasla daha pahalıdır [24-27].

185 nm'de kısa dalga UV radyasyonu, oksidasyon işlemi için aktive edilen ortam havasındaki oksijenden ozon üretmektedir. UV oksidasyonu, çıkış havasındaki kirleticileri parçalayarak dezenfeksiyon sağlamaktadır. Dezenfeksiyon konusunda hassas olan alanlara temiz hava sağlamak için, filtre ve UV ışığının bir kombinasyonu tavsiye edilmiştir. Havadaki UV geçirgenliği (UVT) suya göre daha yüksek olduğu için büyük bir havalandırma kanalında gerekli olan lamba sayısı kullanım açısından makul seviyededir. Yaygın hava yoluyla bulaşan virüs ve bakteriler, UV ile kolayca deaktive edilir. Mantarlar, küfler ve sporlar hava sıcaklığına ve neme bağlı olarak yüksek UV direncine sahip olması nedeniyle dezenfeksiyonda daha yüksek dozlara ihtiyaç duyulmaktadır [28,29].

Hareketli hava akımında, genellikle kuvars manşon olmadan yüksek voltajlı lambalar kullanılmaktadır. UV lamba armatürleri, bakteri ve küfün toplanıp büyüyebileceği yüzeyleri tamamen ışın verecek şekilde yerleştirilmelidir. Bu sistemlerin verimli bir şekilde tasarlanmasını ve doğrulanmasını sağlamak için matematiksel modelleme yazılımı ve biyoassay testleri geliştirilmiştir. Düşük işletme maliyetleri ve uygun ekipman seçimi UVC lambaların kullanımın maliyetini azaltabilmektedir [24, 27,30].

İklimlendirme sistemlerinde UVC lambaları soğutma bataryalarında veya hava akımını doğrudan dezenfekte etmek için kullanılmaktadır. UVC kullanılarak dezenfeksiyonun diğer avantajı koku giderimi tuvaletlerde, otellerde, restoranlarda, yemekhanelerde, karavan römorklarında ve arabalarda, mutfak davlumbazlarında koku giderimi sağlamasıdır. 40°C'nin altındaki hava sıcaklıkları için, standart ozon üreten lambaların kullanımı tercihe bağlıyken daha yüksek sıcaklıklar için ozon üreten lambalarının kullanılması şiddetle tavsiye edilmektedir [28-30].

4. Ozon ile Dezenfeksiyon

Ozon, mikroorganizmaları etkili bir şekilde öldürebilen, iyi bilinen güçlü bir oksidanttır. Havayı dezenfekte etmek için ozonun kullanımına yönelik çalışmalar nispeten sınırlı olmasına, deneysel sonuçlar ozonun suda olduğu gibi etkili bir hava dezenfektanı olabileceğini göstermektedir. Aslında ozon,

klor ve hipoklorit gibi diğer yaygın dezenfektanlardan çok daha güçlü bir oksitleyicidir. Dezenfeksiyon işlemi sırasında trihalometanlar (THM) gibi kanserojen yan ürünlerin oluşma olasılığı nedeniyle birçok ülkede klor veya hipoklorit kullanımı önemli ölçüde azalmıştır. Aksine ozon dezenfeksiyonu herhangi bir zararlı kalıntı üretmez ve kalan ozonun tamamı kısa sürede oksijene dönüşür. Ozon bu nedenle çevre dostu bir dezenfektan olarak kabul edilir. Ozonun güçlü oksitleme gücüne ek olarak, ozonun özellikleri aynı zamanda ideal bir hava dezenfektanı olmasına yardımcı olmaktadır. UV radyasyonu ve HEPA filtrenin aksine ozon, odanın her köşesine nüfuz edebilen bir gazdır, böylece tüm odayı etkili bir şekilde dezenfekte edebilir. Fakat ozon kullanımında en önemli ve kritik nokta 1 ppm'den daha yüksek konsantrasyona sahip ozon, insan sağlığı üzerinde olumsuz etkilere sahiptir ve ozonun hava dezenfeksiyonu için kullanılması, etrafta insanlar varsa genellikle tavsiye edilmemektedir [31-33].

5. Sonuç ve Tartışma

Çalışma kapsamında UV, ozon ve hidrojen peroksitin iç ortam dezenfeksiyonunda kullanımı açıklanmıştır. Buhar hidrojen peroksit yüksek dezenfeksiyon verimine sahip olmasına rağmen kullanılacak alanın sızdırmazlığının sağlanma zorunluluğu kullanımını oldukça sınırlandırmaktadır. Ayrıca hidrojen peroksitin ve suyun yoğunlaşarak ortam yüzeyinde kalması içeride kullanılacak malzemede zamanla korozif etki yaratacağından tavsiye edilmemektedir. Buharın ortam içerisinde homojen halde her yere dağılabilmesi, ortam içerisinde aşınmaya maruz kalacak malzemenin bulunmaması, sızdırmazlığın sağlanması gibi VHP sistemlerinin özel kullanım şartları ameliyathanelerde sağlanabildiği için genellikle bu ortamlarda kullanılmaktadır. VHP sisteminin aksine aerosol hidrojen peroksit kullanımı oldukça küçük boyutlardaki ortamlarda sağlanabilmektedir. Homojen halde dağılmaması ve odanın uzak köşelerine ulaşamaması diğer sistemlere kıyasla büyük bir dezavantajdır.

Ozon kullanımı VHP sistemi kullanımına kıyasla daha avantajlıdır. Sızdırmazlığın sağlanması gerekli değildir ayrıca yoğunlaşma sorunları yaşanmamaktadır. Hidrojen peroksit kadar kuvvetli bir oksitleyici olan ozon daha düşük maliyetli ve işletmesi kolay bir sistemdir. Ancak UVC ile kıyaslandığında sistemin kullanılacağı ortama göre avantaj/dezavantajları değişmektedir. Alanın büyümesiyle birlikte ozon kullanımı maddi açıdan UVC kullanımına göre daha avantajlıdır. Ancak orta ölçekli ve insanların olduğu ortamda UVC kullanımı kalıntı sorunu olmadığı ve sensörlerle çalışarak insan sağlığına olumsuz etkisi bulunmadığı için daha avantajlıdır.

UVC kullanılan sistemler lambaların fiyatlarının yüksek olması nedeniyle kurulum maliyeti yüksek sistemlerdir. Üreticilerin lamba özellikleri hakkında

yeterli bilgi paylaşmaması projelendirmede hatalara sebep olmaktadır. Bu durum dezenfeksiyon verimini düşürmektedir veya maliyeti yükseltmektedir. Belgelendirilmiş UVC lambaların kullanımı hidrojen peroksit buhar ve aerosolü ile dezenfeksiyonuyla karşılaştırıldığında daha yüksek verime sahiptir ve güvenilirdir. Bu sistemlerin kullanımı ortam havasında bulunan kirleticiye, alana, maddi yeterliliğe, malzeme tedarikine bağlı olarak değişmektedir.

Referanslar

[1] Otter JA, Yezli S, French GL. The role played by contaminated surfaces in the transmis- sion of nosocomial pathogens. Infect Control Hosp Epidemiol 2011;32:687–99.

[2] Mitchell BG, Dancer SJ, Anderson M, Dehn E. Risk of organism acquisition from prior room occupants: a systematic review and meta-analysis. J Hosp Infect 2015;91:211–7.

[3] Shaughnessy MK, Micielli RL, DePestel DD, et al. Evaluation of hospital room assign- ment and acquisition of Clostridium difficile infection. Infect Control Hosp Epidemiol 2011;32:201–6.

[4] Huang SS, Datta R, Platt R. Risk of acquiring antibiotic-resistant bacteria from prior room occupants. Arch Intern Med 2006;166:1945–51.

[5] Hayden MK, Blom DW, Lyle EA, Moore CG, Weinstein RA. Risk of hand or glove con- tamination after contact with patients colonized with vancomycin-resistant enterococcus or the colonized patients' environment. Infect Control Hosp Epidemiol 2008;29:149–54.

[6] Stiefel U, Cadnum JL, Eckstein BC, Guerrero DM, Tima MA, Donskey CJ. Contamination of hands with methicillin-resistant Staphylococcus aureus after contact with environmental surfaces and after contact with the skin of colonized patients. Infect Control Hosp Epidemiol 2011;32:185–7.

[7] Kramer A, Schwebke I, Kampf G. How long do nosocomial pathogens persist on inani- mate surfaces? A systematic review. BMC Infect Dis 2006;6:130.

[8] Walder M, Holmdahl T. Reply to Roberts. Infect Control Hosp Epidemiol 2012;33:312–3.

[9] Roberts CG. Hydrogen peroxide vapor and aerosol room decontamination systems. Infect Control Hosp Epidemiol 2012;33:312.

[10] Boyce JM. New approaches to decontamination of rooms after patients are discharged. Infect Control Hosp Epidemiol 2009;30:515–7.

[11] Otter JA, Yezli S. A call for clarity when discussing hydrogen peroxide vapour and aero- sol systems. J Hosp Infect 2011;77:83–4.

[12] Hall L, Otter JA, Chewins J, Wengenack NL. Use of hydrogen peroxide vapor for deac- tivation of Mycobacterium tuberculosis in a biological safety cabinet and a room. J Clin Microbiol 2007;45:810–5.

[13] Ray A, Perez F, Beltramini AM, et al. Use of vaporized hydrogen peroxide decontami- nation during an outbreak of multidrug-resistant Acinetobacter baumannii infection at a long-term acute care hospital. Infect Control Hosp Epidemiol 2010;31:1236–41.

[14] Health Do, Agency NPaS. HCAI Technology Innovation Programme. Showcase Hospitals report number 3. The Bioquell Hydrogen Peroxide Vapour (HPV) Disinfection System; 2009. Available from, www.clean-safe-care.nhs.uk.

[15] Otter JA, Yezli S. Cycle times for hydrogen peroxide vapour decontamination. Can J Microbiol 2010;56:356–7.

[16] Boyce JM, Havill NL, Cianci V, Flanagan G. Compatibility of hydrogen peroxide va- por room decontamination with physiological monitors. Infect Control Hosp Epidemiol 2014;35:92–3.

[17] EPA. Compatibility of material and electronic equipment with hydrogen peroxide and chlorine dioxide fumigation. Assessment and evaluation report; 2010.

[18] Orlando P, Cristina ML, Dallera M, Ottria G, Vitale A, Badolati G. Surface disinfection: evaluation of the efficacy of a nebulization system spraying hydrogen peroxide. J Prev Med Hyg 2008;49:116–9.

[19] Holmdahl T, Lanbeck P, Wullt M, Walder MH. A head-to-head comparison of hydro- gen peroxide vapor and aerosol room decontamination systems. Infect Control Hosp Epidemiol 2011;32:831–6.

[20] Fu TY, Gent P, Kumar V. Efficacy, efficiency and safety aspects of hydrogen peroixde vapour and aerosolized hydrogen peroixde room disinfection systems. J Hosp Infect 2012;80:199–205.

[21] Andersen BM, Rasch M, Hochlin K, Jensen FH, Wismar P, Fredriksen JE. Decontamination of rooms, medical equipment and ambulances using an aerosol of hy- drogen peroxide disinfectant. J Hosp Infect 2006;62:149–55.

[22] Hall L, Otter JA, Chewins J, Wengenack NL. Use of hydrogen peroxide vapor for deac- tivation of Mycobacterium tuberculosis in a biological safety cabinet and a room. J Clin Microbiol 2007;45:810–5.

[23] Mitchell BG, Digney W, Locket P, Dancer SJ. Controlling methicillin-resistant Staphylococcus aureus (MRSA) in a hospital and the role of hydrogen peroxide decon- tamination: an interrupted time series analysis. BMJ Open 2014;4:e004522.

[24] Boyce JM, Havill NL, Moore BA. Terminal decontamination of patient rooms using an automated mobile UV light unit. Infect Control Hosp Epidemiol 2011;32:737–42.

[25] Reeda NG. The history of ultraviolet germicidal irradiation for air disinfection. Public Health Rep 2010;125:15–27.

[26] Memarzadeh F, Olmsted RN, Bartley JM. Applications of ultraviolet germicidal irradi- ation disinfection in healthcare facilities: effective adjunct, but not stand-alone technol- ogy. Am J Infect Cont 2010;38:S13–24.

[27] Harrington BJ, Valigosky M. Monitoring ultraviolet lamps in biological safety cabinets with cultures of standard bacterial strains on TSA blood agar. Lab Med 2007;38.

[28] Tyan YC, Liao JD, Klauser R, Wu I, Weng CC. Assessment and characterization of deg- radation effect for the varied degrees of ultra-violet radiation onto the collagen-bonded polypropylene non-woven fabric surfaces. Biomaterials 2002;23:65–76.

[29] ECRI. Enhanced environmental disinfection systems. Health Devices 2011;40:150–62.

[30] Anderson P. Mutagenesis. Methods Cell Biol 1995;48:31–58.

[31] Sharma M, Hudson JB. Ozone gas is an effective and practical antibacterial agent. Am J Infect Control 2008;36:559–63.

[32] Zoutman D, Shannon M, Mandel A. Effectiveness of a novel ozone-based system for the rapid high-level disinfection of health care spaces and surfaces. Am J Infect Cont 2011;39:873–9.

[33] Li CS, Wang YC. Surface germicidal effects of ozone for microorganisms. AIHA J (Fairfax, Va) 2003;64:533–7.

CHAPTER

3

RESEARCH IN NATURAL AND ENGINEERING SCIENCES

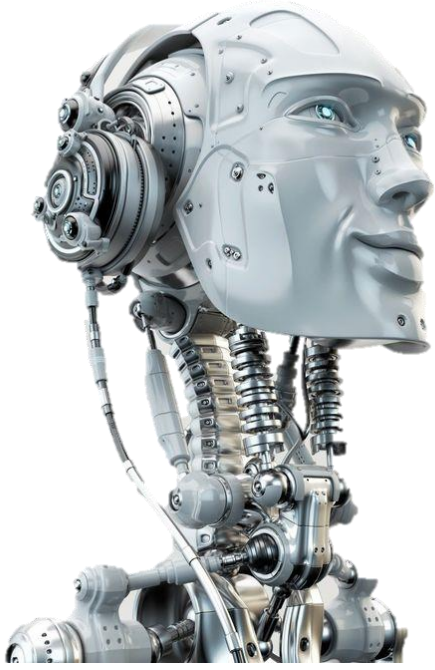

Monthly Variability in the Physical Properties of the Water Masses off Kyrenia (Çağrı Deliceırmak)

Monthly Variability in the Physical Properties of the Water Masses off Kyrenia

Çağrı Deliceırmak
Biosphere Research Centre, University of Kyrenia,
99320, Karakum, Girne, TRNC.
cagri.deliceirmak@kyrenia.edu.tr

Abstract

The first oceanographic time-series study of the Northern Cyprus, the Kıbrıs Time Series study (KTS), was carried out between November 2015 and June 2018, with monthly intervals on a five nautical mile zonal section offshore Kyrenia. Highly systematic, comprehensive and sub-meso scale KTS studies were conducted with relatively high frequency in order to investigate physical oceanographic features, their temporal and spatial variabilities, and interactions between coastal and open water masses in the Kyrenia region, north coast of Cyprus in the southwestern Cilician Basin. The results revealed that the general circulation of the Cilician Basin is a, highly complex and dynamic system, with meandering and reversing currents and reappearing cyclonic / anti-cyclonic mesoscale eddies with temporal and spatial variabilities. The dominant driving mechanism of the general circulation temporally and spatially changes between current systems and quasi-permanent eddies. Mixing and stratification processes, multi-layered vertical structure of the water column, and water masses (i.e. LSW, MAW, LIW and EMDW) identical to the Cilician basin were observed throughout the study. Furthermore, for the first time in literature, the possibility of regional Levantine Intermediate Water (LIW) formation in the Cilician Basin, and particularly in the study area was observed. Significant salinity increases and changes in physical oceanographic characteristics on the upper thermocline were observed in the study area, especially in 2017 and 2018.

Keywords: Oceanographic time series; Kıbrıs Time Series (KTS); LIW formation; Physical Oceanography; Salinity shift; Cilician Basin; Northern Cyprus.

1. Introduction

The Mediterranean Sea is a partially enclosed, practically isolated nonlinear oceanic system which interacts with and exchanges heat, mass and other properties with the North Atlantic Ocean. It is connected to the world ocean through the narrow (~13 km) and shallow (~300 m) Strait of Gibraltar (El-Geziry & Bryden, 2010; Robinson, Leslie, Theocharis, & Lascaratos, 2001). The Mediterranean Sea covers a surface area of about $2.5x10^6$ km^2. It is divided into two sub-basins: The Western Mediterranean Basin ($0.85x10^6$ km^2) and the Eastern Mediterranean Basin ($1.65x10^6$ km^2), linked with the shallow Strait of Sicily where maximum depths are about 500 meters at the western sill (El-Geziry & Bryden, 2010; Hainbucher et al., 2015). The average depth of the Mediterranean Sea is 1500 meters, and the maximum depth is about 5000 meters at the Ionian Sea, in the Eastern Mediterranean Basin (El-Geziry & Bryden, 2010). The geography and bathymetry of the Mediterranean Sea are presented in Figure 0.1.

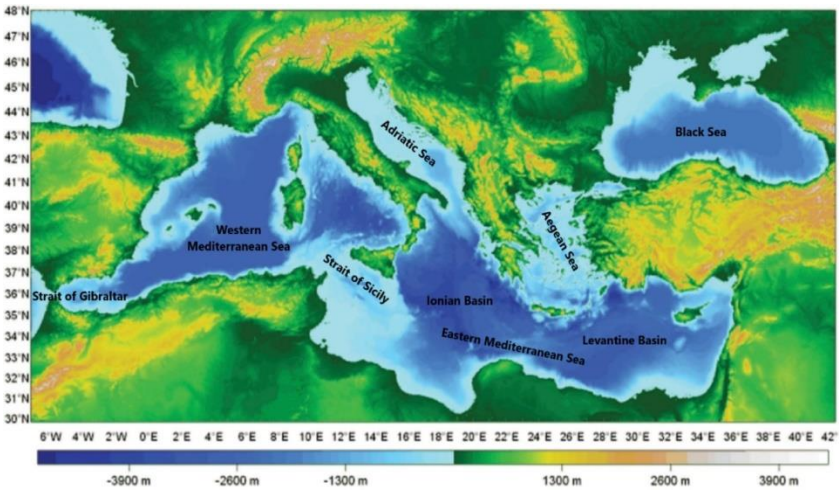

Figure 0.1: The geography and bathymetry of the entire Mediterranean Sea. Modified from (El-Geziry & Bryden, 2010)

The Mediterranean Sea is one of the most important and curious semi-enclosed oceanic systems. It can be considered as a mini oceanic laboratory. Most of the physical processes fundamental to the world ocean also occurs in the Mediterranean Sea either analogously or identically but on smaller spatial and time scales (Marullo, Santoleri, Malanotte-Rizzoli, & Bergamasco, 1999; Robinson et al., 2001; Velaoras, Krokos, Nittis, & Theocharis, 2014). Water mass formations, their transportations, air-sea interactions and

multiscale circulations are the most important physical oceanographic components of the Mediterranean Sea (Robinson & Golnaraghi, 1993). Wind stress, buoyancy fluxes and water exchange through the various straits in the Mediterranean Sea are the major forces that affect the general circulation due to heat and freshwater fluxes (Robinson et al., 2001).

The approximate evaporation rate is 1.27 m/year. Precipitation is 0.59 m/year, and river run-off is 0.010 Sverdrup (Sv). Inflow of the Atlantic Water is 0.72-0.92 Sv and outflow of the Mediterranean water is 0.68-0.88 Sv (Robinson et al., 2001; Tanhua et al., 2013). As the evaporation exceeds precipitation and river run-off, the entire Mediterranean Sea is an evaporation (concentration) basin (Malanotte-Rizzoli & Hecht, 1988; Robinson et al., 2001; Tanhua et al., 2013). Heat and freshwater deficits (Pinardi et al., 2015) are balanced by the two-layered fluxes through the Strait of Gibraltar (Hainbucher et al., 2015; Hecht, Pinardi, & Robinson, 1988; Malanotte-Rizzoli & Hecht, 1988; Pinardi et al., 2015; Salihoğlu et al., 1990). The upper layer is the less saline and relatively warm influx of Atlantic Water at surface and subsurface depths. The lower layer is the saltier and relatively colder efflux of Mediterranean Water at intermediate depths which are separated with salinity and temperature gradients at depths of about 150 meters (Malanotte-Rizzoli & Hecht, 1988; Robinson et al., 2001). Particularly the efflux of Mediterranean Water plays an important role. It is balancing the mass deficit of the Mediterranean Sea, and also transports saltier waters to the North Atlantic Ocean, thus contributes to the North Atlantic Deep Water (NADW) formation process and even possibly to the global thermohaline circulation (Bergamasco & Malanotte-Rizzoli, 2010; Malanotte-Rizzoli & Robinson, 1988; Robinson & Golnaraghi, 1993; Velaoras et al., 2014). The Mediterranean Sea is also connected to the Black Sea through the relatively narrow and shallow Turkish Strait System (The Dardanelles/The Marmara Sea/The Bosphorus) and to the Red Sea through the Suez Canal. According to a review by Unluata et al., (1990), in comparison to the Strait of Gibraltar, water exchanges between the Mediterranean Sea and the Black Sea are relatively small (inflow: 0.039 Sv, outflow: 0.030 Sv) but still significant (Tanhua et al., 2013). Water exchanges through the Suez Canal are not significant due to its small size (Malanotte-Rizzoli & Hecht, 1988).

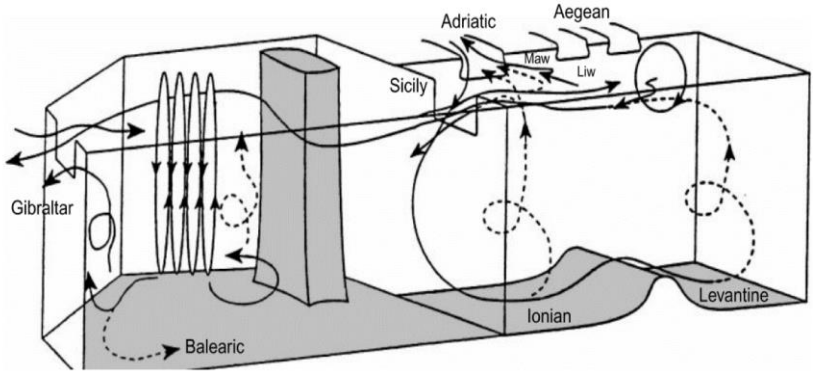

Figure 0.2: Schematic representation of general circulation and thermohaline cells of the Mediterranean Sea (Robinson et al., 2001).

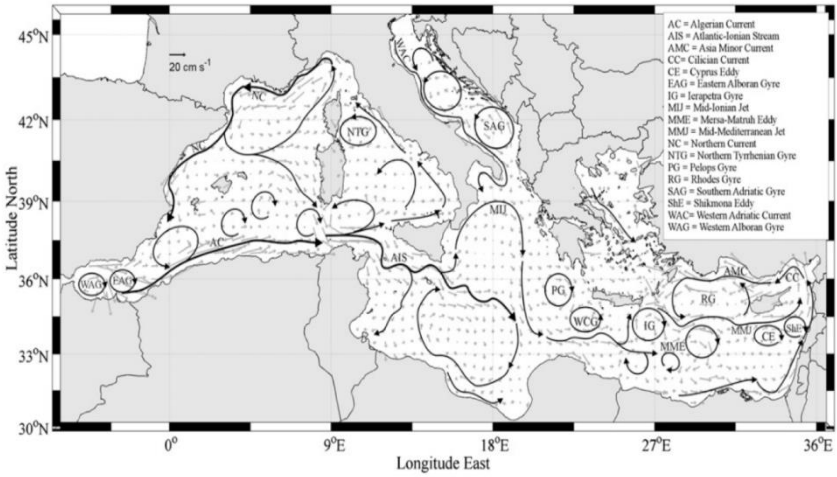

Figure 0.3: Schematized representation of the mean surface geostrophic circulation in the Mediterranean Sea (Poulain et al., 2010).

1.1. General Circulation of the Mediterranean Sea

General circulation of the Mediterranean Sea, including the thermohaline circulation (vertical circulation) (Figure 0.2) is a complex and dynamic system. It composed and interacts on different spatial (i.e. basin scale, sub-basin scale and mesoscale) and temporal scales (Cardin, Civitarese, Hainbucher, Bensi, & Rubino, 2015; Malanotte-Rizzoli & Robinson, 1988; Robinson et al., 1991, 2001; The POEM Group, 1992). The Mediterranean Sea circulation is generally characterised by cyclonic gyres in northern regions and anti-cyclonic gyres in southern regions (Pinardi et al., 2015). General circulation effected by multiple driving forces (i.e. internal dynamics, atmospheric conditions and topography), which forms meandering

and bifurcating currents and jets, permanent and quasi-permanent gyres and energetic eddies (Figure 0.3) (Robinson et al., 2001).

As shown in Figure 0.4, the general circulation pattern of the Mediterranean Sea is determined by three distinguished water masses (surface, intermediate and deep waters) which flow separately and independently both in the Eastern and Western Mediterranean basins (El-Geziry & Bryden, 2010; Hecht et al., 1988). In the surface layer, relatively warm and fresh Atlantic Water (AW) inflows to the Mediterranean Sea through the Strait of Gibraltar. It circulates to the easternmost part of the Mediterranean Sea, to the Levantine Basin, between the sea surface and ~150 meters, with an anti-clockwise pattern (El-Geziry & Bryden, 2010; Hecht et al., 1988; Malanotte-Rizzoli & Hecht, 1988; Salihoğlu et al., 1990). Relatively colder and saltier Levantine Intermediate Water (LIW), which forms locally in the Levantine Basin, flows westward from Levantine Basin at intermediate depths, between 150 and 600 meters, and outflows to the Atlantic Ocean through the Strait of Gibraltar (El-Geziry & Bryden, 2010; Hecht et al., 1988; Malanotte-Rizzoli & Hecht, 1988). Due to the shallow sill at the Strait of Sicily, only AW and LIW exchange between Western and Eastern Mediterranean basins (Hecht et al., 1988; Alex Lascaratos, Roether, Nittis, & Klein, 1999; Pinardi et al., 2015). These two water masses, the AW and the LIW at the surface and intermediate depths, characterise the open cell of the upper thermohaline circulation (thermocline circulation) in the Mediterranean Sea. The AW spreading from the Strait of Gibraltar to the Levantine Basin, transforming to LIW by convecting in Levantine Basin and returning to the Atlantic Ocean through the Strait of Gibraltar (Bergamasco & Malanotte-Rizzoli, 2010; Alex Lascaratos et al., 1999).

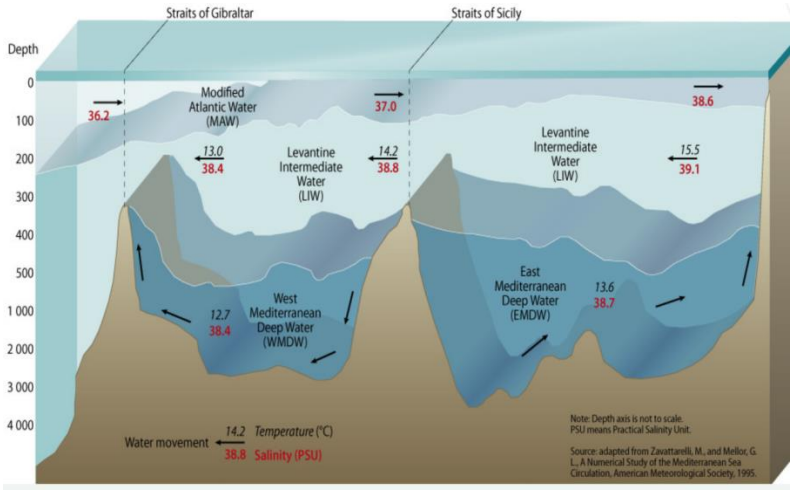

Figure 0.4: Water masses of the Mediterranean Sea (adapted from http://www.grida.no/resources/5885).

Since the shallow sill of the Strait of Sicily acts as a natural barrier between the Eastern and the Western Mediterranean Basins, deep waters forms separately and independently both in the Western and the Eastern Mediterranean Basins (Hainbucher et al., 2015; Alex Lascaratos et al., 1999). Closed-cell internal thermohaline circulations and deep-water formations both in Eastern and Western Basins show distinct differences but also some analogies to each other (Hainbucher et al., 2015; Alex Lascaratos et al., 1999; Pinardi et al., 2015; Robinson et al., 2001). Transformation of surface and intermediate waters to the deep waters characterise closed cells of thermohaline circulations both in the Western and the Eastern Basins (Bergamasco & Malanotte-Rizzoli, 2010; Alex Lascaratos et al., 1999). In the Western Basin, deep waters, referred to as the West Mediterranean Deep Water (WMDW), forms in the Gulf of Lions during winter seasons by excessive cooling and evaporation due to local meteorological events, cold and dry northerly winds, the "Mistrals" (Alex Lascaratos et al., 1999). Presence of cyclonic circulation and the LIW at intermediate depths are crucial in the formation of deep waters in the area (Alex Lascaratos et al., 1999). The properties of the East Mediterranean Deep Water (EMDW) and closed cell of thermohaline circulation are discussed in the next sections.

1.2. The Eastern Mediterranean Basin

The Eastern Mediterranean Basin is the largest body of water (1.65×10^6 km^2) in the Mediterranean Sea which is located at the east of the Sicily Strait (El-Geziry & Bryden, 2010; Malanotte-Rizzoli & Hecht, 1988). The Eastern Mediterranean basin is divided into four sub-basins, namely the Ionian, the Levantine, the Adriatic and the Aegean.

The Ionian is the largest and the deepest basin of the Eastern Mediterranean. The Adriatic lies between Italy and the Balkans. It is connected to the Ionian Sea through the Strait of Otranto. The Aegean is connected to the Levantine Basin through straits between Greece, Turkey, Rhodes and Crete. The Levantine Basin, which is the subject of this study, is located at the easternmost part of the Mediterranean Sea. Average depths of the Levantine Basin are 2500 – 3000 meters, with a maximum depth of 4500 meters located southeast of Rhodes (El-Geziry & Bryden, 2010; Malanotte-Rizzoli & Hecht, 1988). Two major sub-basins of the Eastern Mediterranean Sea are the Ionian and Levantine Basins, divided by the wide (300 km) and deep (1800 m) Cretan Passage. However, the flow between these two sub-basins is not significantly affected due to the large size of the Cretan Passage (Malanotte-Rizzoli & Hecht, 1988).

The Eastern Mediterranean Sea is partially enclosed, and exchanges heat, mass and other properties with adjacent seas (i.e. the Black Sea, the Sea of

Marmara, the Aegean Sea, the Adriatic Sea, the Levantine and Ionian Seas, the West Mediterranean) (Alhammoud, Béranger, Mortier, Crépon, & Dekeyser, 2005; Malanotte-Rizzoli & Hecht, 1988; Robinson et al., 1991). Hydrography and water masses of the Eastern Mediterranean Sea are characterised by local meteorological events, topographic features and water exchanges between the adjacent seas through the various straits (i.e. the Bosphorus and the Dardanelles, the Rhodes, the Karpathos, the Kassos, the Cretan Passage, the Otranto, the Sicily). These passages and straits control and determine the flow between basins (Cardin et al., 2015; Malanotte-Rizzoli & Hecht, 1988; Robinson et al., 1991). Although it is not adjacent to the Eastern Mediterranean Sea, the Strait of Gibraltar is very important for the Eastern Mediterranean hydrography and water masses. It feeds the Eastern Mediterranean with AW inflow and also connecting and controlling the fluxes between the Mediterranean Sea and the Atlantic Ocean (Malanotte-Rizzoli & Hecht, 1988).

1.2.1. Historical Background

The first oceanographic investigation in the Eastern Mediterranean Sea was carried out by the Austro-Hungarian ship Pola back in 1890. In 1912, Nielsen published the first Mediterranean Current Map based on the data collected by the Danish ship Thor in 1910 (Özsoy et al., 1991). Nielsen's picture, which for almost 50 years remained the most accepted and approved pattern, was defined the Mediterranean Sea as linear and stationary ocean with broad currents evolving smoothly and forming continuous circulation pattern from the Western to the Eastern Mediterranean Sea (Bergamasco & Malanotte-Rizzoli, 2010). From 1948 to 1968, several oceanographic cruises conducted in the region by different USA ships, French Calypso and Japanese Shoyo-Maru, but the results of these cruises did not significantly change the Nielsen's pattern (Özsoy et al., 1991).

In 1961, the German oceanographer Georg Wust discovered the water masses in the Mediterranean Sea as well as their formations, evolutions and properties (salinity, temperature, oxygen). He also discovered the open thermohaline circulation cell of the Mediterranean Sea (Bergamasco & Malanotte-Rizzoli, 2010; Tanhua et al., 2013; Wüst, 1961). In his publication (Wüst, 1961), he presented the inflow of AW, intermediate convection in the Levantine Basin and outflow of the tongue-like LIW to the Atlantic Ocean. In the same publication, he also presented the thermohaline circulation and deep-water formation locations in the Gulf of Lions and Southern Adriatic Sea (Bergamasco & Malanotte-Rizzoli, 2010).

During the mid-sixties, Russian oceanographers, led by Ovchinnikov, analysed the data collected from extensive Vavilov cruises in the

Mediterranean Sea and described the driving mechanisms of the Mediterranean Sea circulation, particularly AW and LIW circulation. They presented advanced geopotential maps and more importantly, they revealed the differences between summer and winter circulations (Özsoy et al., 1991).

Since the beginning of the sixties, Israeli oceanographers collected and analysed the data collected in south-eastern Levantine Basin. Contrary to Nielsen's circulation map, they found anti-cyclonic circulation in the region (Özsoy et al., 1991). Beginning from the mid-seventies, Israeli oceanographers started to use modern Conductivity – Temperature – Depth (CTD) methodology. They conducted extensive research, the "Marine Climate (MC Series)", over a period for more than five years in the south-eastern Levantine Basin. The results of MC Series revealed an anti-cyclonic pattern in the region with mesoscale eddies, jets and filaments (Özsoy et al., 1991).

Until the beginning of the eighties, Wust's description remained the undisputed circulation pattern of the Mediterranean Sea (Bergamasco & Malanotte-Rizzoli, 2010). In 1982, an international cooperative research program, the POEM (Physical Oceanography of the Eastern Mediterranean), supported by the IOC of UNESCO was initiated. The program aimed to investigate and determine the circulations patterns, fundamental processes of the Eastern Mediterranean Sea, and also to construct realistic models for physical, chemical and biological studies. Scientists from Turkey, Croatia, Cyprus, Egypt, England, France, Germany, Greece, Israel, Italy, UK and USA participated in the program (The POEM Group, 1992). The first field studies were conducted under the POEM-V program. Five general scientific cruises conducted with oceanographic vessels from Turkey, Israel, Greece, Italy and Germany between 1985 and 1987. Three more general scientific cruises were carried out between 1991 and 1995 under the POEM-BC program, with biological and chemical components. The last fieldwork of the POEM program, the "LIWEX Group (The Levantine Intermediate Water Experiment Group)" was carried out in the winter of 1995 (Bergamasco & Malanotte-Rizzoli, 2010). Basin scale, sub-basin scale and mesoscale upper thermocline circulation of the Eastern Mediterranean Sea, as well as its features, driving dynamics, structure and patterns were revealed by the results of fully reanalysed data of the POEM program. Additionally, results identified the densities of 29.05 – 29.10 kg/m^3 is the primary pathway of the LIW. The results also revealed that the Levantine Basin is a region where multiple and different water mass formations occurs (Bergamasco & Malanotte-Rizzoli, 2010; Hecht et al., 1988; Malanotte-Rizzoli & Hecht, 1988; Malanotte-Rizzoli & Robinson, 1988; Özsoy, Hecht, & Ünlüata, 1989; Özsoy et al., 1993; Robinson et al., 1991; The LIWEX Group, 2003; The POEM Group, 1992).

In late nineties and the 2000s, mostly national but also some international oceanographic researches were conducted in the north-eastern Levantine Basin and the Cilician Basin by the oceanographic institutes in Turkey. "Winter circulation and convection in Antalya Basin" (Onken & Yuce, 2000) and "Circulation, hydrographic and nutrient characteristics of the Cilician Basin" (Kucuksezgin & Pazi, 2006) are some of the relevant studies conducted in the region. In last twenty years, several national and multi-national studies are being continuously carried out by METU IMS in the region. The "Erdemli Time Series" (ETS) study, which is conducting by METU IMS in Mersin Bay over thirty years, is very important for the oceanographic studies in the region.

Most recently, the 114Y139 Code numbered TUBITAK Project (Salihoglu et al., 2019) was carried out in the Cilician Basin to investigate the physical, chemical and biological dynamics of the region.

1.2.2. General Circulation of the Eastern Mediterranean Sea

General circulation of the Eastern Mediterranean Sea is a highly complex and dynamic system. It consists of three different spatial scales (i.e. basin scale, sub-basin scale and mesoscale) in continuous interaction, which determines the general circulation patterns of the Eastern Mediterranean Sea (The POEM Group, 1992). As previously shown in Figure 0.2, the thermohaline circulation consists of an external (open) and an internal (closed) cell. The external thermohaline cell of the Eastern Mediterranean exchange waters with the West Mediterranean, thus with the Atlantic Ocean through the Strait of Sicily and Strait of Gibraltar respectively. The internal thermohaline cell circulates in the Eastern Mediterranean, which comprises the Ionian and the Levantine Basins (The POEM Group, 1992).

Atlantic Water (AW) enters to the Mediterranean Sea through the Strait of Gibraltar with 36.15 - 36.20 per mille of salinity and ~15.0 °C of temperature. It flows eastward with anti-clockwise pattern through the north coast of Africa, penetrates to the Eastern Mediterranean through the Strait of Sicily and spreads to the easternmost part of the Mediterranean Sea, to the Levantine Basin (Figure 0.3) (Bergamasco & Malanotte-Rizzoli, 2010; Hecht et al., 1988). Along its path to the Levantine Basin, AW bifurcates and penetrates to the Balearic Sea, the Tyrrhenian Sea and the Ionian Sea respectively, forms mostly anti-cyclonic gyres and meandering currents (Bergamasco & Malanotte-Rizzoli, 2010; El-Geziry & Bryden, 2010; Hecht et al., 1988; Malanotte-Rizzoli & Hecht, 1988). As it flows eastward, the AW is continuously modifying. Its depth and salinity increase (~37.50 per mille at the Strait of Sicily ~38.60 per mille at the Cretan Passage and >38.60 per mille in the Levantine Basin) due to atmospheric interactions and mixing

with the surface waters and waters underneath, and eventually transform to become Modified Atlantic Water (MAW) (Bergamasco & Malanotte-Rizzoli, 2010; El-Geziry & Bryden, 2010; Hecht et al., 1988; A Lascaratos, Williams, & Tragou, 1993; Malanotte-Rizzoli & Hecht, 1988; Özsoy et al., 1989). Although its salinity increases, MAW still maintains its low salinity characteristic, between 36.15 – 38.70 per mille and can be identified throughout the Mediterranean Sea. It is located just below the warm and saline surface mixed layer, Levantine Surface Water (LSW) in the eastern basin with a salinity of >39.10 per mille and temperature of ~25.0 °C (A Lascaratos et al., 1993), that forms due to excessive heat, evaporation and relatively weak winds during summer season. The LSW thus allows the MAW to maintain its relatively low salinity properties by limiting its atmospheric interaction (Akpinar, Yilmaz, Fach, & Salihoglu, 2016; Malanotte-Rizzoli & Hecht, 1988; Özsoy et al., 1989). During winter intense mixing processes and lower evaporation rates suppress the hot and saline surface water formation (LSW formation), and consequently, MAW depletes faster than in summer (Malanotte-Rizzoli & Hecht, 1988; Özsoy et al., 1989).

Excessive surface heat loss and evaporation due to local meteorological events, cold and dry north-northeasterly winds, the “Poyraz”, cause the LSW to become denser during winter, mix with the MAW and subsequently sink to intermediate depths, forming the Levantine Intermediate Water (LIW) (Akpinar et al., 2016; Bergamasco & Malanotte-Rizzoli, 2010; El-Geziry & Bryden, 2010; Özsoy et al., 1989; Robinson & Golnaraghi, 1993; The LIWEX Group, 2003). Water mass characteristics of the LIW are displayed in Table 0.1. LIW, can be identified throughout the Mediterranean Sea with its subsurface salinity maximum between 38.40 – 39.10 per mille, decreasing towards west (Hecht et al., 1988; Malanotte-Rizzoli & Hecht, 1988). LIW formation is not localised at Rhodes Gyre but occurs at several locations in the northern and southern Levantine basins. (The LIWEX Group, 2003; The POEM Group, 1992). Figure 0.2 The LIW, which is the predominant source of the salty Mediterranean efflux (Alex Lascaratos et al., 1999; Marullo et al., 1999; Robinson & Golnaraghi, 1993; The POEM Group, 1992) flows westward from Levantine Basin to the Strait of Gibraltar, at intermediate depths, between 200 and 600 meters. The LIW circulates below inflowing AW, mixing with the adjacent waters above and underneath, as shown in Figure 1.2. The LIW also mixes with the East Mediterranean Deep Water (EMDW) and the West Mediterranean Deep Water (WMDW) before outflow to the Atlantic Ocean with 38.40 per mille salinity and ~13.5 °C temperature (Bergamasco & Malanotte-Rizzoli, 2010; El-Geziry & Bryden, 2010; Malanotte-Rizzoli & Hecht, 1988; Robinson & Golnaraghi, 1993; Robinson et al., 2001; The POEM Group, 1992). As shown in Figure 0.5, one branch of the LIW recirculates into the Eastern Mediterranean Sea, one branch enters the Adriatic Sea where it contributes to the deep-water formation, and

another branch of the LIW exits through the Strait of Sicily just below inflowing MAW (The POEM Group, 1992). The net influx and efflux through the Strait of Sicily are estimated to be 1 – 1.5 Sv (Robinson & Golnaraghi, 1993; The POEM Group, 1992).

Table 0.1: Water mass characteristics of the Levantine Intermediate Water (LIW).
* adopted from (A Lascaratos et al., 1993).

	Temperature °C	Salinity per mille	Potential Density kg/m^3
*Wust [1961]	15.5	39.10	29.05
*Lacombe and Tchernia [1972]	15.7	39.10	28.98
*Özturgut [1976]	16.2 – 16.4	39.12 - 39.15	28.85 - 28.87
*Ovchinnikov [1984]	14.7 – 14.9	39.03 - 39.06	29.12 - 29.15
*Plakhin and Smirnov [1984]	14.5	38.85	29.06
*Hecht [1986]	15.5 ± 0.4	39.02 ± 0.05	28.91 - 29.01
*Hecht et al. [1988]	15.5 ± 0.5	38.98 ± 0.06	28.86 - 28.99
Küçüksezgin and Pazı [2006]	16.0 – 17.0	39.10 – 39.20	28.90 – 29.20
Salihoğlu et al. [2019]	16.0 – 17.0	39.10	28.87
This study [2015 – 2016]	~16.50	~39.10	~28.87
This study [2017]	~17.50	~39.21	~28.65
This study [2018]	~18.50	~39.39	~28.50

With the preconditioning of density increase due to saltiness, the internal thermohaline cell of the Eastern Mediterranean Basin is similar to the global "conveyor belt" in the North Atlantic but smaller in scale, with ~125 years of renewal time (Bergamasco & Malanotte-Rizzoli, 2010; Robinson & Golnaraghi, 1993; The POEM Group, 1992). Traditionally, the driving source of the internal thermohaline cell of the Eastern Mediterranean is the Adriatic Deep Water (ADW). It formed in the South Adriatic Sea during winter time when waters become denser and sink as a result of cooling and evaporation due to local meteorological events, cold and dry northerly winds, the "Bora" (Bergamasco & Malanotte-Rizzoli, 2010; Alex Lascaratos et al., 1999; Pinardi et al., 2015; Robinson et al., 2001; The POEM Group, 1992). Similar to the Western Basin, open ocean formation processes occur in this area with preconditioning of cyclonic gyre and with contributions of MAW and LIW (Alex Lascaratos et al., 1999; Robinson et al., 2001). ADW spreads out through the Otranto Straits, fills the deepest parts of the Ionian Sea and the Levantine Sea respectively and forms the East Mediterranean Deep Water (EMDW) (Bergamasco & Malanotte-Rizzoli, 2010; Alex Lascaratos et al., 1999; Robinson et al., 2001).

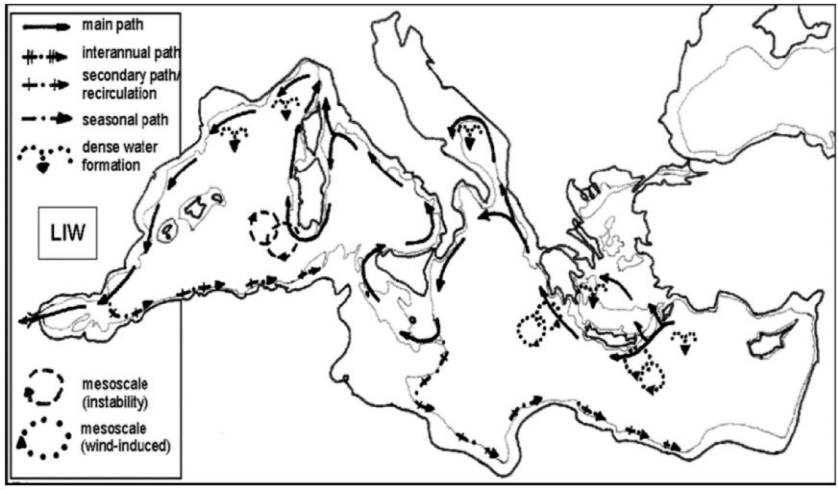

Figure 0.5: Levantine Intermediate Water (LIW) circulation at 500m depth in the Mediterranean basin. Adopted from (El-Geziry & Bryden, 2010).

In late 1980's and early 1990s, the POEM group identified warmer, high saline and denser water mass formations in the Southern Aegean Sea or the Cretan Sea. They also identified a transition, later named as Eastern Mediterranean Transient (EMT) that shifts the driving source of deep waters from the South Adriatic Sea to the South Aegean Sea or Cretan Sea (Figure 0.6) (Bergamasco & Malanotte-Rizzoli, 2010; Robinson et al., 2001). These denser waters, namely Cretan Intermediate Water (CIW) and Cretan Deep Water (CDW), formed in the Cretan Sea due to continuous salinity increases and excessive cooling in the area, spread out through the Cretan Arc Straits to the Ionian and Levantine Basins below the EMDW of Adriatic origin (Bergamasco & Malanotte-Rizzoli, 2010; Alex Lascaratos et al., 1999; Robinson et al., 2001). This transition replaced the old EMDW of Adriatic origin by lifting it several hundred meters in the water column and consequently changing the characteristics of intermediate and deep waters of the Eastern Mediterranean, even possibly the characteristics of the entire Mediterranean Sea (Bergamasco & Malanotte-Rizzoli, 2010; Alex Lascaratos et al., 1999; Robinson et al., 2001).

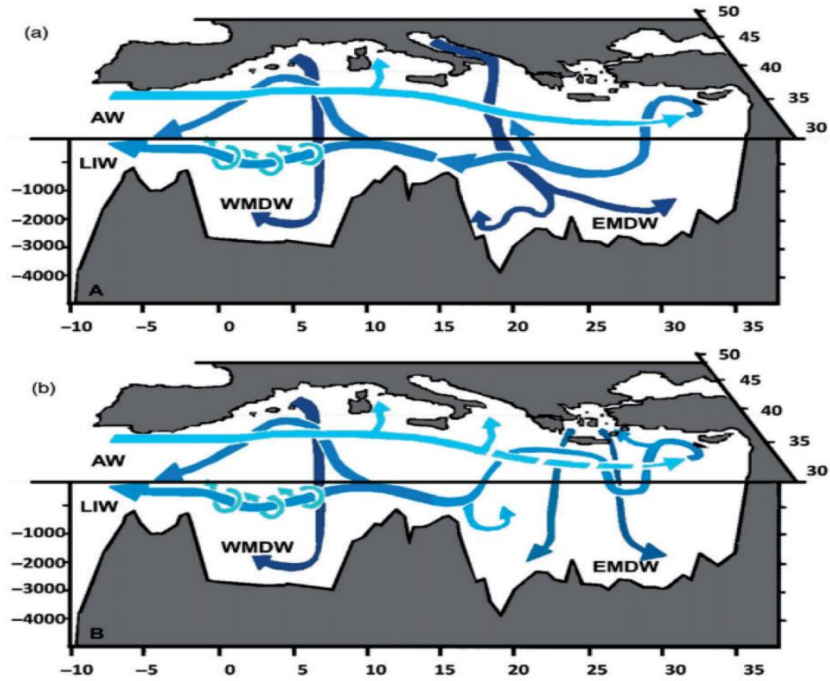

Figure 0.6: The Mediterranean Sea thermohaline circulation scheme. (a) is the behaviour of the Eastern Mediterranean Sea before the EMT. (b) is the behaviour of the Eastern Mediterranean Sea during EMT (Bergamasco & Malanotte-Rizzoli, 2010).

1.2.3. Sub-basin Scale and Meso-scale Circulations of the Eastern Mediterranean Sea

Circulation patterns of the Eastern Mediterranean Basin are characterised by energetic sub-basin scale cyclonic and anti-cyclonic gyres which are linked by interconnecting jets and currents with variable structures (i.e. spatial and temporal variabilities, shape, strength, meander pattern and bifurcation structure) (Robinson et al., 2001; The POEM Group, 1992). The major gyres and streams which determine the main thermocline circulation pattern are shown in Figure 0.7. The anti-cyclonic Ionian and Pelops gyres and cyclonic Cretan gyre are located in the Ionian Basin. The cyclonic Rhodes gyre, anti-cyclonic Mersa-Matruh gyre and anti-cyclonic Shikmona eddy are located in the Levantine Basin, Atlantic-Ionian Stream (AIS), Mid-Ionian Jet (MIJ), Mid-Mediterranean Jet (MMJ), Asia-Minor Current (AMC) and the Cilician Current (CC) are the major streams flows in the Eastern Mediterranean Basin (Robinson et al., 2001; The POEM Group, 1992).

Atlantic originated MAW penetrates to the Eastern Mediterranean Sea by AIS through the Strait of Sicily. It meanders first to the north into the

northern Ionian Sea then to the southeast to feed the MMJ. It continues to flow eastward through the Cretan Passage between Rhodes and Mersa-Matruh gyres to the easternmost part of the Levantine Basin (Bergamasco & Malanotte-Rizzoli, 2010; Robinson et al., 2001; The POEM Group, 1992). According to Bergamasco & Malanotte-Rizzoli (2010), the stream which forms sharp meanders in the Ionian Sea is named as MIJ and then it becomes MMJ, referred as Central Levantine Basin Current (CLBC) in (Özsoy et al., 1993; The LIWEX Group, 2003), before entering the Cretan Passage. Along its path, some part of MMJ encircles the Rhodes Gyre and eventually connects with westward flowing AMC, and some part encircles the Mersa-Matruh Gyre (Özsoy et al., 1993). MMJ bifurcates once more at the southwest of Cyprus where one branch flows northward through the west of Cyprus to feed the AMC (Özsoy et al., 1993; Robinson et al., 2001; The POEM Group, 1992). The second branch continues to flow east through south of Cyprus to the coasts of Israel where it bifurcates again to the north to feed the CC which feeds the AMC, and to the south to the Shikmona eddies (Robinson et al., 2001; The POEM Group, 1992).

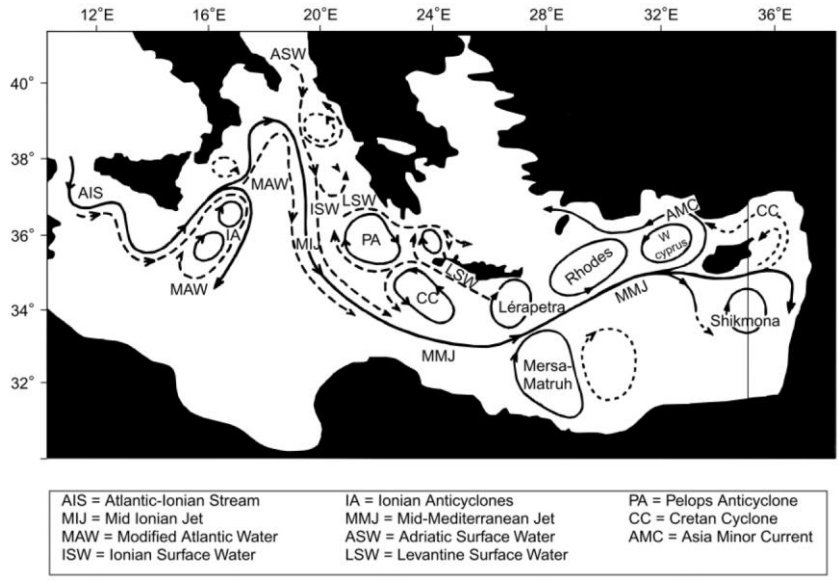

Figure 0.7: Sub-basin scale and mesoscale circulation features in the eastern Mediterranean (Robinson et al., 2001).

In the Ionian Basin, a broad and multi-centred Ionian anti-cyclonic system is located at the northwest Ionian Sea. Quasi-permanent anti-cyclonic Pelops and cyclonic Cretan gyres are located at the south of Peloponnesus Peninsula and Crete respectively (Bergamasco & Malanotte-Rizzoli, 2010). In the

Levantine Basin, the region between Rhodes and Cyprus is a broad cyclonic region, consist of few cyclonic centres including the Rhodes Gyre which the AMC is the northern border and the West Cyprus Gyre (WCG). Meso-scale and quasi-permanent anti-cyclonic eddies of Ierapetra, Antalya and Anaximander located in the southeast of Crete, in Antalya Basin and between the Anaximander Seamount and Turkish coast, respectively (Onken & Yuce, 2000). Mersa-Matruh is a strong anti-cyclonic gyre located off the Egyptian coast. Quasi-permanent Shikmona eddies are part of south-eastern Levantine anti-cyclonic system at south of Cyprus (Robinson et al., 2001; The POEM Group, 1992). Generally, the diameter of the sub-basin scale gyres varies between 200 and 350 km (Robinson et al., 2001). The average speed of the sub-basin scale gyres and jets in upper thermohaline is ~20 cm/s (Robinson et al., 2001; The POEM Group, 1992).

1.3. The Levantine Basin

As mentioned above, the Levantine Basin is the easternmost part of the Mediterranean Sea, encircled by northeast Africa, Asia Minor and Cretan Archipelago. It is the second-largest sub-basin of the Eastern Mediterranean Sea with a total volume of $7.5x10^5$ km^3. Levantine Basin communicates with the Ionian Basin through the Cretan Passage and with the Aegean Sea through the straits of Rhodes, Karpathos and Kassos. The continental shelf of the Levantine Basin is generally narrow except for the Gulf of Iskenderun and the Nile Fan. Major bathymetric features are shown in Figure 0.8; the Hellenic Trench (3000 – 3500 m) and the Herodotus Abyssal Plain (~3000 m) which are separated by the Mediterranean Ridge (~2500 m). Distinct sub-basins are the Rhodes (~4000 m), the Antalya (~2500 m), the Lattakia (~1500 m) and the Cilician (~1000 m), which is the particular subject of this study. The Anaximander Seamount (~1500 m), located between Rhodes and Antalya and the Eratosthenes Seamount (1000 m), located at the south of Cyprus are the other bathymetric features of the Levantine Basin (Özsoy et al., 1989).

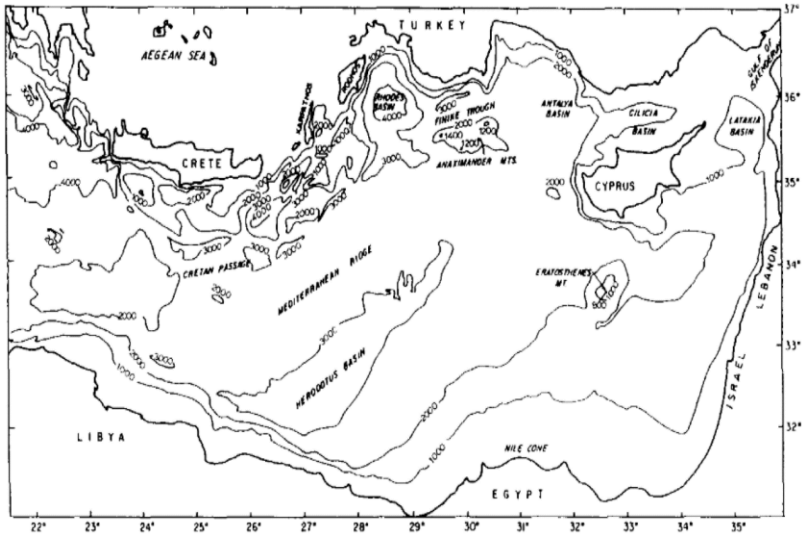

Figure 0.8: Bathymetry of the Levantine Basin (Özsoy et al., 1991).

The Cilician Basin is the north-eastern part of the Levantine Basin, located between the north of Cyprus and south of Turkey, from Antalya Basin to the Iskenderun Bay. The circulation of the Cilician Basin is a highly complex and dynamic system, with meandering and reversing currents and reappearing cyclonic/anti-cyclonic energetic mesoscale eddies with temporal variabilities (Kucuksezgin & Pazi, 2006; Özsoy et al., 1989, 1991). It is connected with the Lattakia Basin by a narrow sill with depths of ~ 700 meters extending from Cyprus (Cape Andreas) to Iskenderun at the east. At the west, it is connected with Antalya Basin through sharp depth gradients from 1000 meters to 2000 meters (Özsoy et al., 1989).

1.3.1. The Meteorology of the Levantine Basin

Meteorological events in the Levantine Basin shows extreme variabilities due to different atmospheric systems and the topography of the region (Akpinar et al., 2016; Özsoy et al., 1989). Summer and autumn seasons are dominated by Westerlies, Etesian and coastal sea breeze system. Northerly Etesian winds in the southern Aegean Sea reinforce dominant Westerlies which result in a west-northwest wind regime blowing over the Levantine Basin. On the other hand, extratropical cyclones and dry local wind systems, such as Poyraz and Sirocco winds, dominates the region during winter and spring seasons. (Özsoy et al., 1989). Extratropical cyclones arrive to the northern Levantine Basin mostly from the Ionian Basin but also North Africa. Following the cyclones, cold and dry north-northeasterly Poyraz winds blow

from the Taurus Mountains at the southeast coast of Turkey. The "Poyraz" wind causes excessive heat and buoyancy losses, which affect the oceanographic variability of the entire region (Özsoy et al., 1989). These significant buoyancy losses due to strong cold and dry winds are considered as the primary source of the LIW formation in the area (Onken & Yuce, 2000; Özsoy et al., 1989; Wüst, 1961). Warm and dry southerly winds, the Sirocco winds, blow from north African and Arabian Deserts, advecting warm and dry air masses to the region, and become humid at the northern Levantine Basin (Özsoy et al., 1989).

1.4. Aim of this Work

This study aims to investigate the formation and dissipation of sub-mesoscale and mesoscale physical oceanographic features, their temporal and spatial variabilities, and the interactions between coastal and open water masses off the coast of Kyrenia, Cyprus. Also, to understand physical oceanographic characteristics of the region and to determine any significant changes occurred since previous regional studies.

2. Materials and Methods

The oceanographic data presented in this study were collected within the framework of TUBITAK Project Code No:114Y139, entitled “Determination of the influence of anthropogenic and natural processes on the Cilician Basin (Between Turkish Republic of Northern Cyprus and Turkey) Marine Ecosystem”.

The project has been carried out from June 2015 to May 2018 in the Cilician Basin, to investigate physical and biogeochemical properties of the region. During the study, a total of eleven seasonal cruises conducted at a total of twenty-six stations (denoted as “T” and “A” stations in Figure 0.9). A further achievement of the project worth mentioning here is the first oceanographic time-series study of the Turkish Republic of Northern Cyprus (T.R.N.C), namely the “Kıbrıs Time Series (KTS)”, was established in November 2015, offshore of Kyrenia (denoted as “K” stations in Figure 0.10).

2.1. Kıbrıs Time Series Studies

Historically the first oceanographic time-series study, “Kıbrıs Time Series” (KTS) of the Turkish Republic of Northern Cyprus (T.R.N.C.), was established under the framework of TUBITAK Project 114Y139. KTS studies were the first oceanographic studies conducted by a local university

in the Turkish Republic of Northern Cyprus. KTS studies have been conducted monthly to investigate physical and biogeochemical properties and variabilities of the study area, and to investigate spatial and temporal interactions between coastal and open sea waters in the area. In this scope, highly systematic and comprehensive researches were conducted under the KTS studies. The first KTS cruise was conducted on 12th of November 2015, and a total of twenty-six cruises were conducted during the project. Although the TUBITAK Project Code No: 114Y139 had been terminated, KTS studies continue to be carried out by the own sources of the University of Kyrenia (UoK).

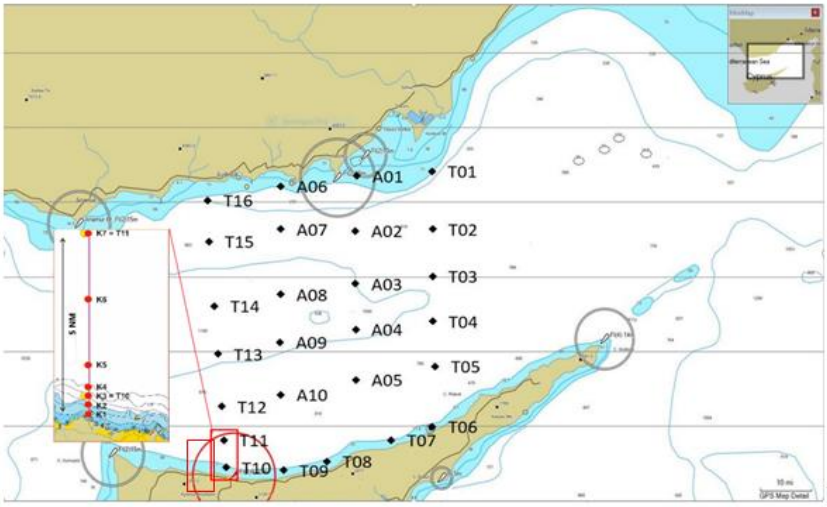

Figure 0.9: TUBITAK Project Code No: 114Y139 sampling stations.

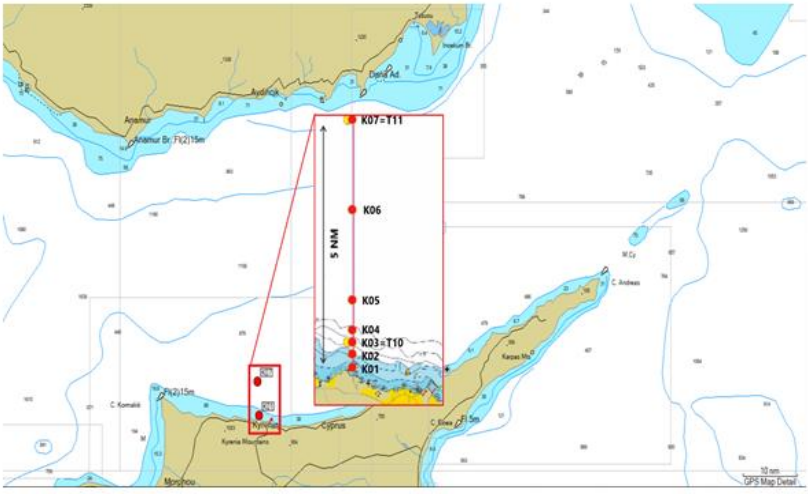

Figure 0.10: "Kıbrıs Time Series" (KTS) sampling stations within the framework of 114Y139 numbered TUBITAK Project.

2.2. KTS Study Area and Sampling Stations

KTS study area is geographically located 2.5 nautical miles (nm) west of Kyrenia Port, offshore of Yılan Adası (Figure 0.9). KTS studies were conducted at seven stations (K01 to K07) on a 5 nm zonal transect, offshore of Kyrenia. Station details are given in Table 0.2.

Since the continental shelf of the region is narrow and deepening rapidly towards offshore, the coastal stations K01, K02, K03 and K04 are distributed within about 0.5 nm to cover the shallow zone as well, so they are very close to each other. While stations K05, K06 and K07 are located respectively at 1.5, 3.5 and 5 nm from the coastline.

Table 0.2: KTS station details.

Station Name	Total Depth	Latitude / Longitude
K01	25 meters	35 21.171 N / 033 17.732 E
K02	50 meters	35 21.339 N / 033 17.710 E
K03	100 meters	35 21.572 N / 033 17.703 E
K04	150 meters	35 21.679 N / 033 17.726 E
K05	425 meters	35 22.525 N / 033 17.671 E
K06	610 meters	35 24.491 N / 033 17.439 E
K07	670 meters	35 26.218 N / 033 17.283 E

2.3. KTS Sampling Strategy

The first KTS cruise was carried out in November 2015. Since then, a total of twenty-seven monthly cruises were conducted until June 2018 (Table 0.3). The K01, K03 and K07 stations were sampled in a way to get a depth profile data, so they were assigned as profile (P) stations. At the stations K02, K04, K05 and K06 only sub-surface samples were collected so they were assigned as surface (S) stations. Detailed description of physical and biogeochemical studies conducted in KTS studies are given in Table 0.4.

Due to its aim, only the physical variables and parameters of the KTS studies were discussed in this study. Biochemical data were used to support the findings, whenever necessary.

Table 0.3: KTS oceanographic cruise dates.

Cruise No	Cruise Code	Cruise Date
1	KTS201511	12-13 November 2015
2	KTS201512	09 December 2015
3	KTS201601	29-30 January 2016
4	KTS201602	17 February 2016
5	KTS201603	9 March 2016
6	KTS201605	31 May 2016
7	KTS201606	13 June 2016
8	KTS201608	08-09 August 2016
9	KTS201609	10-11 September 2016
10	KTS201610	11 October 2016
11	KTS201611	25-26 November 2016
12	KTS201612	20 December 2016
13	KTS201701	23 January 2017
14	KTS201702	25-27 February 2017
15	KTS201703	28 March 2017
16	KTS201704	27 April 2017
17	KTS201705	25 May 2017
18	KTS201706	30 June 2017
19	KTS201707	24 July 2017
20	KTS201709	18 September 2017
21	KTS201710	19 October 2017
22	KTS201711	15 November 2017
23	KTS201801	16 January 2018
24	KTS201802	24 February 2018
25	KTS201803	27 March 2018
26	KTS201804	25-26 April 2018
27	KTS201806	27 June 2018

Table 0.4: KTS sampling parameters.

Station	CTD	pH	Dissolved Oxygen	Nutrients	TP	Chl-a	POC	Pigment HPLC	Phyto*	Zoo	Genetic DNA
K01	P	P	P	P	P^1	P	P^1	P	P	P	P^2
K02	P	S	P	S	-	S	-	S	S	-	-
K03	P	P	P	P	P^1	P	P^1	P	P	P	P^2
K04	P	S	P	S	-	S	-	S	S	-	-
K05	P	S	P	S	-	S	-	S	S	-	-
K06	P	S	P	S	-	S	-	S	S	-	-
K07	P	P	P	P	P^1	P	P^1	P	P	P	P^2

P: Profile Sampling **S: Surface Sampling**

P: Profile
Discrete Sampling Depths
K01: 0, 10, 25m
K03: 0, 10, 25, 50, 75, 100m
K07: 0, 10, 25, 50, 75, 100, 125, 150, 200m
K02, K04, K05, K06: 0m

P^1: POC / TP profile
Discrete Sampling Depths
$K01^1$: 0, 10, 25m
$K03^1$: 0, 10, 50, 100m
K07: 0, 10, 50, 100, 200m

P^2: DNA Profile
Discrete Sampling Depths
$K01^2$: 15m
$K03^2$: 10, 65m
$K07^2$: 10, 50, 150m

Phyto*: *heterotrophicbacteria, flagellates, Synechococcus, diğerleri

2.4. Research Vessel and Instruments

R/V Teal Jr is the first registered research vessel of Turkish Republic of Northern Cyprus, owned and operated by University of Kyrenia. She is a 13.5 meters ex-trawler, modified and equipped with oceanographic research purposes. She has 8 knots cruising speed and about 250 litres per day diesel oil consumption with 1000 litres diesel oil capacity.

She is equipped with two Raymarine 50 – 250 kHz echo sounders. Raymarine E7 Model is the main echo sounder with 1 kilowatt (kW) transducer and the second one, Raymarine Dragon Fly Model, is installed with down vision Chirp Sonar. A hydraulic driven winch system with 1000 meters of 6 millimetres chrome cable, installed to deploy oceanographic instruments such as CTD (Conductivity, Temperature, Depth profiler without rosette sampler), 5 Litre capacity Niskin bottles, WP2 zooplankton net and sediment grab sampler. Main oceanographic instruments on R/V Teal Jr are; Seabird 19 plusV2 SeaCAT profiler, five litres Niskin bottles, WP2 zooplankton net and Hydrobios sediment grab sampler.

CTD was used to obtain a depth profile of the water column from the surface to the bottom. Niskin bottles used to collect water samples from designated depths (discrete seawater sampling) and in each station and WP2 zooplankton net used for vertical sampling of the water column from designated depth to surface. A small wet lab with is equipped with a vacuum filtering apparatus, having the capacity of 12 filtering unit. A deep freezer, cooling to -22 ^{o}C, allows storage of the water samples, filtered samples and processed or non-processed other samples. With these specifications and

instruments, R/V Teal Jr is capable of conducting about four days of continuous research cruises in territorial waters.

Table 0.5: Seabird 19plus V2 SeaCAT profiler technical specifications (from Seabird product manual, version 15, page12).

	Temperature (°C)	Conductivity (S/m)	Pressure
Measurement Range	-5 to +35	0 to 9	0 to full scale range: • *Strain-gauge sensor:* 20 / 100 / 350 / 600 / 1000 / 2000 / 3500 / 7000/10.500 meters
Initial Accuracy	± 0.005	± 0.0005	• *Strain-gauge sensor:* ± 0.1% of full scale range
Typical Stability	0.0002/month	0.0003/month	• *Strain-gauge sensor:* 0.1% of full scale range/year
Resolution	0.0001	• 0.00005 (most oceanic water; resolves 0.4 ppm in salinity). • 0.00007 (high salinity water; resolves 0.4 ppm in salinity). • 0.00001 (fresh water; resolves 0.1 ppm in salinity).	• *Strain-gauge sensor:* 0.002% of full scale range
Sensor Calibration (measurement outside these ranges may be at slightly reduced accuracy due to extrapolation errors)	+1 to +32	0 to 9; physical calibration over range 2.6 to 6 S/m, plus zero conductivity (air)	Ambient pressure to full scale range in 5 steps
Real-Time Clock	32,768 Hz TCXO accurate to ±1 minute/year		
Sampling Speed	4 Hz (4 samples/sec)		
Memory	64 Mbyte non-volatile FLASH memory; maximum of 1000 cast headers		

2.5. Data Sampling

In every cruise and at every station of KTS studies, the CTD, Seabird 19plus V2 SeaCAT Model profiler, equipped with seawater conductivity, temperature, pressure, dissolved oxygen, turbidity, PAR and fluorescence sensors was used to measure and obtain the water column vertical profile from sea surface to the sea bottom. In addition to those sensors, pH and Oxidation Reduction Potential (ORP) sensor installed and used since January 2018. Sampling speed of the CTD was four samples per second, and the downcast and upcast winch speed was between 0.6 and 1.0 meter per second (m/s). Both downcast and upcast data were measured and stored into the CTD memory. Technical specification of CTD are given in Table 0.5. At the end of each cruise, all downcast and upcast data stored in CTD memory had been uploaded to a computer with the aid of Seaterm V2 (Version 2.6.3.104) software.

2.6. Data Analyses

2.6.1. CTD Data Analyses

The recorded CTD data were processed by using SBE Data Processing software (Version 7.26.7). Seven different processing steps had been used to obtain the best average data from the raw data. Total of sixteen different parameters were obtained by using SBE Data Processing software (Table 0.6). Sensors directly measured nine of these parameters and seven were

calculated from CTD measurements by using SBE Data Processing software. Salinity and density values had been calculated from CTD measurements during data processing, by using Practical Salinity Scale 1978 (PSS78) (Fofonoff, 1985; Millero, 2011) and Equation of State 1980 (EOS-80) formula (Fofonoff, 1985; Millero, 2011), respectively.

Excel databases had been created by combination of processed CTD data and relevant cruise data (cruise name, date, time, station position and station bottom depth) for each KTS cruise. Furthermore, these databases were imported to Ocean Data Viewer (ODV) software (Version 5.1.0) and Sigma Plot software (Version 14.0) to create appropriate graphics and plots of each parameter.

Table 0.6: Parameters obtained by using "SBE Data Processing" software.

No	Parameter Name	Method	No	Parameter Name	Method
1	Pressure	Sensor	9	Redox	Sensor
2	Temperature	Sensor	10	Salinity	Calculated
3	Conductivity	Sensor	11	Potential Temperature	Calculated
4	Turbidity	Sensor	12	Potential Density	Calculated
5	Fluorescence	Sensor	13	Oxygen	Calculated
6	PAR (Photosynthetically Active Radiation)	Sensor	14	Oxygen Saturation	Calculated
7	Oxygen raw	Sensor	15	Depth	Calculated
8	pH	Sensor	16	Decent rate	Calculated

2.6.2. Meteorological Data

The meteorological data used in this study was obtained from the Meteorological Office of Turkish Republic of Northern Cyprus (KKTC Meteoroloji Dairesi). The meteorological station is located in Port of Kyrenia, about 2.5 nm east of the KTS site. Detailed list of meteorological parameters obtained from meteorological office is given in Table 0.7.

Table 0.7: List of meteorological parameters obtained from the T.R.N.C Meteorological Office.

Parameter	Unit	Date From	Date To
Wind Direction	degrees	01/08/2016	31/06/2018
Wind Speed	m/s	01/08/2016	31/06/2018
Wave Hight	m	01/08/2016	31/06/2018
Evaporation	mm	01/01/2015	31/06/2018
Mean Pressure	hPa	01/01/2015	31/06/2018
Sea Surface Temperature	^{o}C	01/01/2015	31/06/2018
Air Temperature	^{o}C	01/01/2015	31/06/2018
Humidity	per cent	01/01/2015	31/06/2018

3. Results

3.1. Physical Oceanographic Characteristics of the KTS Region

Station K07 is located at such a depth (about 670 m) that it contains all water masses of interest in the present study. The results of station K07 are presented in this section. Temperature - Salinity (T-S) diagrams, temperature [^{o}C], salinity [per mille], potential density [kg/m^3], and dissolved oxygen [mg/l] versus depth profiles are presented to describe seasonal and annual mixing processes, stratification processes, presence of the LIW and all other water masses (i.e. LSW, MAW and EMDW) at station K07.

Figure 0.11 shows that LIW and all other water masses of the Levantine Basin (i.e. LSW, MAW and EMDW) were present in the area throughout the study, but were most pronounced and had identical properties in 2015 and 2016.

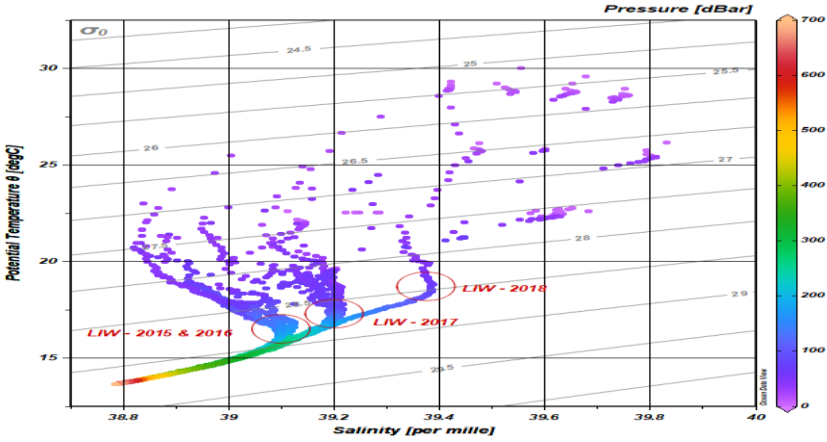

Figure 0.11: T-S diagram of station K07 throughout the KTS studies, form November 2015 to June 2018.

LIW, LSW, MAW and EMDW are clearly observed in all years, with different characteristics. In 2015 and 2016, the LIW in the TS diagram was identical "Scorpion tail" form, temperature (~16.50 °C), salinity (~39.10 per mille) and potential density (~28.87 kg/m^3). However, in 2017 and 2018, significant salinity increases and shifts on temperature and potential density of LIW, LSW and MAW were observed in the upper thermocline.

During the first cruise of KTS studies in November 2015, the water column was well mixed and uniformed from the sea surface to the depths of 50 meters, where thermocline, halocline, pycnocline and oxycline were located, as shown in Figure 0.12. Above thermocline, warm and saline Levantine Surface Water (LSW) with ~22.50 °C of temperature, ~39.30 per mille of salinity and ~27.35 kg/m^3 of potential density was present, as shown in Figure 0.12.

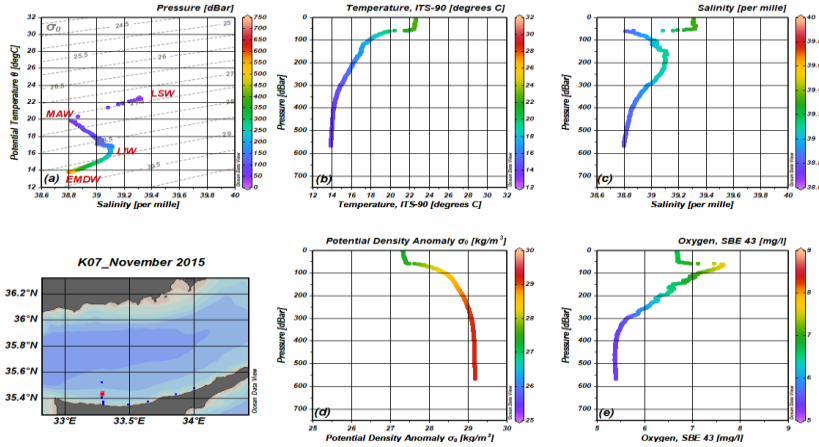

Figure 0.12: November 2015 cruise results of the station K07. (a): T-S diagram. (b): Temperature vs depth profile. (c) Salinity vs depth profile. (d): Potential density vs depth profile. (e): Oxygen vs depth profile.

Below the halocline, Modified Atlantic Water (MAW) was marked at 38.81 per mille of salinity, and 19.90 ℃ of temperature, located at a depth of 60 meters, as shown in Figure 0.12 (a) and (c). It is also observed that MAW was well oxygenated, as shown in Figure 0.12 (e). Further below, as shown in Figure 0.12 (c), the deep salinity maximum Levantine Intermediate Water (LIW) was located at the depths of about 160 meters. LIW was clearly observed at 39.11 per mille of salinity, ~16.85 ℃ of temperature and ~28.75 kg/m^3 of potential density in the T-S diagram, Figure 0.12 (a). At the bottom of the sea, dense and cold East Mediterranean Deep Water (EMDW) was observed with ~13.87 ℃ of temperature, ~38.80 per mille of salinity and ~29.17 kg/m^3 of potential density as shown with orange colour in the T-S diagram, in Figure 0.12 (a).

In the December 2015 cruise, although Sea Surface Temperature (SST) was cooled down to ~19.50 ℃ (Figure 0.13 (b)), the water column was still stratified, though thermocline, halocline, pycnocline and oxycline were located at a depth of 60 meters, Figure 0.13. The upper 60 meters of the water column was well mixed and uniform. Above the thermocline, LSW with ~19.50 ℃ of temperature, ~39.20 per mille of salinity and ~28.10 kg/m^3 of potential density was present (Figure 0.13). Below the halocline, MAW was marked at 38.98 per mille of salinity and 18.13 ℃ of temperature, at a depth of 70 meters, as shown in Figure 0.13 (a) and (c). It is also observed that MAW was well oxygenated, as shown in Figure 0.13 (e). Further below, (Figure.3.3(c)) LIW was located at depths of between 140 and 160 meters. LIW was marked at 39.12 per mille of salinity, ~16.50 ℃ of temperature and ~28.76 kg/m^3 of potential density in the T-S diagram, Figure 0.13 (a). At the

bottom of the sea, dense and cold EMDW was present in the area with ~13.83 °C of temperature, ~38.80 per mille of salinity and ~29.18 kg/m^3 potential density, as shown with orange colour in the T-S diagram, Figure 0.13 (a).

During the January 2016 cruise, the study area was dominated with intense vertical mixing processes. The water column was well mixed and uniform from the sea surface to depths of about 150 meters, as clearly shown in Figure 0.14. LIW, MAW and LSW were disappeared in the study area, as shown in Figure 0.14 (a). Mixed layer temperature was marked at ~17.05 °C of temperature, ~39.14 per mille of salinity and ~28.73 kg/m^3 of potential density. The mixed layer was oxygenated to the depths of about 100 meters, as shown in the oxygen profile, Figure 0.14 (e). At the bottom of the sea, dense and cold EMDW was present in the area with ~13.90 °C of temperature, ~38.82 per mille of salinity and ~29.18 kg/m^3 of potential density, as shown with orange colour in the T-S diagram, Figure 0.14 (a).

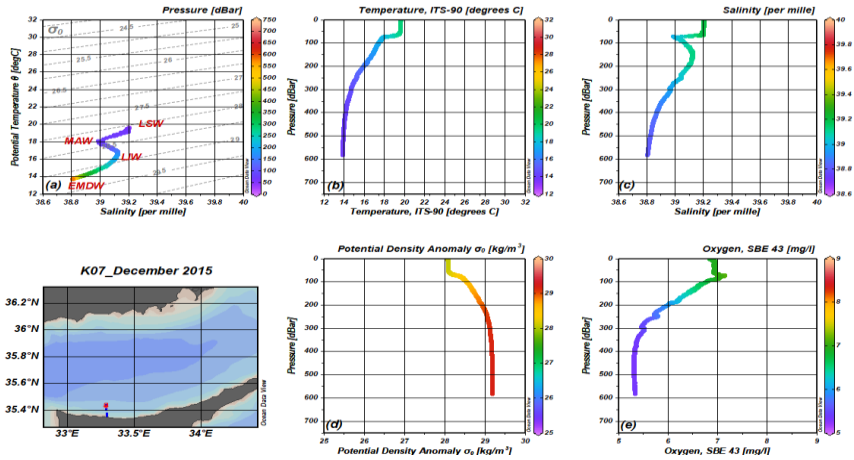

Figure 0.13: December 2015 cruise results of the station K07. (a): T-S diagram. (b): Temperature vs depth profile. (c) Salinity vs depth profile. (d): Potential density vs depth profile. (e): Oxygen vs depth profile.

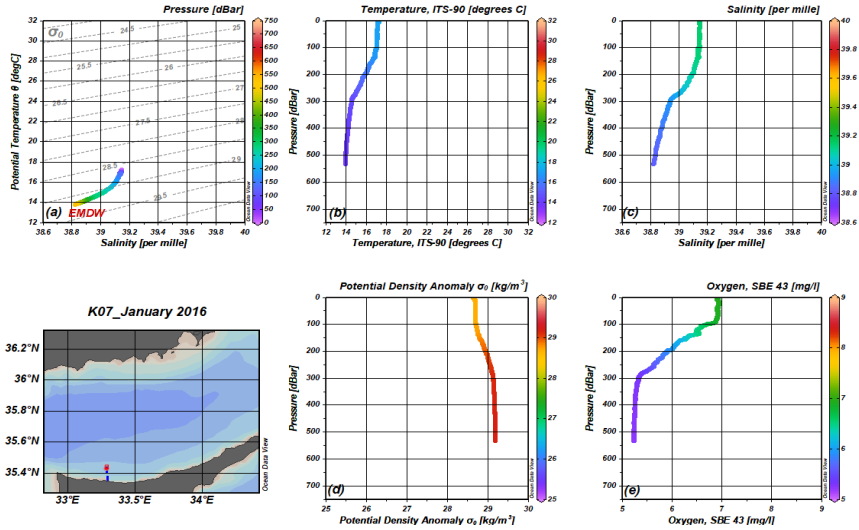

Figure 0.14: January 2016 cruise results of the station K07. (a): T-S diagram. (b): Temperature vs depth profile. (c) Salinity vs depth profile. (d): Potential density vs depth profile. (e): Oxygen vs depth profile.

In February 2016, the study area, as expected, was still dominated with intense vertical mixing processes. The water column was well mixed and uniform from the sea surface to the depths of about 150 meters, as shown in Figure 0.15. LIW, MAW and LSW were not present in the study area, as shown in Figure 0.15 (a). Mixed layer temperature was marked at ~17.10 °C of temperature, ~39.15 per mille of salinity and ~28.73 kg/m^3 of potential density. Mix layer was oxygenated to the depths of about 150 meters, as shown in the oxygen profile, Figure 0.15 (e). At the bottom of the sea, dense and cold EMDW was present in the area with ~13.90 °C of temperature, ~38.82 per mille of salinity and ~29.18 kg/m^3 potential density, as shown with orange colour in the T-S diagram, Figure 0.15 (a).

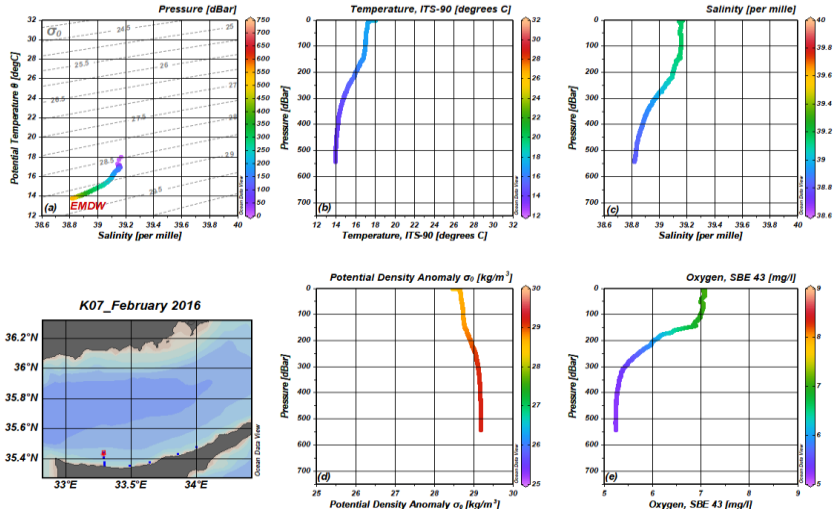

Figure 0.15: February 2016 cruise results of the station K07. (a): T-S diagram. (b): Temperature vs depth profile. (c) Salinity vs depth profile. (d): Potential density vs depth profile. (e): Oxygen vs depth profile.

During the March 2016 cruise, seasonal stratification of the water column was observed to be reformed at a depth of about 25 meters, as shown in Figure 0.16. Upper 25 meters of the water column were warmer and less dense with the temperature marked at ~17.80 °C and potential density at ~28.48 kg/m^3 (Figure 0.16 (b) and (d)). Deep salinity maximum LIW was observed to reappear at the depths of between 70 and 120 meters in the study area. LIW was marked at 39.14 per mille of salinity, ~16.95 °C of temperature and ~28.72 kg/m^3 of potential density in the T-S diagram, Figure 0.16 (a). The water column was oxygenated to the depths of about 150 meters, as shown in the oxygen profile, Figure 0.16 (e). At the bottom of the sea, dense and cold EMDW was present with ~13.91 °C of temperature, ~38.82 per mille of salinity and ~29.18 kg/m^3 potential density, as shown with orange colour in the T-S diagram, Figure 0.16 (a).

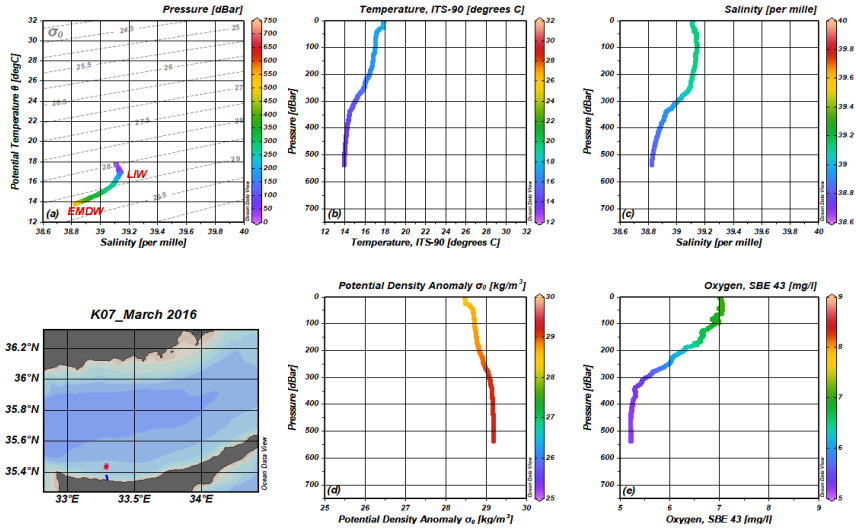

Figure 0.16: March 2016 cruise results of the station K07. (a): T-S diagram. (b): Temperature vs depth profile. (c) Salinity vs depth profile. (d): Potential density vs depth profile. (e): Oxygen vs depth profile.

At the May 2016 cruise, with the increasing temperatures over the course of spring, SST was observed to be warmed up to ~22.40 °C, and as shown in Figure 0.17 (a) and (b), seasonal stratification is observed to be established in the study area. The water column was well mixed and uniform from the sea surface to the depths of ~25 meters, where thermocline, halocline, pycnocline and oxycline were located, as shown in Figure 0.17. Above thermocline, warm and saline LSW with ~22.00 °C of temperature, ~39.15 per mille of salinity and ~27.37 kg/m^3 of potential density was present in the area, as shown in Figure 0.17. Below the halocline, MAW was marked at 38.96 per mille of salinity and 18.66 °C of temperature, at a depth of 43 meters, as shown in Figure 0.17 (a) and (c). It is also observed that MAW was well oxygenated, as shown in Figure 0.17 (e). Further below, as shown in Figure 0.17 (c), deep salinity maximum LIW was located at depths of between 140 and 190 meters. LIW was clearly observed at 39.10 per mille of salinity, ~16.60 °C of temperature and ~28.78 kg/m^3 of potential density in the T-S diagram, Figure 0.17 (a). At the bottom of the sea, dense and cold East Mediterranean Deep Water (EMDW) was present in the area with ~13.79 °C of temperature, ~38.79 per mille of salinity and ~29.19 kg/m^3 potential density, as shown with orange colour in the T-S diagram, Figure 0.17 (a).

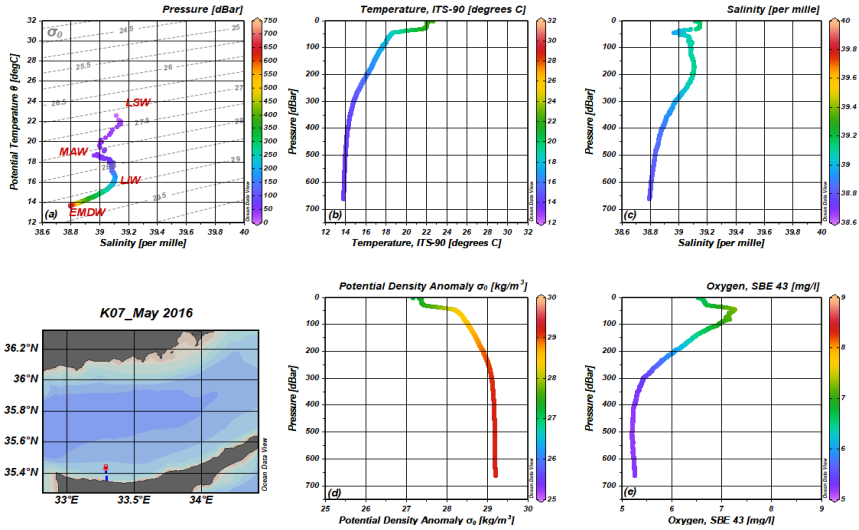

Figure 0.17: May 2016 cruise results of the station K07. (a): T-S diagram. (b): Temperature vs depth profile. (c) Salinity vs depth profile. (d): Potential density vs depth profile. (e): Oxygen vs depth profile.

During the June 2016 cruise, SST was marked at ~25.00 °C, the water column was well mixed and uniform from the sea surface to the depths of ~30 meters, where thermocline, halocline, pycnocline and oxycline were located, as shown in Figure 0.18 (a) and (b). Above thermocline, warm and saline LSW with ~24.00 °C of temperature, ~39.20 per mille of salinity and ~26.85 kg/m^3 of potential density was present in the area as shown in Figure 0.18. Below halocline, MAW was marked at 38.94 per mille of salinity and 20.24 °C of temperature, at a depth of 36 meters, as shown in Figure 0.18 (a) and (c). It is also observed that MAW was well oxygenated, as shown in Figure 0.18 (e). Further below, as shown in Figure 0.18 (c), deep salinity maximum LIW was located at depths of 150 and 190 meters. LIW was clearly observed at 39.10 per mille of salinity, ~16.55 °C of temperature and ~28.78 kg/m^3 of potential density in the T-S diagram, Figure 0.18 (a). At the bottom of the sea, dense and cold East Mediterranean Deep Water (EMDW) was present in the area with ~13.76 °C of temperature, ~38.78 per mille of salinity and ~29.19 kg/m^3 potential density, as shown with orange colour in the T-S diagram, Figure 0.18 (a).

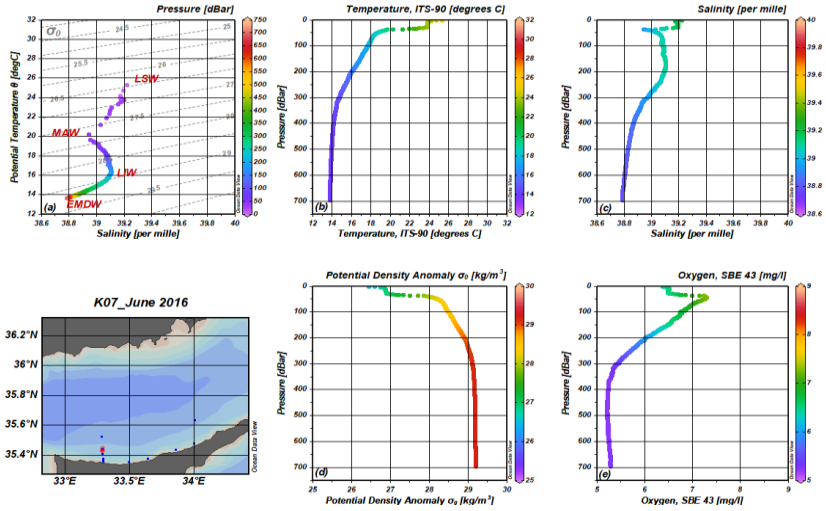

Figure 0.18: June 2016 cruise results of the station K07. (a): T-S diagram. (b): Temperature vs depth profile. (c) Salinity vs depth profile. (d): Potential density vs depth profile. (e): Oxygen vs depth profile.

At the August 2016 cruise, with the increasing temperatures over the course of summer, SST was marked at ~29.35 ℃, and the study area was observed to be dominated by strong seasonal stratification, as shown in Figure 0.19 (a) and (b). The water column was well mixed and uniform from the sea surface to the depths of ~20 meters, where thermocline, halocline, pycnocline and oxycline were located, as shown in Figure 0.19. Above thermocline, warm and saline LSW with ~29.00 ℃ of temperature, ~39.42 per mille of salinity and ~25.40 kg/m^3 of potential density was present in the area, as shown in Figure 0.19. Below halocline, MAW was marked by 38.83 per mille of salinity and 21.65 ℃ of temperature, located at a depth of 26 meters, as shown in Figure 0.19 (a) and (c). It is also observed that MAW was well oxygenated, as shown in Figure 0.19 (e). Further below, as shown in Figure 0.19 (c), deep salinity maximum LIW was located at depths of between 145 and 185 meters. LIW was clearly observed at 39.10 per mille of salinity, ~16.40 ℃ of temperature and 28.80 kg/m^3 of potential density in the T-S diagram, Figure 0.19 (a). At the bottom of the sea, dense and cold EMDW was present in the area with ~13.76 ℃ of temperature, ~38.78 per mille of salinity and ~29.19 kg/m^3 potential density, as shown with orange colour in the T-S diagram, Figure 0.19 (a).

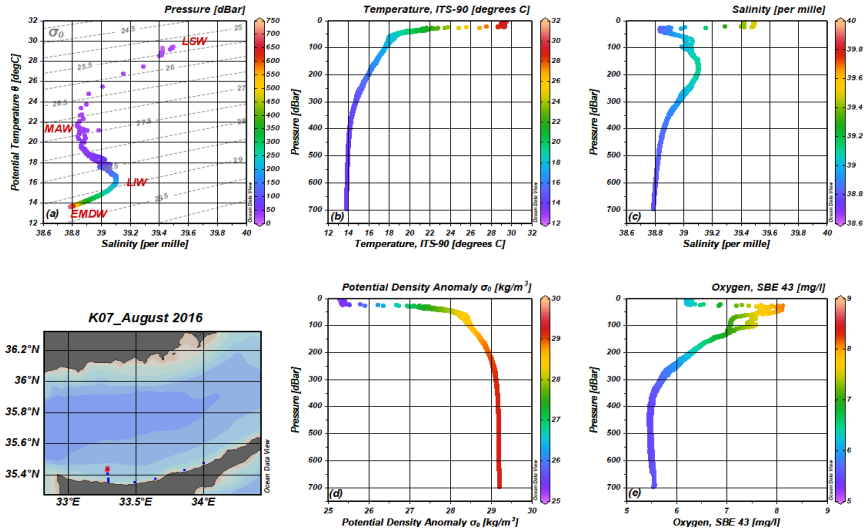

Figure 0.19: August 2016 cruise results of the station K07. (a): T-S diagram. (b): Temperature vs depth profile. (c) Salinity vs depth profile. (d): Potential density vs depth profile. (e): Oxygen vs depth profile.

During the September 2016 cruise, as shown in Figure 0.20 (b), SST was marked at about 29.60 ℃. The water column was well mixed and uniform from the sea surface to the depths of ~28 meters, where thermocline, halocline, pycnocline and oxycline were located, as shown in Figure 0.20. Above thermocline, warm and saline LSW with ~29.00 ℃ of temperature, ~39.65 per mille of salinity and ~25.65 kg/m^3 of potential density was present in the area, as shown in Figure 0.20. Below halocline, MAW was marked at 38.83 per mille of salinity and 21.69 ℃ of temperature, at a depth of 33 meters, as shown in Figure 0.20 (a) and (c). It is also observed that MAW was well oxygenated, as shown in Figure 0.20 (e). Further below, as shown in Figure 0.20 (c), deep salinity maximum LIW located at depths of between 145 and 165 meters. LIW was clearly observed at 39.10 per mille of salinity, ~16.25 ℃ of temperature and 28.85 kg/m^3 of potential density in the T-S diagram, Figure 0.20 (a). At the bottom of the sea, dense and cold EMDW was present in the area with ~13.78 ℃ of temperature, ~38.79 per mille of salinity and ~29.19 kg/m^3 potential density, as shown with orange colour in the T-S diagram, Figure 0.20 (a).

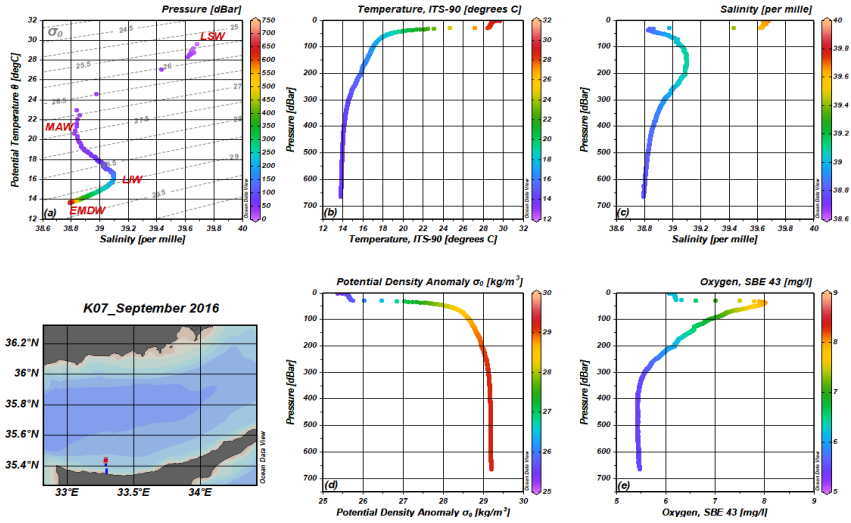

Figure 0.20: September 2016 cruise results of the station K07. (a): T-S diagram. (b): Temperature vs depth profile. (c) Salinity vs depth profile. (d): Potential density vs depth profile. (e): Oxygen vs depth profile.

During the October 2016 cruise, with the beginning of the Autumn, SST was observed to be cooling down and marked at about 25.85 °C, as shown in Figure 0.21 (b). The water column was well mixed and uniform from the sea surface to a depth of 40 meters, where thermocline, halocline, pycnocline and oxycline were located, as shown in Figure 0.21. Above thermocline, warm and saline LSW with ~25.75 °C of temperature, ~39.60 per mille of salinity and ~26.57 kg/m^3 of potential density was present in the area, as shown in Figure 0.21. Below halocline, MAW was marked at 38.82 per mille of salinity and 20.74 °C of temperature, at a depth of 50 meters, as shown in Figure 0.21 (a) and (c). It is also observed that MAW was well oxygenated, as shown in Figure 0.21 (e). Further below, as shown in Figure 0.21 (c), deep salinity maximum LIW was located at depths of between 160 and 180 meters. LIW was clearly observed at 39.10 per mille of salinity, ~16.25 °C of temperature and 28.85 kg/m^3 of potential density in the T-S diagram, Figure 0.21 (a). At the bottom of the sea, dense and cold EMDW was present in the area with ~13.82 °C of temperature, ~38.80 per mille of salinity and ~29.19 kg/m^3 potential density, as shown with orange colour in the T-S diagram, Figure 0.21 (a).

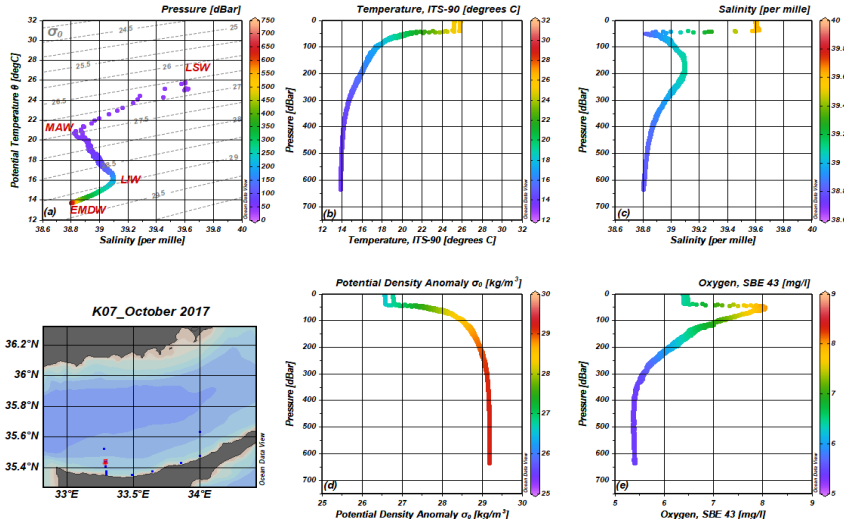

Figure 0.21: October 2016 cruise results of the station K07. (a): T-S diagram. (b): Temperature vs depth profile. (c) Salinity vs depth profile. (d): Potential density vs depth profile. (e): Oxygen vs depth profile.

At the November 2016 cruise, SST was observed to be cool further down to marked at about 21.27 ℃, as shown in Figure 0.22 (b). The water column was well mixed and uniform from the sea surface to a depth of 70 meters, where thermocline, halocline, pycnocline and oxycline were located, as shown in Figure 0.22. Above thermocline, warm and saline LSW with ~21.27 ℃ of temperature, ~39.45 per mille of salinity and ~27.81 kg/m^3 of potential density was present in the area as shown in Figure 0.22. Below halocline, MAW was marked at 38.92 per mille of salinity and 19.00 ℃ of temperature, at a depth of 75 meters, as shown in Figure 0.22 (a) and (c). It is also observed that MAW was well oxygenated, as shown in Figure 0.22 (e). Further below, as shown in Figure 0.22 (c), deep salinity maximum LIW was located at depths of between 190 and 210 meters. LIW was clearly observed at 39.10 per mille of salinity, ~16.25 ℃ of temperature and 28.85 kg/m^3 of potential density in the T-S diagram, Figure 0.22 (a). At the bottom of the sea, dense and cold EMDW was present in the area with ~13.86 ℃ of temperature, ~38.81 per mille of salinity and ~29.19 kg/m^3 potential density, as shown with orange colour in the T-S diagram, Figure 0.22 (a).

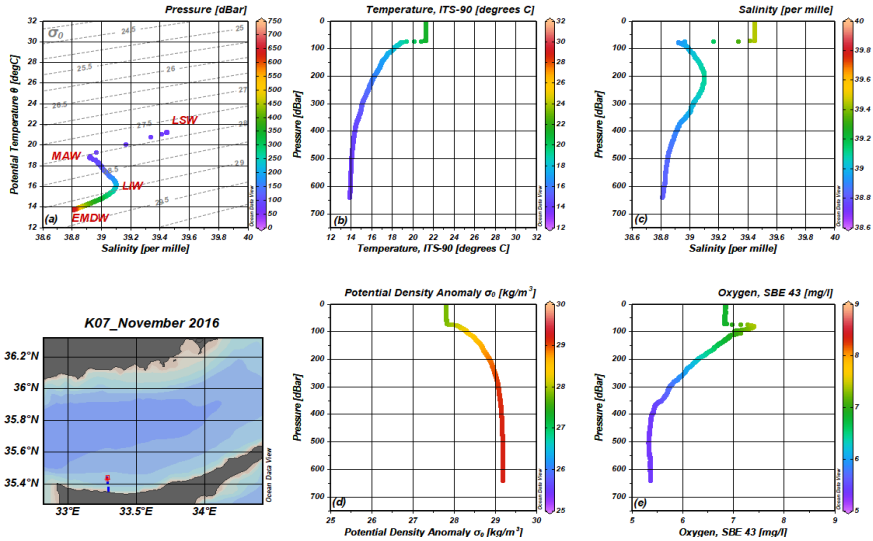

Figure 0.22: November 2016 cruise results of the station K07. (a): T-S diagram. (b): Temperature vs depth profile. (c) Salinity vs depth profile. (d): Potential density vs depth profile. (e): Oxygen vs depth profile.

During the February 2017 cruise, LIW, MAW and LSW were observed to disappear in the study area, as shown in Figure 0.23 (a). Intensive vertical mixing processes dominated the study area, and the water column was well mixed and uniform from the sea surface to depths of ~200 meters, as shown in Figure 0.23. SST was marked at ~17.60 ℃ and mix layer temperature marked at ~16.70 ℃, salinity at ~39.22 per mille and potential density at ~28.85 kg/m^3, as shown in Figure 0.23. Mix layer was oxygenated to the depths of about 200 meters, as shown in oxygen profile, Figure 0.23 (e). At the bottom of the sea, dense and cold EMDW was present in the area with ~13.81 ℃ of temperature, ~38.80 per mille of salinity and ~29.19 kg/m^3 potential density, as shown with orange colour in the T-S diagram, Figure 0.23 (a).

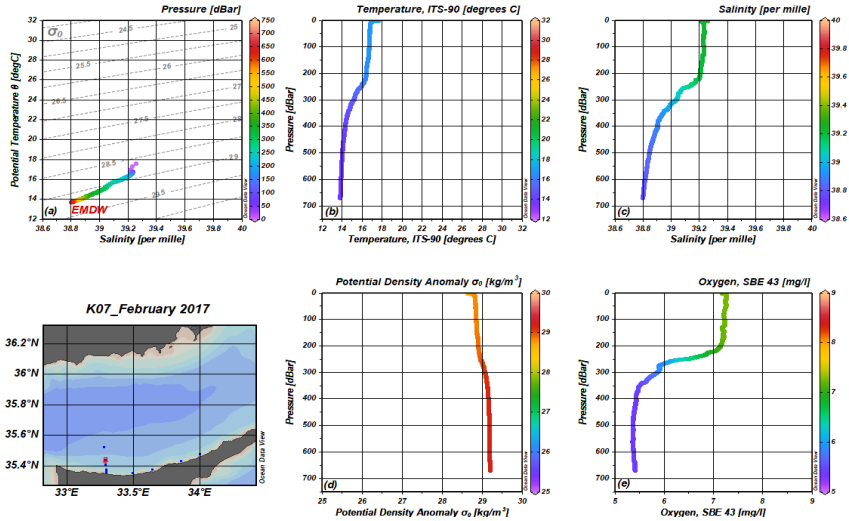

Figure 0.23: February 2017 cruise results of the station K07. (a): T-S diagram. (b): Temperature vs depth profile. (c) Salinity vs depth profile. (d): Potential density vs depth profile. (e): Oxygen vs depth profile.

During the March 2017 cruise, LIW, MAW and LSW were not present in the study area, as shown in Figure 0.24 (a). Although water column was well mixed and uniform to the depths of about 150 meters, upper 20 meters of the water column was slightly warmer and saltier with ~17.50 °C of temperature and 39.24 per mille of salinity, as shown in Figure 0.24 (b) and (c). SST was marked at ~17.60 °C and mix layer temperature marked at ~16.70 °C, salinity at ~39.22 per mille and potential density at ~28.85 kg/m^3, as shown in Figure 0.24. Mix layer was oxygenated to the depths of about 100 meters, as shown in oxygen profile, Figure 0.24 (e). At the bottom of the sea, dense and cold EMDW was present in the area with ~13.77 °C of temperature, ~38.79 per mille of salinity and ~29.19 kg/m^3 potential density, as shown with orange colour in the T-S diagram, Figure 0.24 (a).

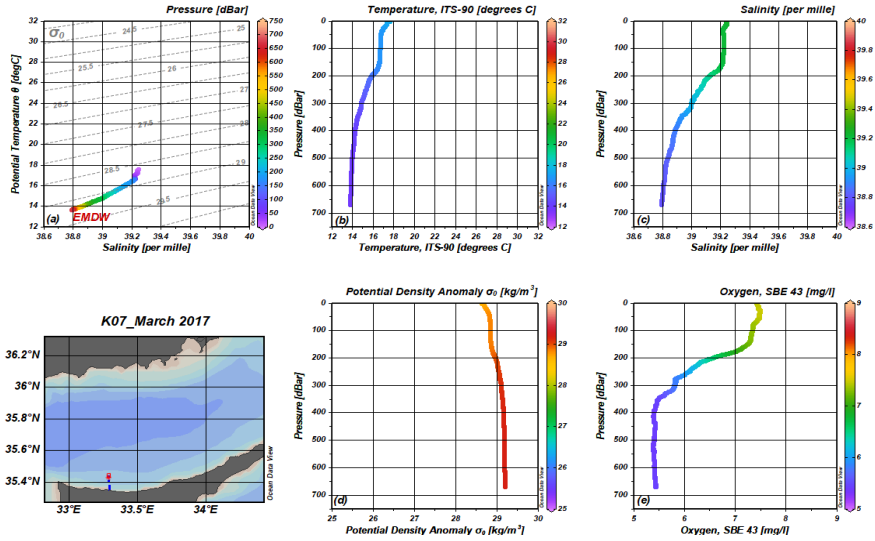

Figure 0.24: March 2017 cruise results of the station K07. (a): T-S diagram. (b): Temperature vs depth profile. (c) Salinity vs depth profile. (d): Potential density vs depth profile. (e): Oxygen vs depth profile.

At the April 2017 cruise, seasonal stratification of the water column was observed to be reformed at the depths of ~20 meters, as shown in Figure 0.25. Upper 20 meters of the water column was warmer and less dense with ~18.80 °C and ~28.30 kg/m^3, as shown in Figure 0.25 (b) and (d). Deep salinity maximum LIW was observed to reappear at depths of between 20 and 60 meters, marked at 39.26 per mille of salinity, ~18.00 °C of temperature and ~28.52 kg/m^3 of potential density in the T-S diagram, Figure 0.25 (a). The water column was oxygenated to the depths of ~100 meters, as shown in oxygen profile, Figure 0.25 (e). At the bottom of the sea, dense and cold EMDW was present in the area with ~13.79 °C of temperature, ~38.89 per mille of salinity and ~29.18 kg/m^3 potential density, as shown with orange colour in the T-S diagram, Figure 0.25 (a).

During the July 2017 cruise, with the increasing temperatures over the course of summer, SST was marked at about 30.00 °C, and the study area was observed to be dominated by strong seasonal stratification, as shown in Figure 0.26 (a) and (b). The water column was well mixed and uniform from the sea surface to the depths of ~15 meters, where thermocline, halocline, pycnocline and oxycline were located, as shown in Figure 0.26. Above thermocline, LSW with ~29.00 °C of temperature, ~39.53 per mille of salinity and ~25.40 kg/m^3 of potential density was present in the area, as shown in Figure 0.26. Below halocline, MAW was marked at 39.06 per mille of salinity and 21.93 °C of temperature, at a depth of 22 meters, as shown in

Figure 0.26 (a) and (c). It is also observed that MAW was well oxygenated, as shown in Figure 0.26 (e). Further below, as shown in Figure 0.26 (c), LIW was located at depths of between 50 and 100 meters. LIW was clearly observed at 39.21 per mille of salinity, ~18.00 ℃ of temperature and ~28.55 kg/m^3 of potential density in the T-S diagram, Figure 0.26 (a). At the bottom of the sea, dense and cold EMDW was present in the area with ~13.83 ℃ of temperature, ~38.80 per mille of salinity and ~29.19 kg/m^3 potential density, as shown with orange colour in the T-S diagram, Figure 0.26 (a).

At the September 2017 cruise, as shown in Figure 0.27 (b), SST was marked at about 29.00 ℃. The water column was well mixed and uniform from the sea surface to a depth of 23 meters, where thermocline, halocline, pycnocline and oxycline were located, as shown in Figure 0.27. Above thermocline, LSW with ~29.50 ℃ of temperature, ~39.75 per mille of salinity and ~25.78 kg/m^3 of potential density was present in the area, as shown in Figure 0.27. Below halocline, MAW was marked at 38.95 per mille of salinity and 21.50 ℃ of temperature, at a depth of 34 meters, as shown in Figure 0.27 (a) and (c). It is also observed that MAW was was well oxygenated, as shown in Figure 0.27 (e). Further below, as shown in Figure 0.27 (c), LIW was located at depths of between 90 and 125 meters. LIW was clearly observed at 39.21 per mille of salinity, ~17.50 ℃ of temperature and 28.63 kg/m^3 of potential density in the T-S diagram, Figure 0.27 (a). At the bottom of the sea, dense and cold EMDW was present in the area with ~13.81 ℃ of temperature, ~38.80 per mille of salinity and ~29.19 kg/m^3 potential density, as shown with orange colour in the T-S diagram, Figure 0.27 (a).

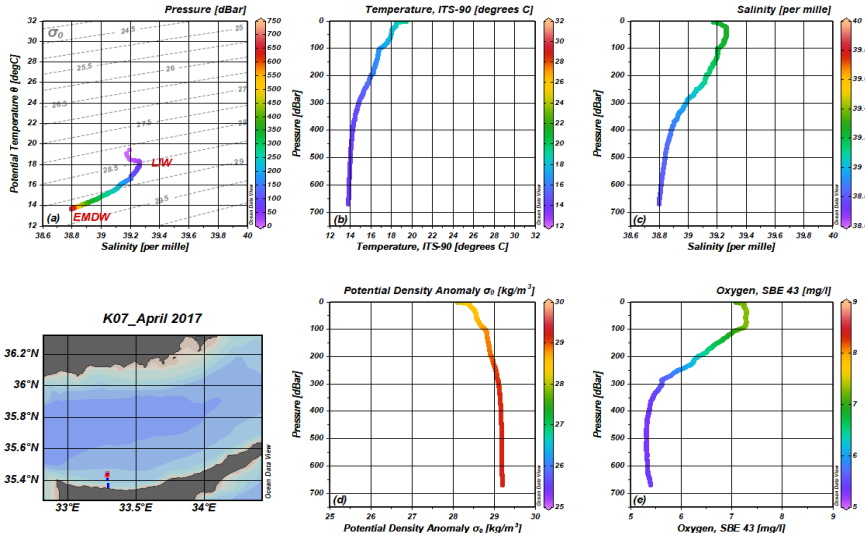

Figure 0.25: April 2017 cruise results of the station K07. (a): T-S diagram. (b): Temperature vs depth profile. (c) Salinity vs depth profile. (d): Potential density vs depth profile. (e): Oxygen vs depth profile.

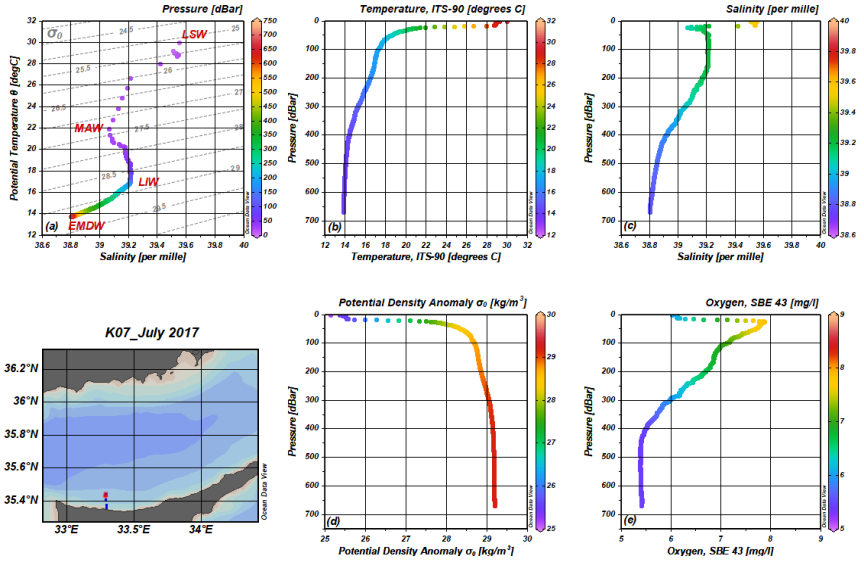

Figure 0.26: July 2017 cruise results of the station K07. (a): T-S diagram. (b): Temperature vs depth profile. (c) Salinity vs depth profile. (d): Potential density vs depth profile. (e): Oxygen vs depth profile.

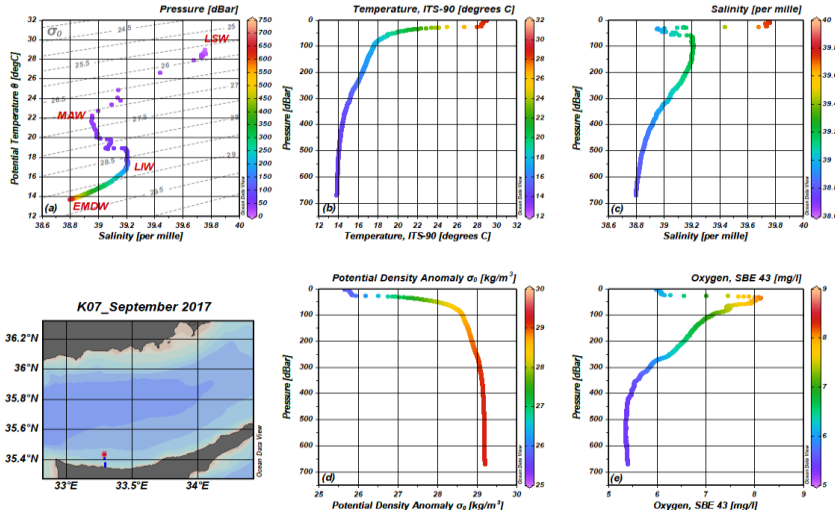

Figure 0.27: September 2017 cruise results of the station K07. (a): T-S diagram. (b): Temperature vs depth profile. (c) Salinity vs depth profile. (d): Potential density vs depth profile. (e): Oxygen vs depth profile.

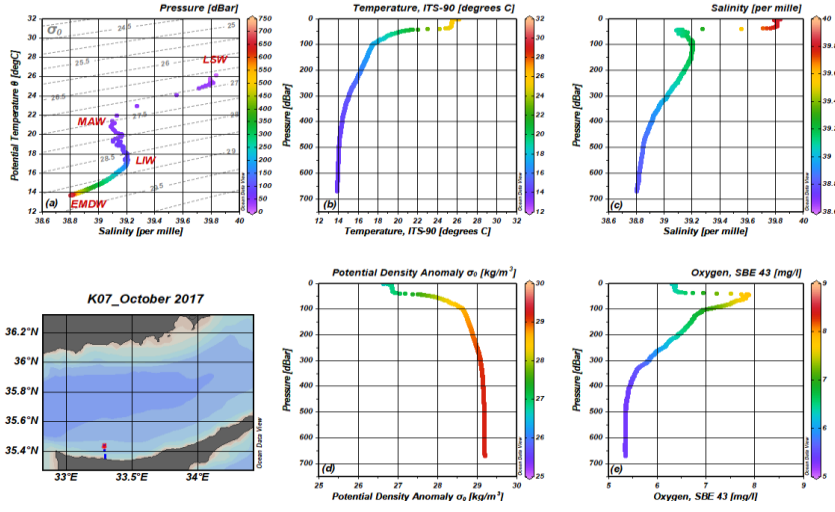

Figure 0.28: October 2017 cruise results of the station K07. (a): T-S diagram. (b): Temperature vs depth profile. (c) Salinity vs depth profile. (d): Potential density vs depth profile. (e): Oxygen vs depth profile.

During the October 2017 cruise, SST was observed to be cool down and marked at ~26.15 °C, as shown in Figure 0.28 (b). The water column was well mixed and uniform from the sea surface to a depth of 35 meters, where thermocline, halocline, pycnocline and oxycline were located, as shown in Figure 0.28. Above thermocline, warm and saline LSW with ~25.40 °C of

temperature, ~39.80 per mille of salinity and ~26.70 kg/m^3 of potential density was present in the area, as shown in Figure 0.28. Below halocline, MAW was marked at 39.08 per mille of salinity and 20.90 °C of temperature, at a depth of 44 meters, as shown in Figure 0.28 (a) and (c). It is also observed that MAW was well oxygenated, as shown in Figure 0.28 (e). Further below, as shown in Figure 0.28 (c), deep salinity maximum LIW was located at depths of between 100 and 130 meters. LIW was clearly observed at 39.21 per mille of salinity, ~17.25 °C of temperature and 28.69 kg/m^3 of potential density in the T-S diagram, Figure 0.28 (a). At the bottom of the sea, dense and cold EMDW was present in the area with ~13.83 °C of temperature, ~38.80 per mille of salinity and ~29.19 kg/m^3 potential density, as shown with orange colour in the T-S diagram, Figure 0.28 (a).

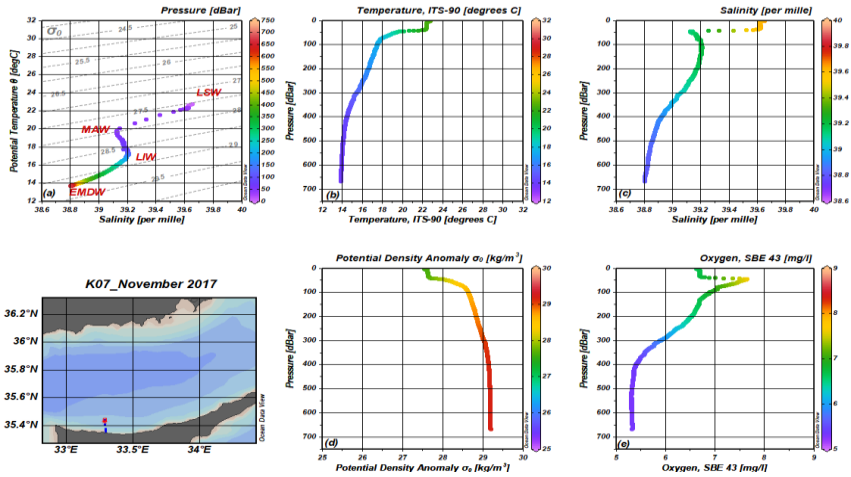

Figure 0.29: November 2017 cruise results of the station K07. (a): T-S diagram. (b): Temperature vs depth profile. (c) Salinity vs depth profile. (d): Potential density vs depth profile. (e): Oxygen vs depth profile.

During the November 2017 cruise, SST observed to be cool further down, and marked at about 21.78 °C, as shown in Figure 0.29 (b). The water column was well mixed and uniform from the sea surface to a depth of 35 meters, where thermocline, halocline, pycnocline and oxycline were located, as shown in Figure 0.29. Above thermocline, warm and saline LSW with ~22.60 °C of temperature, ~39.62 per mille of salinity and ~27.63 kg/m^3 of potential density was present in the area, as shown in Figure 0.29. Below halocline, MAW was marked at 39.12 per mille of salinity and 19.80 °C of temperature, at a depth of 45 meters, as shown in Figure 0.29 (a) and (c). It is also observed that MAW was oxygenated, as shown in Figure 0.29(e). Further below, as shown in Figure 0.29 (c), deep salinity maximum LIW was

located at depths of between 110 and 135 meters. LIW was clearly observed at 39.21 per mille of salinity, ~17.29 ℃ of temperature and 28.868 kg/m^3 of potential density in the T-S diagram, Figure 0.29 (a). At the bottom of the sea, dense and cold EMDW was present in the area with ~13.83 ℃ of temperature, ~38.80 per mille of salinity and ~29.19 kg/m^3 potential density, as shown with orange colour in the T-S diagram, Figure 0.29 (a).

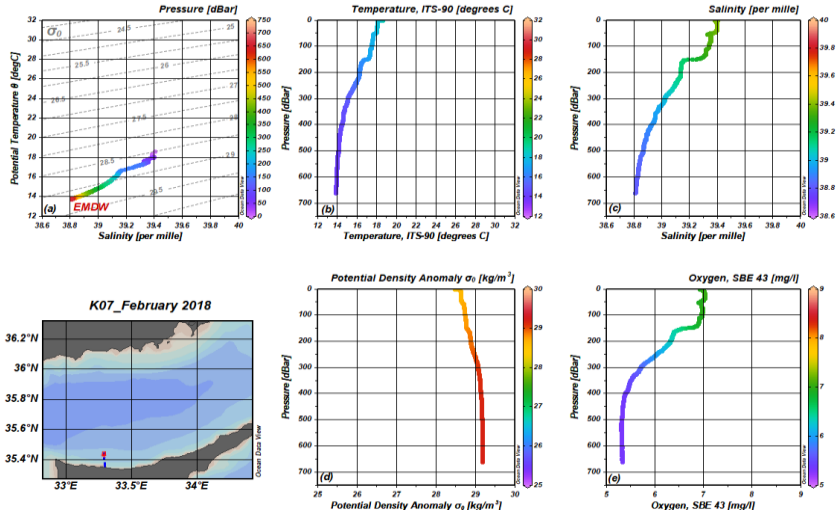

Figure 0.30: February 2018 cruise results of the station K07. (a): T-S diagram. (b): Temperature vs depth profile. (c) Salinity vs depth profile. (d): Potential density vs depth profile. (e): Oxygen vs depth profile.

At the February 2018 cruise, LIW, MAW and LSW were observed to be disappeared from the study area, as shown in Figure 0.30 (a). Although water column was mixed to the depths of about 150 meters, upper 40 meters of the water column was slightly warmer and saltier with ~18.05 ℃ of temperature and 39.38 per mille of salinity, as shown in Figure 0.30 (b) and (c). SST was marked at ~18.64 ℃ and mix layer temperature marked at ~17.50 ℃, salinity at ~39.34 per mille and potential density at ~28.72 kg/m^3, as shown in Figure 0.30. Mix layer was oxygenated to depths of about 130 meters, as shown in the oxygen profile, Figure 0.30 (e). At the bottom of the sea, dense and cold EMDW was present in the area with ~13.86 ℃ of temperature, ~38.81 per mille of salinity and ~29.19 kg/m^3 potential density, as shown with orange colour in the T-S diagram, Figure 0.30 (a).

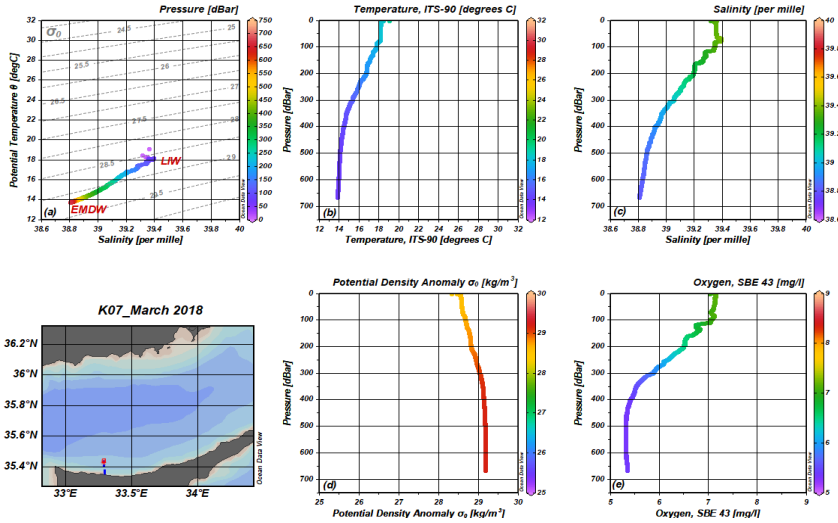

Figure 0.31: March 2018 cruise results of the station K07. (a): T-S diagram. (b): Temperature vs depth profile. (c) Salinity vs depth profile. (d): Potential density vs depth profile. (e): Oxygen vs depth profile.

During the March 2018 cruise, LSW and MAW were not present in the study area, as shown in Figure 0.31 (a). Although water column was well mixed and uniform to the depths of ~80 meters, a saltier and warmer water mass was observed at depths of between 67 and 77 meters with 39.38 per mille of salinity and 18.14 ℃ of temperature, as shown in Figure 0.31. SST was marked at ~19.08 ℃, and mix layer temperature was marked at ~18.15 ℃, salinity at ~39.35 per mille and potential density at ~28.57 kg/m^3, as shown in Figure 0.31. Mix layer was oxygenated to the depths of about 100 meters, as shown in oxygen profile, Figure 0.31 (e). At the bottom of the sea, dense and cold EMDW was present in the area with ~13.84 ℃ of temperature, ~38.80 per mille of salinity and ~29.19 kg/m^3 potential density, as shown with orange colour in the T-S diagram, Figure 0.31 (a).

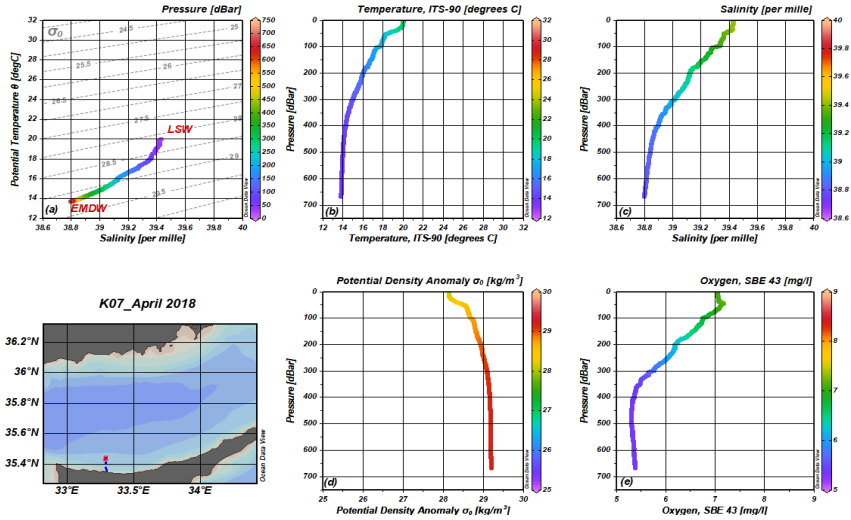

Figure 0.32: April 2018 cruise results of the station K07. (a): T-S diagram. (b): Temperature vs depth profile. (c) Salinity vs depth profile. (d): Potential density vs depth profile. (e): Oxygen vs depth profile.

At the April 2018 cruise, seasonal stratification of the water column was observed to be reformed at depths of ~35 meters, where thermocline, halocline, pycnocline and oxycline were located, as shown in Figure 0.32. SST was marked at 20.02 ℃, as shown in Figure 0.32. Above thermocline, warm and saline LSW with ~20.00 ℃ of temperature, ~39.43 per mille of salinity and ~28.15 kg/m^3 of potential density was present in the area, as shown in Figure 0.32. LIW and MAW were not present in the study, area as shown in Figure 0.32 (a). The water column was oxygenated to the depths of about 70 meters, as shown in the oxygen profile, Figure 0.32 (e). At the bottom of the sea, dense and cold EMDW was present in the area with ~13.80 ℃ of temperature, ~38.79 per mille of salinity and ~29.18 kg/m^3 potential density, as shown with orange colour in the T-S diagram, Figure 0.32 (a).

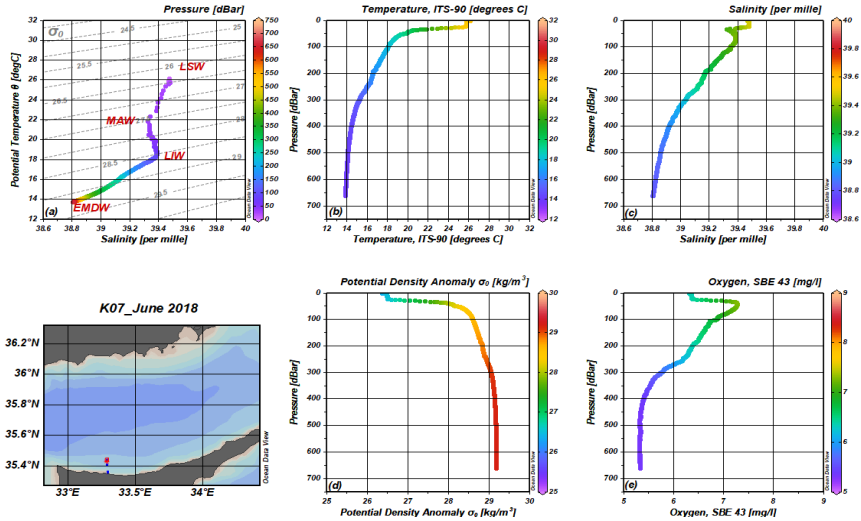

Figure 0.33: June 2018 cruise results of the station K07. (a): T-S diagram. (b): Temperature vs depth profile. (c) Salinity vs depth profile. (d): Potential density vs depth profile. (e): Oxygen vs depth profile.

During the June 2018 cruise, SST was observed to be warmed up to ~26.15 °C, with the increasing temperatures over the course of the spring season, and the study area was observed to be dominated by strong seasonal stratification, as shown in Figure 0.33 (a) and (b). The water column was well mixed and uniform from the sea surface to a depth of 22 meters, where thermocline, halocline, pycnocline and oxycline were located, as shown in Figure 0.33. Above thermocline, warm and saline LSW with ~25.80 °C of temperature, ~39.48 per mille of salinity and ~26.48 kg/m^3 of potential density was present in the area, as shown in Figure 0.33. Below halocline, MAW was marked at 39.32 per mille of salinity and 21.85 °C of temperature, at a depth of 32 meters, as shown in Figure 0.33 (a) and (c). It is also observed that MAW was well oxygenated, as shown in Figure 0.33 (e). Further below, as shown in Figure 0.33 (c), deep salinity maximum LIW was located at depths of between 60 and 85 meters. LIW was clearly observed at 39.38 per mille of salinity, ~18.80 °C of temperature and ~28.45 kg/m^3 of potential density in the T-S diagram, Figure 0.33 (a). At the bottom of the sea, dense and cold EMDW was present in the area with ~13.85 °C of temperature, ~38.80 per mille of salinity and ~29.19 kg/m^3 potential density, as shown with orange colour in the T-S diagram, Figure 0.33 (a).

3.2. Time Series Plots of KTS Studies

Monthly time series plots of temperature [^{o}C], salinity [per mille] and potential density [kg/m^{3}] versus depth [m] (pressure [dBar]) for each KTS station are presented separately in this section to describe seasonal and annual mixing processes, seasonal and permanent stratification layers, vertical structure of the water column and water masses of Levantine Surface Water (LSW), Modified Atlantic Water (MAW), Levantine Intermediate Water (LIW) and East Mediterranean Deep Water (EMDW) or so-called Transition Layer Water (TLW), throughout the study.

3.2.1. Station K07

Station K07 is the deepest and offshore station of the KTS studies. With bottom depths of about 670 meters and a distance of 5 nautical miles from the coastline, it is expected to reveal all physical oceanographic characteristics of the Cilician Basin. K07 considered being the least affected station by direct man impact, shortly as a reference.

Upper 25 meters of the water column was well mixed and uniform, almost throughout the study, as shown in Figure 0.34. During winter seasons, especially between January and March, intense mixing processes were observed in the study area. Thus upper 150 – 200 meters of the water column was dense, well mixed and uniform, as shown with yellow colour in Figure 0.34 (c). With the increasing temperatures over the course of spring and summer seasons, SST was observed to be warm up. Seasonal stratification of the water column, thus seasonal thermocline, halocline and pycnocline (vertical gradients in colours shown in Figure 0.34) were observed at depths of between 25 and 80 meters, especially between May and November. Strong seasonal stratification was observed in summer seasons throughout the study, as shown in Figure 0.34.

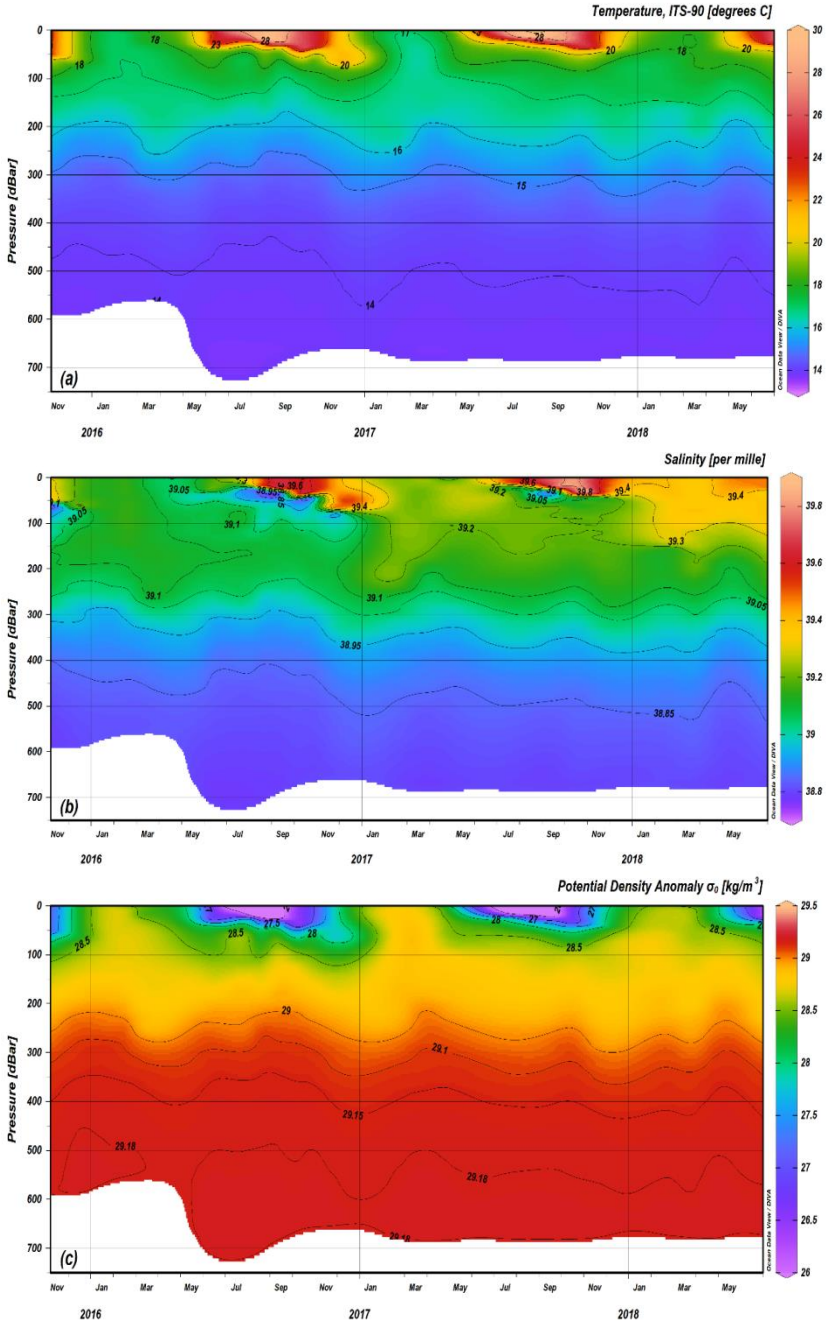

Figure 0.34: Time series plots of station K07. (a): temperature versus depth, (b): salinity versus depth, (c): potential density versus depth at K07.

Permanent stratification layer, thus permanent thermocline, shown as blue to violet colour in Figure 0.34 (a), permanent halocline, shown as blue colour in Figure 0.34 (b) and permanent pycnocline, shown as orange to red colour

in Figure 0.34 (c) was marked at depths of between 300 and 400 meters throughout the study.

All water masses identical to the Levantine Basin (i.e. LSW, MAW, LIW and EMDW) were observed at station K07 throughout the study. Warm and saline water mass (yellow and red colours in Figure 0.34 (a) and (b)) above the seasonal stratification layer represents the Levantine Surface Water (LSW) and was observed annually during stratified seasons, especially between May and November. Relatively less saline water mass which was trapped by two saltier water masses from above and below, and located just below seasonal stratification layer (blue and violet coloured in Figure 0.34 (b)) represents Modified Atlantic Water (MAW), and its origin is Atlantic water. MAW was observed at station K07 during stratified seasons throughout the study, but most pronounced in 2016. Deep salinity maximum water mass (green and yellow coloured in Figure 0.34 (b)) which was located at intermediate depths below MAW, represents the Levantine Intermediate Water (LIW). As shown in Figure 0.34 (b), LIW was observed at station K07 during stratified seasons throughout the study, but with different characteristics between years (green colour in 2016, yellowish in 2017 and yellow in 2018) as shown in Figure 0.34 (b). Below permanent thermocline, uniform and relatively cold (violet colour in Figure 0.34 (a)), fresher (violet colour in Figure 0.34 (b)) and dense (red colour in Figure 0.34 (c)) water mass with <14 ^{o}C temperatures, <38.85 per mille salinities and >29.180 kg/m^{3} potential density was observed continuously at the bottom of the sea. This water mass represented EMDW and located at depths of 500 meters and more throughout the study.

During the study, as shown in Figure 0.34, annual and seasonal cycles of mixing and stratification processes, and presence of water mass (i.e. LSW, MAW, LIW, EMDW) identical to the Cilician Basin were observed at station K07. Furthermore, significant salinity increases and changes of physical oceanographic characteristics on the upper thermocline were observed at the surface and intermediate depths consecutively every year, as shown in Figure 0.34 (b).

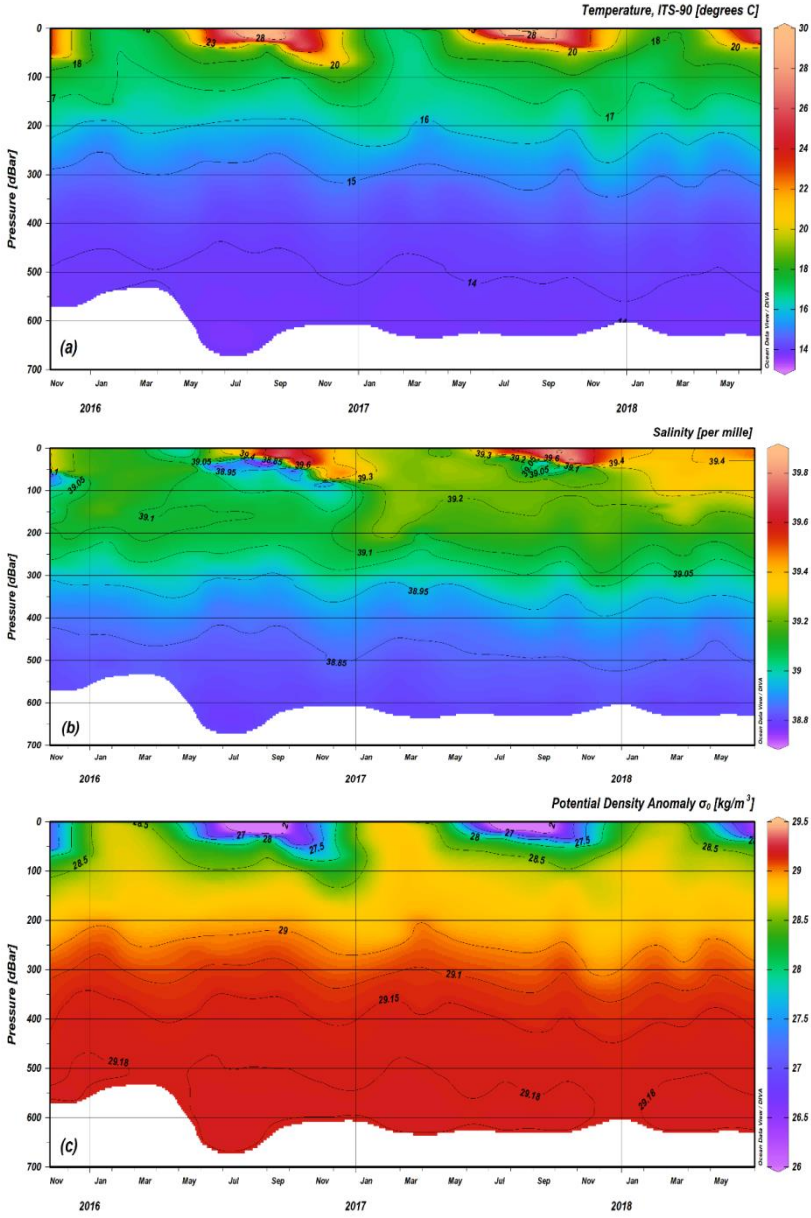

Figure 0.35: Time series plots of station K06. (a): temperature versus depth, (b): salinity versus depth, (c): potential density versus depth at K06.

3.2.2. Station K06

Along with station K07, station K06 with bottom depths of about 610 meters and distance of 3.5 nm from the coastline, considered as one of the

two open sea stations in KTS, and expected to reveal similar physical oceanographic characteristics with station K07.

As shown in Figure 0.35, upper 25 meters of the water column was well mixed and uniform, almost all along the study. During winter seasons, especially between January and March intense mixing processes were observed in the study area; thus upper 150 – 200 meters of the water column was dense, well mixed and uniform, as shown with yellow colour in Figure 0.35 (c). With increasing temperatures over the course of spring and summer seasons (Figure 0.35 (a)), SST was observed to be warmed up, and especially between May and November, seasonal stratification of the water column; thus seasonal thermocline, halocline and pycnocline (vertical gradients in colours shown in Figure 0.35) was observed at depths of between 25 and 80 meters. Strong seasonal stratification was observed in summer seasons throughout the study, as shown in Figure 0.35.

Permanent stratification layer, thus permanent thermocline, shown as blue to violet colour in Figure 0.35 (a), permanent halocline, shown as blue colour in Figure 0.35 (b) and permanent pycnocline, shown as orange to red colour in Figure 0.35 (c) was marked at depths of between 300 and 400 meters throughout the study.

All water masses identical to the Levantine Basin (i.e. LSW, MAW, LIW and EMDW) were observed at station K06 throughout the study. Warm and saline LSW (yellow and red colours in Figure 0.35 (a) and (b)) was observed annually during stratified seasons, especially between May and November. Relatively less saline MAW was located just below seasonal stratification layer (blue and violet coloured in Figure 0.35 (b)) and trapped by two saltier water masses from above and below, was observed at station K06 during stratified seasons throughout the study, but most pronounced in 2016. Deep salinity maximum LIW (green and yellow coloured in Figure 0.35 (b)) was located at intermediate depths below MAW. As shown in Figure 0.35(b), LIW was observed at station K06 during stratified seasons throughout the study, but with different characteristics between years (green colour in 2016, yellowish in 2017 and yellow in 2018), as shown in Figure 0.35 (b). Below permanent thermocline, at depths of 500 meters and more, uniform and relatively cold (violet colour in Figure 0.35 (a)), fresher (violet colour in Figure 0.35(b)) and dense (red colour in Figure 0.35 (c)) EMDW with <14 ^{o}C temperatures, <38.85 per mille salinities and >29.180 kg/m^3 potential density was observed continuously at the bottom of the sea throughout the study.

During the study, annual and seasonal cycles of mixing and stratification processes, and presence of water mass (i.e. LSW, MAW, LIW, EMDW) identical to the Cilician Basin were clearly observed at station K06, as shown in Figure 0.35. Furthermore, as shown in Figure 0.35 (b), significant salinity

increases and changes of physical oceanographic characteristics on the upper thermocline were observed at the surface and intermediate depths consecutively every year.

3.2.3. Station K05

Station K05 is a relatively shallow and coastal station with bottom depths of about 425 meters and distance of 1.5 nm from coastline. Due to its location, deepwater formations identical to the Cilician Basin is not expected to be observed in this station.

As shown in Figure 0.36, upper 25 meters of the water column was well mixed and uniform, almost all along the study. During winter seasons, especially between January and March intense mixing processes were observed in the study area; thus upper 150 – 200 meters of the water column was dense, well mixed and uniform, as shown with yellow colour in Figure 0.36 (c). Over the course of spring and summer seasons, SST observed to be warmed up (Figure 0.36 (a)), and especially between May and November seasonal stratification of the water column, thus seasonal thermocline, halocline and pycnocline (vertical gradients in colours shown in Figure 0.36) was observed at depths of between 25 and 80 meters. Strong seasonal stratification was observed in summer seasons throughout the study, as shown in Figure 0.36.

Permanent stratification layer, thus permanent thermocline, shown as blue to violet colour in Figure 0.36 (a), permanent halocline, shown as blue colour in Figure 0.36 (b) and permanent pycnocline, shown as orange to red colour in Figure 0.36 (c) was marked at depths of about 300 meters throughout the study.

Due to the bottom depth of this station, only the surface and intermediate water masses identical to the Levantine Basin (i.e. LSW, MAW and LIW) was observed at station K05 throughout the study. LSW (yellow and red colours in Figure 0.36 (a) and (b)) was observed annually above seasonal stratification layer during stratified seasons, especially between May and November. MAW was located just below seasonal stratification layer (blue and violet coloured in Figure 0.36 (b)), and trapped by two saltier water masses from above and below, observed at station K05 during stratified seasons, but most pronounced in 2016. LIW (green and yellow coloured in Figure 0.36 (b)) was located at intermediate depths below MAW. As shown in Figure 0.36 (b), LIW was observed at station K05 during stratified seasons throughout the study, but with different characteristics between years (green colour in 2016, yellowish in 2017 and yellow in 2018), as shown in Figure 0.36 (b).

As shown in Figure 0.36, annual and seasonal cycles of mixing and stratification processes and presence of water mass (i.e. LSW, MAW and LIW) identical to the Cilician Basin were observed at station K05 throughout the study. Furthermore, significant salinity increases and changes of physical oceanographic characteristics on the upper thermocline were observed at the surface and intermediate depths consecutively every year, as shown in Figure 0.36 (b).

3.2.4. Station K04

Station K04 is one of four coastal stations distributed within 0.5 nm in KTS to cover the neritic zone. With bottom depths of about 150 meters, K04 is the deepest coastal station in KTS and expected to reveal physical oceanographic characteristics of subsurface and intermediate waters of the Cilician Basin.

As shown in Figure 0.37, upper 25 meters of the water column was well mixed and uniform, almost all along the study. Due to intense mixing processes during winter seasons, especially between January and March, water column observed to be dense, well mixed and uniform from sea surface to the bottom of the sea, as shown with yellow colour in Figure 0.37(c). With increasing temperatures over the course of spring and summer seasons (Figure 0.37 (a)), surface waters warmed up and especially between May and November, seasonal stratification of the water column, thus seasonal thermocline, halocline and pycnocline (vertical gradients in colours shown in Figure 0.37) observed at depths of between 25 and 80 meters. Strong seasonal stratification observed in summer seasons throughout the study, as shown in Figure 0.37.

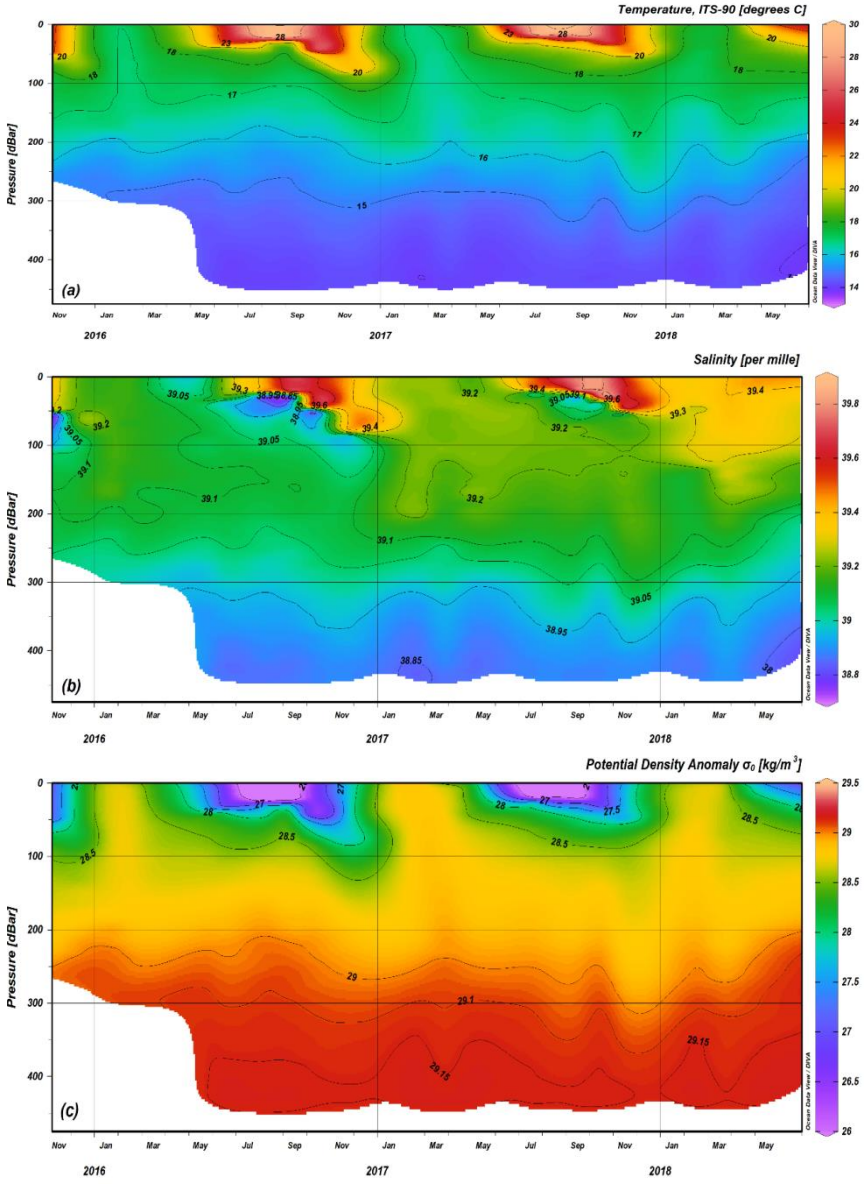

Figure 0.36: Time series plots of station K05. (a): temperature versus depth, (b): salinity versus depth, (c): potential density versus depth at K05.

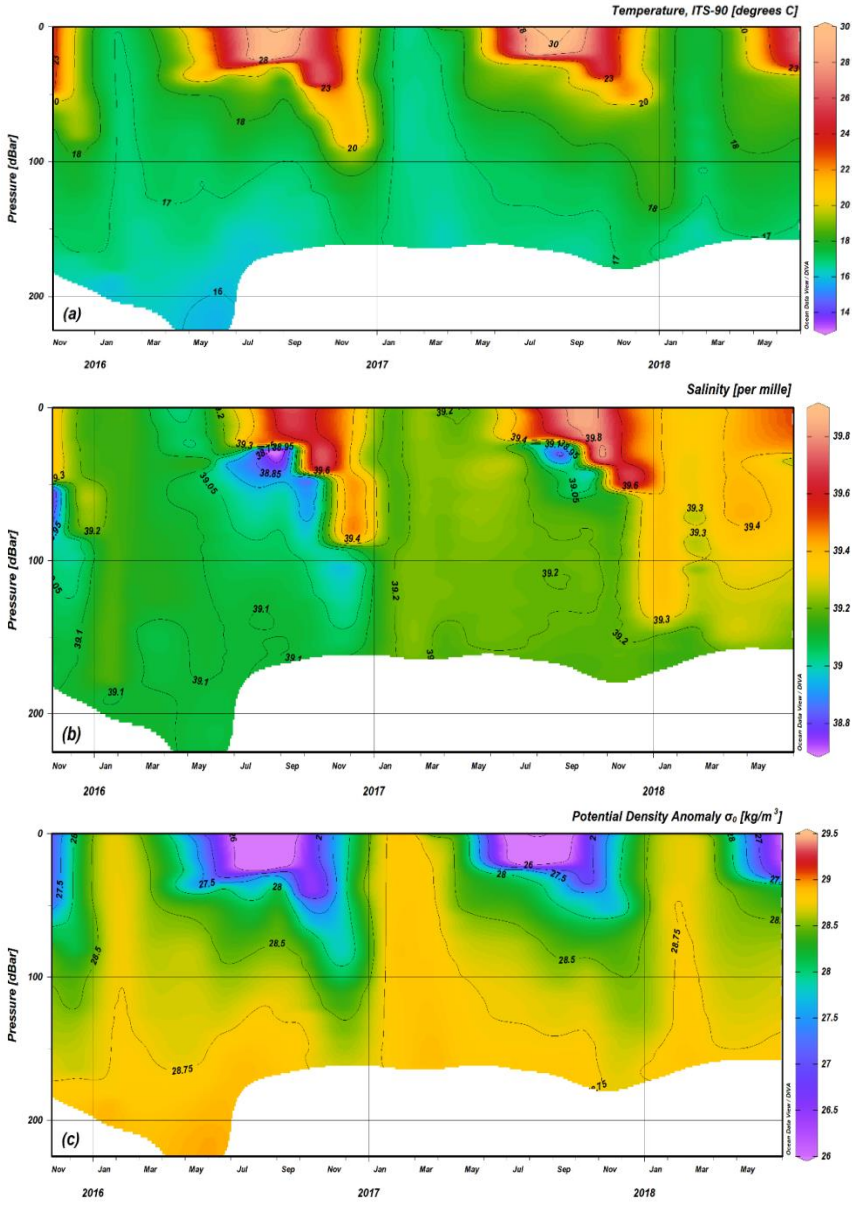

Figure 0.37: Time series plots of station K04. (a): temperature versus depth, (b): salinity versus depth, (c): potential density versus depth at K04.

Due to the bottom depth of this station, only the surface and intermediate water masses identical to the Levantine Basin (i.e. LSW, MAW and LIW) was observed at station K04 throughout the study. Warm and saline LSW (yellow and red colours in Figure 0.37 (a) and (b)) above seasonal stratification observed annually during stratified seasons, especially between May and November. Relatively less saline MAW, trapped by two saltier

water masses from above and below was observed just below seasonal stratification layer (blue and violet coloured in Figure 0.37 (b)) during stratified seasons throughout the study, but most pronounced in 2016. Deep salinity maximum LIW (green and yellow coloured in Figure 0.37 (b)) was located at intermediate depths, between MAW and bottom of the sea. As shown in Figure 0.37 (b), LIW was observed at station K04 during stratified seasons throughout the study, but with different characteristics between years (green colour in 2016, yellowish in 2017 and yellow in 2018) as shown in Figure 0.37 (b).

During the study, as shown in Figure 0.37, annual and seasonal cycles of mixing and stratification processes, and presence of water mass (i.e. LSW, MAW and LIW) identical to the basin itself were observed at station K04. Furthermore, as shown in Figure 0.37 (b), significant salinity increases and changes of physical oceanographic characteristics on the upper thermocline were observed at the surface and intermediate depths consecutively every year.

3.2.5. Station K03

Station K03 is one of four coastal stations distributed within 0.5 nm in KTS to cover the neritic zone. With bottom depths of about 100 meters, it is expected to reveal physical oceanographic characteristics of subsurface and intermediate waters of the Cilician Basin. Along with stations K01 and K02, station K03 considered to be most affected by anthropogenic processes in KTS.

As shown in Figure 0.38, upper 25 meters of the water column was well mixed and uniform, almost all along the study. During winter seasons, especially between January and March, intense mixing processes observed in the study area, thus water column was dense, well mixed and uniform from the sea surface to the bottom of the sea as shown with yellow colour in Figure 0.38 (c). With increasing temperatures over the course of spring and summer seasons (Figure 0.38 (a)), SST was observed to be warmed up and especially between May and November, seasonal stratification of the water column, thus seasonal thermocline, halocline and pycnocline (vertical gradients in colours shown in Figure 0.38) was observed at depths of between 25 and 75 meters. Strong seasonal stratification observed in summer seasons throughout the study, as shown in Figure 0.38.

Due to the relatively shallow bottom depth of this station, only the surface and subsurface water masses identical to the Levantine Basin (i.e. LSW, MAW and LIW) were observed at station K03 throughout the study. Warm and saline LSW (yellow and red colours in Figure 0.38 (a) and (b)) was

observed annually above seasonal stratification layer, during the stratified seasons, especially between May and November. Relatively less saline MAW was located just below seasonal stratification (blue and violet coloured in Figure 0.38 (b)), trapped by two saltier water masses from above and below, observed at station K03 during stratified seasons throughout the study, but most pronounced in 2016. Due to relatively shallow bottom depth of the station, the only upper portion of the LIW (green and yellow coloured in Figure 0.38 (b)) was observed at intermediate depths, between MAW and the bottom of the sea. As shown in Figure 0.38 (b), LIW was observed at station K03 during stratified seasons throughout the study, but with different characteristics between years (green colour in 2016, yellowish in 2017 and yellow in 2018) as shown in Figure 0.38 (b).

As shown in Figure 0.38, annual and seasonal cycles of mixing and stratification processes, and presence of water mass (i.e. LSW, MAW and LIW) identical to the Cilician Basin were clearly observed at station K03, throughout the study. Furthermore, significant salinity increases and changes of physical oceanographic characteristics on the upper thermocline were observed at the surface and intermediate depths consecutively every year, as shown in Figure 0.38 (b).

3.2.6. Station K02

Station K02 is one of four coastal stations distributed within 0.5 nm in KTS to cover the neritic zone. With bottom depths of about 50 meters, it is expected to reveal physical oceanographic characteristics of surface and subsurface waters of the Cilician Basin. Along with stations K01 and K03, station K02 considered being most affected by anthropogenic processes in KTS.

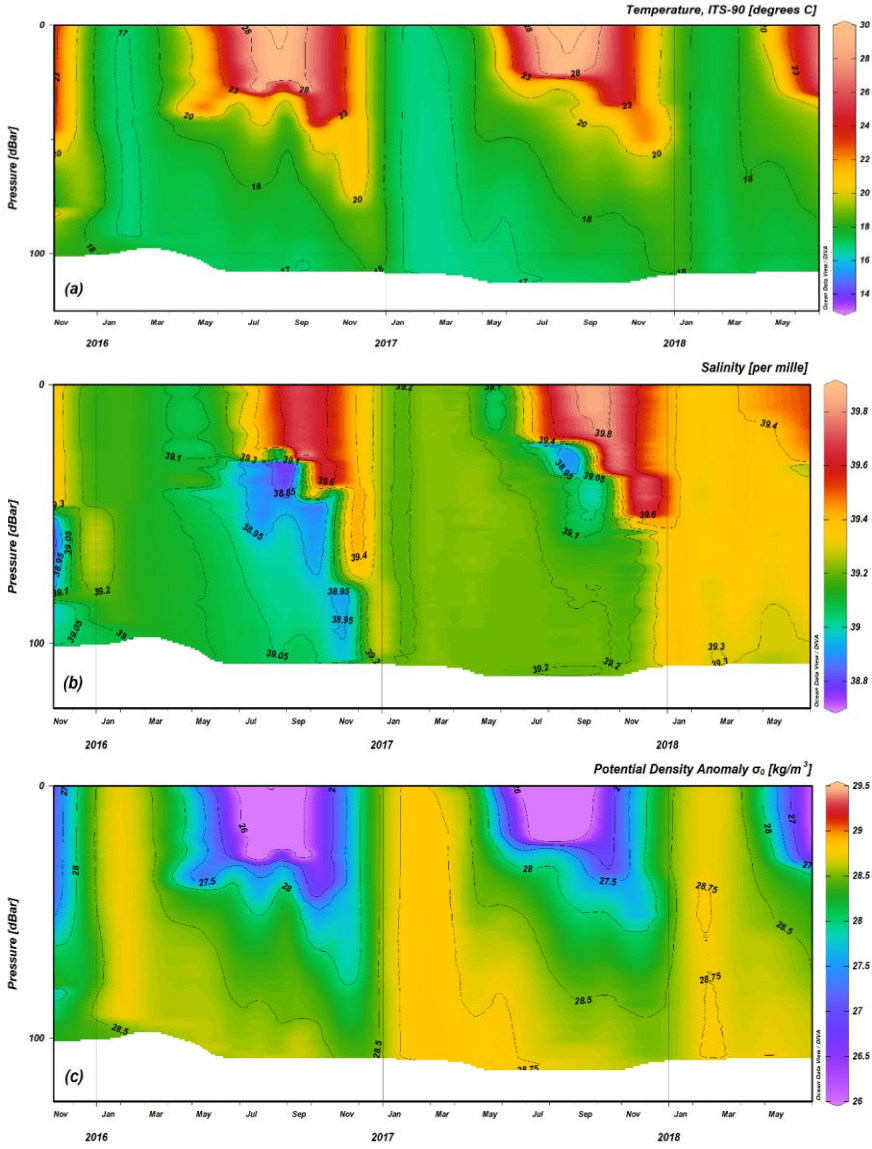

Figure 0.38: Time series plots of station K03. (a): temperature versus depth, (b): salinity versus depth, (c): potential density versus depth at K03.

As shown in Figure 0.39, upper 25 meters of the water column was well mixed and uniform, almost all along the study. During winter seasons, especially between January and March intense mixing processes were observed in the study area; thus water column was dense, well mixed and uniform from the sea surface to the bottom of the sea as shown with yellow colour in Figure 0.39 (c). With increasing temperatures over the course of spring and summer seasons (Figure 0.39 (a)), SST was observed to be warmed up and especially between May and November, seasonal

stratification of the water column, thus seasonal thermocline, halocline and pycnocline (vertical gradients in colours shown in Figure 0.39) was observed at depths of between 25 meters and bottom of the sea. Strong seasonal stratification was observed in summer seasons throughout the study, as shown in Figure 0.39.

Due to the relatively shallow bottom depth of this station, only the surface and subsurface water masses identical to the Levantine Basin (i.e. LSW and MAW) were observed at station K02 throughout the study. Warm and saline LSW (yellow and red colours in Figure 0.39 (a) and (b)) was observed annually above seasonal stratification layer during stratified seasons, especially between May and November. Relatively less saline MAW was located just below the seasonal stratification layer (blue and violet coloured in Figure 0.39 (b)). MAW was observed at station K02 during stratified seasons throughout the study, but most pronounced in 2016, where located between seasonal halocline and bottom of the sea. In 2017, MAW was less pronounced but present in the area, trapped by two saltier water masses from above and below, as shown in Figure 0.39(b).

As shown in Figure 0.39, annual and seasonal cycles of mixing and stratification processes and presence of water mass (i.e. LSW and MAW) identical to the Cilician Basin were observed at station K02. Furthermore, as shown in Figure 0.39 (b), significant salinity increases and changes of physical oceanographic characteristics on the upper thermocline were observed at the surface and intermediate depths consecutively every year in this station.

3.2.7. Station K01

Station K01 is one of four coastal stations distributed within 0.5 nm to cover the neritic zone. With bottom depths of about 25 meters, it is expected to reveal physical oceanographic characteristics of surface waters of the Cilician Basin.

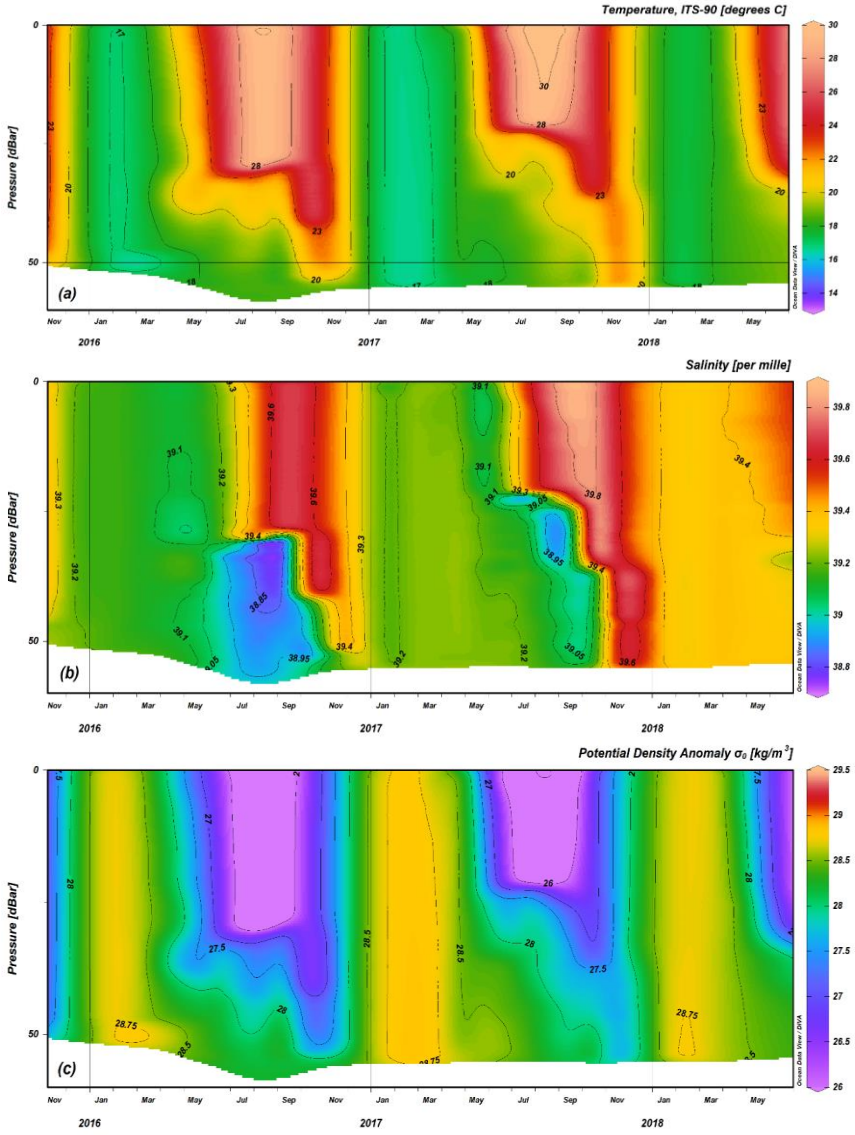

Figure 0.39: Time series plots of station K02. (a): temperature versus depth, (b): salinity versus depth, (c): potential density versus depth at K02.

As it is the shallowest and nearest station to the coastline in KTS studies, it is expected to be the most affected station by anthropogenic processes in KTS region.

As shown in Figure 0.40, due to relatively shallow bottom depths, the water column was well mixed and uniform from sea surface to the bottom of the sea in all seasons throughout the study, except summer of 2017. In summer of 2017, seasonal stratification layer, thus seasonal thermocline, halocline and pycnocline (vertical gradients in colours shown in Figure 0.40),

was observed at depths of about 20 meters, between June and September. Intense mixing processes were dominant in the area during the winter seasons. The water column was dense, well mixed and uniform from the sea surface to the bottom of the sea as shown with yellow colour in Figure 0.40 (c), especially between January and March.

Due to the shallow bottom depth of this station, only the surface and subsurface water masses identical to the Levantine Basin (i.e. LSW and MAW) were observed at station K01 throughout the study. With increasing temperatures throughout spring and summer, SST was observed to be warmed up as shown with yellow, red and beige colours in Figure 0.40 (a). Warm and saline LSW was observed annually from June to November, as shown in yellow, red and beige colours in Figure 0.40 (a) and (b). MAW (violet and blue coloured in Figure 0.40 (b)) was observed only in summer of 2017, just below halocline from June to September in station K01.

During the study, seasonal mixing cycles, seasonal stratification, and presence of water masses (i.e. LSW, MAW) identical to Cilician Basin were observed in station K01, as shown in Figure 0.40. Furthermore, significant salinity increases and changes of physical oceanographic characteristics on the upper thermocline were observed at the surface and intermediate depths consecutively every year in this station, as shown in Figure 0.40 (b).

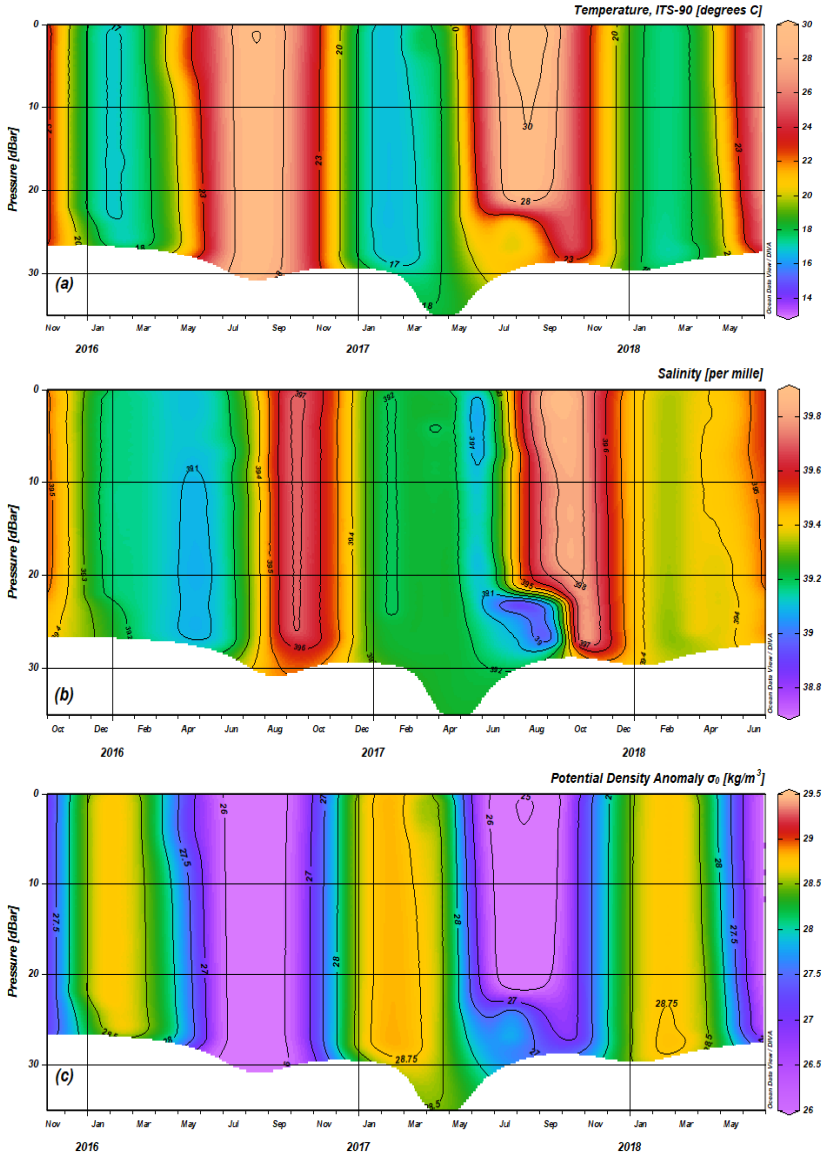

Figure 0.40: Time series plots of station K01. (a): temperature versus depth, (b): salinity versus depth, (c): potential density versus depth at K01.

4. Discussions

The results of the KTS data sets presented in this study were collected within the framework of the 114Y139 Code numbered TUBITAK project. The project mentioned above (Salihoglu et al., 2019) is the most recent, comprehensive and systematic study conducted in the Cilician Basin after the

POEM studies of which the fieldwork was completed in 1995 by the study of the Levantine Intermediate Water Experiment (The LIWEX Group, 2003).

In this study, analysis of high-frequency data sets which were collected in a total of twenty-seven monthly cruises during the Kıbrıs Time Series (KTS) studies is presented to investigate sub-mesoscale physical oceanographic characteristics of the south-western Cilician Basin (offshore of Kyrenia, Northern Cyprus). The two major subjects discussed in this study are;

i. The water masses and the physical oceanographic characteristics which are identical to the Levantine Basin, thus to the Cilician Basin were extensively investigated in the study area. The possibility of regional LIW formation has been investigated.

ii. Consecutive salinity shifts thus temperature and potential density changes in water mass characteristics at the surface and intermediate layers (i.e. LSW, MAW and LIW) on upper thermocline has been observed and recorded.

4.1. Physical Oceanographic Characteristics of the Study Area

The general circulation of the Cilician Basin is a highly complex and dynamic system with meandering and reversing currents and reappearing cyclonic/anti-cyclonic energetic mesoscale eddies with temporal and spatial variabilities. The dominant driving mechanism of the general circulation temporarily and spatially change between the current systems (i.e. Cilician Current and Asia Minor Current) and the eddies (Salihoglu et al., 2019).

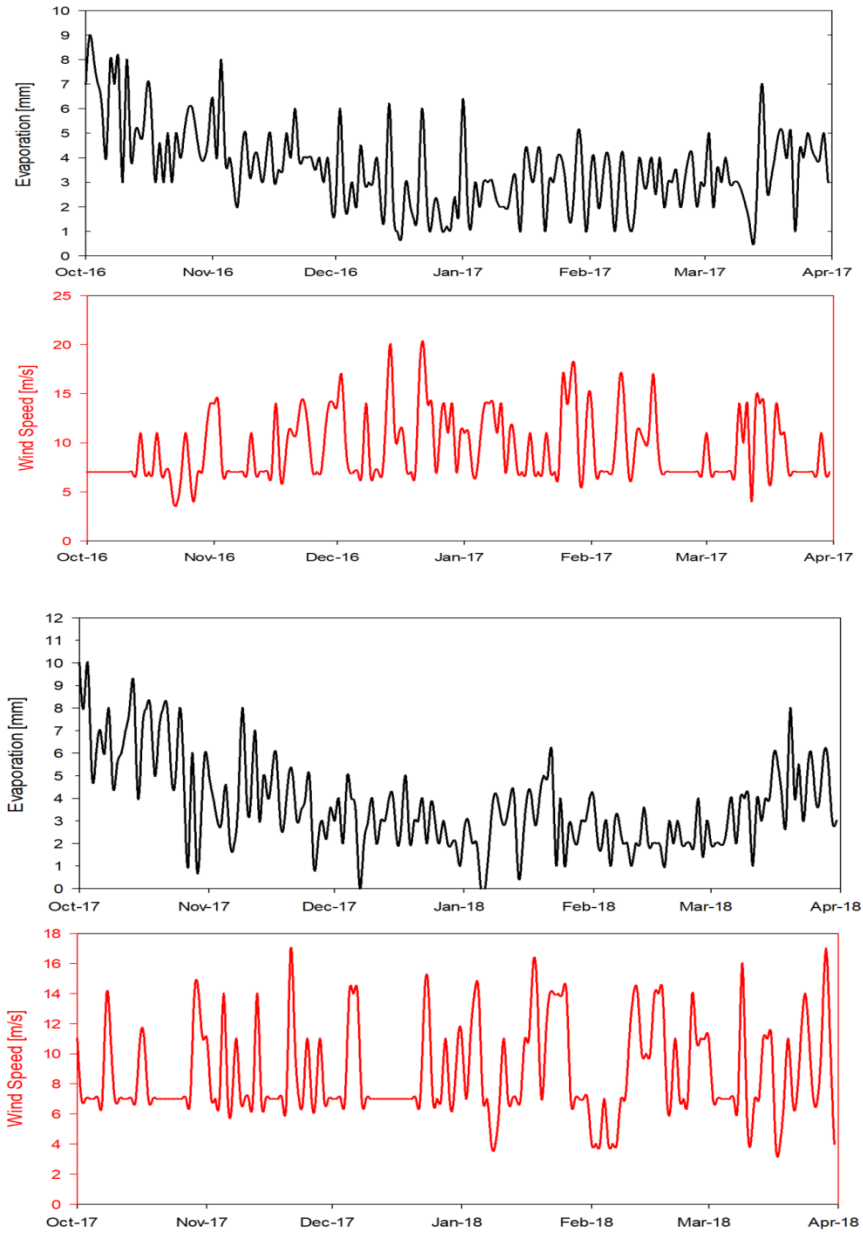

Figure 0.41: Evaporation and wind speed data from October 2016 to April 2017 (upper figure) and October 2017 to April 2018 (lower figure).

All physical oceanographic characteristics identical to the Levantine Basin revealed to be present in the study area. Due to the excessive heat, evaporation and atmospheric interactions, upper 25 meters of the water column was well mixed and uniform, almost all along the study. In winter seasons, especially between January and March, the study region was

dominated by intense vertical mixing processes due to wind and sinking of relatively high-density water masses to the depths of about 150 to 200 meters. This sinking of relatively high-density water masses occurred due to evaporative cooling coinciding with strong winds, as shown in Figure 0.41. Between April and December, vertical structure of the water column indicated strong seasonal stratification, especially intensifying during summer seasons. All these processes and vertical structure of the water column observed in the study area were consistent with the previous studies (Bergamasco & Malanotte-Rizzoli, 2010; Hecht et al., 1988; Kucuksezgin & Pazi, 2006; Malanotte-Rizzoli & Hecht, 1988; Malanotte-Rizzoli & Robinson, 1988; Onken & Yuce, 2000; Özsoy et al., 1989, 1993; Robinson et al., 1991; The LIWEX Group, 2003; The POEM Group, 1992), except salinity shifts and changes observed in characteristics of water mass on upper thermocline, especially in the latter part of the study.

Various water masses identical to the physical oceanographic characteristic of the Levantine Basin (i.e. LSW, MAW, LIW and EMDW) were present in the study area. As shown in Figure 0.42, typical "Scorpion Tail" form of the multi-layered vertical structure of the water column observed throughout the study during stratified seasons, especially between May and November. Warm and saline LSW located within the surface mix layer, above the seasonal thermocline. Regionally formed deep salinity maximum LIW located at intermediate depths and Atlantic originated subsurface salinity minimum MAW trapped between LSW and LIW. Permanent halocline located at depths of about 300 - 400 meters, throughout the study. The EMDW were consistently present in the study area with ~13.85 °C of temperature, 38.80 per mille of salinity and 29.18 kg/m^3 of potential density below the permanent halocline, at depths of about 500 meters and below.

As it is well known in the literature, salty and warm LSW forms in entire Levantine Basin due to excessive heat, evaporation and relatively weak winds during summer seasons (Malanotte-Rizzoli & Hecht, 1988; Özsoy et al., 1989). As presented in Chapter 3 of this study, the surface layer of the study area was dominated by the warm and saline LSW during the stratified seasons throughout the study, especially between May and November. In winter seasons, high salinity content LSW became denser due to excessive heat loss and evaporative cooling caused by dry and cold “Poyraz” winds. These processes reduced the stability of the water column, and eventually caused convective mixing of the water column to intermediate depths and sinking of relatively saline and high-density water to the depths of about 200 meters, as can be seen in temperature, salinity and potential density anomaly plots, in Chapter 3 of this study.

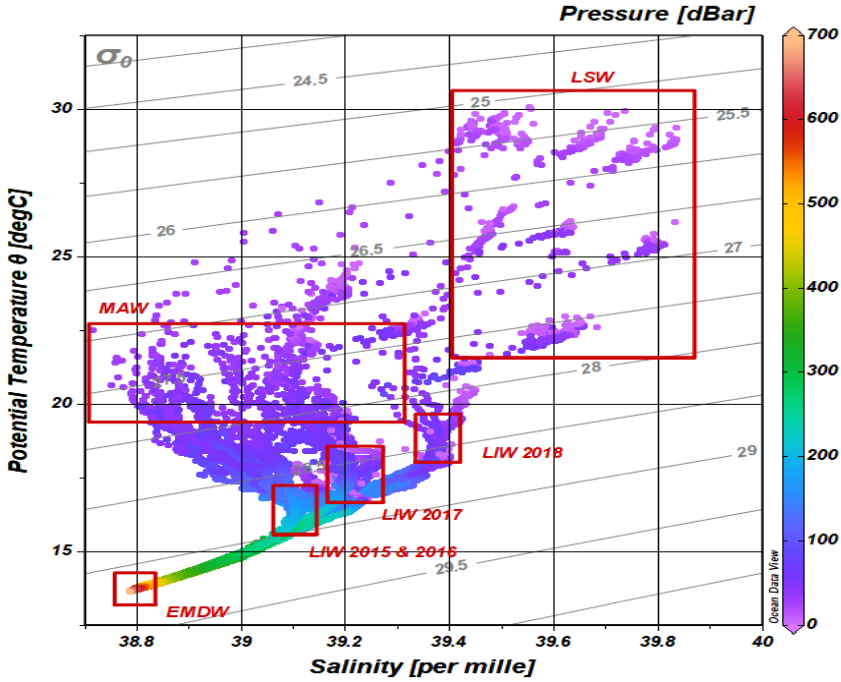

Figure 0.42: Water masses defined in the T-S diagram of the KTS studies.

Analysed results of the high-frequency KTS studies revealed that, physical oceanographic characteristics of the winter mixed layer, which forms every year in winter seasons due to convective mixing processes, and the physical oceanographic characteristics of the LIW (Table 0.8), which was located at intermediate depths during the stratified seasons in each year, were similar throughout the study . It is observed and recorded that, each year, the physical oceanographic characteristics of the LIW (Table 0.8) were defined by the physical oceanographic characteristics of the winter mixed layer. Physical oceanographic characteristics of the LIW, which was located at intermediate depths during stratified seasons, and the dense water mass which was formed each year within the winter mix layer, were similar in each year, as shown in T-S diagrams and Time Series Plots in sections Chapter 2 and 0. Furthermore, consecutive salinity shifts and changes of physical oceanographic characteristics observed on upper thermocline is possibly an indicator of local formation of the LIW. It is also observed that, depth range or centre of the LIW located in the study area was within the depth range or above the depth of the winter mixed layer in each year. These results suggest that LIW located in the study area during the study is locally formed within the winter mix layer in the study area.

Table 0.8: LIW characteristics at KTS station K07.

Date	Temperature [°C]	Salinity [per mille]	Potential Density [kg/m^3]	Depth Range [m]
November 2015	16.97 – 16.17	39.10	28.68 – 28.87	150 - 200
December 2015	16.92 – 16.42	39.12	28.70 – 28.83	140 - 170
May 2016	16.91 – 16.26	39.10	28.69 – 28.86	140 - 190
June 2016	16.88 – 16.17	39.10	28.70 – 28.87	150 - 190
August 2016	16.75 – 16.10	39.10	28.74 – 28.89	145 - 185
September 2016	16.46 – 16.00	39.10	28.80 – 28.91	140 - 170
October 2016	16.27 – 16.02	39.10	28.85 – 28.90	165 - 185
November 2016	16.41 – 16.01	39.10	28.82 – 28.91	190 - 215
April 2017	18.36 – 17.86	39.26	28.45 – 28.58	20 - 60
July 2017	18.57 – 17.26	39.21	28.36 – 28.69	50 - 100
September 2017	17.65 – 17.23	39.21	28.59 – 28.69	90 - 125
October 2017	17.43 – 17.03	39.21	28.64 – 28.74	100 - 130
November 2017	17.37 – 17.15	39.21	28.76 – 28.71	110 - 135
March 2018	18.15 – 18.09	39.39	28.60 – 28.62	67 - 77
April 2018	NA	NA	NA	NA
June 2018	18.95 – 18.29	39.39	28.39 – 28.56	60 - 85

NA: Not Applicable. Possibly due to mixing processes in the water column.

In literature, Rhodes Gyre and Antalya Basin described as the main LIW formation sites in several studies. Additionally, in the same studies, the north-eastern part of the Levantine Basin, the Cilician Basin was discussed as a potential LIW formation region (The LIWEX Group, 2003; The POEM Group, 1992). The preconditioning and formation phases of LIW formation in Rhodes Gyre evidently described by the LIWEX Group (2003). Very salty surface waters produced due to excessive evaporation in summer seasons. By the end of autumn and beginning of winter, dry and cold "Poyraz" winds cause excessive heat loss on surface layers of the water column. These processes induce evaporative cooling of the sea surface which increases the salinity, hence the density of the surface waters that reduce the stability of the water column, though even weak winds can induce vertical mixing of the water column through the intermediate depths in winter seasons. By the end of winter mixing processes, these newly formed water masses spreads along from the convection site by isopycnal surfaces, driven by cyclonic / anti-cyclonic eddies on upper thermocline (The LIWEX Group, 2003).

The similar conditions of above mentioned LIW formation processes in the Rhodes Gyre (The LIWEX Group, 2003) were present in the study area during the entire study period. Furthermore, the results of the model study by Lascaratos and colleagues (1993) revealed that the LIW should be centred within or above the winter mixed layer depth in the formation region. If not and centred below the winter mixed layer depth, it suggests that LIW is not locally formed and advected by other source region (A Lascaratos et al., 1993). In the northern Levantine Basin, the formation of LIW was observed

and recorded only in the Rhodes Gyre and Antalya Basin (Onken & Yuce, 2000; Özsoy et al., 1993; The LIWEX Group, 2003; The POEM Group, 1992). Yet in literature, there is no evidence that the cyclonic circulation of the Rhodes Gyre penetrates to the Cilician Basin, therefore the LIW observed in the study is not an advection from the Rhodes Gyre.

The study of Kücüksezgin and Pazı (2006) revealed that the LIW was present in the Cilician Basin during their three separate cruises, respectively in May 1997, July 1998 and October 2003. Multi-layered vertical structure, the "Scorpion Tail" form of the water column and the presence of the LIW was observed in the study area during July 1998 and October 2003 cruises. However, the "Scorpion Tail" form of the water column was not formed in the study area during their May 1997 cruise.

114Y139 code numbered TUBITAK Project (Salihoglu et al., 2019) which also comprised the subject of this study, the KTS studies, is the most recent oceanographic study conducted in the Cilician Basin between 2015 and 2018.

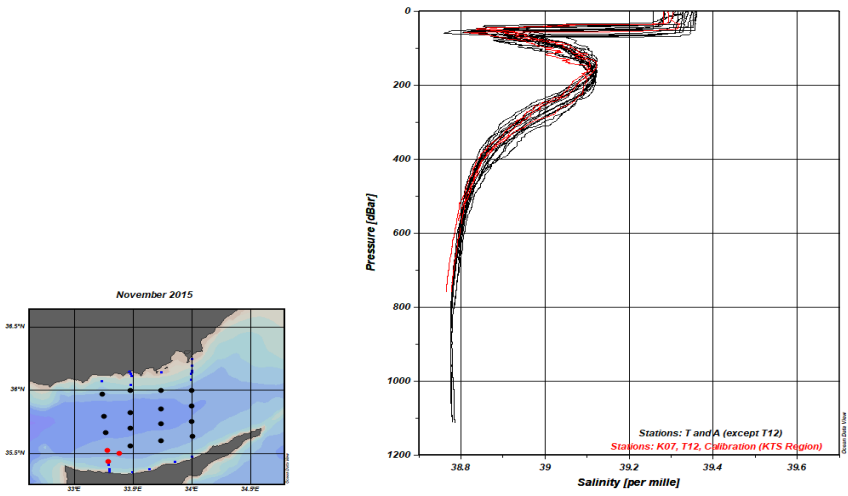

Figure 0.43: Salinity profiles of 114Y139 Code numbered TUBITAK Project stations in November 2015.

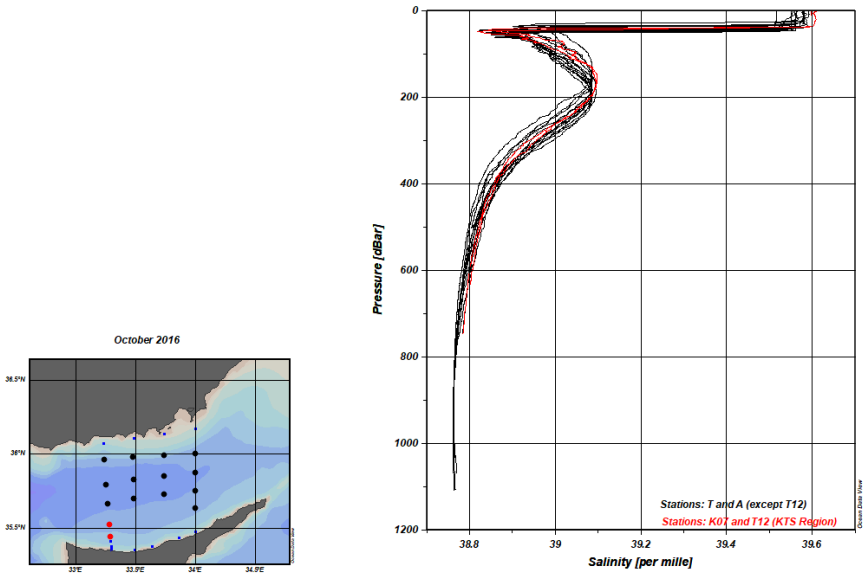

Figure 0.44: Salinity profiles of 114Y139 Code numbered TUBITAK Project stations in October 2016.

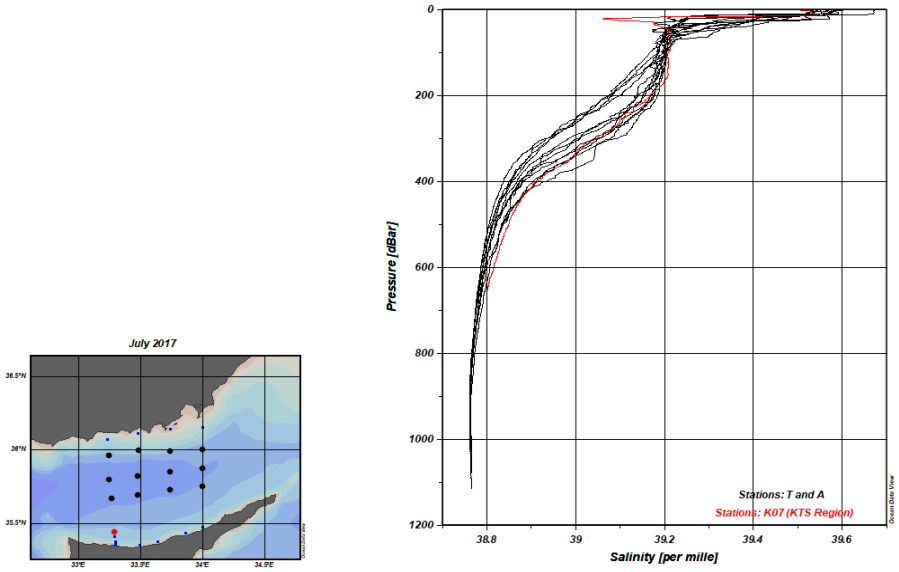

Figure 0.45: Salinity profiles of 114Y139 Code numbered TUBITAK Project stations in July 2017.

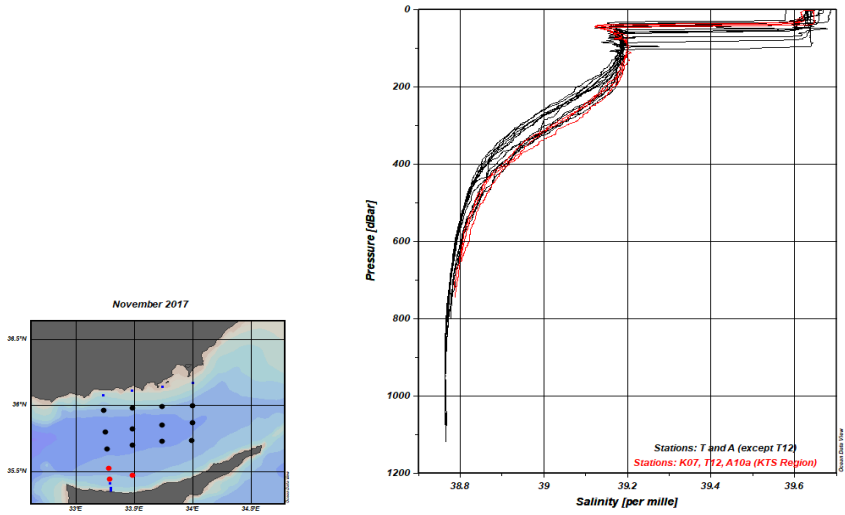

Figure 0.46: Salinity profiles of 114Y139 Code numbered TUBITAK Project stations in November 2017.

In order to analyse and understand physical oceanographic characteristics of the Cilician Basin, the results of KTS stations were compared with all the other stations (“T” and “A” stations in Figure 0.9) of the project mentioned above. At the first part of the study, in 2015 and 2016, the results are observed to be similar and consistent, as shown in Figure 0.43 and Figure 0.44. With ~39.10 per mille of salinity, characteristics of the LIW and the "Scorpion Tail" form of the water column were identical in 2015 and 2016, within the project and with the previous studies. However, in 2017, significant changes and differences were observed on the physical oceanographic characteristics in the upper thermocline, hence in the LIW. In July 2017, the LIW and the "Scorpion Tail" form of the water column was observed only in KTS station K07, as shown in Figure 0.45. As already described in Chapter 3, the LIW and the “Scorpion Tail” form of the water column was observed at station K07 all along the stratified seasons in 2017. On the other hand, at the other stations (“T” and “A” stations) of the project, presence of the LIW and multi-layered structure of the water column was observed only in November 2017, as shown in Figure 0.46.

Results of this study revealed that in each year, the deep salinity maximum LIW was present in the study area during stratified seasons, and disappeared in winter seasons due to mixing processes. By the end of mixing processes, LIW was reappeared at intermediate depths in similar characteristics with winter mixed layer, repeatedly every year.

Based on the results of this study and facts from literature, this study concluded that the study area is possibly a formation site of LIW and yet, it is the first study to reveal that the LIW forms locally in the Cilician Basin.

4.2. Salinity Shift and Change of Upper Thermocline Characteristics in KTS Area

Although results of 2015 and 2016 of this study seems to be similar and consistent with the results of the POEM Group (1993) and also with the results of Onken and Yuce (2000), and Kucuksezgin and Pazi (2006), the analyses of the whole data set revealed consecutive salinity increases, thus changes in temperature and potential density on upper thermocline, (i.e. LSW, MAW and LIW), throughout the study, especially in 2017 and 2018. Compared to the results of 2015 and 2016 of this study and the previous studies, significant and consecutive changes in salinity with increasing trend and shifts in temperature and potential density on upper thermocline characteristics were observed in 2017 and 2018. In total of about 0.30 per mille of salinity increase in LIW was observed throughout the study, between November 2015 and June 2018. Compared to the previous year, about 0.10 per mille of salinity increases were recorded in 2017 and 0.20 per mille in 2018. Below the permanent halocline, physical oceanographic characteristics were observed to be unaffected and unchanged.

Upper thermocline circulation and water masses of the northern Levantine Basin, their features, characteristics, driving dynamics, structure and patterns were revealed by the studies of the POEM Group (Bergamasco & Malanotte-Rizzoli, 2010; Hecht et al., 1988; Malanotte-Rizzoli & Hecht, 1988; Malanotte-Rizzoli & Robinson, 1988; Özsoy et al., 1989, 1993; Robinson et al., 1991; The LIWEX Group, 2003; The POEM Group, 1992). Additionally, the studies of Onken and Yuce (2000) and Kucuksezgin and Pazi (2006) in north-eastern Levantine Basin were revealed similar and consistent results with the POEM studies (Kucuksezgin & Pazi, 2006; Onken & Yuce, 2000). In literature, characteristics of LIW defined as shown in Table 0.1. The POEM Group consistently detected the LIW with 39.10 – 39.20 per mille of salinity, ~16.00 °C of temperature and 28.90 kg/m^3 of potential density in their study between 1985 and 1991 with the exception of ≥39.30 per mille of salinity in March 1991 which high surface salinity caused by increased surface fluxes in summer of 1990, concluded as the possible reason (Özsoy et al., 1993).

Figure 0.42, Figure 0.47, Figure 0.48, Figure 0.49 and Table 0.8 presented to discuss and describe salinity increases and changes in physical oceanographic characteristics of water masses observed in the upper thermocline at the study area.

Figure 0.42 and Figure 0.47, the T-S diagrams of the KTS studies revealed that identical "Scorpion Tail" form of the multi-layered vertical structure of the water column was present in the area throughout the study. However, in 2017 and 2018, significant shifts and changes were observed in physical oceanographic characteristics of LSW, LIW and MAW. In 2015 and 2016, LIW was marked at ~39.10 per mille salinity, 16.00 – 16.75 °C temperature and 28.75 – 28.87 kg/m^3 potential density anomaly, as described in literature (A Lascaratos et al., 1993; Onken & Yuce, 2000; Özsoy et al., 1989, 1993; Robinson et al., 1991; The LIWEX Group, 2003). In 2017 and 2018, although the "Scorpion Tail" form was present in the area, LIW was marked at ~39.20 per mille salinity, 17.00 – 17.75 °C temperature, 28.65 – 28.75 kg/m^3 potential density anomaly and ~39.39 per mille salinity, 18.20 – 19.00 °C temperature, 28.45 – 28.55 kg/m^3 potential density anomaly, respectively. In the same period, MAW was marked with salinities at 38.80 – 38.99 per mille in 2015 and 2016, at 38.95 – 39.12 per mille in 2017 and at 39.32 per mille in 2018, respectively. Significant salinity increases were also observed in LSW, especially between summer seasons of 2016 and 2017. LSW was recorded at ~39.65 per mille in September 2016 and ~39.80 per mille at the beginning of October 2017, respectively.

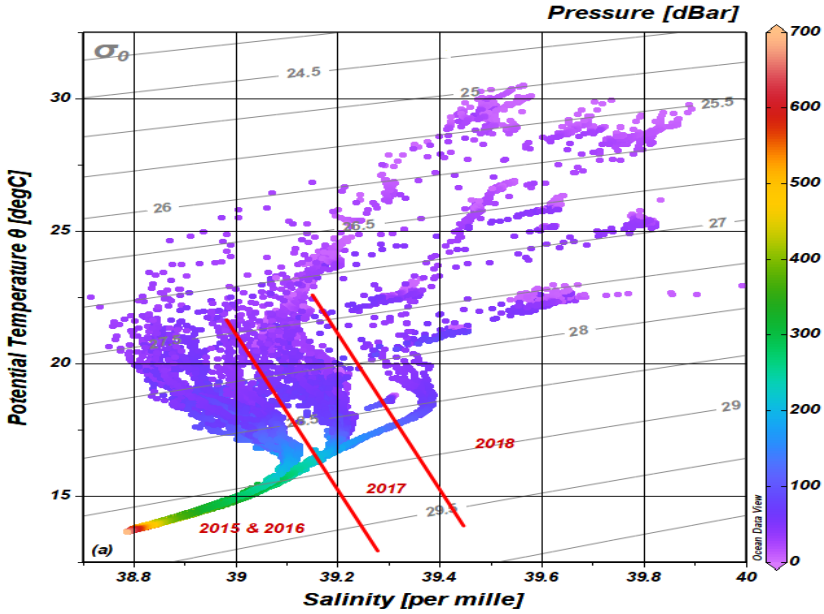

Figure 0.47: Shifts of water mass characteristics between years observed on the T-S diagram of KTS studies.

As shown in Figure 0.48, salinity shifts and changes in physical oceanographic characteristics of the water masses on upper thermocline were clearly observed consecutively every year in the study area. About 0.20 per mille of salinity increase was recorded in the surface mixed layer, which is dominated by the salty LSW during stratified seasons, between 2016 and 2017. Highest increase was recorded in MAW with 0.50 per mille of salinity. Possibly the most critical and significant salinity increase and changes of physical oceanographic characteristics were recorded in LIW. As shown in Table 0.8 and Figure 0.48, along with ~0.30 per mille of salinity increase, increases in temperature and eventually decreases in potential density were caused significant shoaling in LIW.

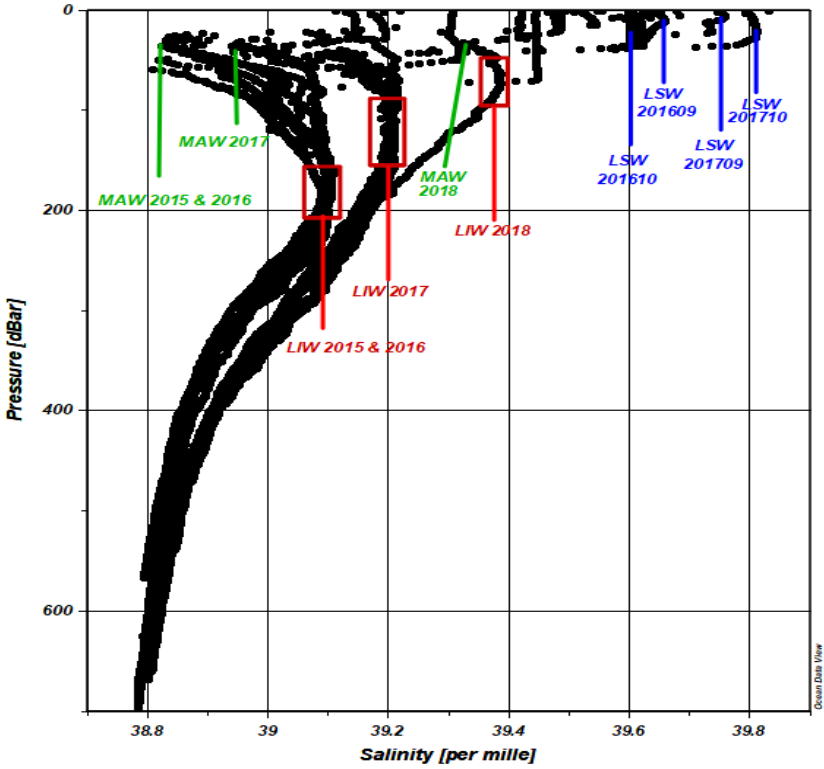

Figure 0.48: Salinity profiles of KTS station K07 during stratified seasons between 2015 and 2018.

Colour scaling of time series plots of salinity measurements at stations K01, K03 and K07 which is presented in Figure 0.49 are self-explanatory on seasonal and annual salinity shift which was observed throughout the study in the area. As shown in Figure 0.49, coloured scaling of salinities in winter

mixed layer were blue (~39.10 per mille) in 2016, green (~39.20 per mille) in 2017 and dark green to yellow (~39.40 per mille) in 2018. In summer seasons of 2016 and 2017, the coloured scale of the surface mixed layer was orange and red, respectively.

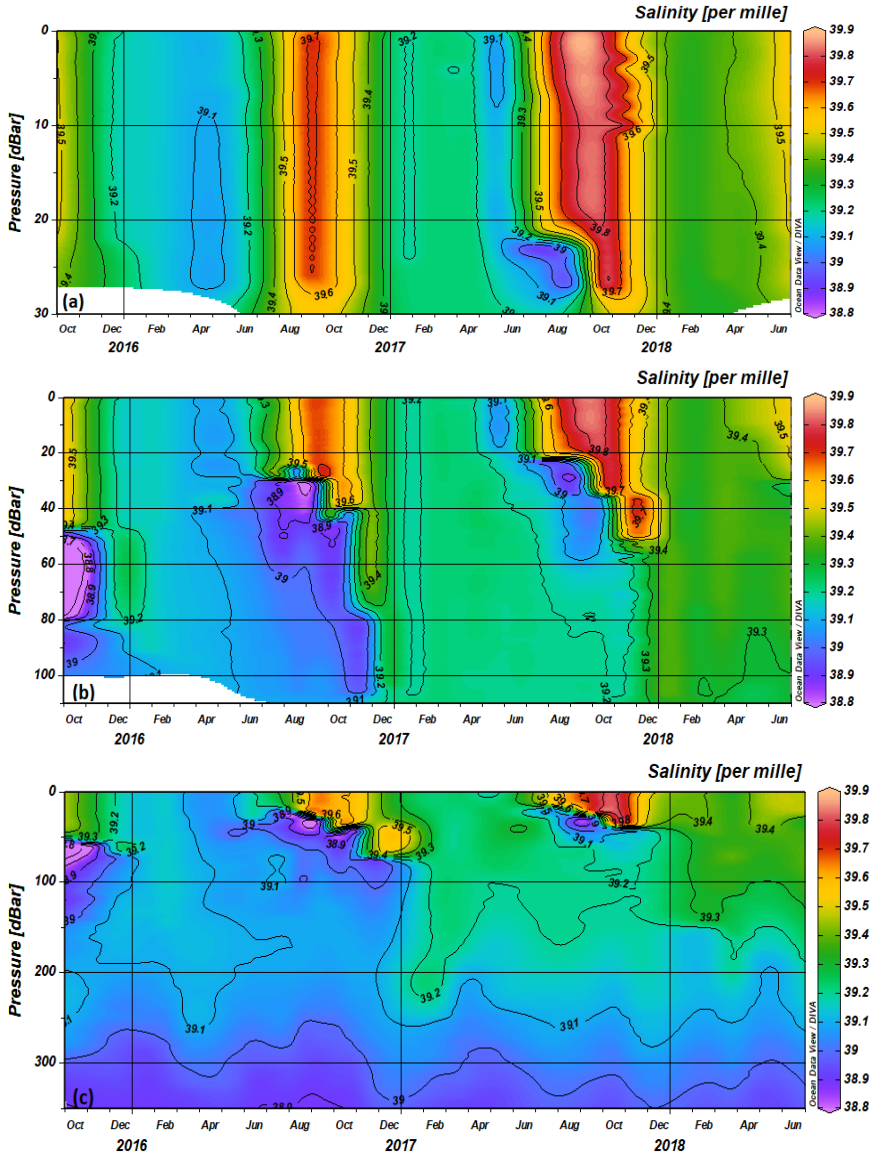

Figure 0.49: Time series plots of salinity measurements vs depth. (a): Station K01. (b): Station K03. (c): Station K07.

The study of Salihoglu and colleagues in 2019 revealed that similar salinity increases were observed in the Cilician Basin during the seasonal cruises between 2015 and 2017. Possibly due to the frequency (seasonal cruises) of the study, salinity shift at "T" and "A" stations were not as pronounced as KTS stations.

By the contribution of METU – IMS, the data sets of "Erdemli Time Series" (ETS) study analysed in order to understand if the observed phenomena are local to the KTS study region, or it is basin-wide. The ETS results revealed that, salinity shift and changes in physical oceanographic characteristics on upper thermocline is observed not only in the KTS study region, but in the entire Cilician Basin, especially in 2018. Salinity was recorded with 39.93 per mille in surface mixed layer in September 2018, and with 39,56 per mille in winter mixed layer in December 2018. However, in 2019, a significant decrease in salinity was observed in the ETS studies.

Evaporation data of the study region and possibility of instrumental error (CTD, SBE 19Plus V2 SeaCAT Profiler) analysed to investigate if there were any correlation or explanation to the salinity increases observed during the study.

Evaporation data between January 2015 and June 2018 (Figure 0.50, Table 0.9, and Table 0.10) analysed to investigate if there were any correlation or explanation to the salinity increases observed during the study. Approximately 30 to 35 mm of total annual evaporation increases were recorded consecutively every year. Cumulatively, about 70 mm of total evaporation increases were recorded during the study period. Seasonal distribution of total evaporation was observed to be almost same in oceanographic spring and summer seasons. The differences occurred in oceanographic autumn and winter seasons, as shown in Table 0.9 and Table 0.10.

70 mm of total evaporation increases shall not be sufficient to change salinity characteristics on the upper thermocline, as presented in this study. Therefore, this study conclude that the salinity increases observed during the study shall not be due to evaporation. This subject requires further investigation and available data of this study is not sufficient to show if these salinity shifts are because of regional processes or global changes.

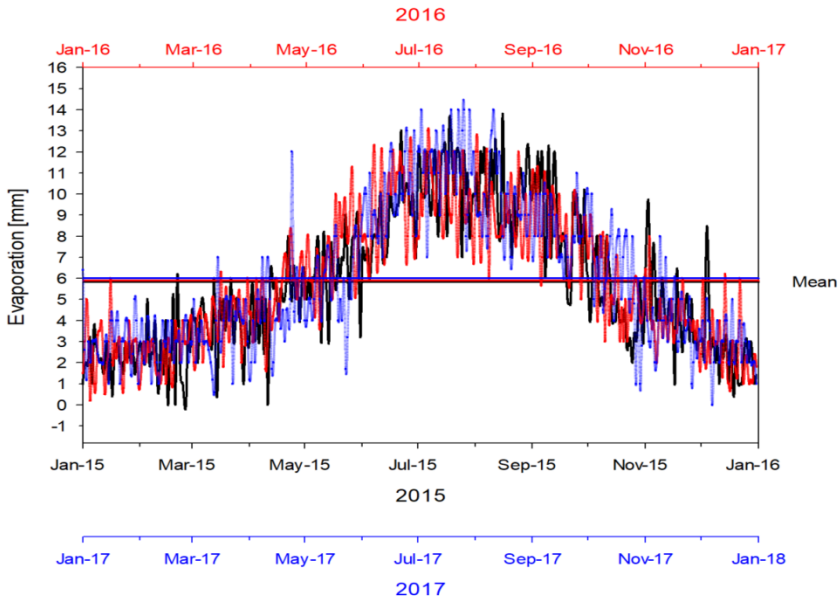

Figure 0.50: Total annual evaporation data between January 2015 and January 2018.

Table 0.9: Monthly comparison of total annual evaporation between January 2015 to June 2018.

EVAPORATION [mm]	2015	2016	2017	2018
January	67.10	78.10	90.50	90.30
February	67.80	73.20	82.60	63.80
March	116.80	123.90	110.60	120.60
April	146.50	158.90	137.90	167.70
May	197.30	227.40	175.50	250.20
June	258.90	282.10	295.00	277.50
July	328.50	308.40	358.00	
August	316.60	281.50	298.00	
September	264.20	257.00	248.00	
October	145.80	169.60	194.60	
November	139.00	121.10	116.90	
December	79.40	79.60	89.30	
TOTAL EVAPORATION [mm]	2127.90	2160.80	2196.90	970.10

Table 0.10: Total evaporation in oceanographic spring and summer seasons between 2015 and 2018.

EVAPORATION [mm]	2015	2016	2017	2018
April	146.50	158.90	137.90	167.70
May	197.30	227.40	175.50	250.20
June	258.90	282.10	295.00	277.50
July	328.50	308.40	358.00	
August	316.60	281.50	298.00	
September	264.20	257.00	248.00	
TOTAL EVAPORATION [mm]	1512.00	1515.30	1512.40	695.40

Finally, we shall conclude that the most significant outcomes of this study are;

i. The study area is possibly a formation site of LIW.

ii. Salinity shifts and changes of physical oceanographic characteristics observed on upper thermocline shall be explained neither by evaporation nor instrumental error (CTD). Therefore, it requires further investigation in order to explain the observed phenomena.

iii. Oceanographic time-series studies and high-frequency sub-mesoscale oceanographic researches are crucial to determine physical oceanographic features of the region. Also, to investigate temporal and spatial effects of these physical oceanographic features and changes of unstable, stable and quasi-stable physical oceanographic characteristics observed in the area.

5. Acknowledgements

This study was supported by the Scientific and Technological Research Council of Turkey (TUBITAK) grants: CAYDAG - 114Y139 “Determination of the influence of anthropogenic and natural processes on the Cilician Basin (between the Turkish Republic of Northern Cyprus and Turkey) Marine Ecosystem. The scientific cruises were supported both financially and in-kind by the University of Kyrenia, Near East University, and Middle East Technical University, Institute of Marine Sciences.

I would like to express my special appreciation and gratitude to my advisor, Prof. Dr. İlkay Salihoğlu, for his support, patience, guidance and immense knowledge. I am grateful to have the opportunity to study and work with him. He is the one who inspired and encouraged me to learn and study

about oceanography. It was not possible to deepen my knowledge and interest without him. He is a great mentor that each student and each scientist would like to have. He has been a great mentor to me not only in science but in every manner. Thanks for everything Hocam.

I would to thank Prof. Dr. Mohammed Abdul Latif for his help, support and kindness. His help is not limited to the interpretation of the physical oceanographic data, but he taught and inspired me a lot about physical oceanography. I will always remember not only the scientific contributions he made, but also his kindness, patience, guidance and knowledge.

I need to mention special thanks and appreciations to Assist. Prof. Dr Devrim Tezcan, Dr Hasan Örek and Dr Yeşim Ak Örek. They were there whenever I need them. They helped, supported and trusted me in every manner from the beginning. I learned how to conduct oceanographic cruises and oceanographic fieldwork. I learned a lot from them. They have been advisors, and they have been friends. Thanks for everything.

Many thanks to Myroshnychenko Volodymyr for his help with data processing.

I am also grateful to the crew of R/V Teal Jr, Zekeriya Dogan, Akin Hurdeniz, Lutfu Sirac and Ercan Bayar for their help and contribution.

Last but not least, I want to thank my beloved one, Selin. She is my motivation; she is my everything.

And of course, great thanks to my family, by all means.

References

Akpinar, A., Yilmaz, E., Fach, B. A., & Salihoglu, B. (2016). Physical oceanography of the Eastern Mediterranean Sea. In *The Turkish Part of the Mediterranean Sea* (Vol. 43, p. 250).

Alhammoud, B., Béranger, K., Mortier, L., Crépon, M., & Dekeyser, I. (2005). Surface circulation of the Levantine Basin: Comparison of model results with observations. *Progress in Oceanography, 66*(2–4), 299–320. https://doi.org/10.1016/j.pocean. 2004.07.015

Bergamasco, A., & Malanotte-Rizzoli, P. (2010). The circulation of the Mediterranean Sea: a historical review of experimental investigations. *Advances in Oceanography and Limnology*, *1*(1), 11–28. https://doi.org/10.1080/19475721.2010.491656

Cardin, V., Civitarese, G., Hainbucher, D., Bensi, M., & Rubino, A. (2015). Thermohaline properties in the Eastern Mediterranean in the last three decades: Is the basin returning to the pre-EMT situation? *Ocean Science*, *11*(1), 53–66. https://doi.org/10.5194/os-11-53-2015

El-Geziry, T. M., & Bryden, I. G. (2010). The circulation pattern in the Mediterranean Sea: issues for modeller consideration. *Journal of Operational Oceanography*, *3*(2), 39–46. https://doi.org/10.1080/1755876X.2010.11020116

Fofonoff, N. P. (1985). Physical properties of seawater: A new salinity scale and equation of state for seawater. *Journal of Geophysical Research*, *90*(C2), 3332. https://doi.org/10.1029/jc090ic02p03332

Hainbucher, D., Cardin, V., Siena, G., Hübner, U., Moritz, M., Drübbisch, U., & Basan, F. (2015). Hydrography in the Mediterranean Sea during a cruise with RV Poseidon in April 2014. *Earth System Science Data*, *7*(2), 231–237. https://doi.org/10.5194/essd-7-231-2015

Hecht, A., Pinardi, N., & Robinson, A. R. (1988). Currents, Water Masses, Eddies and Jets in the Mediterranean Levantine Basin. *Journal of Physical Oceanography*.

Kucuksezgin, F., & Pazi, I. (2006). Circulation, hydrographic and nutrient characteristics of the Cilician Basin, Northeastern Mediterranean Sea. *Journal of Marine Systems*, *59*(3–4), 189–200. https://doi.org/10.1016/j.jmarsys.2005.10.003

Lascaratos, A, Williams, R. G., & Tragou, E. (1993). A mixed-layer study of the formation of Levantine Intermediate Water. *Journal of Geophysical Research*, *98*(C8), 14739–14749. https://doi.org/10.1029/93JC00912

Lascaratos, Alex, Roether, W., Nittis, K., & Klein, B. (1999). Recent changes in deep water formation and spreading in the Eastern Mediterranean Sea: A review. *Progress in Oceanography*, *44*(1–3), 5–36. https://doi.org/10.1016/S0079-6611(99)00019-1

Malanotte-Rizzoli,P., & Hecht, A. (1988). Large-scale properties of the eastern Mediterranean: a review. *Oceanologica Acta*, *11*(4), 323–335. https://doi.org/10.1016 /S0967-0645(99)00020-X

Malanotte-Rizzoli, P., & Robinson, A. R. (1988). POEM: Physical Oceanography Eastern Mediterranean. *Eos*, *69*(14), 194–196, 203.

Marullo, S., Santoleri, R., Malanotte-Rizzoli, P., & Bergamasco, A. (1999). The sea surface temperature field in the Eastern Mediterranean from advanced very high resolution radiometer (AVHRR) data: Part I. Seasonal variability. *Journal of Marine Systems*, *20*(1–4), 63–81. https://doi.org/10.1016/S0924-7963(98)00071-2

Millero, F. (2011). History of the Equation of State of Seawater. *Oceanography*, *23*(3), 18–33. https://doi.org/10.5670/oceanog.2010.21

Onken, R., & Yuce, H. (2000). Winter circulation and convection in the Antalya Basin (Eastern Mediterranean). *Journal of Physical Oceanography*, *30*(5), 1099–1110. https://doi.org/10.1175/1520-0485(2000)030<1099:WCACIT>2.0.CO;2

Özsoy, E., Hecht, A., & Ünlüata, Ü. (1989). Circulation and hydrography of the Levantine Basin. Results of POEM coordinated experiments 1985-1986. *Progress in Oceanography*, *22*(2), 125–170. https://doi.org/10.1016/0079-6611(89)90004-9

Özsoy, E., Hecht, A., Ünlüata, Ü., Brenner, S., Oğuz, T., Bishop, J., … Rozentraub, Z. (1991). A review of the Levantine Basin circulation and its variability during 1985-1988. *Dynamics of Atmospheres and Oceans*, *15*(3–5), 421–456. https://doi.org/10.1016/0377-0265(91)90027-D

Özsoy, E., Hecht, A., Ünlüata, Ü., Brenner, S., Sur, H. I., Bishop, J., … Oğuz, T. (1993). A synthesis of the Levantine Basin circulation and hydrography, 1985-1990. *Deep-Sea Research Part II*, *40*(6), 1075–1119. https://doi.org/10.1016/0967-0645(93)90063-S

Pinardi, N., Zavatarelli, M., Adani, M., Coppini, G., Fratianni, C., Oddo, P., … Bonaduce, A. (2015). Mediterranean Sea large-scale low-frequency ocean variability and water mass formation rates from 1987 to 2007: A retrospective analysis. *Progress in Oceanography*, *132*, 318–332. https://doi.org/10.1016/j.pocean.2013.11.003

Robinson, A. R., & Golnaraghi, M. (1993). The physical and dynamical oceanography of the Mediterranean Sea. In *Proceedings of the 4th National Symposium on Oceanography and Fisheries, Rhodes Island* (pp. 9–13).

Robinson, A. R., Golnaraghi, M., Leslie, W. G., Artegiani, A., Hecht, A., Lazzoni, E., … Ünlüata, Ü. (1991). The Eastern Mediterranean general circulation: features, structure and variability. *Dynamics of Atmospheres and Oceans*, *15*(3–5), 215–240. https://doi.org/10.1016/0377-0265(91)90021-7

Robinson, A. R., Leslie, W. G., Theocharis, A., & Lascaratos, A. (2001). Mediterranean Sea Circulation. *RWOS*, 1–19. https://doi.org/10.1016/rwos.2001.0376

Salihoğlu, I., Saydam, C., Baştürk, Ö., Yilmaz, K., Göçmen, D., Hatipoğlu, E., & Yilmaz, A. (1990). Transport and distribution of nutrients and chlorophyll-a by mesoscale eddies in the northeastern Mediterranean. *Marine Chemistry*, *29*(C), 375–390. https://doi.org/10.1016/0304-4203(90)90024-7

Salihoglu, I., Tugrul, S., Gucu, A. C., Salihoglu, B., Kocak, M., Tezcan, D., … Temel, O. (2019). Determination of influence of anthropogenic and natural processes on the Cilician Basin (Between Turkish Republic of Northern Cyprus and Turkey) marine ecosystem. Girne, Mersin.

Tanhua, T., Hainbucher, D., Schroeder, K., Cardin, V., Álvarez, M., & Civitarese, G. (2013). The Mediterranean Sea system: A review and an introduction to the special issue. *Ocean Science*, *9*(5), 789–803. https://doi.org/10.5194/os-9-789-2013

The LIWEX Group (2003). The Levantine Intermediate Water Experiment (LIWEX) Group: Levantine basin—A laboratory for multiple water mass formation processes. *Journal of Geophysical Research*, *108*(C9), 8101. https://doi.org/10.1029/2002JC001643

The POEM Group (1992). General circulation of the Eastern Mediterranean. *Earth-Science Reviews*, *32*(4), 285–309. https://doi.org/http://dx.doi.org/10.1016/0012-8252(92)90002-B

Velaoras, D., Krokos, G., Nittis, K., & Theocharis, A. (2014). Dense intermediate water outflow from the Cretan Sea: A salinity driven, recurrent phenomenon, connected to thermohaline circulation changes. *Journal of Geophysical Research, Oceans*, *119*, 4797–4820. https://doi.org/10.1002/2014JC009937

Wüst, G. (1961). On the vertical circulation of the Mediterranean Sea. *Journal of Geophysical Research*, *66*(10), 3261–3271. https://doi.org/10.1029/JZ066i010p03261

CHAPTER

4

RESEARCH IN NATURAL AND ENGINEERING SCIENCES

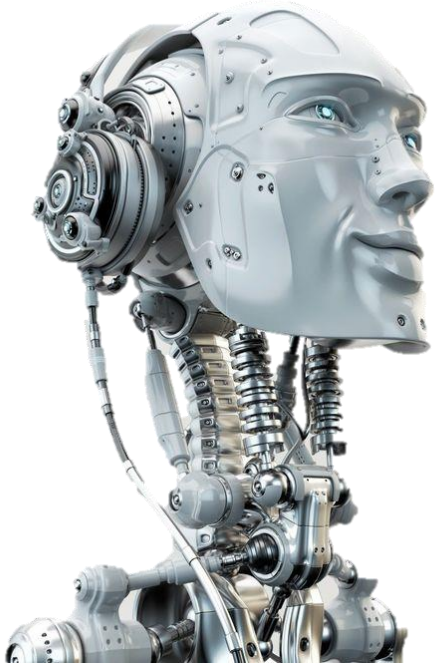

Deep Learning in Breast Cancer Diagnosis (Çetin Gençer, Ramazan Alioğlu, Mustafa Yıldırım)

Deep Learning in Breast Cancer Diagnosis

Çetin GENÇER[1], Ramazan ALİOĞLU[2], Mustafa YILDIRIM[3]

[1]Fırat University, E-mail: cgencer@firat.edu.tr
[2]Fırat Üniversity, E-mail: ramazanalioglu@hotmail.com
[3]Fethi Sekin City Hospital, E-mail: mustafa23468@outlook.com

1. Introduction

Breast cancer is the widespread cancer for female. With respect to the National Cancer Institute estimates that one out of eight women in the United States will indicate breast cancer at some period during her lifetime [1].

In primarily stages, the invention and diagnosis of breast cancer, the patient has changes for complete recovery after sucessfully treatment. Several radiological techniques have been used for early finding of breast cancer[2]. Screening mammography is currently the ideal radiological technique and it is vital to classify breast cancer images quickly and accurately with the help of computer-aided systems[3].

The most widespread semptoms which may point out breast cancer are clumps and calcifications. In some state, fine signs such as architectonic deformity and bilateral asymmetry that can also guiding a breast cancer diagnosis. Breast abnormalities are characterized with large area of features and may be easily miss fired or misunderstand by radiologists while reading large amount of mammographic images assuming in screening programs. The structure of the breast tissue, work density, experience, etc. are the reasons for incorrect assesment of mamograms [4]. By examining mammography images, the stage of cancer disease and the type of tumor can be determined. However, many mistakes are still made in diagnoses made with mammography images. In patients who have been diagnosed with breast cancer by looking at mammographies by specialist physicians, most of these diagnoses have been determined by the biopsy carried out [5]. After all, a computer-aided detection (CADe) and computer-aided diagnosis (CADx) algorithms are being sophisticated to assistance radiologists provide an adefinite diagnosis. CADe and CADx algorithms help to radiologist with respect to decreasing the number of incorrect positives [4].

There are several shape of abnormality that may effect breast tissue. These abnormalities are often classified into three families: the opacities, microcalcifications and architectural distortions[6].

Bulks are occupying lesions, seen on different shapes. They are characterized by their shape (lobulated, irregular, oval, round), their form (microlobulated, circumscribed, blank out, spiculated, unclear) and intensity (low fat, middle, hight) [2]. When a potential mass is seen in a single view it is named “density” until its natura is confirmed. Mass usually appear as areas brighter than the surrounding tissue due to increased attenuation of X-rays if they possess higher density. But they can also result in a equal density or less density regionsregions on the mamogram [7].

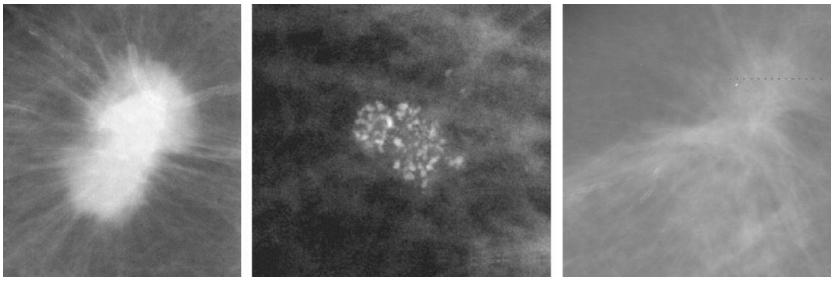

Figure 51: Examples of a spiculated pile (left), cluster of microcalcifications (center), and architectural distortion (right). The images were obtained from Digital Database for Screening Mammography (DDSM) [8].

There are many studies in the literature that use computer-aided diagnosis (CBT) methods to evaluate mammography images. Deep learning was successful in visual object recognition and detection, so deep learning was also popular in mammography image processing[9].

In this study, the mammography image was firstly processed using the morphological method. Tissues that are likely to be malignant/benign and calcifications have been identified. In the next step, these suspicious regions were diagnosed about mammography image using deep learning. The region determined by the system is marked and local image enhancement is performed. The final decision will be made by the radiologist. With this system, which can be considered as a second eye for the radiologist, it was aimed to reduce false negative / positive ratios.

2. Research and Findings

In this study, digital mammography images belonging to MIAS (Mammographic Image Analysis Society) Database and DDSM (Digital Database for Screening Mammography) were used. Each MIAS mammogram is 1024x1024 pixels in size; There are a total of 322

mammography images from MIAS database and 378 images from DDSM (DDSM contains nearly 2,500 works, each work covers two images of each breast).

2.1. Region of interest (rois) detection and morphological image processing

Suspicious areas on the digital mammogram were roughly detected using the morphological method first. In mammogram, the cyst / mass sections appear brighter and lighter than the normal structure of the breast[10]. Different sized region (ROIs) that appear brighter than their surroundings, have been detect by comparison with their surroundings by morfolojical method (Fig. 2).

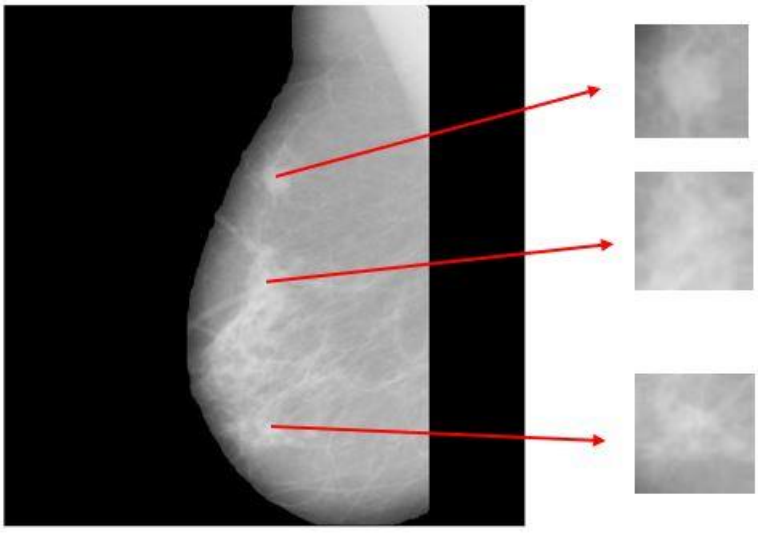

Figure 52: Examples of suspicious regions

With the morphological image processing method, 3 suspicious areas (ROIs) were identified in the picture (Figure 2). In the next stage, these 3 suspicious areas were processed with trained artificial neural network and finally evaluated by the system. In some pictures, even one suspect region was not found, while in some pictures 5, 10 or even more suspect regions were found.

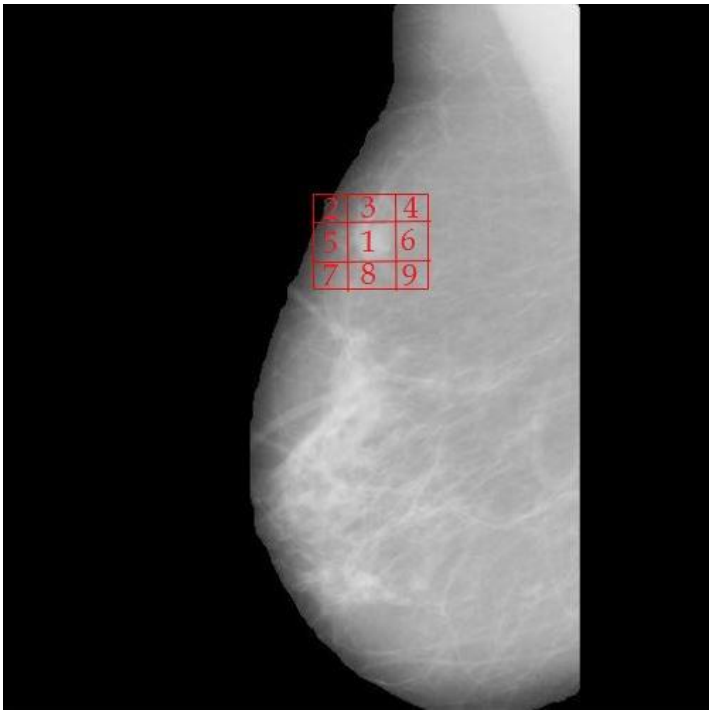

Figure 53: Floating windows

9 windows of different sizes were slid together on the picture, the center window (3) was compared to the other windows (Figure 2). The dimensions of the windows were determined by measuring the dimensions of the cystic tissues in the pictures used in this study. Thus, possible lesions brighter than their surroundings were detected. This procedure was repeated with windows of different sizes, since the lesions may have different sizes.

2.2. Diognosis with deep neural network

Deep Learning-based Classifier (DLC) can manage raw image directly which means, there should be no need for pre-processing, segmentation and feature seperation. However,most deep learning approaches require alter the size of image due to the limit on input values. While some techniques do need intensity normalization and contrast enhancement which may be avoided if data augmentation techniques discussed later are employed during training. Resultantly, DLC has higher classification accuracy as it can avoid errors associated with incorrect feature vector or indefinite segmentation [11,12].

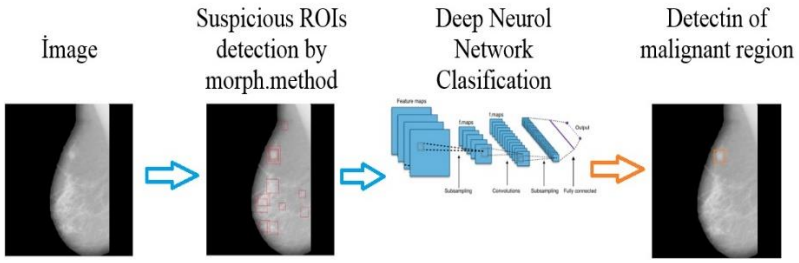

Figure 54: Image- Morfological Method- DeepNeurolNetworkC- Detection of malignant

Neurol network was trained using pictures of different sizes showing cystic areas and other suspicious areas. 2560 pictures (ROIs) were used for this training. We used a AlexNet like structure which has 8 layers in our study. While Alexnet network can classify images into 1000 object categories, our proposed network can classify images into 3 catagories.

3. Results

With the proposed method, ROIs were correctly detected in 138 of 150 images and 92% success was achieved. If more pictures are used for training in later studies, the success rate can be increased.

References

[1] Shahare, N., Yadav, M., Early Stage Detectıon Of Mıcrocalcıfıcatıons In Mammograms: A Survey., International Journal of Industrial Electronics and ElectricalEngineering, ISSN: 2347-6982 Volume-4, Issue-11, Nov 2016

[2] Hela, B., Hela, M., Kamel, H., Sana, B., & Najla, M. *Breast cancer detection: A review on mammograms analysis techniques.* In Systems, Signals & Devices (SSD), 2013 10th International Multi-Conference on (pp. 1-6). IEEE.

[3] Suri, Jasjit S., and Rangaraj M. Rangayyan. *Recent Advances in Breast Imaging, Mammography, and Computer-Aided Diagnosis of Breast Cancer*. Bellingham, Wash: SPIE Press, 2006.

[4] Bozek J., Mustra M., Delac K., Grgic M. *A Survey of Image Processing Algorithms in Digital Mammography*. In: Grgic M., Delac K., Ghanbari M. (eds) Recent Advances in Multimedia Signal Processing and Communications. Studies in Computational Intelligence,. vol 231. Springer, Berlin, Heidelberg, 2009.

[5] American Cancer Society Guidelines for The Early Detection of Cancer, 2001.

[6] Le Bouedec G, Feillel V, Dauplat J. *Chirurgie des lésions mammaires infracliniques [Surgery for subclinical breast lesions]*. J Chir (Paris). 1998.Dec;135(6):267-72. French. PMID: 10228915.

[7] Casti, P., Mencattini, A., Salmeri, M., Rangayyan, R., *Computerized Analysis of mamographic İmages for Detection and Characterization of Breast Canser*. Synthesis Lectures on Biomedical Engineering, 2017.

[8] kitap...Sampat, M.P., Markey, M.K., Bovik, A.C. *Computer-aided detection and diagnosis in mammography*. In: Bovik, A.C. (Ed.), The Handbook of Image and Video Processing, second ed. Elsevier, New York, 2005. pp. 1195–1217.

[9] Shen, L., Margolies, L.R., Rothstein, J.H. *et al. Deep Learning to Improve Breast Cancer Detection on Screening Mammography*. *Sci Rep* 9, 2020. 12495. https://doi.org/10.1038/s41598-019-48995-4

[10] Pak F, Kanan HR, Alikhassi A. *Breast cancer detection and classification in digital mammography based on Non-Subsampled Contourlet Transform (NSCT) and Super Resolution.* Comput Methods Programs Biomed 2015. 122:89–107. doi:10.1016/j.cmpb.2015.06.009.

[11] Rizwan I., Neubert J. Deep learning approaches to biomedical image segmentation. Informatics in Medicine Unlocked 2020. Volume 18, 100297

[12] Suzuki K. Overview of deep learning in medical imaging. Radiol. Phys. Technol, 2017. 10(3):257–73

CHAPTER

5

RESEARCH IN NATURAL AND ENGINEERING SCIENCES

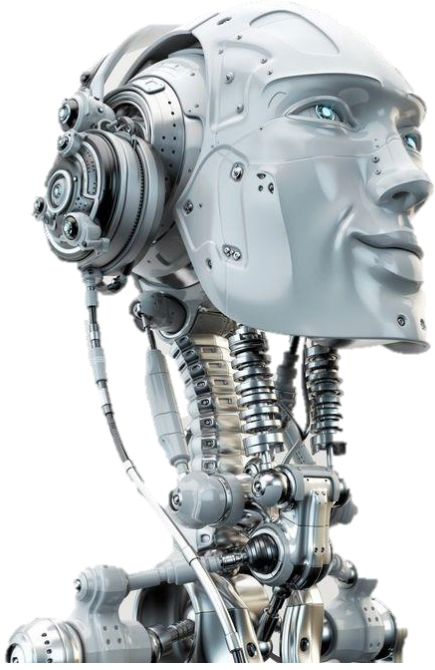

Basınç Dayanımının Yerinde Tayininde Kullanılan Yönetmelikler Üzerine Bir Saha Çalışması (Mustafa Koçer)

Basınç Dayanımının Yerinde Tayininde Kullanılan Yönetmelikler Üzerine Bir Saha Çalışması

Mustafa KOÇER[1]
[1]*Konya Teknik Üniversitesi, E-mail: mkocer@ktun.edu.tr*

1. Giriş

Mevcut betonarme binaların deprem performansına etki eden en kritik parametrelerden biri beton dayanımıdır[1]. Beton dayanımının belirlenmesi tahribatlı ve tahribatsız olmak üzere iki yöntemle gerçekleştirilmektedir. Tahribatsız yöntemler (ultrases geçiş hızı ile ölçüm, çekiç okuma vb.) ile mevcut yapının beton kalitesi değerlendirilmesinde, sonuçlar çok kaba kaldığı için sadece fikir elde edinilmektedir. Ayrıca TS EN 13791 madde 8.2'de belirtildiği üzere tahribatsız yöntemlerle elde edilen deney sonuçları ile beton dayanımı arasında bağıntının, karot deneyleri yoluyla tehsis edilmesi gerektiğini vurgulamaktadır[2]. Bu yüzden, daha gerçekçi sonuçların elde edilmesi için mevcut yapıların beton dayanımları karot alma yöntemi ile TS EN 13791 ve TS EN 12504-1 standartları ile gerçekleştirilmektedir[2, 3]. TS EN 13791'de beton yapılar ve öndökümlü beton bileşenlerde, basınç dayanımının yerinde (yapıda) tayini için uygulanacak teknikler verilmektedir[2]. Mevcut yapının karakteristik beton dayanımı iki farklı yaklaşım ile belirmektedir. Bu yönetmeliğe göre mevcut yapıdan 15 adetten fazla karot alınması durumunda A yaklaşımı ile 3-14 arasında karot alınması durumunda ise B yaklaşımına göre beton basınç dayanımı tayin edilmektedir.

Ülkemizde 2018 yılında yürürlüğe giren Türkiye Bina Deprem Yönetmeliği 2018 (TBDY 2018) [4] Bölüm 15'de yer alan mevcut binaların deprem etkisi altında değerlendirilmesi kısmında, betonarme mevcut beton dayanımı TS EN 12504'e göre uygun olarak alınan karot örneği üzerinden belirlenmektedir. Burada, mevcut yapının beton dayanımı binadan alınan karot sayısına göre istatiksel veya istatistiki olarak değerlendirme yapılmaksızın iki yöntemle belirlenmektedir.

Bu çalışmada ise mevcut binalardan alınan beton karot örnekleri üzerinde yapılan beton basınç deney sonuçlarının TS EN 13791 standardında yer alan yaklaşımlar ile TBDY 2018 yönetmeliğinde, mevcut bir binanın deprem performansının değerlendirilmesi sırasında malzeme özelliğinin tayin edilmesinde kullanılan istatistiki yöntemlerle karşılaştırılmıştır. Örneklerde yer alan mevcut binaların, her iki standarda göre mevcut beton kalitesi belirlenerek tutarsızlıklar irdelenmiştir.

2. Yapılardaki Karakteristik Basınç Dayanımının Belirlenmesi

Yapılardan alınan karot numuneler beton basınç presi ile beton dayanım testine maruz bırakılırlar. Burada numunenin taşıdığı yük, numunenin en kesit alanına bölünerek her bir numunenin beton basınç mukavemeti belirlenir. Elde edilen sonuçlar, yönetmeliklerde yer alan yaklaşımlara göre değerlendirilerek betonun karakteristik basınç dayanımı belirlenmektedir. Betonun karakteristik basınç dayanımı TS EN 13791 ve TBDY 2018'e göre aşağıdaki gibi değerlendirilmektedir.

2.1.TS EN 13791'e göre Karakteristik Basınç Dayanımı

TS EN 13791'de **modifiye edilecek, yeniden tasarımlanacak veya hasar görmüş "eski" yapının değerlendirilmesinde**, beton numunelerin karakteristik basınç dayanımları A ve B yaklaşımı olmak üzere iki farklı yaklaşımla değerlendirilmektedir. Mevcut yapıdan alınan karot numunelerinin sayısı 15'den fazla ise A yaklaşımına göre, 3-14 arasında ise B yaklaşımına göre değerlendirilmektedir.

2.1.1. A Yaklaşımı

Deney bölgesinin karakteristik basınç dayanımı aşağıda verilen Denklem 1 ve Denklem 2'den **küçük** olanıdır:

$$f_{ck,is} = f_{m(n),is} - k_2 \times s \quad (1)$$

$$f_{ck,is} = f_{is,en\ düşük} + 4 \quad (2)$$

Burada, $f_{ck,is}$ yapıdaki karakteristik basınç dayanımı, $f_{m(n),is}$ n adet yerinde basınç dayanımının ortalaması, $f_{is,en\ düşük}$ yapıdaki basınç dayanımlarından en düşüğü, s deney sonuçlarının standart sapması veya 2.0 N/mm^2 büyük olanı, k_2 hüküm belirten milli dokümanlarda verilen değer alınır veya böyle bir değer verilmemişse 1,48 olarak alınır.

2.1.2. B Yaklaşımı

Deney bölgesinin karakteristik basınç dayanımı aşağıda verilen Denklem 3 ve Denklem 4'den **küçük** olanıdır:

$$f_{ck,is} = f_{m(n),is} - k \quad (1)$$

$$f_{ck,is} = f_{is,en\ düşük} + 4 \quad (2)$$

Burada, $f_{ck,is}$ yapıdaki karakteristik basınç dayanımı, $f_{m(n),is}$ n adet yerinde basınç dayanımının ortalaması, $f_{is,\ en\ düşük}$ yapıdaki basınç dayanımlarından en düşüğü, k deney sonucu adedi n'ye bağlı olarak Tablo 1'den seçilen değerdir.

Tablo 11: Numune sayısına bağlı k değerleri[2]

n	k
10-14	5
7-9	6
3-6	7

B yaklaşımında standart, yapıdan alınan karot sayısının az olmasından kaynaklanan belirsizlik ve güvenilirlik seviyesinin sağlanması sebebiyle, yapıdan alınan karot numune sayısı azaldıkça k değerini artırarak bir tür emniyetli tarafta kalma eğilimine gitmiştir.

2.2. TBDY 2018'e göre Karakteristik Basınç Dayanımı

TBDY 2018 yönetmeliğinde, mevcut yapıların beton kalitesi, TS EN 12504-1 belirtilen koşullara uygun şekilde alınan en az 3 karot numunesi üzerinde basınç dayanım testleri yapılmasını öngörmektedir. Binalardan alınan karot numunelerin boy ve çapları eşit ve 100 mm ise herhangi bir kayşayı uygulamaksızın basınç dayanım sonuçları mevcut beton dayanımı olarak kullanılmaktadır. Binadan alınan karot sayısı 3 adet ise herhangi bir istatistiki değerlendirme yapılmaksızın, örneklerden elde edilen en küçük basınç dayanımı *mevcut beton dayanımı* olarak alınacaktır (Denklem 3).

$$f_{ck} = f_{ck,min} \tag{3}$$

Binalardan alınan karot numune sayısı 3'den fazla ise Denklem 4 ve Denklem 5'de elde edilen sonuçlardan **büyük** olanı, *mevcut beton dayanımı* olarak değerlendirilecektir.

$$f_{ck} = f_{ck,ort} - S_s \tag{4}$$

$$f_{ck} = 0.85 \times f_{ck,ort} \tag{5}$$

Bir grup karot numunesine yapılan basınç deneyi sonunda, grup ortalamasının %75 daha küçük beton dayanım değerleri, istatistiki sapan değer olarak değerlendirilecek ve mevcut beton dayanım tayininde kullanılmayacaktır.

3. Yöntem ve Değerlendirme

Konya ili sınırlarında yer alan, yaşları 0 ile 3 yıl arasında değişen 3 adet binadan alınan toplam 33 adet karot numunesi üzerinde beton dayanım testi yapılmıştır. Mevcut binalardan alınan karot numunelerin sayıları, yönetmeliklerde yer alan değerlendirme yaklaşımları arasında farkındalık göstermesi açısından değişkenlik göstermektedir. Böylece her bir yaklaşıma karşılık gelen değerlendirme yöntemleri arasında karşılaştırmalar yapılmıştır.

Toplam 24 adet karot numunesi alınan birinci bina, 3 yaşında olup, Bodrum+Zemin+5 kattan oluşmaktadır. 6 adet karot numunesi alınan ikinci bina, 1 yıllıktır ve 2 katlıdır. 3. bina, henüz inşa aşamasında olup, 28 günlük yaş beton numune dayanımlarının projede öngörülen değerden az olması sebebiyle zemin kattan alınan karot numune örnekleridir. Şekil 1'de binaların dıştan görünüşü, Şekil 2'de, binalardan numunelerinin alınışı ve alındıktan sonra karot deliklerinin yüksek mukavemet harçları ile dolduruluşu gösterilmiştir.

Şekil 1. Betonarme binaların dıştan görünüşü

Şekil 2. Karot örneklerinin alınışı ve deliklerin harçla doldurulması

Tablo 1'de ilk binadan alınan 24 adet karot numunesinin beton dayanım sonuçları gösterilmiştir.

Tablo 1. Birinci binaya ait karot dayanım sonuçları

			TS EN 13657			TBDY 2018-Bölüm 15		
Karot No	Karot Adı	Basınç Dayanımı N/mm²	Ort. Dayanım N/mm²	Standart Sapma N/mm²	$f_{ck}>0.85*f_{ort}$		Ort. Dayanım N/mm²	Standart Sapma N/mm²
1	1B1	50.69			Kabul	50.69		
2	1B2	44.18			Kabul	44.18		
3	1B3	37.60			Kabul	37.6		
4	1Z1	45.74			Kabul	45.74		
5	1Z2	53.20			Kabul	53.2		
6	1Z3	47.84			Kabul	47.84		
7	111	43.61			Kabul	43.61		
8	112	46.57			Kabul	46.57		
9	113	50.73			Kabul	50.73		
10	121	35.07			Red	-		
11	122	42.51			Kabul	42.51		
12	123	50.47	**42.75**	**7.25**	Kabul	50.47	44.86	5.87
13	131	50.11			Kabul	50.11		
14	132	41.04			Kabul	41.04		
15	133	37.18			Kabul	37.18		
16	141	29.04			Red	-		
17	142	37.60			Kabul	37.6		
18	143	37.92			Kabul	37.92		
19	151	42.81			Kabul	42.81		
20	152	33.94			Red	-		
21	153	30.88			Red	-		
22	161	40.92			Kabul	40.92		
23	162	57.39			Kabul	57.39		
24	163	38.99			Kabul	38.99		
TS EN 13657		$f_{ck,is} = f_{m(n),is} - k_2 \times s$			=32.02		**32.02**	
		$f_{ck,is} = f_{is,en\ düşük} + 4$			=33.04			
TBDY 2018		$f_{ck} = f_{ck,ort} - S_s$			=38.98		**38.98**	
		$f_{ck} = 0.85 \times f_{ck,ort}$			=38.13			

Tablo 1 incelendiğinde, binadan toplam 24 adet karot alındığı için TS EN 13657 standardına göre A yaklaşımı, TBDY 2018 yönetmeliğine göre istatistiki bir değerlendirme yapılmıştır. TS EN 13657 standardına göre beton dayanım sonuçları 32.02 MPa ve 33.04 MPa elde edilmiştir ve bu değerlerden küçük olan 32.02 MPa mevcut beton dayanımı olarak kabul edilmiştir. Aynı binanın TBDY 2018 yönetmeliğine göre değerlendirilmesi sonucu beton dayanım sonuçları 38.98 MPa ve 38.13 MPa olarak belirlenmiştir ve bu değerlerden büyük olan 38.98 MPa mevcut beton dayanımı olarak kabul edilmektedir. Her iki standartta verilen iki formülün değerlendirme sonuçları, birbirine oldukça yakındır, fakat iki yönetmelik arasında bir karşılaştırma yapıldığında TS EN 13657 daha tutucu tarafta kalmaktadır. Tablo 2'de ikinci binadan alınan 6 adet karot numunesinin karot dayanım sonuçları gösterilmiştir.

Tablo 2. İkinci binaya ait karot dayanım sonuçları

			TS EN 13657		TBDY 2018-Bölüm 15			
Karot No	**Karot Adı**	**Basınç Dayanımı N/mm²**	**Ort. Basınç Dayanımı N/mm²**	**Standart Sapma N/mm²**	**$f_{ck}>0.85*f_{ort}$**		**Ort. Basınç Dayanımı N/mm²**	**Standart Sapma N/mm²**
1	1B1	36.92	39.89	3.39	Kabul	36.92	39.89	3.39
2	1B2	42.49			Kabul	42.49		
3	1B3	42.39			Kabul	42.39		
4	1Z1	43.63			Kabul	43.63		
5	1Z2	38.43			Kabul	38.43		
6	1Z3	35.47			Kabul	35.47		
TS EN 13657		$f_{ck,is} = f_{m(n),is} - k$			=32.89		**32.89**	
		$f_{ck,is} = f_{is,en\ düşük} + 4$			=39.47			
TBDY 2018		$f_{ck} = f_{ck,ort} - S_s$			=36.50		**36.50**	
		$f_{ck} = 0.85 \times f_{ck,ort}$			=33.91			

Tablo 2 incelendiğinde, binadan toplam 6 adet karot alındığı için TS EN 13657 standardına göre B yaklaşımı, TBDY 2018 yönetmeliğine göre istatistiki bir değerlendirme yapılmıştır. TS EN 13657 standardına göre beton dayanım sonuçları 32.89 MPa ve 39.47 MPa elde edilmiştir ve bu değerlerden küçük olan 32.89 MPa mevcut beton dayanımı olarak kabul edilmiştir. Aynı binanın TBDY 2018 yönetmeliğine göre değerlendirilmesi sonucu, beton dayanım sonuçları 36.50 MPa ve 33.91 MPa olarak belirlenmiştir ve bu değerlerden büyük olan 38.98 MPa mevcut beton dayanımı olarak kabul edilmektedir. Binalardan alınan karot numunesi sayısı azaldıkça yönetmeliklerde verilen formüller arasındaki fark arttığı görülmüştür. Ayrıca, TS EN 13657 standardında 15 numuneden az olan numunelerin B yaklaşımına göre değerlendirilmesi sırasında Tablo 1'den alınan k sayısının etkisi oldukça fazladır ve Tablo 1'e göre 3-6 arasında numune alınan binalarda ortalama karot basınç dayanımından 7 MPa düşülmektedir. Buda her iki formülle belirlenen dayanım sonuçları arasındaki

farkı artırmaktadır. Bu fark TS EN 13657 standardında %20 iken TBDY 2018 % 7 seviyelerindedir. Tablo 3'de üçüncü binadan alınan 3 adet karot numunesinin karot dayanım sonuçları gösterilmiştir.

Tablo 3. Üçüncü binaya ait karot dayanım sonuçları

			TS EN 13657		TBDY 2018-Bölüm 15			
Karot No	**Karot Adı**	**Basınç Dayanımı N/mm²**	**Ort. Basınç Dayanımı N/mm²**	**Standart Sapma N/mm²**	**$f_{ck}>0.85*f_{ort}$**		**Ort. Basınç Dayanımı N/mm²**	**Standart Sapma N/mm²**
1	1B1	47.81			Kabul	47.81		
2	1B2	40.24	43.84	3.80	Kabul	40.24	43.84	3.80
3	1B3	43.47			Kabul	43.47		
TS EN 13657		$f_{ck,is} = f_{m(n),is} - k$			=36.84		**36.84**	
		$f_{ck,is} = f_{is,en\ düşük} + 4$			=44.24			
TBDY 2018		$f_{ck} = f_{ck,min}$			=40.24		**40.24**	

Tablo 3 incelendiğinde, binadan toplam 3 adet karot alındığı için TS EN 13657 standardına göre B yaklaşımı, TBDY 2018 yönetmeliğine göre bir istatistiki değerlendirme yapılmaksızın, örneklerden elde edilen en küçük basınç dayanımı mevcut beton dayanımı olarak değerlendirilmiştir. TS EN 13657 standardına göre beton dayanım sonuçları 36.84 MPa ve 44.24 MPa elde edilmiştir ve bu değerlerden küçük olan 36.84 MPa mevcut beton dayanımı olarak kabul edilmiştir. Aynı binanın TBDY 2018 yönetmeliğine göre değerlendirilmesi sonucu, beton dayanım sonucu, karot basınç dayanımlarının en küçüğü olan 40.24 MPa mevcut beton dayanımı olarak kabul edilmektedir. TS EN 13657 standardında verilen formüller arasında ki yine %20 olarak elde edilmiştir.

4. Sonuçlar

3 adet mevcut betonarme binadan alınan karot örnekleri üzerinde TS EN 13657 ve TBDY 2018 verilen yaklaşımlar doğrultusunda, beton dayanım sonuçları değerlendirilmiştir. 3 farklı binadan farklı sayılarda alınan karot numunelerin TS EN 13657 standardına ve TBDY 2018 yönetmeliğine göre beton dayanım sonuçları sırasıyla, 32.02 MPa, 32.89 MPa, 36.84 MPa ve 39.98 MPa, 36.50 MPa ve 40.24 MPa olarak elde edilmiştir. Yapılan saha çalışmasında, mevcut binalardan elde edilen mevcut beton dayanım sonuçlarına göre TBDY 2018 yönetmeliği, TS EN 13657 standardına göre binalardan sırasıyla, %24.8, %10.9 ve % 9.2 daha elverişli sonuçlar verdiği görülmektedir. Bu sonuçlarda, her iki yönetmelikte belirlenen yaklaşımların biri küçük değeri, diğeri büyük değeri, mevcut beton dayanımı olarak kabul etmesi ve TS EN 13657 standardına göre 15 numuneden az olan B yaklaşımında Tablo 1'deki azaltma katsayısı ile bir nevi binaların cezalandırılmasından dolayı, TBDY 2018'den elde edilen sonuçlar daha

elverişlidir. Diğer taraftan karot sayısı fazla olan ilk bina örneğine baktığımızda, TS EN 13657 standardının A yaklaşımındaki formüllerden elde edilen dayanım sonuçları arasında ki fark, 24 adet karot numunesi olmasına rağmen, TBDY 2018 yönetmeliğine göre yine B yaklaşımında olduğu gibi oldukça fazladır. Deprem performansında beton kalitesinin önemi düşünüldüğünde, her iki yönetmelikten elde edilen sonuçların deprem performansında kullanılabileceği veya TS EN 13657 göre projesinde öngörülen taze beton dayanımı sağlayamayan bir binanın, TBDY 2018 yaklaşımları ile elde edilen dayanım sonuçları doğrultusunda deprem performansını sağlayabileceği çelişkisi de ayrıca düşünülmelidir.

Referanslar

[1] M. İnel, H.B. Özmen, B.T. Çaycı, H. Ün, Mevcut Betonarme Yapilarda Karot Numune Sayisi İle Beton Basinç Dayanimi İlişisinin Değerlendirilmesi, 2. Türkiye Deprem Mühendisliği ve Sismoloji Konferansı, Hatay, 2013.

[2] TS-EN13791, Basınç Dayanımının Yapılar ve Öndökümlü Beton Bileşenlerde Yerinde Tayini, Türk Standartları Enstitüsü, Ankara, 2019.

[3] TS-EN12504-1, Beton – Yapıda Beton Deneyleri, Karot Numuneler – Karot Alma, Muayene ve Basınç Dayanımının Tayini, Türk Standartları Enstitüsü, Ankara, 2019.

[4] TBDY, Türkiye Bina Deprem Yönetmeliği, , Afet ve Acil Durum Yönetim Başkanlığı, Ankara, 2018.

CHAPTER

6

RESEARCH IN NATURAL AND ENGINEERING SCIENCES

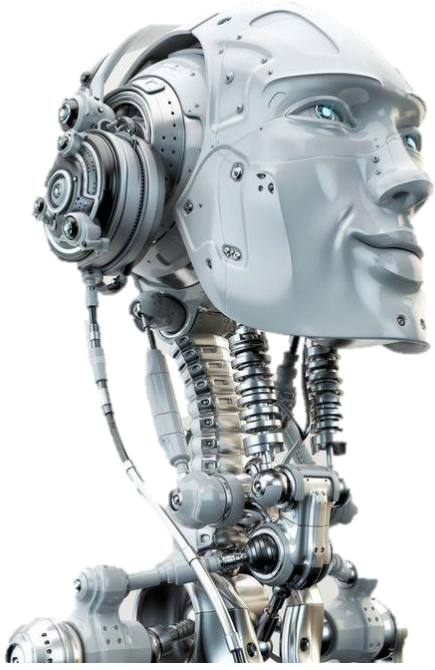

Effect of Ferula halophila Ekstracts on Aduld Emergence Ratio of Galleria mellonella L. (Lepidoptera: Pyralidae)

(Rahile Öztürk)

Effect of *Ferula halophila* Ekstracts on Aduld Emergence Ratio of *Galleria mellonella* L. (Lepidoptera: Pyralidae)

Rahile Öztürk[1]
[1]*Selçuk Üniversitesi Fen Fakültesi Biyoloji Bölümü, Konya. E-mail: rozturk@selcuk.edu.tr*

Abstract

Introduction:
Lepidoptera orders belonging to the *Galleria mellonella* L., damaging honeycomb in beekeeping, is an insect pest holometabol economically. Confidence larvae, pollen and great harm to the feeding combs, beehives. *G. mellonella*, and to have a short life cycle and high efficiency, and also to be recognized as an important insect species because it can grow well on a variety of biological and chemical control studies on artificial food. Tuz çakşırı known as *Ferula halophila* Peşmen; Apiaceae belonging to the family, many years, is an endemic plants spread around 60- 90 cm in length and Salt Lake. This species of this plant is a plant halophytes danger category VI (damage), respectively.

Methods:
In this study, grown in laboratory conditions *G. mellonella* 's applied to the larval extracts of *F. Halophila*, its effects on insect adult emergence rate were investigated. Larvae respectively four different concentrations (25, 50, 75 and 100 ppm) was fed to the plant extract, were researched maturation rate of the individual.

Results:
According to the obtained results, *F. halophila* with increasing concentrations of the extracts of the prolonged period of maturation, but the number of mature individuals occurring after the application has been determined that no significant changes compared to the control group.

Conclusion:
The development of insects, and the length of life and productivity features such as genetics, although the effect on the environment is very important. Last year in pesticides used in pest control, insect physiology and biochemistry on the mechanisms of action are being investigated. In this study, the aphrodisiac effect of some species of the genus known Ferula *F. halophila*' s to assess the effects of insect physiology *G. mellonella* was used as a live model.

Keywords: Adult emergence ratio, *Ferula halophila, Galleria mellonella*

1. Introduction

Wax is one of the most useful products of honey bees. It is used in the pharamaceutical industry, dentistry and cosmetics. Wax contains many nutrients, pollen and honey and is therefore attacked by various pests (Ebadi 1975). The wax moth, *G. mellonella,* is one of the most devastating and economically important pests of wax in the world (Smith 1965, Burges 1978, Haewoon et al. 1995). This insect feeds on comb wax in larval stage and damages it severely. The larvae of the wax moth, cause considerable damage to combs left unattended by bees. Combs in weak or dead colonies and in storage areas are subject to attack (Caron 1992). Adult female moths fly at night and deposit masses of eggs on unprotected honeycombs and in the cracks between hive bodies. After a few days these larvae hatch, crawl onto the comb, and begin their feeding activity. They damage or destroy the combs by boring through the cells as they feed on cocoons, cast skins, and pollen. As they chew through the wax, they spin silken galleries for protection. Full grown caterpillars vary in color but are generally a dirty white, 1.5 inches long. Adult moths are grayish to purplish brown, have dark markings and lead-colored tips on the forewings, pale brownish or yellowish hind wings and a wingspan of about 1 to 1.25 inch. The wings are held over the back when at rest (Chang& Hsieh 1992).

In the control studies against this pest, the following methods are widely used in the world and in our country:

* Chemical substances (paradichlorobenzene, ethylene dibromide, sulfur dioxide, acetic acid, calcium cyanide, methylbromide)

* Physical applications (heating, cooling)

* Biological applications (*Bacillus thuringiensis bacteria*)

* Storing the honeycombs below 10°C, for example in cold air tanks, prevents the opening of moth eggs and development of larvae in honeycombs (3 hours at -12°C or 2 hours at -15°C kill the mystery of developmental periods).

Ferula L. is the third largest genus in the family Apiaceae. The genus contains 180- 185 species (Pimenov& Leonov 2004) and distributed mainly central and South- West Asia, but also occur as far east as North India and in the Mediterranean basin (Ajani& Ajani 2008). The first revision of the genus Ferula in Turkey was performed by Peşmen (1972). He recognized 18 species, of which one was incompletely known and nine were endemic. The

hazard category of this plant is VU (Potentially Damageable) (Ekim et al. 2000, IUCN 2001).

In some studies, the antimicrobial and antibacterial activities and antifungal effects of this plant were investigated (Türküsay and Onoğur 1998, Baldemir et al. 2006, Tunç et al. 2013).

In addition to ecology and physiology, cultivation of artificial nutrients of the harmful species of the Lepidoptera team also allows for the investigation of some metabolic events at different stages of their metabolism (Mandato et al., 1997; Pohlon and Badwin 2001; Büyükgüzel et al., 2002; Tunaz et al., 2003). Thus, the effects of the new insecticides on the insect are investigated in laboratory conditions before application of the land. *Galleria mellonella* L. can be easily cultured in laboratory conditions with a very good physiological model for this work (Wiedenmann et al. 1992, Gupta et al. 1996, Büyükgüzel 2001). Currently, the use of Lepidoptera species on the biological struggle of some parasitoid species causing significant damage in agricultural areas is increasing the importance of the training of these strains in the artificial environment under laboratory conditions. Because of this, high mature yield and short life cycle, dark- colored incubation honey as a natural food and good development on various artificial nutrients, the candle-friendly *G. mellonella* host- parasitoid interaction constitutes an important experimental model for biological and chemical control studies (Jarosz 1989).

Previous studies conducted in different insect species exposed to chemicals, pre- adult development, sex ratio, fertility, adult longevity, adult size, amounts of protein, lipid, glycogen and malondialdehyde (MDA), hemocytes of larvae, activity of some enzymes and diapause time was influenced significantly (Uçkan et al. 2008, Sak and Uçkan 2009, Sezer ve Özalp 2011).

The phytochemicals which have been in growing plantt residues and green manures opened a new area for synthesis of plant-based nematicides so called botanical pesticides. Also, the various plant extracts, which has been obtained some plants that have been contributed some substances such as highly degree negative of nematicidal and nematostatic effect on the multiplication of plant- parasitic nematodes, too. Botanical compounds in various phytochemical composition that have got nematicidal activity are such as polythienyls, acetylenes, alkaloids, carboxylic acids, fatty acids and phenolics, glucosinolates and derivative of terpenoids. Nevertheless, it is not known whether the nematicidal activity was originated of only a single

compound or complex compounds, whether the effect mechanisms was been and/or interactions (Tan 2011).

Although many plants in the area are known to have pesticide effect, few of them are used in practice. The reasons include limited natural resources, standardization and difficulties in obtaining licenses (Isman 1997). In this study, it is aimed to present data obtained on the determination of the effects of some plants and parts of plants and other substances obtained from these plants for the purpose of medical, aromatic or agricultural control for centuries in the lives of human beings in the world and in our country.

2. Methods

The culture of *G. mellonella* was raised in semi- synthetic food prepared by profiting Bronskill. Different doses (25, 50, 75 and 100 ppm) was fed with artificial food containing extracts of *F. halophila*. Adult emergence ratio of immature individuals were identified. The same procedures, without the application of extracts, control group was made for.

The emerging changes were compared through the One Way Variance Analysis SPSS 15.0 (SPSS Version 15.0 for Windows). The arcsine square-roots of the values calculated in percentages were taken before the variance analyses (Sokal and Rohlf 1995). The differences between the averages were determined by the Tukey honestly significant difference (Tukey HSD) tests. Within the evaluations, the significance level was taken as a base a α=0.05.

3. Results

Table 1. After application, pre- adult development time (day)

Amount of extracts *F. halophila* (ppm)	**Pre- adult development time (day)**
0	28,59±0,41d
25	37,40±0,39bc
50	38,87±0,53bc
75	42,20±0,30a
100	40,67±1,33ab

Measures are average of 3 repeats each consists 10 persons.

(ANOVA) Tukey's test which is one of the paired comparision was applied.

Table 2. After application, adult emergence (%)

Amount of extracts *F. halophila* (ppm)	**Total (%)**	**Sex of parasitoid (%)** ♀	♂
0	90,01	55,00a	45,00a
25	84,32	52,00a	48,00a
50	77,63	53,00a	47,00a
75	65,68	54,67a	45,33a
100	20,00	78,67a	21,33a

Measures are average of 3 repeats each consists 10 persons.

(ANOVA) Tukey's test which is one of the paired comparision was applied.

4. Discussion

The great waxy relief that has spread in almost every region of the world beekeeping is one of the most important detriments of honey bees. Larvae of *G. mellonella*; Wax, honey and stored pollen (Tutkun and Boşgelmez 2003). Many of the chemical substances used against the great wax juiciness are leaving or destroying wax and honey, reducing or eliminating the product' s market prospects. In this respect, it is now inevitable to seek new discoveries by considering the residual status of drugs used against pests and the ease of application (Allan 2000).

In determining the effects of a substance on the insect, biochemical and physiological response mechanisms as well as biological activity parameters such as survival, development, longevity and egg yield should be well known.

According to the obtained results, *F. halophila* with increasing concentrations of the extracts of the prolonged period of maturation, but the number of mature individuals occurring after the application has been determined that no significant changes compared to the control group.

As a result, many extracts of vegetable origin seem to be hopeful for human, plant and animal health, as well as for future generations of environment- related perspectives based on consumption of healthier products. With the understanding of the beneficial characteristics of endemic plant species that are specific to many countries of the world, it is necessary to identify competent authorities for the control and control of phytochemicals in order to ensure the safety and quality of these phytochemicals and to ensure environmental safety at the places of use.

This work on the pest of hive products that make a significant contribution to our national economy will guide the initiative to remove the effects of hive pest insects.

References

Ajani, Y. and Ajani, M. 2008. A new species of Ferula (Umbellıferae) from southern Iran. Edinb. J. Bot., 65: 425- 431.

Allan, L. 2000. Wax Moth and Its Control. Department of Agriculture Western Australia. http://www.agric.wa.gov.au/agency/pubns/farmnote/2000/f00697.htm.

Baldemir, A., Coşkun, M. and Yıldız, S. 2006. Antimicrobial activity of *Ferula halophila* Peflmen. FABAD J. Pharm. Sci., 31(2), 57-61.

Bonskill, J. 1961. A Cage to Simplify the Rearing of the Greater Wax Moth, *Galleria mellonella* (Pyralidae). J. Lep.Soc., Vol. 15, No 2, 102-104.

Burges, H.D. 1978. Control of Wax Moth: Physical, chemical and biological methods. Bee World, 59(4),129-138.

Büyükgüzel, K. 2001. Positive effects of some gyrase inhibitors on survival and development of *Pimpla turionellae* L. (Hymenoptera: Ichneumonidae) larvae reared on an artificial diet. J. Econ. Entomol., 94: 21-26.

Büyükgüzel, K., Tunaz, H., Putnam, S.M. and Standey, D.W. 2002. Prostaglandin biosynthesis by midgut tissue isolated from the tobacco hornworm, *Manduca sexta*. Insect Biochem. Molec., Vol. 32, no 4, pp. 435-443.

Caron, D.M. 1992. Wax moth. American Bee Journal, 132(10), 647-649.

Chang, C.P. and Hsieh, F.K. 1992. Morphology and bionomics of *Galleria mellonella*. Chinian Journal of Entomology, 12(2);121-129.

Ebadi, R. 1975. Wax of bee. Journal of Iranian Entomology, 10(4), 61-64.

Ekim, T., Koyuncu, M., Vural, M., Duman, H., Aytaç, Z. and Adıgüzel, N. 2000. Red Data Book of Turkish Plants (Peridophyta and Spermatophyta). Türkiye Tabiatını Koruma Derneği, Yayın No: 18.

Gupta, P., Sloan, A., Dillard, C.R. and Frekovich, S.M. 1996. Parasitism of factitious host, *Galleria mellonella* (Lepidoptera: Pyralidae) by an endoparasitoid: ovoposition and emergence of *Microplitis croceipes* (Hymenoptera: Braconidae). Fla. Entomol., Vol. 79(2), 221-229.

Haewoon, O., Young, M. and Chang, Y. 1995. Developing periods of damage patterns of combs by the wax moth, *Galleria mellonella*. Journal of Apiculture Research, 10(1),5-10.

Isman, M. B. 1997. Neem and other botanical insecticides: Barriers to commercialization.
Phytoparasitica, 25(4): 339-344.

IUCN. 2001. IUCN Red List Categories: Version 3.1. Prepared by the IUCN Species Survial Commission. IUCN, Gland Switzerland and Cambridge, UK.

Jarosz, J. 1989. Simplified technique for prepearing germ- free specimens of greater wax moth (Lepidoptera: Pyralidae) larvae. J. Econ. Entomol., Vol. 82, 1478-1481.

Mantado, C.A., Diehl- Jones, W.L., Moore, S.J. and Downer, R.G.H. 1997. The effects of eicosanoids biosynthesisinhibitors on prophenoloxidase activation, phagosytosis and cell spreading in *Galleria mellonella*. J. Insect Physiol., Vol. 43(1), pp. 1-8.

Pimenov, M.G. and M.V. Leonov. 2004. The Asian Apiaceae biodiversity database (ASIUM) with particular reference to south- west Asian taxa. Turk. J. Bot., 6: 139-145.

Peşmen, H. 1972. Ferula L. In: (Ed.): P.H. Davis, Flora of Turkey and the East Aegean Islands. Edinburg University Pres, Edinburg, 4: 440-453.

Sak, O. and Uçkan, F. 2009. Cypermethrinin *Galleria mellonella* L. (Lepidoptera: Pyralidae)'nın puplaşma ve ölüm oranlarına etkisi. U.Arı Drg., 9(3): 88-96.

Sezer, B. and Özalp, P. 2011. Azadirachtinin *Galleria mellonella* larvalarında total glikojen miktarına etkisi. Ekoloji, 20, 81, 67-72.

Smith, T.L. 1965. External morphology of the larva, pupa and adult of the wax moth *Galleria mellonella.* Journal of Kansas Entomology Society, 38(3),287-310.

Sokal, R.R. and Rohlf, F.J. 1995. Biometry. Freeman, San Francisco, CA.

SPSS Inc. 1999. SPSS 10.0 Statistics, SPSS, Chicago, IL.

Tan, A.N. 2011. Nematisit etkili bitkiler ve bitki ekstraktları, Nematicide effective plants and plant extracts. Ege Üniv. Ziraat Fak. Derg., 48(2): 165-173, ISSN 1018- 8851.

Tunaz, H., Park, Y., Büyükgüzel, K., Bedick, J.C., Nor Aliza, A.R. and Standey, D.W. 2003. Eicosanoids in insect immunity: bacterial infection stimulates hemocytic phospholipase A2 activityin tobacco hornworms, Arch. Insect Biochem., Vol.52(1), pp.1-6.

Tunç, K., Konca, T. and Hoş, A. 2013. Antibacterial activity of *Punica granatum* Linn. SAU J. Sci., Vol 17, No 2, p. 167-172.

Tutkun, E. and Boşgelmez, A. 2003. Bal Arısı Zararlıları ve Hastalıkları Teşhis ve Tedavi Yöntemleri. Bizim Büro Basımevi, Ankara.

Türküsay, H. and Onoğur, E. 1998. Studies on antifungal effects of some plant extracts in vitro. Tr. J. of Agriculture and Forestry, 22, 267-271.

Uçkan, F., Tüven, A., Er, A. and Ergin, E. 2008. Effects of giberellic acid on biological parameters of the larval endoparasitoid *Apanteles galleriae* (Hymenoptera: Braconidae). Entomol Ann Soc Am., 101(3): 593-597.

Pohlon, E. and Baldwin, I.T. 2001. Artificial dies 'capture' the dynamics of jasmonate induced defenses in plants. Entomologia Experimentalis et Applicata, 100:1, 127-130.

Wiedenmann, R.N., Smith J.W. and Darnell, P.O. 1992. Laboratory rearing and biology of the parasite *Cotesia flavipes* (Hymenoptera: Braconidae) using *Diatraea saccharalis* (Lepidoptera: Pyralidae) as a host. Environ. Entomol., Vol. 21, 1160- 1167.

CHAPTER

7

RESEARCH IN NATURAL AND ENGINEERING SCIENCES

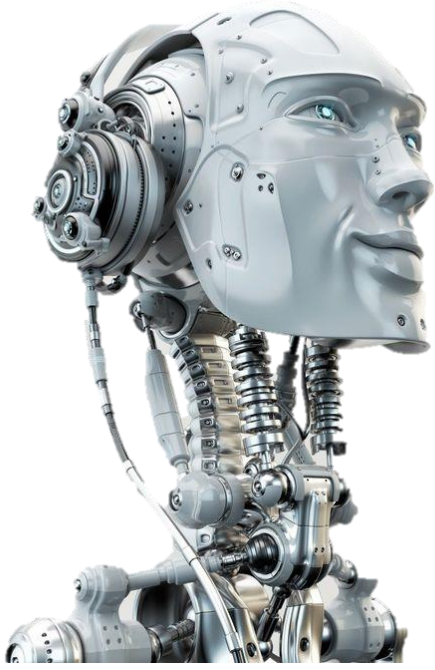

Güneş Enerjisi Santrallerinde Saha Analizi (Furkan Dinçer)

Güneş Enerjisi Santrallerinde Saha Analizi

Furkan Dinçer
Kahramanmaraş Sütçü İmam Üniversitesi, Müh.-Mim. Fakültesi,
Elektrik-Elektronik Mühendisliği Bölümü, Kahramanmaraş
furkandincer@ksu.edu.tr

1. Giriş

Elektrik enerjisi talebinin artması ile beraber ülkemizde elektrik enerji santrallerinin kurulu gücü de artmaktadır. TEİAŞ'ın verilerine göre, Eylül 2020 dönemi itibariyle Türkiye'nin kurulu gücü 93.207,1 MW olmuştur. Bu kurulu güç değerinde güneş enerjisinin payı önemli durumdadır. Güneş enerjisinden elektrik enerjisi üretimi yapan santrallerin sayısı hızlı bir şekilde artmaktadır. TEİAŞ'ın verilerine göre ülkemizde 7.267 adet güneş enerjisi santrali olup kurulu güç değeri 6.361,1 MW'tır [1].

Güneş enerjisi santralleri kurulum tipi açısından sınıflandırıldığında; arazi tipi ve çatı tipi olmak üzere ikiye ayrılmaktadır. Geçmiş yıllarda arazi tipi santraller çokça yaygınken, son çıkan yönetmelikler ve yasal düzenlemeler ile çatı tipi güneş enerjisi santrallerinin sayısı da hızla artmış ve artmaya devam etmektedir. Geçtiğimiz aylarda su üzerine de güneş enerjisi santrali kurulmasının önü açılmıştır. Bu santral tiplerine yüzer güneş enerjisi santrali adı verilmektedir. Ülkemizde henüz prototip aşamada olan bu uygulama da ilerleyen yıllarda yaygınlaşacak konumdadır. Özellikle barajların geniş su yüzey alanı bulunduğundan yüzer güneş enerjisi santralleri ekonomik ve maliyet etkin olacaktır.

Güneş enerjisi santralleri bağlantı tipi açısından sınıflandırıldığında şebeke bağlantılı (on-gird) ve şebeke bağlantısı (off-grid) olmak üzere ikiye ayrılmaktadır. Ülkemizdeki güneş enerjisi santrallerinin önemli bir bölümü şebeke bağlantılı olan güneş enerjisi santralleridir. Şebeke bağlantılı olan güneş enerjisi santralleri isterse şebekeden enerji çekebilir, isterse şebekeye ürettiği fazla enerjiyi verebilir durumdadır. Şebeke bağlantısız güneş enerjisi santrallerinde ise şebeke bağlantısı olmayıp ada modu konumundadır. Yani bağımsız konumda olup, sadece kendi ürettiği enerjiyi kullanabilir durumdadır. Şebeke ile herhangi bir bağlantı konumu olmaz [2-4].

Güneş enerjisi santralleri hızla kurulurken, kurulum sırasında da çeşitli hatalar yapılmaktadır. Yapılan saha uygulamalarındaki hatalar tespit edilmesi kurulacak yeni sahalar için de aydınlatıcı olacaktır. Bundan ötürü; bu çalışmada şebeke bağlantılı güneş enerjisi santrallerinde saha ve performans analizi gerçekleştirilmiştir. Bu analiz için örnek bir saha seçilmiş ve test edilmiştir.

Şekil 1: Güneş enerjisi santralinden görünüm

2. Güneş Paneli

Ülkemizde otuzun üzerinde güneş paneli yerli üreticisi bulunmaktadır. Çok sayıda firma güneş paneli üretmektedir. Güneş santrallerinde yerli ve yabancı olmak üzere çok farklı firmalara ait güneş panelleri bulunmaktadır.

Ülkemizde üretilen güneş panellerinin önemli bir kısmı mono-perc denilen hücreden yapılmakta olup 60 hücreli veya 72 hücreli olarak üretilmektedir. Geçmiş yıllarda polykristal hücre tipinden ağırlıklı olarak güneş paneli üretilmekteydi. Mono-perc hücre yapısı ile aynı alanda daha fazla güç elde edilebildiği için yeni güneş panellerinde bu hücre tipi kullanılmaktadır. İncelenen saha 3-4 yıllık kurulu bir saha olduğu için bu sahada polykristal hücre tipinde güneş paneli kullanılmıştır.

Kurulum yapılan sahalarda güneş paneli sehpası istenilen şekilde tasarlanabilmektedir. Genellikle yapılan tasarımlar ağırlıklı olarak 3'lü yatay, 4'lü yatay ve 2'li dikey şeklinde olabilmektedir. Her çeşit tasarımın kendi içerisinde çeşitli avantaj ve dezavantajları bulunmaktadır. Üretim ve performans odaklı bakıldığı zaman 4'lü yatay en çok tercih edilmesi gereken sehpa tipidir. Şekil 2'de 4'lü yatay sehpa örneği gösterilmektedir.

Şekil 2: 4'lü yatay sehpa modeli

Şekil 3: 2'li dikey sehpa modeli

Şekil 3'te, 2'li dikey sehpa modeli gösterilmektedir. Panellerin dikey konumda olması özellikle kış aylarında gölge kaybını artıracaktır. Santralin tamamı 2 dikey olacak şekilde projelendirilmiştir. 2 dikey panel uygulaması gölge kaybının daha yüksek olmasından dolayı tercih edilmemektedir.

Panellerin dikey konumda olması durumunda alttaki panele 10 cm gölge durumunda panelin tamamı devre dışı kalır ve üretim kaybı olur. Yatay konumlandırılan panellerde 10 cm gölgelenmesi durumunda panelin 1/3 devre dışı kalır. 2/3 üretime devam eder. Özellikle sonbahar ve kış aylarında önemli üretim kaybı olmaktadır. Özellikle sonbahar ve kış aylarında önemli ölçüde gölge kaybı olacağı için üretim kaybı olacaktır. Şekil 4'te, güneş paneli üzerinde gölge kaybı ve bypass diyotlarının durumu gösterilmektedir.

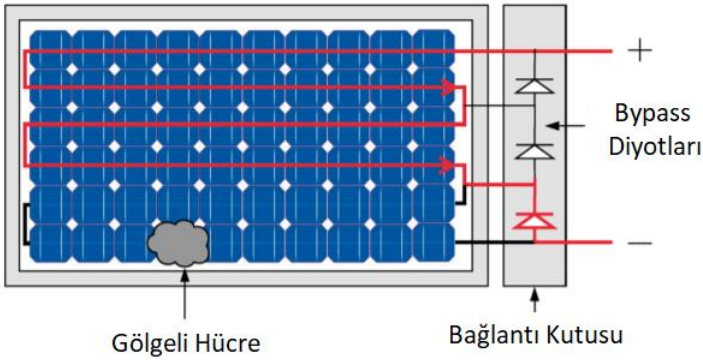

Şekil 4: Güneş paneli üzerinde gölge kaybı ve bypass diyotlarının durumu [5]

3. Güneş Panellerinde Termal Test Uygulaması

Güneş enerjisi santralindeki güneş panelleri üzerinde termal kamera ile test yapılmıştır. Termal kamera ile güneş panelleri üzerindeki hot-spot noktalar ve ölü hücreler direkt olarak tespit edilebilmektedir. Şekil 5'te güneş paneli üzerinde termal test fotoğrafları gösterilmektedir. Güneş paneli hücresinde kılcal çatlaklar meydana geldiği zaman kılcal çatlak olan hücreler termal kamerada yüksek sıcaklık ile kendini direkt göstermektedir. Bu noktalar hot-spot denilen noktalardır. Üretim değerinin iyi olduğu zamanlarda bu noktaların sıcaklık değerleri 80 0C civarlarında olabilmektedir. Gün batımı sonrası ise çok düşük sıcaklık değerine sahip olmaktadır. Bu yüksek sıcaklık farklıları zamanla hücrenin ölmesine, panelin backsheet denilen arka tabakasında yanma ve patlamalara sebebiyet verebilmektedir.

Tamamen ölmüş bir hücrede ise sıcaklık mevcut çalışan hücrelere göre çok daha düşük olur. Termal kamera ile de bu durum rahatlıkla tespit edilebilmektedir. Ölü hücre de elektrik enerjisi üretmez ve bağlı bulunduğu bölümü de kendi gibi çalıştırır. Yani bir panelde üç adet bypass diyotu var ise o panelin üçte biri çalışmaz duruma gelmektedir.

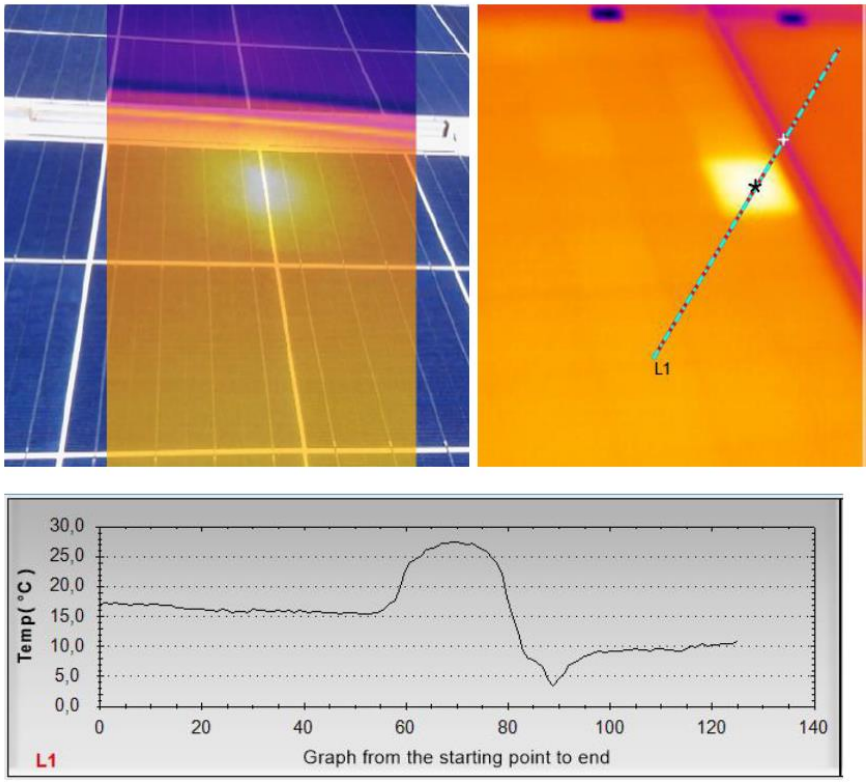

Şekil 5: Güneş paneli üzerinde termal test

Şekil 5'ten de görüleceği üzere panel üzerinde normal hücredeki sıcaklık değerleri 15 ^{0}C civarlarındayken kılcal çatlak bulunan hücrede bu değerler 30 ^{0}C civarlarındadır. Üretim durumuna göre bu sıcaklık değerleri değişkenlik göstermektedir.

4. Güneş Panellerinde Mekanik İnceleme

Güneş panellerin çerçevesi alüminyum olup, literatürde panellerin nasıl montajlanacağına dair çok sayıda çalışma mevcuttur. Mevcut sahada kullanılan güneş paneli montaj şekli hiçbir literatürde olmayan şekilde konumlandırılmış ve riskli durumdadır. Güneş panellerin içerisinde bulunan hücreler rüzgârda sallanması durumunda hücreler içerisinde kılcal çatlaklar oluşur ve bu durum güneş panelinin ömrünü azaltır. Kılcal çatlaklı hücreler bulunduran güneş panellerinin performansı da daha düşük olur. Güneş panellerinde panel tutucu konumları Şekil 6'da açık bir şekilde gösterilmiştir.

Soldaki şekilde sabitleme yerleri doğru olarak verilirken, sağdaki şekildeki gibi bir konumlandırma panel için sakıncalı olup doğru değildir. Güneş panelinin konumlandırılmasında panel eşit noktalarda yük dağılımına sahip olmalı ve dışarıdan gelebilecek rüzgâr gibi yüklere dayanıklı olmalıdır.

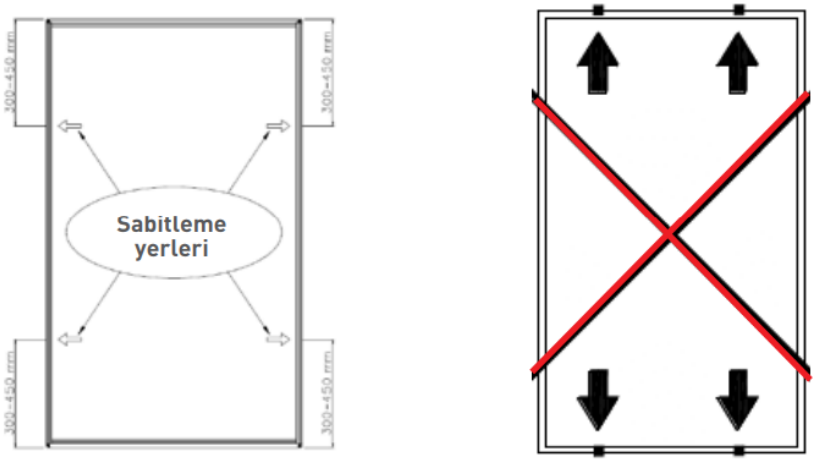

Şekil 6: Güneş panellerinde panel tutucu konumları

Güneş panelleri genellikle uzun kenarlarından monte edilirler. Güneş panellerin kısa kenarından monte edilmesine bazı üreticiler, bazı durumlarda izin vermez (monte edilirse garanti kapsamı dışına çıkar). Kar, rüzgâr gibi hava şartlarından dolayı panellere uygulanan mekanik stres bölgeden bölgeye değişim gösterir. Panellerin dayanabildiği maksimum stres genelde 2400 Pa ile 5400 Pa arasındadır.

İncelenen örnek sahada ise güneş panel tutucuları aşağıdaki gibi yerleştirilmiştir (Şekil 7). Bu sistemde 3 âşık kullanılmış ve âşıktan tasarruf edilmiştir. Yani sahada kullanılan çelik tonajı azaltılmıştır. Ancak panel tutucular standart dışı kullanılmış ve tutucular arası mesafe uzun olduğu için güneş panellerinin rüzgârdan zarar görme ihtimali yüksektir. 2'li dikey montaj sisteminde 4 aşık olması gerekirken 3 aşık kullanılmıştır. Şekil 8'de ise sahada kullanılan sehpa montaj sistemine ait olması gereken görünüm açık bir şekilde gösterilmiştir.

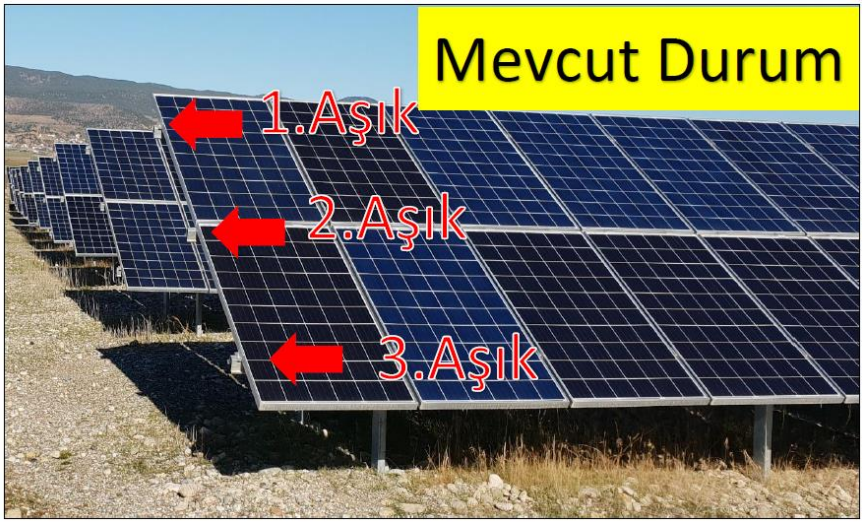

Şekil 7: Sahada kullanılan sehpa montaj sistemine ait mevcut durum görünümü

Şekil 8: Sahada kullanılan sehpa montaj sistemine ait olması gereken görünüm

Şekil 9'da sahada kullanılan sehpa montaj sistemine ait mevcut panel tutucu görünümü gösterilmiştir. Görüldüğü üzere güneş panellerinin tutturulma kısımları standart panel tutumlarına göre uygun değildir. Panel tutucular arasındaki mesafeler oldukça yüksektir. Şekil 10'da ise sahada kullanılan sehpa montaj sistemine ait olması gereken panel tutucu görünümü gösterilmiştir.

Şekil 9: Sahada kullanılan sehpa montaj sistemine ait mevcut panel tutucu görünümü

Şekil 10: Sahada kullanılan sehpa montaj sistemine ait olması gereken panel tutucu görünümü

Şekil 11'de sahada kullanılan sehpa montaj sistemine ait mevcut panel tutucular arasındaki mesafe 130 cm'den daha uzundur. Panel tutucular için standart dışı bir uygulamadır. Böyle bir montaj şekline güneş paneli üreticileri de garanti vermeyecek ve paneli garanti kapsamı dışına çıkarabilir durumdadır.

Şekil 11: Sahada kullanılan sehpa montaj sistemine ait mevcut panel tutucular arasındaki mesafe

5. Sonuç

Bu çalışmada mevcut bir güneş enerjisi santralini analiz edilmiştir. Saha içerisinde güneş panelleri üzerinde termal test ve mekanik inceleme ayrıntılı olarak yapılmıştır. Mevcut saha içerisinde güneş panelleri üzerinde kılcal çatlaklıklar olduğu termal kamera ile açık bir şekilde tespit edilmiştir. Ayrıca mekanik inceleme kısmında sehpa montaj sistemleri tartışılmış ve mevcut montaj sisteminin verimli olmadığı detaylandırılmıştır. Önerilen montaj sistemi yatay yerleşim şeklindedir. Sahaların durumuna göre bu yatay yerleşim 3'lü, 4'lü, 5'li veya 6'lı şekilde olabilir. Ancak, yatay yerleşimin performansı gölge analizi açısından daha iyi konumdadır. Ayrıca mevcut sahadaki güneş paneli tutucularının, aşıkların da yanlış şekilde konumlandırıldığı tespit edilmiştir. Mevcut durumlar ve olması gereken durumlar açık bir şekilde ayrıntılı olarak gösterilmiştir. Mevcut saha daha detaylı olarak incelenebilir ve oluşturulan çalışma daha detaylandırılabilir.

Referanslar

[1]. Türkiye Elektrik İletim A.Ş. https://www.teias.gov.tr/, 9 Ekim 2020.

[2]. Saban Yilmaz, Hasan Riza Ozcalik, Osman Dogmus, Furkan Dincer, Oguzhan Akgol, Muharrem Karaaslan, Design of two axes sun tracking controller with analytically solar radiation calculations, Renewable and Sustainable Energy Reviews, 43, March 2015, Pages 997-1005.

[3]. Sabir Rustemli, Furkan Dincer, Emin Unal, Muharrem Karaaslan, Cumali Sabah, The analysis on sun tracking and cooling systems for photovoltaic panels, Renewable and Sustainable Energy Reviews, 22, June 2013, Pages 598-603.

[4]. Saban Yilmaz, Furkan Dincer, Optimal design of hybrid PV-Diesel-Battery systems for isolated lands: A case study for Kilis, Turkey, Renewable and Sustainable Energy Reviews, 77, September 2017, Pages 344-352.

[5]. Romênia G. Vieira, Fábio M. U. de Araújo, Mahmoud Dhimish, Maria I. S. Guerra, A Comprehensive Review on Bypass Diode Application on Photovoltaic Modules, Energies 2020, 13, 2472; doi:10.3390/en13102472.

CHAPTER

8

RESEARCH IN NATURAL AND ENGINEERING SCIENCES

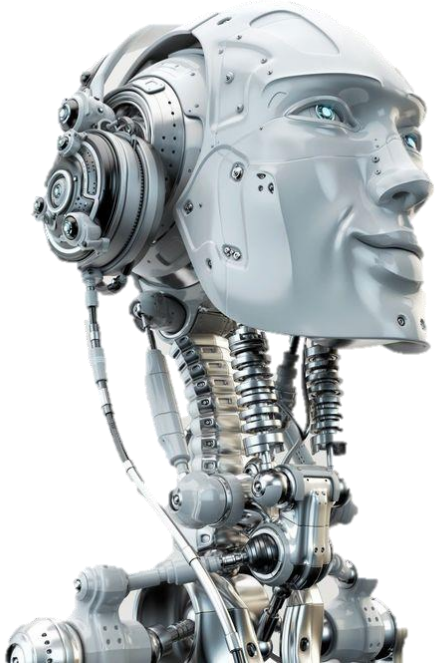

İstanbul Şartlarında 300 kW Kurulu Güce Sahip Bir Güneş Enerjisi Santralinin Tasarlanması, Gölgelenme ve Enerji Üretim Analizinin Gerçekleştirilmesi (Furkan Dinçer)

İstanbul Şartlarında 300 kW Kurulu Güce Sahip Bir Güneş Enerjisi Santralinin Tasarlanması, Gölgelenme ve Enerji Üretim Analizinin Gerçekleştirilmesi

Furkan Dinçer
Kahramanmaraş Sütçü İmam Üniversitesi, Müh.-Mim. Fakültesi,
Elektrik-Elektronik Mühendisliği Bölümü, Kahramanmaraş
furkandincer@ksu.edu.tr

1. Giriş

Canlı hayatının enerji kaynağı olan güneş, sadece dünyamızı aydınlatmak ile kalmayıp aynı zamanda ısı enerjisi yayarak da canlılara yaşama olanağı sunmaktadır. Güneş enerjisinin oluşması ise güneşte meydana gelen füzyon sürecinin bir sonucudur [1]. Bu oluşum ile birlikte açığa çıkan enerji dünyamızda temelde iki şekilde kullanılmaktadır; (i) yoğunlaştırılmış güneş enerjisinden sıcak su elde etmek (ii) fotovoltaik paneller kullanarak elektrik enerjisi elde etmektir [2, 3].

Bilindiği üzere fosil yakıtlarının rezervleri gün geçtikçe azalmaktadır [4]. Buna bağlı olarak da fotovoltaik panellerin kullanılması ile güneş enerjisinden elektrik enerjisi üretimi kurulu gücü hızlı bir şekilde artmaktadır [5]. Bu durum beraberinde santrallerde çeşitli hataların da meydana gelmesine neden olabilmektedir. Buna yol açan en önemli nedenler; yeterli fizibilite çalışmasının yapılmaması ve gölgelenme faktörünün yeteri kadar dikkate alınmaması şeklinde sıralanabilir.

Bir bölgeye güneş enerjisi ile ilgili yatırım yapılmak isteniyorsa daha önceden bölgede birtakım çalışmaların yapılmış olması gerekmektedir. Bu çalışmalar;

- •Kurulacak olan arazinin fiyatının çıkartılması
- •Arazinin güneş enerjisi santraline uygunluğu
- •Gerekli yasal izinlerin alınması
- •Arazi için fizibilite raporunun hazırlanması
- •Kurulması planlanan santralin yıllık getirisi
- •Yıllık fotovoltaik panelleri üzerine düşün güneş enerjisinin hesaplanması
- •Amortisman süresi

Daha birçok kalemden oluşan bu çalışmaları önceden belirlemek oldukça güç ve hata olasılığı oldukça yüksektir [6].

Küçük güçlü güneş enerjisi santrallerinde hataların telafisi mümkün olsa da santrallerin kurulu güçlerinin yüksek olması durumunda bu küçük hatalar, büyük kayıplara neden olmaktadır. Bu gibi problemleri en aza indirmek için simülasyon programları ile analiz ve fizibilite büyük önem arz etmektedir. Bu

sayede santralle oluşabilecek tüm kayıpların santral kurulmadan önce belirlenerek gerekli önlemlerin alınması sağlanabilecektir. Yapılan bu çalışmada PVSOL Demo yazılımı ile İstanbul ili için 300 kW kurulu güce sahip bir güneş enerjisi santrali tasarlanmıştır. Santral için gölgelenme ve enerji üretim analizleri detaylı olarak incelenerek, sonuç ve değerlendirme sunulmuştur. Bu sayede güneş enerjisi santralleri kurmadan önce oluşabilecek sorunları tespit etmek, sistemin kurulacağı bölgenin yıllık üretim kapasitesini belirlemek ve çevresel faktörlerin santrale olan etkilerini önceden görmek mümkün olmaktadır.

2. Tasarımı Yapılan Güneş Enerjisi Santraline ait Lokasyon, İstanbul

Öncelikli olarak yapılması gereken İstanbul iline ait güneş enerjisi yıllık güneşlenme süresi ve yıllık radyasyon değerlerinin bilinmesi gerekmektedir. Elektrik İşleri Etüt İdaresi (EİE) tarafında hazırlanan rapora göre İstanbul için yıllık güneşlenme süresi 2,446 (saat/yıl), ve yıllık güneş enerjisi radyasyon değeri 1400-1450 (kWh/m²-yıl) arasında olduğu bilinmektedir [7]. Şekil 1'de santralin kurulacağı lokasyon ve Şekil 2'de bu lokasyona ait yıllık radyasyon değerleri verilmektedir.

Şekil 1. Güneş enerjisi santralinin kurulduğu lokasyona ait harita [8]

Şekil 2. İstanbul iline ait yıllık toplam güneş radyasyon değerleri [7]

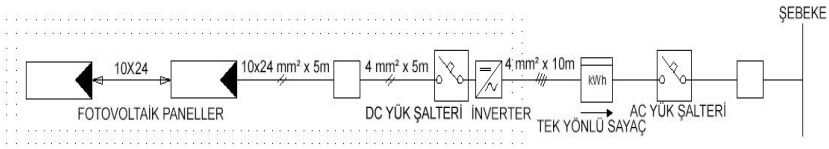

Şekil 3. Tasarlanan güneş enerjisi santraline ait tek hat şeması

Güneş enerjisi santral kurulumları amaçlarına göre temelde iki şekilde bağlantı tipine sahiplerdir. Şebeke bağlantılı sistemler (on-grid sistem), şebeke bağlantısız sistemler (off-grid sistem), bunların dışında ikisinin bir arada olduğu, akü grubunun dahil edildiği ve son zamanlarda kullanımı artan elektrik araçların da dahil edildiği sistemler de kullanılmaktadır [9]. Kullanılan program içerisinde bunların hepsini de bulmak mümkündür. Yapılan çalışmada iç tüketimin olmadığı sadece üretip şebekeye aktarıldığı on-grid sistem üzerine santral tasarlanmıştır. Şekil 3'de iç tüketimi olmayan on-grid sistem ve sistemdeki temel ekipmanlar gösterilmektedir.

İstanbul ili için yıllık güneşlenme ve kurulacak olan şebeke tipi seçildikten sonra tesisin kurulacağı arazi tipi belirlenmelidir. PVSOL Demo programında iki tür arazi yapısı bulunmakta bunlar (i) eğimli arazi, (ii) düz arazi. Bu çalışmada düz bir arazi üzerine santral kurulmaktadır. Arazi seçimi yapıldıktan sonra tesisin kaplayacağı alan belirlenir ve bu alanı PVSOL Demo programı çalışma alanı olarak belirler. Şekil 4'te program üzerinde oluşturulmuş olan çalışma alanı görülmektedir. Burada kurulacak olan tesisin büyüklüğüne göre boyutlar değişmektedir.

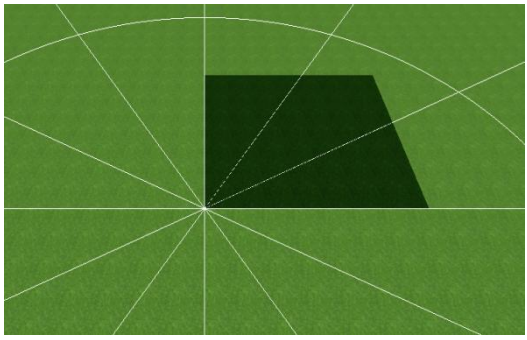

Şekil 4. Güneş enerjisi tesisi için çalışma alanı

Program kendi içerisinde panel yönleri olarak Güney'i kabul etmektedir. Ülkemiz de kuzey yarım kürede bulunduğu için tesis yönü olarak santral kurulumunda güney yönü seçilmelidir.

Bilindiği üzere güneş enerjisi santralleri kurulan arazinin çevresinin boş olması istenir. Fakat bazı durumlarda bunun gerçekleşmesi mümkün olmayabilir. Santral çevresinde bulunan ağaçlar, evler santral üzerinde büyük etki oluşturmaktadır. Bu gibi durumlarda bu nesnelerin santral üzerindeki etkileri iyi analiz edilmelidir. Bu çalışmada da santralin kurulduğu lokasyon da dikkate alınarak santralin çevresine ev ve ağaç gibi nesneler yerleştirilmiştir. Şekil 5'te program üzerinde oluşturulan nesnelerin santralin kurulduğu arazideki yerleşimi gösterilmektedir.

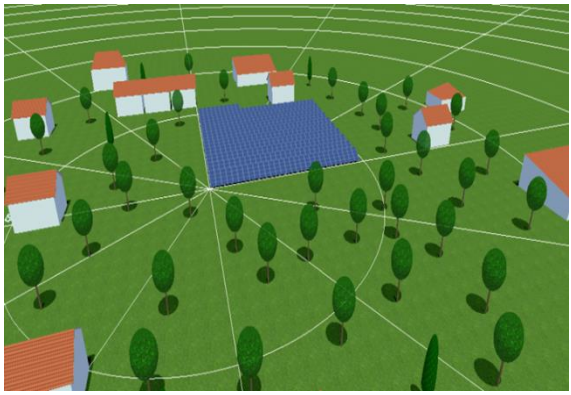

Şekil 5. Arazide bulunan ev, ağaç gibi nesnelerin yerleşimi

Arazi seçimi yapıldıktan sonra panellerin seçilmesi gerekmektedir. Paneller yapılarına göre farklı şekilde imal edilmektedirler. Aynı zamanda çıkış gerilimleri de farklılık göstermektedir. Fotovoltaik paneller genellikle mono kristal ve polikristal olarak imal edilmektedir [9, 10]. Daha çok mono kristal paneller tercih edilir, bu panellerin tercih edilmesinin sebebi polikristal panellere göre biraz daha verimlerinin yüksek olmasıdır. Monokristal paneller %12-16 arasında bir verim ile çalışırlar. Laboratuvar çalışmalarında daha verimli panellerde test edilmektedir [11].

Bu çalışmada Türkiye genelin çok geniş bir pazar payına sahip olan Solar Türk firmasının üretmiş olduğu Solar Türk Enerji STH P 250 W tipi fotovoltaik paneller kullandık. Bu panelin yüksekliği 1,675 cm, genişlik ise 1,001 cm olarak imal edilmektedir. Üretici firma datasheet de verdiği gibi PVSOL programında da aynı değerler bulunmaktadır. Tablo 1'de Solar Türk firmasına ait STH P 250W panelin datasheeti bulunmaktadır.

Çizelge 1. STH P 250W panelin özellikleri [12]

Değerler	Birimleri	STH P 250W
Nominal Güç	(Pmax-W)	250
Nominal Güç Voltajı	(Vmp-V)	29,98
Nominal Güç Akımı	(Imp-A)	8,34
Açık Devre Voltajı	(Voc-V)	37,41
Kısa Devre Akımı	(Isc-A)	8,79
Modül Verimliliği	(η-%)	15,36

Standart Test Koşulları Altında (Işınım 1000W/m²), Hücre Sıcaklığı 25°C

Panel seçiminden sonra montajı yapılacak olan panellerin dikey veya yatay olarak yerleşimi belirlenir. Panellerin dikey ve yatay yönünün belirlenmesinin temelde iki nedeni bulunmaktadır. (i) arazinin alanının büyüklüğü, (ii) gölgelenme faktörünün etkileri. Doğru hesaplama yapılmadan yerleştirilen panellerde ciddi oranlarda enerji kaybı meydana gelmektedir. Bu çalışma santrale paneller yatay olarak yerleştirilmektedir. Bu sayede hem arazinin alanı küçük tutulmakta hem de gölgelenme faktöründen etkisi en aza indirilmek istenmiştir. Şekil 6'da yatay olarak yerleştirilen panellerin oluşturduğu diziler görülmektedir.

Paneller üzerinde oluşan gölgelenme faktörü; dikey olarak yerleştirilen fotovoltaik panel üzerinde bulunan busbarların dikey olarak birbirine lehimlenmesi ile oluştuğundan en altta bulunan hücrenin gölgelenmeye maruz kalmasından dolayı o dizide bulunan hücrelerinde gölgelenmeye maruz kaldığını ifade etmesidir. Dolayısıyla üretim minimum seviyeye düşürmektedir. Yatay da ise hücrenin bir sırasının gölgede kalması sadece bağlı bulunduğu diziyi etkilediğinden sadece o dizide bulunan hücrelerde üretim minimum seviyeye düşürmektedir [13]. Şekil 7'de gölgelenme faktörünün dikey ve yatay yönlü etkisi gösterilmektedir.

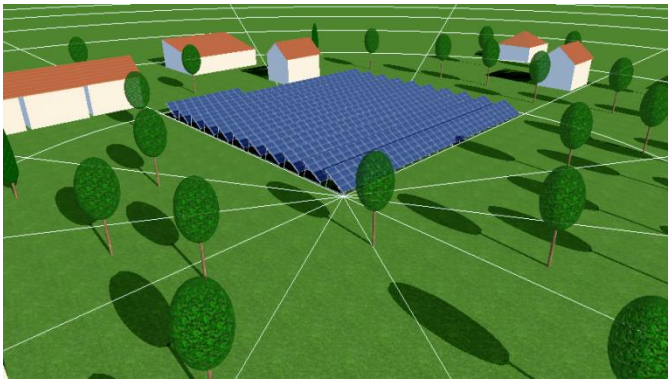

Şekil 6. Panellerin yatay olarak oluşturduğu diziler

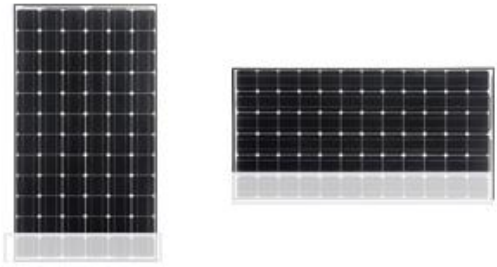

Şekil 7. Panellerin durumuna göre gölgelenme faktörü

Fotovoltaik diziler arasında uzaklık, panelin uzunluğu ve eğim açısına bağlı olarak değişmektedir. Ülkemiz de güneye baktığı için panel eğimi, İstanbul için 30º olarak alınmıştır. PVSOL programı bu işlemi bize kendi içerisinde hesaplamakta ve en uygun uzaklık mesafesini bize vermektedir. Şekil 8'de programın kendi içerisindeki hesaplama yöntemi gösterilmektedir.

Burada önemli olan nokta d - d_1 arasındaki uzaklıktır. Bu uzaklık panellerin birbiri üzerindeki gölgelenme etkisini vermektedir. Programda panellerin yerleşimini yaptıktan sonra program kendi içerisinde animasyon ile yıllık olarak çevresel etkenlerin (ev, ağaç vb.) Güneş enerjisi santrali üzerine etkilerinin görsel olarak sunmaktadır. Bu sayede santral kurulmadan önce yaşanacak olan durumlar gözlenmiş olacak ve gerekli önlemlerin alınmasına kolaylık sağlanmış olacaktır. Şekil 9'da çevresel faktörlerin kurulan santrale etkilerinin günün belirli vakitlerinde santral üzerinde oluşturduğu etkiler görülmektedir.

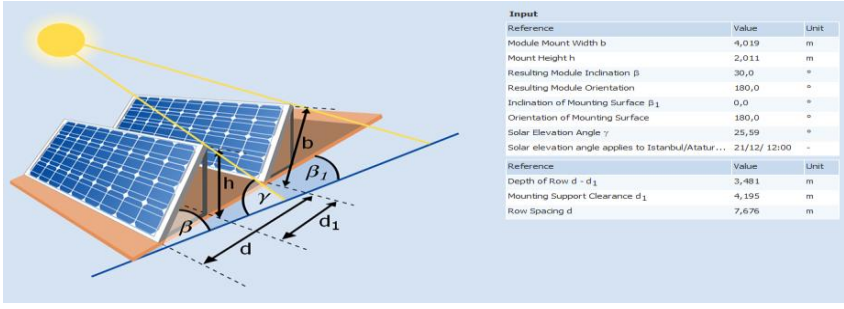

Input

Reference	Value	Unit
Module Mount Width b	4,019	m
Mount Height h	2,011	m
Resulting Module Inclination β	30,0	°
Resulting Module Orientation	180,0	°
Inclination of Mounting Surface β_1	0,0	°
Orientation of Mounting Surface	180,0	°
Solar Elevation Angle γ	25,59	°
Solar elevation angle applies to Istanbul/Atatur...	21/12/ 12:00	-

Reference	Value	Unit
Depth of Row d - d_1	3,481	m
Mounting Support Clearance d_1	4,195	m
Row Spacing d	7,676	m

Şekil 8. PVSOL paneller arasındaki mesafenin hesaplanması

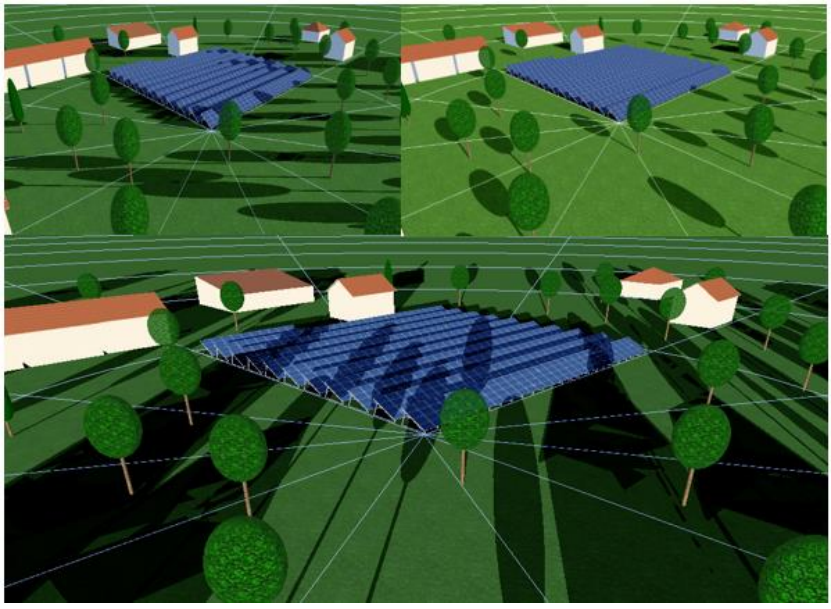

Şekil 9. Sabah, öğle ve akşam vakitlerinde çevredeki nesnelerin santrale olan etkileri

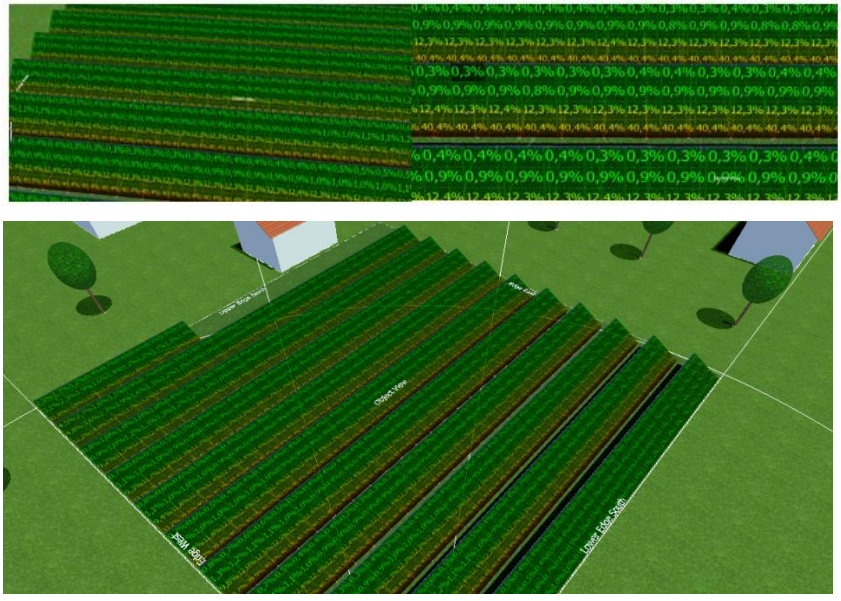

Şekil 10. Gölgelenme faktörüne bağlı olarak yaşanan enerji kayıpları

Santrale etki eden gölgelenme faktörüne bağlı olarak santralde oluşan enerji kayıplarının paneller üzerinde oluşturduğu kayıplar Şekil 10'da verilmektedir. Şekilde de anlaşıldığı gibi dizilerin alt kısımlarında bulunan panellerde enerji kayıpları %40 civarlarına ulaşmaktadır. Burada bir öncesinde bulunan panellerin gölgesinden kalması ve eğim açısının değerine bağlı olarak enerji kaybı değerleri değişmektedir.

Bir güneş panelinin çıkışında üretilen DA enerji ile sadece DA çalışan sistemler çalıştırılabilir. Oysa günlük yaşantımızda kullandığımız birçok elektrikli cihazlar AA ile çalışmaktadır. Dolayısıyla güneş panellerinin çıkışında üretilen DA elektrik enerjisi doğrudan kullanılmamaktadır. Bu nedenle üretilen DA elektrik enerjisinin AA elektrik enerjisine çevrilmesi gerekmektedir [14]. Üretilen DA elektrik enerjisine göre inverter hesabı yapılmalıdır. Kurulan fotovoltaik sistem için seçilen inverter panellerde üretilen enerjiyi yüksek bir verimlilik ile çevirip uzun süre kullanmaya uygun olmalıdır [15]. Yanlış bir hesaplama sonucu seçilen inverter hem istenilen verimlilikte çalışmaz hem de parasal olarak kayıplara neden olmaktadır. Şekil 11'de panel ve inverterdeki çevrim gösterilmektedir.

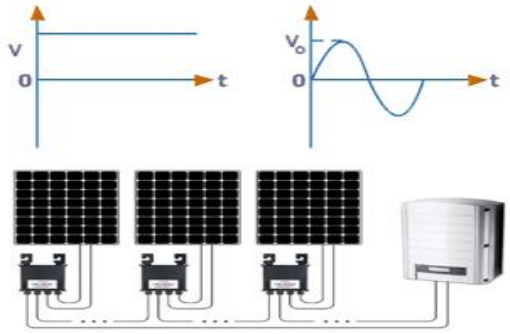

Şekil 11. Panel ve inverterdeki enerji çevrimi

300 kW santral için kullanılan toplam panel sayımıza ve santralin toplam kurulu gücüne bağlı olarak inverter seçimi yapılmaktadır. Santralde SMA America STP 60-US-10 tipi inverterler kullanılabilmektedir. Santral için uygun olan inverter seçiminden sonra program kurulan santrale ait dataları vermektedir. Bu sayede sistem kurulmadan oluşabilecek değerler gözlemlenmektedir. Bu şekilde dataların verilmesinin en önemli yanı kurulan santralin yıllık üretim verisi, toplam oluşabilecek kayıplar, gölgelenmenin santral üzerindeki etkileri, aylara göre üretim verileri ve amortisman süresi kolayca okunabilmektedir. Şekil 12'de aylara göre üretim tahmini verileri verilmektedir.

Şekil 12'de de görüldüğü gibi en fazla üretim değerleri Mayıs- Ağustos ayları arasında oluşmaktadır. Bu şekilde oluşmasının nedeni ülkemizin kuzey

yarım kürede yer almasıdır. Bu değerlere bağlı olarak da santralin performansının hangi aylarda daha verimli çalıştığı Şekil 13'te görülmektedir.

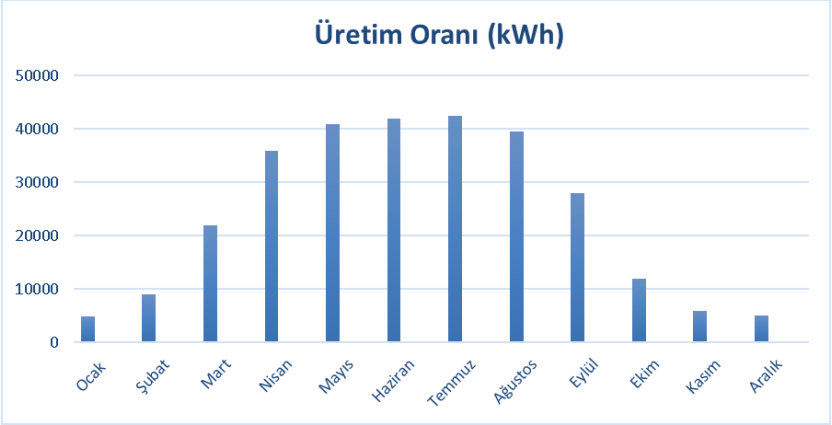

Şekil 12. Aylara göre elektrik enerjisi üretim verileri

Verilerden de görüldüğü gibi santral %100 değerlerine ulaşmamaktadır. Bunun nedenleri; santral kurulan ilin yıllık güneşlenme süresi ve santralin çevresinde bulunan nesnelerin santral üzerindeki etkilerinden kaynaklanmaktadır. Ülkemizde güney yönlerine doğru gidildiğinde santralden alınan verimlilikte artmaktadır.

Müşteri tarafından gözlemlenecek önemli değerlerden bir tanesi de amortisman süresidir. Amortisman süresini; santralin kurulu gücünün büyüklüğü, santralin kurulduğu bölge ve fotovoltaik panellerin güçleri etkilemektedir. Amortisman süresi ne kadar kısa olursa santral de hızlı bir şekilde kara geçer. Bazı durumlarda aynı güce sahip santrallerin amortisman sürelerinin farklı olduğu gözlemlenmektedir. Bu farklılıkların oluşmasında en önemli etken santral kurulan yerin yıllık güneşlenme süresidir. Yapılan bu çalışma da İstanbul için yıllık güneşlenme süresi 2,446 (saat/yıl) ve yıllık güneş enerjisi radyasyon değeri 1400-1450 (kWh/m²-yıl) arasında olduğu bilinmektedir [7]. Güney bölgelerine doğru ise bu değerler artmaktadır dolayısıyla bu amortisman süresini de kısaltmaktadır. Şekil 14'te 300 kWp'lik santralin İstanbul ili için amortisman süresi verilmektedir.

Kurulan güneş enerjisi santrali 12 ve 13. yılları arasında amortisman süresinin tamamlayarak kazanca geçmektedir. Burada hesaplama yapılırken yıllık oluşabilecek maliyet artışları %3 olarak kabul edilmektedir. Elektrik enerjisinin satış fiyatı ise 0,40 TL/kWh olarak kabul edilmektedir.

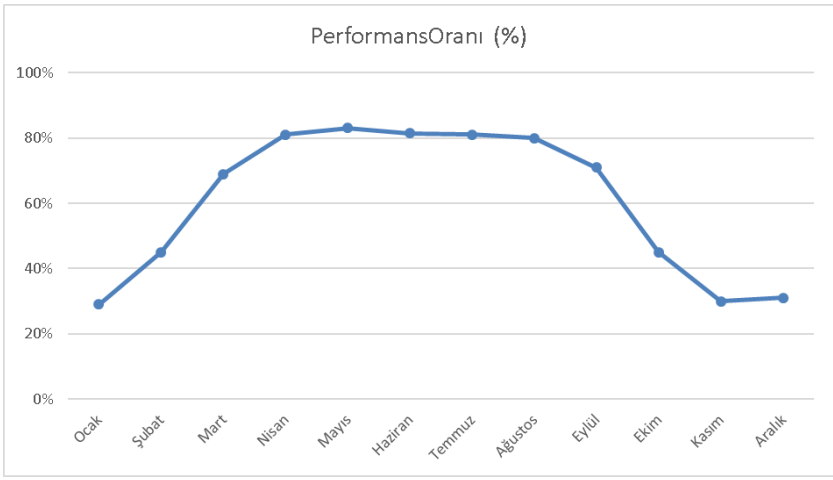

Şekil 13. Santrale ait aylık performans değerleri

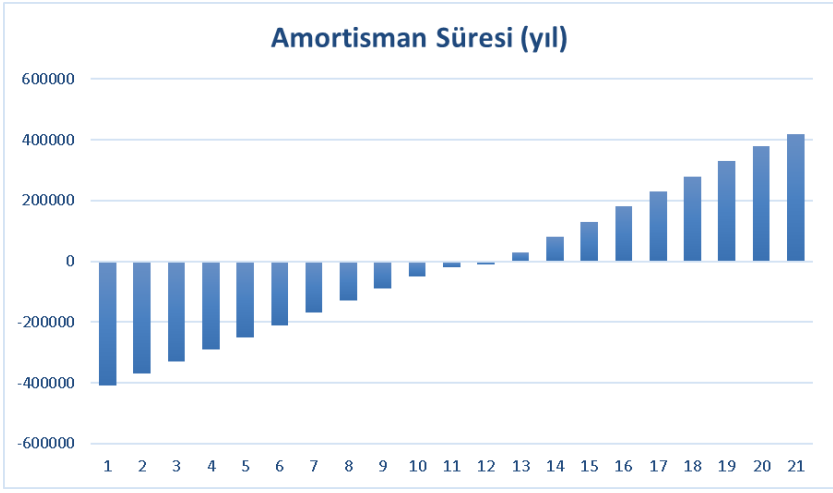

Şekil 14. Amortisman süresi

3. Sonuç ve Değerlendirme

Yapılan bu çalışmada da görüldüğü üzere, santral kurulmadan yaşanabilecek olası durumları santral kurulmadan görülmektedir. Oluşabilecek enerji kayıpları, santralin kurulduğu arazide bulunan (ev, ağaç vb.) nesnelerin santrale olan etkileri ve buna bağlı olarak yaşanan enerji kayıpları bu çalışmada verilmeye çalışılmaktadır.

Santral kurulmadan yapılan ölçümlerde yapılan yanlış hesaplamamlar ve ölçümler kullanılan bu program ile ortadan kalkmaktadır. Verilerin gerçek değerlere yakın olması açısından ölçümler uzun yıllar elde edilen değerlerin ortalaması alınarak yapılmaktadır. Manuel yapılan hesaplamalarda ise

ölçümler genellikle son birkaç yıla ait verilerden oluşmaktadır. Ayrıca enerji verimliliğinin belirlenmesi, üretimin hangi aylarda fazlalaştığı, amortisman süresinin kaç yıl olabileceği gibi önemli fizibilite parametreleri elde edilmiştir. Böyle bir çalışma, diğer güneş enerjisi santrallerine ve kurulum öncesi yapılan çalışmalara katkı sunacaktır.

Kaynaklar

1. Koryürek E (2008), Fotovoltaik Sistemlerin Binalarda Kullanımı, Yüksek Lisans Tezi (Yıldız Teknik Üniversitesi, Fen Bilimleri Enstitüsü).

2. Arslan E (2015), Güneş Enerjisi Potansiyelinin Bölgesel Analizi ve Enerji Üretim Sistemlerine Uyarlanması, Yüksek Lisans Tezi (Gazi Üniversitesi, Fen Bilimleri Enstitüsü).

3. Yilmaz S., Ozcalik H.R., Dincer F.: "Assessment and analysis on numerical and experimental performance of the photovoltaic systems for Germany and Turkey", Journal of Renewable and Sustainable Energy, 7, pp. 053114, 2015.

4. Kesler S., Kivrak S., Dincer F., Rustemli S., Karaaslan M., Unal E., Erdiven U.: "The Analysis of PV Power Potential and System Installation in Manavgat, Turkey-A Case Study in Winter Season", Renewable and Sustainable Energy Reviews, 31, pp. 671-680, 2014.

5. Yilmaz S., Ozcalik H. R., Dogmus O., Dincer F., Akgol O., Karaaslan M.: "Design Of Two Axes Sun Tracking Controller With Analytically Solar Radiation Calculations", Renewable and Sustainable Energy Reviews, 43, pp. 997-1005, 2015.

6. Dünya Enerji Konseyi Türk Milli Komitesi, Dünya'da ve Türkiye'de Güneş Enerjisi, < http://www.dektmk.org.tr/upresimler/GUNES.pdf>, erişim: 30 Aralık 2016.

7. Türkiye'nin Güneş Enerjisi Potansiyeli Atlası, <http://www.enerjiatlasi.com/gunes-enerjisi-haritasi/turkiye>, erişim: 10 Ocak 2017.

8. Google Haritalar, https://maps.google.com/, erişim: 15 Ocak 2017.

9. Ekinci M. (2015), Taşınabilir Güneş Takip Sistemli Pv Panel Dizaynı ve Uygulaması, Yüksek Lisans Tezi (Erciyes Üniversitesi, Fen Bilimleri Enstitüsü).

10. Beyit O. Dervişoğulları Ş. (2013), Güneş Pilleri ve Güneş Enerji Sistemleri, Elektrik Mühendisleri Odası Bilim Dergisi 23-09, sayfa 50-59.

11. Altıntaş A. (2012), Dünyada Yenilenebilir Enerji Kaynaklarından Güneş Enerjisinin Elektrik Üretimi Açısından Ekonomik Etkileri: Avrupa Birliği Ve Türkiye Uygulamaları, Doktora Tezi, (İstanbul Üniversitesi, Sosyal Bilimler Enstitüsü).

12. Solar Türk 2015-1 (2015), Hitit Serisi, <http://www.solarturk.com.tr/uploads/377/HTT-SERS-2015-1.pdf>, erişim: 30 Aralık 2016.

13. Ünlü M, Çamur S, Arifoğlu B, 'Fotovoltaik Enerji Dönüşüm Sistemlerinde Parçalı Gölgelenme Durum Analizi' Kaynak Elektrik Enerji, Elektrik, Aydınlatma, Elektronik ve Otomasyon Mühendisliği Dergisi, 314, 83-87.

14. Bahtiyar B. (2006), Fotovoltaik Sistemler İçin Gerçek Zamanlı Bir İzleme Merkezi Tasarımı ve Uygulaması, Yüksek Lisans Tezi (Muğla Üniversitesi, Fen Bilimleri Enstitüsü).

15. Grid-connected photovoltaic power systems: survey of inverter and related protection equipments, International Energy Agency, Report IEA PVPS T5-05:2002.

CHAPTER

9

RESEARCH IN NATURAL AND ENGINEERING SCIENCES

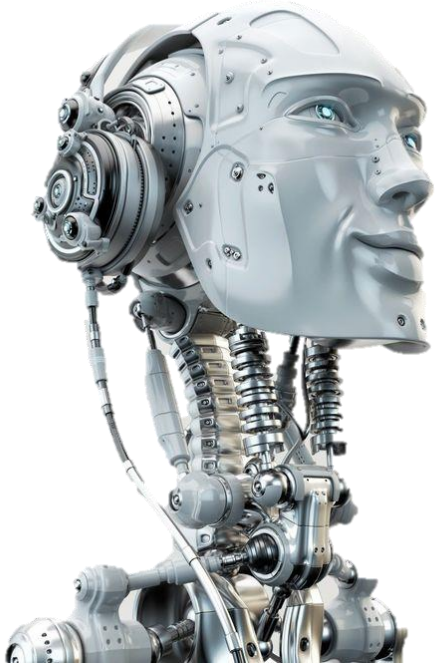

Warp Drive and the Kardashev Scale: Our Competence of Travelling Faster than Light (Emir Haliki)

Warp Drive and the Kardashev Scale: Our Competence of Travelling Faster than Light

Emir Haliki
Ege Üniversitesi Fen Fakültesi Fizik Bölümü, E-mail:emir.haliki@ege.edu.tr

1. Introduction

One of the common sense tells us the speed of light is not a limit needed to be exceeded to explore the universe in which we live, or to take over space journeys. Of course, it is enough to reach a speed of a few hundred kilometers per second to turn our solar system into our playground, and the mankind is in a position to do so in a near future. Likewise, there would not be a problem in reaching percentages very close to the speed of light in order to go distant stars. This would also not be a problem for the crew of the spacecraft due to the time dilation. Unless they think of going back.

If it is not desired to be an advanced civilization whose individuals reside in different states of spacetime, and if it is desired to have synchronized communication between those individuals apart from each other in very large distances, the speed of light must be exceeded, albeit indirectly. Despite the dimensions of space and greatness of distances, many physicists dream of travelling faster than light for a long time. A real solution of the Einstein's theory of general relativity allow this hyper-fast travel. Therefore, in 1994, Alcubierre constructed a warp field, which is based on some real physics, by manipulating the Einstein's field equations in the mathematical language of general relativity **[1]**. Alcubierre's manipulation was a purely geometric one and his equations were mathematically consistent solutions of field equations. All these theoretical processes gave birth to the concept of the warp drive.

The basic notion of the warp drive is actually straight forward. By various proposed definitions, a spacecraft could create a warp bubble around itself where in front of it, space could all shrunk down, and behind it, could expand (Figure 1). Also, the idea of warp drive does not contradict the principle of cosmic speed limit. The cosmic speed limit only applies to objects traveling within space, not the movement of space itself. Then the space could move at any speed. According to the general relativity there is no limit on the relative speeds of two separate patches of spacetime. For instance, very distant galaxies are moving apart faster than light. Besides, beyond the event horizons of black holes particles break the cosmic speed limit.

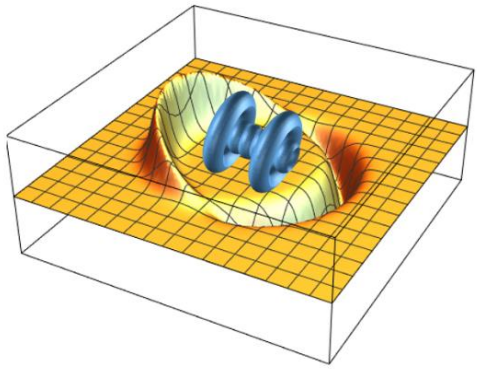

Figure 1: A possible structure of a warp drive. The spatial region, which is shown in a deformed 2D plane, contracts in front of the spacecraft (front border of the bubble) and expands behind it.

Alcubierre figured out a geometry that could fold space in such a way that a ship could not move in its frame of reference, but the space that it was resting on, would travel. This type of hyper-fast travel would be very handy for a high-tech civilization since it not only allows the spacecraft to go faster than light, but also to accelerate and decelerate from those effective speeds without damaging the spacecraft and its crew. Physics tells us that if some non-clarified problems turn out to be clarified, it is possible to build a warp engine, building block to allow a jump through interstellar or intergalactic space in relatively short time scales.

By using the 3+1 formalism of general relativity, spacetime could be described by a foliation of hypersurfaces of coordinate time t. General form of the spacetime metric could be defined as follows:

$$ds^2 = -(\alpha^2 - \beta_i\beta^i)dt^2 + 2\beta_i dx^i dt + \gamma_{ij}dx^i dx^j \quad (1)$$

where α is the lapse function giving the interval of proper time between hypersurfaces, β^i is the shift vector relating coordinates on different hypersurfaces and γ_{ij} is a metric on each hypersurface. Assuming the spacecraft moves along the x axis, a metric to push the spacecraft in a trajectory could be described by an arbitrary function, $x_s(t)$. Particularly, a metric having this property could be given by ($G = c = 1$):

$$\alpha = 1, \quad (2)$$

$$\beta^x = -v_s(t)f\big(r_s(t)\big), \quad (3)$$

$$\beta^y = \beta^z = 0, \quad (4)$$

$$\gamma_{ij} = \delta_{ij}, \tag{5}$$

where

$$v_s(t) = \frac{dx_s(t)}{dt}, \tag{6}$$

$$r_s(t) = \left[\left(x - x_s(t)\right)^2 + y^2 + z^2\right]^{1/2} \tag{7}$$

and

$$f(r_s) = \frac{\tanh(\sigma(r_s + R)) - \tanh(\sigma(r_s - R))}{2\tanh(\sigma R)}. \tag{8}$$

Here $R > 0$ and $\sigma > 0$ are arbitrary parameters. With the above equations, metric in the eq. (1) could be rewritten as follows:

$$ds^2 = -dt^2 + (dx - v_s f(r_s)dt)^2 + dy^2 + dz^2. \tag{9}$$

By the metric in eq. (9), Alcubierre stated that it would not be very difficult to build a spacetime even though it is globally hyperbolic and contains no closed causal curves. Moreover, the trajectory of the warp drive is a time-like curve regardless of the value $V_s(t)$. When the metric is rearranged by substituting $x_s(t)$ for x, one could see

$$d\tau = dt. \tag{10}$$

The proper time is equal to coordinate time, meaning that there would not be any time dilation. In such a situation, the absence of time dilation effects could make space journeys like trips on our planet.

2. Journey Speed and Thermodynamics

When a warp drive reaches luminal velocities horizons could also begin to develop. This would be a problem for controlling the speed of the spacecraft. If the warp bubble causally disconnected from the spacecraft, then the crew's frame could not turn off or control the bubble to reduce the spacecraft's velocity. In order to explore the superluminal control problem of the warp drive, it would be necessary to write a two-dimensional ESAA (Ex Somnium Ad Astra, which means "From a dream to the stars") metric in Alcubierre formalism **[2]**. The equation of this metric is as follows:

$$ds^2 = -A^2dt^2 + (dx - v_s f(r_s)dt)^2. \quad (11)$$

where $dx = dx' + v_s dt$. By writing $1 - f(r_s) = S(r_s)$, one could write

$$ds^2 = \left[A^2 - \left(v_s S(r_s)\right)^2\right]dt^2 - 2v_s S(r_s)dx'dt - dx'^2. \quad (12)$$

The parameter A defined as a Pfenning-Piecewise style function **[3]**, which could resolve the superluminal problem of the warp drive. Parameter A does not change its behavior when the bubble so as the spacecraft passes from subluminal to superluminal speeds. Even though the source for the nature of A still arguable, its final form could be written as follows:

$$A = \left\{\frac{1 + \tanh[\sigma(r_s - R)]^2}{2}\right\}^{2/\Delta}. \quad (13)$$

where $\Delta = \frac{2}{\sigma}$.

In 2007, Gonzalez-Diaz **[4]** derived the thermodynamic properties of the warp drive and show that the temperature of the spacecraft inside the bubble rises up as its apparent velocity increases. The study extended the state metric to a three-dimensional hyperboloid. By a propagator formalism, a thermal bath filling the spacecraft's bubble at a temperature which was zero at the luminal limit (c) and increased with the warp drive's velocity. Any spacecraft having a warp engine would be filled with a thermal bath of radiation at temperature

$$T = \frac{\sigma}{2\pi \coth^{-1}(v_0)}. \quad (14)$$

The above equation could be interpreted as the crew would measure the isotropic background of the warp drive as the motion of thermal radiation within the spacecraft accelerates at a rising temperature. Because all geodesics must be equivalent inside the spacecraft, any other crew would detect an isotropic bath at the same temperature, even if it is moving relative to the first ones. Finally, to interpret the result of increasing temperature at increasing speeds, the thermal bath temperature depends on the square root of the cosmological constant, which is similar to the opposite of radius of the event horizon. As it is understood, that study reviewed the spacetime of such a construct and extended it to contain a black hole inside the warp bubble. Similar to the black hole's shrinking of space, some phenomenological objects may be needed for space to expand. These theoretical objects, called white holes, suggest the notions of negative mass and negative energy,

although their existence is not proven. The negative mass matter is a type of hypothetical exotic matter where physical properties violate the known laws of physics.

3. Negative Energy

Leaving aside the black hole and white hole ideas within the warp drive, space is a stiff fabric due to the order of the equation $c^4/(8\pi G)$, which is a very large number. To make the warpage locally around a war drive requires a lot of mass or its energy equivalent ($E = mc^2$). Also, this mass must be densely concentrated around the spacecraft. Since gravity shrinks the spacetime, there must be one more quantity that should expand it. Thus, the space expanding mass at the back of the bubble must be negative. One needs anti-gravity ($-E = -mc^2$) in order to do such an expansion. The problem is negative mass matter is not known to exist and may not even be. There is not a known distribution of energy that could produce anti-gravity or negative mass. However, none of them are forbidden in Einstein field equations.

Our civilization could create a negative pressure on quantum scales via Casimir effect. Two conducting plates are brought very close together (10 nm or so). Then, a certain proportion of the virtual particle frequencies between them are excluded. Because not all frequencies would fit between the 10 nm space. All frequencies would fit outside the plates, causing the outer pressure is being greater than the inner one. This causes a physical attraction between plates bringing them together. The thought was if the total vacuum energy is zero, then the energy between the plates must be negative. But while the energy between plates is less than the vacuum energy, it is not negative, still positive. As another example for the behavior of negative energy, quantum optics researchers have created some special states of fields where destructive quantum interference suppresses the vacuum fluctuations. These vacuum states are called squeezed states which seems to involve negative energy. More precisely, those squeezed states are associated with regions of alternating negative and positive energy. Like a doubling event, squeezing the vacuum creates some negative energy at the price of extra positive energy. Also, the total averaged energy over the space remains positive. One could say about the Casimir effect and the squeezed states, only some indirect effects of negative energy have been measured **[5]**.

Some evidences of the existence of negative energy may also be encountered in nature alongside with theoretical calculations. The Hawking radiation allows black holes to come into thermal equilibrium in their environment. Event horizon is a one-way path through which energy could only flow in. In this case, the reason a black hole could give energy to the outside must be the presence of the negative energy accompanying positive energy with flowing into the black hole, due to the conservation of energy.

The negative energy would be produced by spacetime curvature near the event horizon, disturbing vacuum fluctuations. Therefore, the unification of thermodynamics and black hole physics require the existence of negative energy. Also, the black hole is not the only thing where negative energy seems to play a role. There is the concept of wormhole, which is a hypothetical type of tunnel connecting two different regions of space (Figure 2). Wormholes may exist on the very finest length scales. They may be bubbling in and out of existence like virtual particles. However, as the universe expanded, it is quite possible that some of them also expanded to much larger dimensions. The predicted Einstein-Rosen wormholes might be impractical for travel because they may collapse very quickly. However, more recent researches have found that if a wormhole contains enough exotic matter that allows it to remain open without collapse, it could remain unchanged for a long time. If a wormhole is made up of enough exotic material - whether naturally formed or artificially added - it could theoretically be used as a method of traveling or sending information across space. On the other hand, adding exotic matter to a wormhole could make it so stable that a spacecraft could safely pass through it. But the question is where are exotic matter with negative mass and how to find it. Otherwise, it may not even be possible to create negative energy densities on large enough scales.

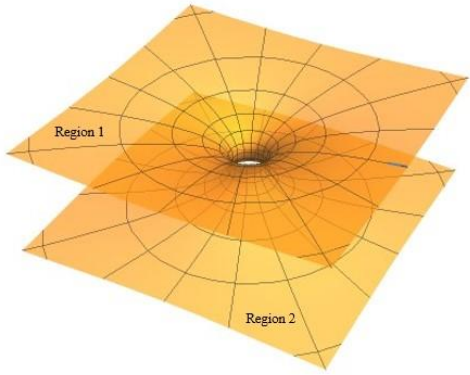

Figure 2**:** A demonstration of a wormhole connecting two different regions of space. It is shown here by bending a two-dimensional space in three dimensions. As a three-dimensional space bends in four dimensions, a wormhole's visual projection from our perspective is thought to be spherical.

The similarities between the working principle of wormholes and warp drive also take us to the same point. How much energy is needed for a warp engine, so that we could compensate for it with negative mass that could be produced in very small numbers anyway. Alcubierre's formalism of the warp drive suffered from a problem that also plagues wormholes. It violates weak, strong and dominant energy conditions (WEC, SEC and DEC respectively)

of general relativity. Particularly, WEC violations originate from vacuum fluctuations of quantum fields. They subject to an uncertainty principle. If an inertial observer measures the energy density $\hat{p}$, which is averaged over a sampling time τ_0, then it could be written as:

$$\hat{p}{\tau_0}^4 \geq -\frac{3}{32\pi^2}\frac{\hbar}{c^3}. \tag{15}$$

Here τ_0 is very smaller than the spacetime's local curvature radius, divided by c. By considering $\frac{\hbar}{c^3} \sim 3 \times 10^{60} \frac{\mathrm{J}}{\mathrm{m}^3}\mathrm{s}^4$ and the fourth power of τ_0, there is a restriction.

In the manner of this quantum inequality, wall of the warp bubble should not be thicker than $100\ \mathrm{l_p}$ (Planck lengths) for velocities in the order of c **[6]**. The calculated total energy of a macroscopic warp bubble is given by:

$$E = -\frac{1}{12}v^2\frac{c^2}{G}\frac{r^2}{\Delta}, \tag{16}$$

where r is the bubble's radius, Δ is the wall thickness and v is the apparent velocity of the warp drive. Finally, for a bubble with a wall thickness of $100\ \mathrm{l_p}$, a radius of 100 m and $v = c$:

$$E \sim -10^{63}\ \mathrm{kg} \times c^2, \tag{17}$$

which is a serious problem. 10^{63} is approximately ten orders of magnitude larger than the energy of the entire visible universe **[7]**.

Recent works on bubble geometry get the negative mass/energy requirement down to the equivalent of the moon or even an asteroid. Rapidly oscillating the warp field hypothetically soften the fabric of space via higher dimensional effects. This could drastically decrease the mass requirement to several hundred kilograms **[8]**. Additionally, according to some field equation solutions, one could even shrink down the warp bubble while expanding the internal volume, decreasing the negative mass need to miligrams. Theoretically, if the bubble is small enough, then one may not even need actual exotic matter. Quantum scale manipulation of the vacuum energy may be enough. But these are theories that have not yet been validated.

4. Benefits and Problems

One could list the benefits of warp drive as follows:

- Faster than light (FTL) travel: The interstellar or even intergalactic distance barrier would no longer be a restriction of space travels. This would also be effective for up close observing astrophysical

phenomena.

- Conventional transport: There would be no tearing of spacetime fabric like wormholes. Warp drive is a simple transport through space from origin to destination.
- No time dilation effects: Special relativity does not play a role in this type of motion scheme. Spacecrafts with warp engines move at subluminal speeds inside the bubble.
- No relativistic mass increase: Spacecraft rest at the center of the bubble and the bubble also rest with respect to space.
- No rocket propulsion needed: Since there is an increase in mass at relativistic speeds, thrust could reach very high amounts while accelerating. In warp drive, these speeds are not considered.
- Technology and economy: Conventional FTL travels would bring about a serious technological leap in a civilization. Economic development would also follow.

However, there are a bunch of problems:

- Realizable metric: Could the metric of the warp drive be macroscopically realized in reality? Required shape functions require complex disturbance of the geometry of space.
- Violation of energy: The exotic matter and its result, the negative energy is a violation of general relativity energy conditions. For instance, WEC states that the energy density should be non-negative due to an observer's frame.
- Drastic energy requirements: Warp drive requires very large amounts of negative energy, which is required from the quantum field.
- Energy source: Negative energy sources are unknown. It is not restricted in quantum mechanics, but restricted in classical physics.
- Quantum instability: When the warp drive reach superluminal speeds, a negative energy related vacuum stress-energy tensor of a quantized scalar field would diverge to infinite energy.
- Conservation of energy: Any warp engine powering source must apparently produce a lot more energy than has gone into to create it.
- Second law of thermodynamics: Any amount of negative energy would produce a larger amount of positive energy without an external input, violating the second law.
- Stability and control: It is not yet clear how negative energy could be controlled and stabilized.
- Black hole: Fundamentals of quantum fields could produce negative energy. But, any failure to control extreme field density would create a singularity.

- Conservation of momentum: As opposed to rocket motion, warp drive would be moving on spacetime itself. Whether spacetime could form a reaction mass is unknown.
- Quantum inequalities: Validity of the positive energy constraint by quantum inequality principle might also involve negative energy.
- Warp bubble thickness: The energy density of a $100\,l_p$ thick wall would even exceed nuclear density. No electromagnetic radiation like radio signals could get out of the bubble.
- Collision with space debris: Rock and dust that approach the forward end of the warp bubble would experience huge amount of compression, causing them to explode.
- Blue-shift: Photons that approach the forward end of the warp bubble would definitely be blue-shifted. They could create harmful radiation to the spacecraft and its crew.
- Energy distribution at superluminal speeds: A warp drive must distribute the negative energy source ahead of it. But if the bubble is superluminal, then a paradox occurs.
- Causal disconnection: Warp bubble and external negative energy region would disconnect. Then, negative energy could not be controlled.
- Tidal forces: There would be enormous tidal forces between the interior and the exterior of the warp bubble, due to the extreme warpage of spacetime.

Also, there are some minor issues. Regardless of the time dilation, any FTL travel could be used as a time machine which contradicts the chronology protection conjecture. Hawking stated that quantum mechanics would always stop causality-breaking actions **[9]**. Alongside with that, the extreme spacetime curvature of the warp bubble walls would destroy the interior with a high amount of Hawking radiation. Moreover, assuming that one could even produce negative mass matter, some of it would need to go outside the warp bubble, which means it gets left behind. Laying down the external negative energy conditions along the path one leave, like a warp highway, could be the solution but without time efficiency. Because the highway building trip has to be made at sub light speed. All the benefits and problems mentioned here could arise with the production of a suitable warp engine **[10]**. However, as it is seen, most of the problems are also related to negative mass, and one of the biggest problem is its amount. At this point, we would proceed with a model developed by Harold White and his team **[8]** in which the negative mass requirement of warp drive is 700 kg. $700c^2$ is still a very big number. But the previous energy requirement in eq. (17) has been drastically reduced. Assuming that negative energy could be produced, when the mankind would be able to produce this amount of energy? In order to

estimate that, one need to know the aspects of the famous Kardashev Scale. Then

5. Kardashev Scale and Space Travel

Nikolai Kardashev categorized the possible civilizations in the universe into various types according to their amount of energy consumption rates in the Kardashev Scale, which is written in 1964 **[11]**. This scale defines the civilization levels as numerical values of energy consumption rates, $4 \times 10^{19} \mathrm{erg\,s^{-1}}$ for Type-I, $4 \times 10^{33} \mathrm{erg\,s^{-1}}$ for Type-II and $4 \times 10^{44} \mathrm{erg\,s^{-1}}$ for Type-III. Type-I civilizations are considered planetary, Type-II as stellar and Type-III as galactic. Extension of that scale is also described in other various types. But they may have energy harnessing technologies far beyond what we could ever imagine within our basic science and engineering knowledge **[12]**. A formula for civilization levels is given as follows:

$$K = \frac{\log_{10} P - 6}{10} \tag{18}$$

where P is the energy consumption rate in Watts. According to this formula, a Type-0 civilization would consume 1 MW of energy, and mankind's rating in 1973 was about 10 TW, meaning Type-0.7. The last measured approximate result (17.54 TW) was in 2012, which means a value of 0.724 between Type-0 and Type-I. As one could see, even in order to become a planetary civilization, our civilization have a bit way to go. But, based on the consumption rate of energy corresponding to 700 kg per second, which is 2.1×10^{11} W, the civilization level needed to build a warp engine is 0.53. In other words, we are able to meet the amount of power. The graph of the Kardashev Scale and the value of the power required for warp drive is shown in figure 3.

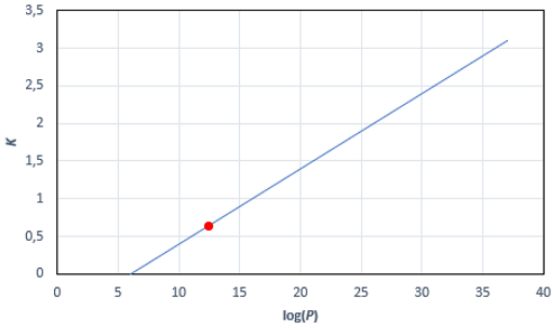

Figure 3: The behavior of energy consumption rates on the Kardashev scale versus civilization levels. The red dot here corresponds to the required power value for the warp engine. Mankind could be considered near Type-I.

As it is seen from the graph above, our civilization is above the minimum energy consumption rate required to make a warp drive. So we don't even need to be a Type-I civilization to be able to manufacture a spacecraft with a warp engine. However, this calculation is originated from the theoretically reduced energy requirement of White **[8]**. The handicap in this matter is not the amount of energy but the type of it.

How long would it take to reach nearby stars and even galaxies if traveling with a warp drive? A suitable calculation method could be expressed as follows **[13]**. One could consider two destinations A and B, which are apart from each other in Euclidean spacetime. A spacecraft with a warp engine starts its propulsion from A with a velocity $v < c$. At a distance d ($d \ll D$), spacecraft starts to create its warp bubble. The acceleration of the warp bubble would be $\boldsymbol{a}$ at the halfway. Then, at the other half of the journey, bubble is controlled so as to invert the acceleration from $\boldsymbol{a}$ to $-\boldsymbol{a}$. As the absolute values of $\boldsymbol{a}$ and $-\boldsymbol{a}$ are assumed equal, the warp drive would be at rest at a distance d away from destination B. The journey finally completed at a speed $v < c$. Total coordinate time of the journey is

$$T = t_{\text{self-propulsion}} + t_{\text{bubble}}. \tag{19}$$

Considering the acceleration constant along the distance $D - 2d$, it could be written:

$$t_{\text{bubble}}{}^2 = \frac{2(D-2d)}{\boldsymbol{a}}. \tag{20}$$

By taking $t_{\text{self-propulsion}} = d/v$,

$$T = 2\left(\frac{d}{v} + \sqrt{\frac{(D-2d)}{2\boldsymbol{a}}}\right). \tag{21}$$

Since both destinations remain in flat space, $T = \tau$. The proper time measured on the warp drive would be:

$$\tau = 2\left(\frac{d}{\gamma v} + \sqrt{\frac{(D-2d)}{2\boldsymbol{a}}}\right), \tag{22}$$

where γ is the Lorentz factor. If the bubble radius r satisfies $r \ll d \ll D$, one could see the approximation

$$T \approx \tau \approx \sqrt{\frac{2D}{\boldsymbol{a}}}. \tag{23}$$

The magnitudes of time that the warp drive would spend on interstellar travels are shown in figure 4 with a weighted network model. Here, each stellar journey direction arrow (edge) is weighted according to the time spent. Similarly, a weighted network model for intergalactic travel is illustrated in figure 5. Note that, since a warp drive could move at different speeds and accelerations, in all graphs, a fixed value $\boldsymbol{a}$ has been chosen and edge weights have been determined according to the distances between destinations. Weights of the edges also indicates the ratio of power needed to accomplish the travels.

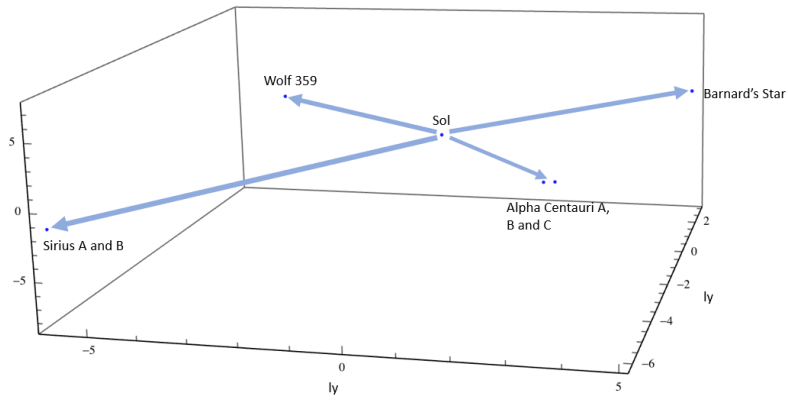

Figure 4: Warp drive's hyper-fast travel in our stellar neighborhood. Edge weights are not much different from each other. Because there are no big differences between the distances. Still, it takes one and a half times more time to navigate the Sirius system than the Alpha Centauri system.

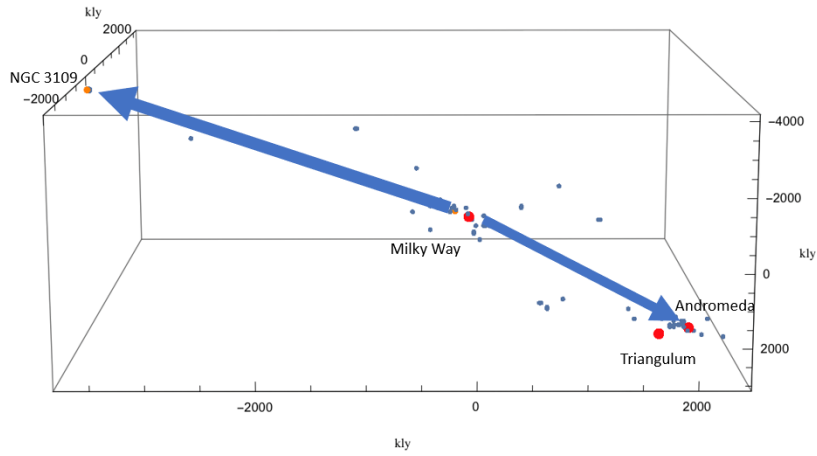

Figure 5: Warp drive's hyper-fast travel in our galactic neighborhood (Only Andromeda and NGC 3109 destinations have been shown). Although the edges here are drawn to one tenth of the scale of the interstellar edges, they are still much thicker than interstellar ones.

6. Conclusion

If our civilization would come up with negative mass and do not need whole planets' masses, if it turns out we would keep the warp field stable and either there is no Hawking Radiation burning the warp drive and the crew, and if we could build one without the need to pre-position mass or at least without needing another FTL spacecraft to preposition it, then we may finally have a working warp drive. Of course we really don't know how much energy it takes to make a new piece of space since theory and evidence on vacuum energy slightly mismatch. The difference is like 100 orders of magnitude, and this has indicated the vacuum catastrophe which is one of the worst theoretical predictions in the history of physics. Still, at a strictly theoretical level, it ought to be possible to artificially create or delete pieces of space. We are able to contract space, where gravity does that all the time, and if negative mass or energy exists we could expand it also. Although we don't have an evidence indicating the negative mass does exist, we do have better indications that negative energy behavior does. Therefore, the ability to contract and expand space, and thus construct a warp bubble does seem like it might really be on the future plans of mankind. Although, Alcubierre tended to require an amount of negative mass like those of enormous objects or even more, newer calculations have indicated we might be able to do it with even several hundred kilograms. If we would get our warp bubble even in primitive conditions, there would be a good reason to think it might really be possible.

It is possible that our civilization would reach the stars with sub light speed spacecrafts or probes long before we construct a warp drive. Because, even the Kugelblitz drive, which create black holes made of light to power spacecrafts, seems to have fewer problems than the warp drive. We need to solve all the problems to motivate the monumental advancements needed to build the very first one. There is one more thing giving us hope about the warp drive. The dark energy, which behaves like anti-gravity (and the negative energy), making the expansion of space is the main thing in order to succeed in hyper-fast travel.

References

1) Alcubierre, M. (1994). The warp drive: hyper-fast travel within general relativity. Classical and Quantum Gravity, 11(5), L73.

2) Loup, F., Held, R., Waite, D., Halerewicz Jr, E., Stabno, M., Kuntzman, M., & Sims, R. (2002). A causally connected superluminal Warp Drive spacetime. arXiv preprint gr-qc/0202021.

3) Pfenning, M. J., & Ford, L. H. (1998). Quantum inequality restrictions on negative energy densities in curved spacetimes. arXiv preprint gr-qc/9805037.

4) González-Diaz, P. F. (2007). Superluminal warp drive. Physics Letters B, 653(2007) 129-133.

5) Ford, L. H., & Roman, T. A. (2000). Negative energy, wormholes and warp drive. Scientific American, 282(1), 46-53.

6) Pfenning, M. J., & Ford, L. H. (1997). The unphysical nature of warp drive'. Classical and Quantum Gravity, 14(7), 1743.

7) Van Den Broeck, C. (2000, January). Alcubierre's warp drive: Problems and prospects. In AIP Conference Proceedings (Vol. 504, No. 1, pp. 1105-1110). American Institute of Physics.

8) White, H. (2013). Warp field mechanics 101. Journal of the British Interplanetary Society, 66, 242-247.

9) Hawking, S. W. (1992). Chronology protection conjecture. Physical Review D, 46(2), 603.

10) Long, K. F. (2008). The status of the warp drive. Journal of the British Interplanetary Society, 61(9), 347-352.

11) Kardashev, N. S. (1964). Transmission of information by extraterrestrial civilizations. Soviet Astronomy, 8, 217.

12) Benjamin, G. (2016). Type IV culture or, is it possible to define a framework for universal creativity? Digital Creativity, 27, 24-36.

13) Marquet, P. (2009). The generalized warp drive concept in the EGR theory. The Abraham Zelmanov Journal, 2, 261-287.

CHAPTER

10

RESEARCH IN NATURAL AND ENGINEERING SCIENCES

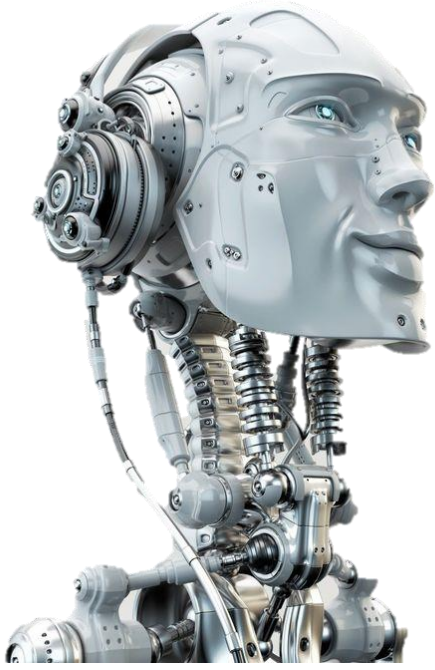

Moleküler Biyolojide Kullanılan Nanopartikül Türleri

(Yeşim Dağlıoğlu, Betül Yılmaz Öztürk)

Moleküler Biyolojide Kullanılan Nanopartikül Türleri

Yeşim DAĞLIOĞLU [1], Betül YILMAZ ÖZTÜRK[2]

[1]Ordu üniversitesi, Moleküler Biyoloji ve Genetik, E-mail:yozkan52@gmail.com
[2]Eskişehir Osmangazi üniversitesi, Merkezi Araştırma Laboratuvarı Uygulama ve Araştırma Merkezi Central (ARUM), E mail: byozturk@ogu.edu.tr.

1.Giriş

Nanopartiküller (NP'ler), hızla gelişen nanoteknoloji alanının öncüsü konumundadır. Eşsiz boyutlarına bağlı özellikleri, bu malzemeleri insan faaliyetlerinin birçok alanında üstün ve vazgeçilmez kılmıştır. Moleküler biyoloji ve uygulamaları için farklı boyut, şekil, kompozisyon ve işlevselliklere sahip birçok NP çeşidi vardır. Ayrıca, her bir NP türü için çok farklı üretim teknikleri mevcuttur. Örneğin, kimyasal buhar yoğunlaştırma, hidrojen redüksiyonu, asal gaz yoğunlaştırma gibi fiziksel ve kimyasal temelli üretimi yapılabildiği gibi son yıllarda daha popüler olan biyolojik yöntemlerle de sentezlenmektedir. Moleküler biyoloji uygulamalarına bağlı olarak (örn. tanı, görüntüleme veya tedavi amaçlı) bazıları birden fazla amaç için kullanılan farklı NP tipleri vardır[1-4]. Bu bölümde, hücre, moleküler biyoloji, biyomedikal ve biyoteknolojide yoğun bir şekilde kullanılan NP türleri gruplandırılıp alt başlıklara ayrılarak biyomedikal araştırmalarla ilgili temel özellikleri ve işlevleri tartışılacaktır.

1.1.Miseller

Miseller, polimerler veya lipitler gibi amfifilik moleküllerden yapılan nanoyapılardır[5]. Sulu ortamlara maruz kaldıklarında, hidrofobik gruplarını yapı içinde saklarlar ve hidrofilik gruplarını açığa çıkarırlar. Öte yandan, lipit açısından zengin ortamlarda, yapıları ters bir şekilde düzenlenebilir. Suda çözünürlükleri yetersiz olan ilaçlar, misellerin hidrofobik çekirdeğine yüklenebilir, amfifilik ilaçlar ise misel hidrofilik grupların ilaç polar grupları ile misel amfifilik yapı ile düzenlenebilir. Miseller, amfifilik blok kopolimerlerin sulu çözeltilerinde kendiliğinden oluşur ve çekirdek-kabuk yapılarına sahiptir. Daha kapsamlı çalışmalara ihtiyaç duyulmakla beraber, blok kopolimerleri (Pluronics) ve TAT-poli (etilen glikol)-blok-kolesterolü olan polimerik miseller, beynin onarımını veya rejenerasyonunu desteklemeyi amaçlayan ilaçların iletilmesi için yeni yollar açabileceği düşünülmektedir. Bu sistemler çekirdeklerinde büyük miktarlarda ilacı bozunmadan koruyabilirken kimyasal bileşimi, boyutu ve morfolojisi kolaylıkla değiştirilebilir. Polimerik misellerin yüzeyi ayrıca kan-beyin bariyerini geçebilecek şekilde işlevseleştirilebilir. Belki de en önemlisi, bu materyallerle kullanılabilen terapötik moleküller, proteinler, oligonükleotidler ve görüntüleme ajanları oldukça çeşitlidir[5].

1.2.Dendrimer

Birinci dereceden alt konu başlığı 10 punto ile yazılmalıdır. Bununla beraber her kelimenin ilk harfi büyük diğerleri küçük olmalıdır ve alt konu başlığı kalın olacak şekilde yazılmalıdır. Dendrimerler iyi tanımlanmış bir şekle, büyüklüğe (2–20 nm) ve dar polidispersiteye sahiptir. Hücrelerin içine ve dışına kolayca taşınırlar. Yüzey fonksiyonel grupları, çoklu ilaç moleküllerinin yüzeye bağlanmasını sağlar. Tipik doğrusal polimerler ile karşılaştırıldığında, yüzey fonksiyonel grupları, çoklu ilaç moleküllerinin, yüksek ilaç yükü sağlayan yüzeye bağlanmasını sağlar[6-7]. Yüzey fonksiyonel gruplar, çoklu görüntüleme parçalarının, ilaçların ve ligandların bağlanmasını sağlaması bakımından son derece uygundur. Polyamidoamin (PAMAM) dendrimerler, yüzey işlevselliğine bağlı olarak farklı hücre giriş yollarına sahip olabilirler. Anyonik PAMAM dendrimerler esas olarak bir kaveol aracılı süreç boyunca endositozlanırken, nötr ve katyonik dendrimerlerin hücrelerde klatrin aracılı internalizasyonu takip ettiği bildirilmiştir[6,8]. Bu hücresel içselleştirme işlemleri, kornea ve retinadaki epitelyal ve retinal bariyerlerin geçişinde oldukça faydalı olabilir. Ayrıca, dendrimerlerin yüzey modifikasyonlarının, dendrimerlerin biyolojik zarlarla çok değerlikli etkileşimlerini arttırdığı, böylece hücresel içselleştirme sürecini ve hücre giriş kinetiklerini geliştirdiği bildirilmiştir[6];[9-10].

1.3.Lipit temelli nanopartiküller/Lipozomlar

İlk NP türü lipozomlardır. Lipozomlar, 1965 yılında hücresel zarların bir modeli olarak keşfedilmiş ve son on yılda yaygın olarak çalışılan geleneksel lipid bazlı formülasyon modelleri olmuştur[11-13]. Lipozomlar, sulu sistemlerde kendiliğinden toplanan/agregat oluşturan tek veya çok katmanlı lipit yapıları içeren küresel keseciklerdir[14]. Lipozom, iki tabakalı zarla çevrelenmiş sulu bir iç boşluk ile küresel bir kesecik olarak tanımlanır. Son yıllarda dermatolojik, ilaç ve kozmetik çalışmaları için araştırılmışlardır. Lipozomlar, ilacın enzim bozulmasına karşı korunması, düşük toksisite, esneklik, biyouyumluluk, tamamen biyo-bozunabilirlik ve immünojenik olma gibi farmasötik taşıyıcı olarak benzersiz avantajlara sahiptir[13];[15-17]. Bu avantajları, biyolojik araştırmalarda hücrelere genetik materyalin (lipofeksiyon) transfeksiyonunda ajan olarak iyi karakterize edilmelerini ve geniş çaplı lipozom kullanımını sağlamıştır[18-19]. Lipofeksiyonda, genellikle anyonik genetik materyal ile agregat oluşturmak için katyonik lipit kullanılır. Lipozomların bir başka önemli uygulaması da terapötik taşıyıcılar olarak kullanılmalarıdır. Çünkü tasarımları, çift tabakalı lipitin kendi içinde bulunan hidrofilik bileşiklerin ve hidrofobik ilaçların içine girmesine izin verebilir[11]. Dolaşımlarını yarı ömürlerini ve *in vivo* stabilitelerini arttırmak için lipozomlar, polietilen glikol (PEG) gibi biyo-uyumlu polimerler ile konjuge edilmiştir[14]. Lipozomlar ayrıca, istenen hücreler içinde teşhis ve terapötik ajanların birikmesini arttırmak amacıyla hedefleme ligandları ile fonksiyonel

hale getirilebilir. Bugün, on iki tane klinik olarak onaylanmış lipozom bazlı terapötik ilaçlar bulunmaktadır[19]. Bununla birlikte, lipofeksiyon uygulamalarının birçoğu, kısa raf ömrü, zayıf stabilite, düşük kapsülleme etkinliği, retiküloendotelyal sistem (RES) tarafından hızlı bir şekilde uzaklaştırılması, hücre etkileşimleri veya adsorpsiyon ve intermembran transferi ile hızlı bir şekilde uzaklaştırması gibi bazı dezavantajlar nedeniyle sınırlıdır[20]. Lipozomlar, terapötiklerin bölgelere özel olarak iletilmesi için lipid nanopartiküllerin (LNPler) ayırt edici özelliği olmuştur[13]. Katı lipit nanopartiküller (KLNP'leri) ve nanoyapılı lipit taşıyıcılar (NLT'lar) iki ana tip lipid bazlı nanopartiküllerdir.

a. Katı lipit nanopartiküller (KLNP'ler)

1991 yılında üretilen katı lipit nanopartikülleri (KLNP'leri), emülsiyonlar, lipozomlar ile polimerik, mikro partiküller ve NP'ler gibi geleneksel kolloidal taşıyıcılara alternatif taşıyıcı sistem olarak ortaya çıkmıştır[21]. KLNP'ler ve nanoyapılı lipit taşıyıcılar (NLT'ler), doğal bileşenleri nedeniyle potansiyel olarak dikkat çekici ve pazarlanabilir özelliktedirler[22]. Küresel bir morfolojiye sahip olan bu KLNP'lerinin ortalama büyüklüğü 40 ila 1000 nm olup katı fazlı lipit ve yüzey aktif maddeleri içerirler[23].Dağılmış faz katı yağdır ve yüzey aktif maddeler emülgatör olarak kullanılır. KLNP'lerin lipit bileşenleri, hem vücutta hem de ortam sıcaklığında katıdır ve yüksek oranda saflaştırılmış trigliseritler, kompleks gliserit karışımları ve hatta mumlardan üretilebilir[13];[24-25]. Sürfaktanlar, stabiliteyi arttırmak için yaklaşık %0.5 ila %5'lik konsantrasyonlarda kullanılır. Lipitlerin ve yüzey aktif maddelerin doğru seçilmesi, partikül büyüklüğü ve ilaç yüklemesi gibi bu moleküllerin fizikokimyasal özelliklerini ve kalitesini etkileyebilir[26]. Lipozomlarla karşılaştırıldığında, ilaç stabilitesine ve uzun süreli salıma sahiptirler ve organik çözücülerin üretim aşamında kullanımından kaçınılmasından dolayı polimerik taşıyıcılardan daha güvenlidirler[13]. Bunun yanısıra büyük ölçeklerde üretilmesi büyük bir avantajdır. Kontrollü ilaç salımı ve ilaç hedefleme potansiyeli sayesinde KLNP'ler kolloidal taşıyıcılara nazaran oldukça önemli avantajlara sahiptirler. Bu avantajlardan bazıları şunlardır; ilaç stabilitesinin artması, yüksek ilaç yükü, lipofilik ve hidrofilik ilaçların dahil edilmesi, biyotoksitesinin olmayışı, organik çözücülerin kullanılmaması, büyük ölçekli üretimi ve sterilizasyon ile ilgili problemlerin giderilmesidir. Ayrıca, KLNP'leri, yüzey aktif maddelerle stabilize edilen katı lipit matrislerden oluşur. KLNP'lerin hazırlanması kolaydır, aynı zamanda düşük sitotoksisiteye ve iyi fiziksel stabiliteye sahiptirler. Bunun yanısıra kararsız ilaçları bozunmadan koruyabilirler ve kontrollü ilaç salımını sağlayabilirler [5];[27-28]. Gliomanın sıçan modellerinde yapılan bir çalışmada, beyin tümör tedavisinde birkaç antineoplastik ajanın iletilmesi için KLNP'lerin etkinliği, *in vitro* ve *in vivo* olarak, gösterilmiştir[32]. Bu

nanotaşıyıcı sistemler, atazanavir gibi HIV proteaz inhibitörleri de dâhil olmak üzere bir dizi başka bileşiğin beyin tarafından alımını arttırmak için kullanılmıştır[5];[29]. Ancak KLNP'lerin ortak dezavantajları, katı lipitin kristal yapısından kaynaklanan öngörülemeyen jelasyon eğilimi ve doğal düşük katılım oranlarıdır[30-31].

b. Nanoyapılı lipit taşıyıcılar (NLT'ler)

KLN kullanımında ortaya çıkabilecek muhtemel zorluklarının üstesinden gelebilmek için 1990'ların sonlarında KLN'lerin yeni jenerasyonu olarak nanoyapılı lipit taşıyıcılar (NLT'ler) sunulmuştur[33-34]. NLT'lar, stabiliteyi ve yükleme kapasitesini iyileştirirken depolama sırasında ilacın çıkmasını da önlemaktedir. NLT'ler, katı matrisin bileşimi tarafından KLN'lerden tespit edilebilir. NLT'ler lipit fazın ortam sıcaklığında hem katı (yağ) hem de sıvı (yağ) lipidleri içerdiği modifiye KLNlerdir[35]. Aslında NLT'ler, stabilite ve yükleme kapasitesini geliştiren, biçimsiz bir matris oluşturan katı ve sıvı fazın (yağ) bir karışımını sunan KLN'lerin değiştirilmiş jenerasyonlarıdır[36]. NLT'ler KLN'ler ile kontrast gösterir, bazı ilaçlar için daha fazla yükleme kapasitesi, dispersiyonda biraz daha az su, depolama sırasında ilacın çıkmasını önler veya en aza indirir, ancak KLN'lerin ve NLT'lerin biyotoksisitesi arasında önemli bir fark yoktur[36-39]. NLT'lerdeki lipit fazı, hem katı hem de sıvı lipidlerde oda ve ortam sıcaklığında bulunur[13];[37]. Biçimlendirilmemiş, kusurlu ve çoklu tipler olmak üzere üç tip NLT vardır[40]. KLN'ler ve NLT'ler, ilaçların parenteral, dermal, pulmoner ve bölgesel olarak iletilmesi için yararlı olan oldukça geniş özelliklere sahiptir. Bu ürünler, yüksek derecede güçlü ilaçların toksik yan etkilerini azaltmak ve tedavinin etkinliğini arttırmak için geliştirilmiştir. Bunun yanı sıra, gen transferi, kozmetik ve gıda endüstrisinde iyi bir potansiyel sunmuşlardır[41-43].

1.4.Karbon temelli nanopartiküller

Karbon nanotüpler (KNT'ler), çeşitli alanlarda çeşitli uygulamalar için çekici olduklarından, endüstriyel ölçeklerde kullanışlı ürünlere dönüştürülecek benzersiz özelliklere ve potansiyele sahiptir[44]. KNT'ler önemli elektriksel, kimyasal, termal, mekanik, optik ve yapısal özelliklerin olağanüstü kombinasyonunu sağlayan benzersiz yapıları içermektedir ve biyomedikal araştırmalarda bu nitelikleri büyük bir araştırma konusu olmuştur[45-46]. Ayrıca, metalik, yarı iletken ve süper iletken elektron taşıma özelliklerine sahiptirler. Diğer tüm materyallere kıyasla yüksek elastik modülleriyle de bilinmektedirler[45]. Son onbeş yılda biyomedikal alanda KNT'lerin uygulanması konusunda çok sayıda çalışma yapılmıştır[44];[47]. KNT'lerin, radyasyon onkolojisi, biyosensörler, problar ve kuantum noktaları, nanoakışkan sistemler, ilaç dağıtımı ve ilaç keşfi, nanosensör ve nanorobotlar gibi implante edilebilir biyomedikal cihazlar ile doku mühendisliği uygulamaları gibi biyofarmasötik uygulamalar da dahil olmak

üzere teşhis aletleri ve cihazları gibi birçok alanda kullanılabileceği gösterilmiştir[44;47-49]. KNT'lerin hücre ve biyomedikal uygulamalarda daha geniş çapta kullanılması için biyolojik özelliklerinin, davranışlarının ve performanslarının tam olarak anlaşılması gerekmektedir[50]. Büyük ölçeklerde üretildiğinde, KNT'ler iyi karakterize edilmiş biyolojik, çevresel ve güvenlik profillerine sahip olmalıdır. Bununla birlikte, KNT'ler kimyasal ajanlarının çoğunun aksine, her zaman iyi tanımlanmış bir yapıya ve saflığa sahip değildirler. KNTler, bunları sentezlemek için kullanılan preparasyon, saflaştırma ve fonksiyonelleştirme yöntemine dayanan büyüklük, morfoloji, yapı ve saflık bakımından önemli ölçüde farklılık gösterebilir[50]. Bu nedenle, KNT'ler ile biyolojik çevre arasındaki etkileşimi çok karmaşık ve bazen öngörülemez olmaktadır. Benzer şekilde, araştırmacılar KNT'lerin üretim yöntemlerine, yüzey-hacim oranına, şekline, konsantrasyona, en boy oranına, oksidasyonun kapsamına, bileşime, fonksiyonel gruplara ve uygulanan dozaja bağlı olarak farklı toksisite seviyeleri gösterebildiğini kaydetmişlerdir[1;51-53]. Bununla birlikte, KNT'lerin oldukça hidrofobik olması biyolojik uyumluluklarını azaltmada önemli bir rol oynar[54]. DNA ve hücre zarına da zarar verebilirler. Ayrıca oksidatif stres, mitokondriyal aktivite modifikasyonu, protein sentezi ve değiştirilmiş hücre içi metabolik yollarla toksisiteye neden olabilirler[53]. Sitotoksisiteye yol açan en yaygın KNT mekanizmaları nekroz ve apoptozdur[44;53].

KNT'ler, çeşitli biyomedikal uygulamalar için umut verici malzeme haline getiren sayısız benzersiz özelliğe sahiptirler. KNT'ler doğada hidrofobik olmasına rağmen, belirli uygulamalarla fonksiyonel hale getirilebilirler. Bu fonksiyonelleştirme tekniklerinin bir kısmı yararlı biyomedikal uygulamalara sahiptir. İşlevselleştirme kısımları, KNT'lere içselleştirmelerine rehberlik edebilecek hücre yüzeyi reseptörleri ile özel olarak etkileşime girecek şekilde sokulabilir. Bu reseptör aracılı hedefleme stratejileri, spesifik hücre yüklemesini kolaylaştırabilir, böylece tedavide ihtiyaç duyulan ilaçların miktarını azaltabilir. Ek olarak, bu stratejiler sistemik toksisite ve inflamasyonu en aza indirmede yardımcı olabilir[47]. KNT'lerin en yaygın kullanım alanları ilaç ve ilaç dağıtım sistemleridir. Birçok ilaç dağıtım sisteminde, çeşitli hastalıkların tedavisi için KNT'ler kullanılarak ilaçlar tasarlanmıştır. KNT-bazlı antikanser ilaçlar çok dikkat çekmiştir ve birçoğu temelde iki stratejiye dayanmaktadır. Birincisi, spesifik tümör reseptörleri ile fonksiyonelleştirme yoluyla gerçekleştirilen seçici hedefleme, ikincisi, genellikle tümör ortamında mevcut olan ilaçların daha düşük pH'da kontrollü salınımıdır [44;55-59]. KNT'ler, sistemik toksisitenin en aza indirgenmesi ve normal antikanser ilaçların istenmeyen yan etkilerinin azaltılması ile belirli tümör bölgesine küçük miktarlarda ilaç iletimi olanağı sağlar. Örneğin Cheng ve arkadaşları, 2011'de, çoklu ilaca dirençli kanser hücre problemini aşan ve aynı zamanda hücre proliferasyonunu ve hücre döngüsünü etkilemeden hassas kanser hücreleri üzerinde etkili olan KNT-

bazlı antikanser bir ilaç geliştirmiştir[60]. KNT bazlı ilaçların, örneğin, bazı antijenlere karşı immünizasyonu için taşıyıcı olarak KNT'lerin kullanılması gibi birçok başka önemli tipi vardır. Karbon nanotüplerin tek duvarlı karbon nanotüpler ve çok duvarlı karbon nanotüpler olmak üzere iki tipi vardır.

a. Tek duvarlı karbon nanotüp

Tek duvarlı karbon nanotüpler (TDKNT'ler) tek bir grafen silindirden oluşur ve çapları 0.4 ila 2 nm arasında değişir[61-63]. TDKNT'ler genellikle, nanotüplerin van der Walls kuvvetleri tarafından bir arada tutulduğu altıgene yakın paketlenmiş demetler halinde meydana gelir[64]. Bir çok çalışmada, TDKNT'lerin çok yönlü biyosensörler/biyoalgılama olarak kullanımını gösterilmiştir[64]. Mevcut biyoalgılama teknikleri oldukça hassas ve özgül olmakla birlikte, minyatürleştirilmesi zordur. TDKNT bazlı biyosensörler, karbon nanotüplerin küçük boyutları ve yapısal özellikleri nedeniyle minyatürleşmeye katkıda bulunurlar. TDKNT'ler ile her karbon atomu yüzeyde bulunur, böylece ilgili moleküllerle etkileşimleri için geniş hacim oranına ulaşır. Buna ilaveten, benzersiz elektronik yapıları ve balistik iletkenlikleri nedeniyle, TDKNT'ler bağlanma olaylarının elektriksel tespiti için kullanılabilir ve böylece çok basit bir biyoalgılama aracı sağlar[65-68]. TDKNT'ler, küçük biyomoleküllerin ve proteinlerin varlığına yanıt olarak önemli bir iletkenlik değişimi sergiledikleri gösterilmiştir[65-68]. Örneğin mitokondrinin respiratuar zincirinde bir redoks katalizörü olan sitokrom c'nin adsorpsiyonu, bir TDKNT cihazı kullanılarak yerinde tespit edilmiştir[64];[68]. Biyotin-modifiye TDKNT'ler biyotin-streptavidin bağlanmasını elektronik olarak saptamak için kullanılmıştır[65]. Streptavidinin biyotin ile işlevselleştirilmiş TDKNT'lere bağlanmasının, karbon nanotüplerin iletkenliğinin azalması ile sonuçlandığı gösterilmiştir. TDKNT'lerin gösterdiği kimyasal algılama mekanizması kesin olarak belirlenememesine rağmen, bu cihazların uğradığı direnç değişikliklerinin, TDKNT'ler ve analit arasındaki etkileşimlerle ilişkili olan yük transfer süreçlerinin bir sonucu olarak karbon nanotüplerin katkısından kaynaklanması muhtemel görünmektedir[64]. Bazı durumlarda iletkenlik değişimi, adsorpsiyon sırasında metal nanotüp temaslarında meydana gelen elektronik etkilerden kaynaklanır. TDKNT'lerin etkileşime girme ve bu nedenle biyolojik molekülleri anlama yeteneği, hidrojen peroksit, indirgenmiş β-nikotinamid adenin dinükleotid (NADH) ve KNT'lerin geleneksel karbon elektrotlara kıyasla üstün performans gösterdiği yer olan dopamin gibi biyolojik olarak ilgili moleküllerin elektrokimyasal özellikleri ile ilgili çalışmalarda kullanılmıştır[69-71].

b. Çok duvarlı karbon nanotüp

Çok duvarlı karbon nanotüpler (ÇDKNT'ler), her biri içi boş bir göbeği çevreleyen tek bir grafen tabakadan yapılmış birkaç koaksiyel silindirden

oluşur. ÇDKNT'lerin dış çapı 2 ila 100 nm arasında değişirken, iç çap 1–3 nm aralığındadır ve uzunlukları 1 ila birkaç μm arasındadır[75]. Kimyasal ve hücre penetrasyon yapılarının çeşitliliği, CNT'lerin ilaç, DNA, proteinler ve diğer moleküler probların memeli hücrelerine taşınması için taşıyıcılar olarak kullanılmasını sağlar[76-77]. Böyle bir görev için ön koşullardan biri, taşıyıcının biyolojik olarak ilgili moleküllere bağlanma kabiliyetidir. ÇDKNT'ler ve proteinler arasındaki etkileşimlerle ilgili deneysel çalışmalar, streptavidin moleküllerinin kendi kendini organize ettiğini ve nanotüp yüzeyindeki sarmal kristallerinin büyümesini ortaya çıkarmıştır [64];[78]. Benzer şekilde, DNA molekülleri ÇDKNT'ler üzerine adsorbe edilebilir ve sitokrom c ve β-Laktaz I gibi küçük protein molekülleri açık karbon nanotüplerin iç boşluğu içine sokulabilir[79].

1.5.DNA nanopartiküller

Nükleik asitler, çok işlevli NP'lerin önemli rol oynadığı, nano-ölçekli nesnelerin ilaç dağıtım potansiyel alanlarındaki uygulamaların inşası için çok çekici yapı taşlarıdır[80]. Hücre zarından DNA taşınması, oligonükleotidleri ve plazmid DNA'yı kullanan gen terapisi için zorunlu bir gerekliliktir. Viral vektörler gen terapisinde etkili olmakla birlikte, viral proteinlerin yol açtığı bağışıklık tepkisi önemli bir problem oluşturmaktadır. Bu problemi aşmak için, nonviral DNA dağıtım araçlarının geliştirilmesi amaçlanmıştır. Poliaminler, polikatyonik lipitler ve nötr polimerler 20-100 nm yarıçaplı DNA'yı nanopartiküllere yoğunlaştırabilen yapılardır. DNA yoğunlaştırılmasında yer alan yapısal ve enerjik kuvvetler son 25 yıldır fiziksel biyokimyacılar tarafından incelenmektedir. Çeşitli insan hastalıklarıyla mücadele etmek için gen terapisi protokollerinin geliştirilmesi için biyoteknologların ilgisini çekmiştir. Gen terapisi için başlıca gereksinim, iyi tanımlanmış işlemlerle DNA'nın hücre zarı içinden etkili bir şekilde taşınmasıdır[81-82]. Gen transfeksiyonu için mekanistik yol, uzamış DNA zincirlerinin sadece bir veya birkaç molekül içeren kompakt, düzenli parçacıklar halinde çökmesidir[83-84]. DNA yoğuşması olarak bilinen bu süreç, son yıllarda virüs başlarında DNA paketlemesinde ve gen dağıtım araçlarının geliştirilmesinde biyolojik önemi nedeniyle büyük ilgi görmüştür[83-87]. Poliaminler, pozitif yüklü polimerler ve peptidler gibi multivalent katyonların, DNA'nın elektron mikroskobu altında, çubuklar, toroidler veya sferoidler olarak görünen nanopartiküllere yoğunlaşmasına neden olduğu bilinmektedir. Son çalışmalar, poliaminler ve diğer çok değerlikli katyonların varlığında, DNA'nın sütunlu altıgen sıvı kristalli paketini göstermiştir[88-90]. DNA yoğunlaşması, kolayca geri dönüşümlü olan ve DNA fosfat grupları etrafındaki çok değerlikli katyonların birleşmesi tarafından tercih edilen polimer globül geçişinin bir örneğidir[83];[91-95]. Katyonlar, çubukların ve toroid benzeri yapıların oluşumunu kolaylaştıran, yük nötralizasyonunun kritik ölçüde DNA'nın lokalize bükülmesine veya bozulmasına neden olur[96-97].

DNA üzerindeki net yükü azaltmaya ek olarak, katyonlar istenmeyen DNA segment-segment etkileşimlerini azaltmayada yardımcı olur[98]. DNA'nın katyonik polimerler ve poliamin analoglarının varlığında yoğunlaşmasıyla oluşturulan NP'ler, oligonükleotidlerin ve plazmid DNA'nın hücre zarı içinden taşınması için gereklidir[90];[99-108]. Küçük katyonik moleküller, seyreltme ve aynı zamanda polianyonik etkileşimler üzerinde tersine çevrilebilirken, yoğunlaştırma maddesinin kimyasal modifikasyonu, komplekslere stabilite kazandırır ve transfeksiyon etkinliğini arttırır[109-110]. Pollard ve diğ. DNA komplekslerinin iyonik yükünden ziyade plazmid DNA'nın küresel parçacıklara sıkıştırılmasının nükleer değiş-tokuş mekanizmalarında önemli olduğunu öne sürmüştür[90]. Şimdiye kadar, çok çeşitli yoğuşma ajanları ile oluşturulan DNA nanopartikülleri mevcuttur. Örneğin, spermidin yoğunlaştırıcı ile T4, T7, viral f29,PM2, λ veya buzağı timus DNA'sından 45-130 nm[111-114] ile ve λ veya plazmid DNA pEGlacZ'den 50-130 nm[115-116], poli-L-lizin (pLys) yoğunlaştırıcı ile plasmid DNAsı ile 10-100nm[117-118], boyutlu nanopartiküller oluşturulmuştur. Sonuç olarak, son yıllarda DNA nanopartikül oluşumu alanındaki araştırmalar, terapötik gen transferine olan bağlantısı nedeniyle önemli bir ivme kazanmıştır. Etkili gen dağıtım araçlarının araştırılması, geniş bir yelpazede yeni DNA yoğunlaştırma ajanlarının keşfine yol açmıştır.

1.6.Polimerik nanopartiküller

Polimer nanopartiküllerin (PNP'lerin) elektronik, fotonikler, malzemelerin sensörlere iletilmesi, tıp, biyoteknoloji, çevre teknolojinde kirlilik kontrolü gibi çok çeşitli uygulamalarda benzersiz özelliklerinden dolayı rol oynar[119-122]. PNP'lerin özellikleri, belirli uygulamalara bağlı olarak optimize edilmelidir. İlgilenilen özelliklerin elde edilmesi için, hazırlık modu hayati bir rol oynar. Bu nedenle, belirli bir uygulama için istenen özelliklere sahip olan PNP'leri elde etmek için elde hazırlama tekniklerine sahip olması oldukça avantajlıdır[123]. PNP terimi, özellikle nanoküreler ve nanokapsüller olmak üzere her türlü polimer nanopartikülü için verilen toplu terimdir. Nanoküreler (nanosferler) matris partikülleridir. Tüm kütlesi katı ve moleküller olan partiküller küre yüzeyinde adsorbe edilebilir veya partikül içinde kapsüllenebilir[123]. Genel olarak küreseldirler, ancak küresel olmayan bir şekle sahip "nanosferler" de literatürde tanımlanmıştır[124]. Geçtiğimiz yıllarda polimerik nanopartiküller, hedefe yönelik ve kontrollü ilaç dağıtımı için oldukça umut verici ve uygun bir teknoloji platformu olarak ortaya çıkmıştır[125-127]. Virüsler gibi bu partiküller tipik olarak yaklaşık 20-250 nm'lik altmikron boyutlarına ve poli (etilen glikol) (PEG), poli (etilen oksit) (PEO), dekstran ve poli (akrilik asit) (PAA) gibi suda çözünebilen kirletici olmayan polimerlerden yapılmış gizli bir yüzeye sahiptir. Taşıyıcı olarak, ideal NP'ler yüksek ilaç yükleme kapasitelerine sahip olmakla yükümlü olup, ilacın belirli bir patolojik bölgeye ve/veya hedef hücrelere ilaç sızıntısı

olmadan iletilmesini sağlarken, bir yandan da eylem sahasında ilacı hızla boşaltılmasını sağlar. Bu amaçla, pH, redoks, sıcaklık, manyetik ve ışık gibi iç veya dış uyaranlara tepki olarak ilaç salgılayan çeşitli "akıllı" polimerik NP'ler aktif olarak takip edilmiştir. Bu uyarana cevap veren NP'ler ile, değişen derecelerde olsa da, *in vitro* ve/veya *in vivo* ilaç salım profilleri geliştirilmiştir[128]. Klinik öncesi ve klinik çalışmalar, ilaç yüklü polimerik NP'lerin, uzun süreli dolaşımı, artmış geçirgenlik ve retansiyon (EPR) etkisi, azaltılmış ilaç yan etkileri, gelişmiş ilaç toleransı ve/veya daha iyi ilaç biyoyararlılığı yoluyla tümör bölgelerinde artan birikim sağladığını göstermiştir[129-131]. Bununla birlikte, poli (ε kaprolakton) (PCL), polilaktit (PLA) ve poli (laktit-ko-glikolid) (PLGA) gibi biyo-bozunabilir alifatik poliesterlere dayanan mevcut polimerik NP'ler de mevcuttur. Bu NP'ler ilaç salım profiline göre optimal olmaktan uzaktır. Çünkü, yetersiz stabilite sonucu enjeksiyon sırasında önemli miktarda ilaç salınırken, ilacın yavaş biyo-bozunması nedeniyle patolojik bölgelere ve veya hedef kanser hücrelerine ulaştıktan sonra kolayca NP'lerden salınamaz[128];[132-133]. Bu çelişkili ilaç salım davranışı, ilaç yüklü NP'lerin *in vitro* ve *in vivo* antitümör etkinliğinin azalması için kritik bir sorundur. Bir iç uyarana (örneğin pH, glikoz, redoks potansiyeli ve lizozomal enzimler) veya dış uyarana (örneğin sıcaklık, manyetik alan, ultrason ve ışık) cevap olarak çözünen, şişen veya çökelen, çeşitli çevrelere duyarlı polimerik nanopartiküller, hedef alanda (uzamsal kontrol) ve /veya doğru zamanda artan ilaç salımını gerçekleştirmek için aktif olarak geliştirilmiştir[134-136]. Örneğin, kandaki ve normal dokulardaki 7.4'teki fizyolojik pH ile karşılaştırıldığında kanserli dokularda (pH 6.5-7.2), endozomlarda (pH 5.0-6.5) ve lizozomlarda (pH 4.5-5.0) hafif asidik ortamların avantajlarını kullanmak, pH'a duyarlı NP'lerin, tümör bölgesi ve/veya endo/lizozomal bölmelerdeki ilaçların salınması için tasarlanması ve geliştirilmesini sağlamıştır [128];[137-138].

1.7.Nanokristaller ve Kuantum noktalar

2–6 nm boyutlarındaki metal ve yarı iletken NP'ler, sadece kendine özgü büyüklüklere bağlı özelliklerinden dolayı değil, aynı zamanda biyolojik makromoleküllerle (örn., nükleik asitler ve proteinler) boyutsal benzerliklerinden dolayı dikkat çekmiştir[139-142]. Bu benzerlikleri sayesinde, nanoteknoloji ve biyolojinin entegrasyonuna izin vererek tıbbi teşhis, hedefe yönelik terapötikler, yüksek verimli ilaç taraması uygulamalarında biyolojik moleküller ile bütünleşmesiyle moleküler biyoloji ve hücre biyolojisinde büyük ilerlemelere yol açabilir[143]. Son yapılan araştırmalarda, kolloidal NP'ler peptitler, proteinler ve DNA gibi biyomoleküllere bağlamıştır[144-150]. Bu nanopartikül biyo-konjugatlar, homojen biyoanalizler geliştirmek için yeni materyaller ve ultra duyarlı tespit ve görüntüleme için çok renkli flüoresan etiketler olarak kullanılmaktadır[144];[147-150]. Kuantum noktaları (KN) yarı iletken nanokristaller olarak bilinir. Bu nanokristaller genellikle

periyodik cetvelde II-VI veya III-V elementlerinden oluşan atomlardan oluşur ve eksiton bohr yarıçapından daha küçük fiziksel boyutlara sahip parçacıklar olarak tanımlanır. Örneğin, küresel CdSe partikülleri için, bu parçacık çapı yaklaşık 10 nm'den az olduğunda ortaya çıkar. Kuantum sınırlamasının etkisi, ayrık atomlarda veya bulk katılarda bulunmayan benzersiz optik ve elektronik özelliklere yol açar[139-142]. Kuantum noktalarının ilk pratik uygulamaların biyoloji ve tıpta meydana gelmiştir. Örneğin, yapılan bir çalışmada, son derece parlak yarı iletken kuantum noktaları (çinko sülfür-başlıklı kadmiyum selenit) ultra duyarlı biyolojik algılamada kullanılmak üzere biyomoleküllere kovalent olarak bağlanmıştır. Rodamin gibi organik boyalar ile karşılaştırıldığında bu sınıf lüminesan etiketler 20 kat daha parlaktır. Bu nanometre boyutlu konjugatlar suda çözünür ve biyo uyumludur. Transferin protein ile etiketlenmiş kuantum noktaları, kültüre edilmiş HeLa hücrelerinde reseptör aracılı endositoza maruz kalmıştır ve immünomoleküller ile etiketlenmiş noktalar, spesifik antikorları veya antijenleri tanımıştır[151]. Daha sonraları, kuantum nokta etiketleri, DNA hibritleme tespiti, immünoassay'ler ve hedef olaylar için problamaya floresan rezonans enerji transferi (FRET) kullanarak bağlanma testleri gibi çeşitli biyoanalitik amaçlar için başarıyla kullanılmıştır[152-157]. Bu iyi bilinen uygulamalarda, iyi sonuçlara sahip organik boyalar kullanmıştır, ancak KN'lerinin kullanımı, dar ve yoğun emisyon spektrumları nedeniyle yüksek hassasiyetli çoğullanmış metotlara izin verebilir. *İn vitro* çalışmalar için KN'lerin biyoanalitik araçlar olarak kullanımındaki önemli gelişmeler immünolojik testler ve biyosensörler alanlarında yapılmıştır[152,158-160]. Floresan immünolojik testler, bir florofor etiketli antikorun bir destek substratına bağlanmış olan bir analit molekülüne bağlanmasını tespit eder. Kısa bir inkübasyon periyodundan sonra, bağlanmamış antikor yıkanabilir ve bağlı antikor miktarı belirlenebilir. Kuantum nokta-etiketli antikorlar deneylerde kullanılmıştır ve genel olarak uygulanabilir olduğu gösterilmiş olsa da, organik floroforlara karşı duyarlılıkta herhangi bir artış gözlenmemiştir[152,156,160]. Başka bir çalışmada, immünolojik testlerde kuantum tabanlı etiketlerin kullanılmasının faydaları nanokristal floroforların çoğul kabiliyetinden yararlanılarak gerçekleştirilmiştir. Yani, tek bir ışık kaynağı kullanarak aynı anda birkaç etiketli türün uyarılması ve tespit edilmesi yeteneğine sahiptir[159]. Biyosensör alanında, KN'ları, uzun süreli fotostabiliteleri nedeniyle gerçek zamanlı ve sürekli izlemeye izin verdiği için özellikle çekicidir. Algılama uygulamalarında KN'lerin kullanılmasına yönelik bir yöntem, floresan rezonans enerji transferi (FRET) aracılığıyla "açık / kapalı" bir anahtarlama yeteneği oluşur, böylece KN'ları (donör) ve bir alıcı molekül arasında ışınım dışı enerji transferi gerçekleşir[161-162]. KN'ler, sürekli olarak ayarlanabilen emisyonları nedeniyle FRET tabanlı uygulamalar için gelecek vadeden donörlerdir. KN'ler herhangi bir istenen alıcıya ve geniş bant absorpsiyonuna eşleştirilebilir, böylece alıcıyı doğrudan etkilemeyen

kısa bir dalga boyunda uyarmaya izin verir. Yakın zamanda yapılan çalışmalarda, KN'lerin, organik fluoroforlar veya boyalar gibi çeşitli alıcılar ve diğer KN'ler veya metalik NP'ler ile birleştiğinde yüksek verimli FRET donörleri olarak hareket edebileceği bildirilmiştir[152];[158];[163-166]. Bir başka biyoanalitik uygulama, yüksek verimli tarama ve genlerin, proteinlerin ve kimyasal kütüphanelerin analizinde kullanılabilecek optik olarak kodlanmış polimer mikro küreleri (mikrosferleri) oluşturmak için KN'lerin kullanılmasıdır[167-16]. Polimer boncuk içindeki KN popülasyonlarının kapsüllenmesiyle, özel bir spektroskopik imza belirleyebilir ve bu da boncuklara bağlanan belirli/özel biyotanıma molekülünü tanımlar. Daha sonra, karmaşık bir analit molekülleri karışımına maruz kaldığında, mikro küreye bağlananlar belirlenebilir. KN'ler tarafından sergilenen dar emisyon profillerinden dolayı, kodlanmış spektroskopik imzanın altı tane kadar renk içermesi mümkündür. Bu bireysel renkler için 10 yoğunluk seviyesi kullanılmışsa, toplam 10^6 şeklinde benzersiz bir kod oluşturulabilir. Pratik açıdan, 1000 özgün kod, en son teknoloji analizleri için yeterli olmaktan çok daha fazlasıdır. Çünkü, organik florofor ile boyanmış polimer mikroküreleri kullanan teknikler 100 özgün kodun üretilmesi ile sınırlıdır[152]. Bir çalışmada, tek bir nükleotidi farklı olan DNA sekansları; tek nükleotid polimorfizmlerini (TNP'ler) saptamak için kullanılmıştır[167];[170]. Bu terim, nadir rastlanan olayların aksine (mutasyonlar gibi), organizma populasyonları içinde sıkça ortaya çıkan genetik farklılıkları tanımlar. Bu teknik, insan sitokrom P450 gen ailesinin spesifik alellerinde bulunan TNP'lerin, bir akış sitometrisi sistemi ile bağlantılı olarak optik olarak kodlanmış boncuklar kullanılarak hızlı ve doğru bir şekilde tanımlanmasını sağlamıştır. KN-kodlu boncuklar, iyi bir emisyon piklerine sahiptir ve sadece tek bir uyarım kaynağı gerektirdiği için enstrümantasyonu büyük ölçüde basitleştirmiştir. Bu sayede yüksek verimli analizin güvenilirliğini arttırmıştır. Şifrelenmiş mikrosfer kütüphaneleri geliştirilerek, bilim adamlarının, çoğullamalı algılama. kullanarak çok miktarda genomik bilgiyi ve gen ekspresyon verilerini hızlı ve ekonomik olarak toplayabilmeleri sağlanabilecektir.[152];[171]. KN'ler, *in vivo* görüntüleme için hücresel reseptörler ve kontrast ajanları için etiket olarak hızla kullanılmaktadır[172-174]. Bu uygulamalarda, organik boyalara göre KN'lerin yüksek fotostabilitesi, biyolojik işlemlerin uzun süreli takibini mümkün kılar[177]. Örneğin, Dubertret ve ark., tarafından KN biyokonjugatlarının *Xenopus* embriyolarına mikroenjeksiyonu ve birkaç gün boyunca iribaş gelişimi sırasında çeşitli hücrelere ayrılmalarının izlenmesi ile gösterilmiştir[172]. Ek olarak, KN'lerin dar emisyon spektrumları, çoklu moleküler belirteçlere dayanan habis tümörlerin erken tespit ve tanımlanması için imkan sağlayarak, canlı hücrelerin içinde veya üzerinde çoklu hedeflerin eşzamanlı olarak görüntülenmesini sağlmaıştır[175]. KN'leri kullanarak çok renkli görüntüleme, analiz sürelerini azaltarak ve incelenebilen biyomarkerlerin (biyobelirteçlerin) sayısını arttırarak doku örneklerinin

analizinde yararlı olabilir[176]. 1998 yılında, biyolojik etiketler olarak KN'lerin ilk uygulamaları, sabit fare fibroblastlarının çok renkli etiketlenmesiyle gösterilmiştir. Burada kırmızı KN'ler, hücre iskeleti ve seçici olarak hücre çekirdeği için seçici tanıma molekülleriyle bağlantılıdır ve yeşil KN'ler, hücre çekirdeği için seçici tanıma moleküllerine ve canlı HeLa hücreleri tarafından transferrin-KN konjugatlarının alınmasına bağlanmıştır[180]. Bazı durumlarda KN'lerin spesifik olmayan bir alım mekanizması yoluyla hücrelere girebileceği de gözlenmiştir[177-179].Aslında, bu spesifik olmayan alım, meme tümör hücrelerinin KN'lerle kaplı destek substratı boyunca hareketini izlemek için kullanılmıştır. Substrattaki KN'lerin tükenmesi, göç eden hücrelerin yollarını ortaya çıkarmıştır[178]. Tüm bu çalışmalar, KN'lerin uzun süre canlı hücreler içinde görüntülenebilir olduğu fikrini güçlendirir ve bu geleneksel organik floroforlara göre önemli bir avantaj sağlamıştır. Yine, KN'ler, immünokimyasal tekniklerle sabit hücrelerdeki hücresel yapıların yüksek çözünürlüklü görüntülemesinde kullanılmıştır[175].

1.8.Albümin temlli nanopartiküller

Kan-beyin bariyeri (KBB), ilaçların çoğunluğunun beyine girmesi için önemli bir engel teşkil eder ve bu nedenle beyin tümörleri, HIV, alzheimer ve diğer nörodejeneratif hastalıklar gibi birçok CNS hastalığının tedavisini ciddi şekilde kısıtlar. Bunun üstesinden gelmek için albümin klinik ortamda ilaç taşıyıcı olarak artan bir rol oynamaktadır. Temel olarak, üç ilaç dağıtım teknolojisi ayırt edilebilir: düşük moleküler ağırlıklı ilaçların ekzojen veya endojen albümin ile birleştirilmesi, biyoaktif proteinlerle konjugasyon ve ilaçların albümin NP'lerine kapsüllenmesidir. Albümin, ilaç hedeflemesi için ve peptit veya protein bazlı ilaçların farmakokinetik profilini geliştirmek için çok yönlü bir protein taşıyıcısı olarak ortaya çıkmaktadır. Albumin malign ve iltihaplı dokuda, eksik veya kusurlu lenfatik drenaj sistemi ile kombine edilen sızıntılı kapiller nedeniyle birikmektedir. Klinik öncesi modellerde tümör alımı, hızlı ve sıkı bir şekilde albümin dolaşımına bağlanan ve deri altından büyüyen tümörlerin enjeksiyondan birkaç saat sonra maviye dönüşmesini sağlayan boya (evans mavisi) enjekte edilerek kolaylıkla görselleştirilebilir. İlaç hedeflemesine bir alternatif olarak, terapötik peptidler veya sitokinlerin albümin ile konjuge edilmesi, vücuttaki albüminin uzun-yarı ömrü nedeniyle farmakokinetik profilini geliştirmeye yönelik çekici bir yaklaşımdır[181]. Albumin~~in~~, biyolojik olarak bozunabilen, toksik olmayan, zararsız bozunma ürünleri üretmek için *in vivo* metabolize edilebilen, immünojenik olmayan, suda kolay temizlenebilen ve çözülebilen ve böylece nanopartikül preparasyonu için ideal bir aday olan çekici bir makromoleküler taşıyıcıdır[182-184]. Albumin bazlı nanopartikül taşıyıcı sistemler, çekici bir stratejidir, çünkü albümin molekülünde bulunan farklı ilaç bağlama bölgeleri nedeniyle partikül matrisine önemli miktarda ilaç eklenebilir[185]. Tanımlı albümin birincil yapısı ve yüklü amino asitlerin (örneğin lisin) yüksek içeriği

nedeniyle, albümin bazlı NP'ler diğer bileşikler olmaksızın pozitif (örneğin gansiklovir) veya negatif yüklü (örneğin oligonükleotid) moleküllerin elektrostatik adsorpsiyonuna izin verebilir[186-187]. Ayrıca albümin NP'leri, koaservasyon, kontrollü desolvasyon veya emülsiyon oluşumu ile yumuşak koşullar altında kolaylıkla hazırlanabilir. Mikropartiküller ile karşılaştırıldığında daha küçük bir boyuta (50 ila 300 nm) ve genel olarak, lipozomlardan daha iyi kontrollü salım özellikleri gösterirler, bu da hasta kabulünü ve uyumunu geliştirebilir. Ticari olarak, yumurta akı (ovalbumin), sığır serumu (sığır serumu albümini, SSA) ve insan serumu (insan serum albümini, İSA) ile soya fasulyesi, süt ve tahıllardan önemli miktarlarda albümin elde edilebilir.

Teşekkür

Babam Murat ÖZKAN'a çocuklarına verdiği emeklerinden dolayı teşekkür ederim. Allah rahmet eylesin, ruhun huzur içinde yatsın.

Referanslar

1. Parveen S, Misra R, Sahoo S. Biol. Med. 2012;8(2):147- 166.
2. Cartaxo ALP. Nanoparticles types and properties – understanding these promising devices in the biomedical area.
3. Dağlıoğlu, Y, Yılmaz Öztürk, B. (2018). Journal of Boron, 3 (3), 157-165. DOI: 10.30728/boron.295746
4. Dağlıoğlu, Y, Öztürk, B. Y. (2019). Rendiconti Lincei. Scienze Fisiche e Naturali, 30(3), 611-621.
5. Orive G, Anitua E, Pedraz J, Emerich D. Nat. Rev. Neurosci. 2009;10(9):682-692.
6. Kambhampati SP, Kannan RM. *Journal of Ocular* Pharmacology and Therapeutics, 2013;29(2):151-165.
7. Menjoge AR, Kannan RM, Tomalia TA. Drug Discov. Today. 2010;15:171–185.
8. Perumal OP, Inapagolla R, Kannan S, Kannan RM. The effect of surface functionality on cellular trafficking of dendrimers. Biomaterials 2008;29:3469–3476.
9. Saovapakhiran A, D'Emanuele A, Attwood D, Penny J. Bioconjug. Chem. 2009;20:693–701.
10. Albertazzi L, Serresi M, Albanese A. Mol. Pharm. 2010;7:680–688,

11. Bangham A. D. Chemistry and Physics of Lipids 1993;64:275-285.

12. Mukherjee S, Ray S, Thakur RS. Indian J Pharm Sci. 2009;71(4):349–58. doi: 10.4103/0250-474X.57282.

13. Naseri N, Valizadeh H., Zekeri-Milani P. Adv Pharm Bull. 2015;5(3):305–313.

14. Torchilin V. P. Nat Rev Drug Discov 2005, *4*. 145-160.

15. Ekambaram P, Sathali A, Priyanka K. Solid lipid nanoparticles: a review. Sci Rev Chem Commun. 2012;2(1):80–102.

16. Kamble MS, Vaidya KK, Bhosale AV, Chaudhari PD. Int J Pharm chem Biol Sci. 2012;2(4):681–91.

17. Kumar A, Badde S, Kamble R, Pokharkar VB. Int J Pharm Pharm Sci. 2010;2(4):87–9.

18. Felgner PL, Gadek TR, Holm M, Roman R, Chan HW, Wenz M, Northrop JP, Ringold GM. Proceedings of the National Academy of Sciences 1987;84:7413-7417.

19. Wang EC, Wang AZ. Integrative Biology, 2014;6(1):9-26.

20. Dwivedi C, Sahu R, Tiwari SP, Satapathy T, Roy A. J Drug Deliv Therap.2014;4(2):116–29.

21. Patidar A, Thakur DS, Kumar P, Verma J. Int J Pharm Pharm Sci. 2010;2(4):30–5.

22. Madan JR, Khude PA, Dua K. Int J Pharm Investig. 2014;4(2):60–4. doi: 10.4103/2230-973X.133047.

23. Attama AA, Momoh MA, Builders PF. In: Sezer AD, editor. Pharmacology, Toxicology and Pharmaceutical Science. Croatia: InTech Open Access Publisher; 2012.

24. Elnaggar YS, El-Massik MA, Abdallah OY. Int J Nanomedicine. 2011;6:3195–205. doi: 10.2147/IJN.S25825.

25. Kaur J, Singh G, Saini S, Rana A. J Drug Deliv Therap 2012;2(5).

26. Waghmare A, Grampurohit N, Gadhave M, Gaikwad D, Jadhav S. Int Res J Pharm. 2012;3(4):100–7.

27. Blasi P, Giovagnoli S, Schoubben A, Ricci M, Rossi C. Adv. Drug Del. Rev. 2007;59, 454–477.

28. Kaur IP, Bhandari R, Bhandari S, Kakkar V. J. Control Rel. 2008;127:97–109.

29. Chattopadhyay, Zastre j, Wong H, Wu XY, Bendayan R. Pharm. Res. 2008;25, 2262–2271.

30. Das S, Chaudhury A. AAPS PharmSciTech. 2011;12(1):62–76. doi: 10.1208/s12249-010-9563-0.

31. Sinha VR, Srivastava S, Goel H, Jindal V. Int J Adv Pharm Sci 2011;1(3).

32. Brioschi A, Zenga F, Zara GP, Gasco MR, Ducati A, Mauro A. Neurological research, 2007;29(3):324-330.

33. Mehnert W, Mader K. Adv Drug Deliv Rev. 2001;47(2-3):165–96.

34. Müller RH, Staufenbiel S, Keck CM Househ Personal Care. 2014;9(2):18–25.

35. Tamjidi F, Shahedi M, Varshosaz J, Nasirpour A. Innov Food Sci Emerg Tech. 2013;19(0):29–43.

36. Beloqui A, Solinis MA, des Rieux A, Preat V, Rodriguez-Gascon A. Int J Pharm. 2014;468(1-2):105–11.

37. Pardeike J, Hommoss A, Muller RH. Int J Pharm. 2009;366(1-2):170–84.

38. Uner M, Yener G. Int J Nanomedicine. 2007;2(3):289–300.

39. Araujo J, Gonzalez-Mira E, Egea MA, Garcia ML, Souto EB. Int J Pharm. 2010;393(1-2):167–75.

40. Thatipamula R, Palem C, Gannu R, Mudragada S, Yamsani M.. Daru. 2011;19(1):23–32.

41. Lima AM, Pizzol CD, Monteiro FB, Creczynski-Pasa TB, Andrade GP, Ribeiro AO. et al. J Photochem Photobiol B. 2013;125:146–54. doi: 10.1016/j.jphotobiol.2013.05.010.

42. Pardeshi C, Rajput P, Belgamwar V, Tekade A, Patil G, Chaudhary K. et al. Acta Pharm. 2012;62(4):433–72. doi: 10.2478/v10007-012-0040-z.

43. Wen Z, Liu B, Zheng Z, You X, Pu Y, Li Q.. Chem Eng Res Des. 2010;88(8):1102–7.

44. Alshehri R, Ilyas AM, Hasan A, Arnaout A, Ahmed F, Memic A. (2016). Miniperspective. Journal of medicinal chemistry, *59*(18):8149-8167.

45. Wang J. Electroanalysis 2005;17:7−14.

46. Kunzmann A, Andersson B, Thurnherr T, Krug H, Scheynius A, Fadeel B. Biochim. Biophys. Acta, Gen. Subj. 2011;1810:361−373.

47. Sinha N, Yeow JT.. IEEE Trans. Nanobiosci. 2005:4:180−195.

48. Beg S, Rizwan M, Sheikh AM, Hasnain MS, Anwer K, Kohli K.. J. Pharm. Pharmacol. 2011;63:141−163.

49. Bianco A, Kostarelos K, Partidos CD, Prato M. Chem. Commun. 2005;5:571−577.

50. Karousis N, Papi RM, Siskos A, Vakalopoulou P, Glezakos P, Sarigiannis Y, Stavropoulos G, Kyriakidis, DA, Tagmatarchis N. Carbon 2009;47:3550−3558.

51. Bhirde AA, Patel S, Sousa AA, Patel V, Molinolo AA, Ji Y, Leapman RD, Gutkind JS, Rusling JF. Nanomedicine 2010;5:1535−1546.

52. Foldvari M, Bagonluri M. Nanomedicine 2008;4:183−200.

53. Vardharajula S, Ali SZ, Tiwari PM, Eroğlu E, Vig K, Dennis VA, Singh SR. Int. J. Nanomed. 2012;7:5361−5374.

54. Yan L, Zhao F, Li S, Hu Z, Zhao Y Nanoscale 2011;3:362−382.

55. Chen J, Chen S, Zhao X, Kuznetsova LV, Wong SS, Ojima I. J. Am. Chem. Soc. 2008;130:16778−16785

56. Zhang X, Meng L, Lu Q, Fei Z, Dyson PJ. Biomaterials 2009;30:6041−6047.

57. Ji Z, Lin G, Lu Q, Meng L, Shen X, Dong L, Fu C, Zhang X. J. Colloid Interface Sci. 2012;365:143−149.

58. Huang H,Yuan Q, Shah JS, Misra RD. Adv. Drug Delivery Rev. 2011;63:1332−1339.

59. Chen C, Xie XX, Zhou Q, Zhang FY, Wang QL, Liu YQ, Zou Y, Tao Q, Ji XM, Yu SQ. Nanotechnology 2012;23:045104.

60. Cheng J, Meziani MJ, Sun YP, Cheng SHToxicol. Appl. Pharmacol. 2011;250:184−193.

61. Lijima S, Ichihashi T.. Nature. 1993;363:603.

62. Qin LC, Zhao X, Hirahara K, Miyamoto Y, Ando Y, Iijima S..Nature. 2000;408:50.

63. Wang N, Tang ZK, Li GD, Chen JS. Nature. 2000;408:50.

64. Bekyarova E, Ni Y, Malarkey BE, MontanaV, McWilliams LJ, Haddon CR, Parpura V. J Biomed Nanotechnol. 2005;1(1): 3–17.

65. Star A, Gabriel JCP, Bradley K, Gruner G. Nano Lett. 2003;3:459.

66. Besteman K, Lee JO, Wiertz FG, Heering HA, Dekker C. Nano Lett. 2003;3:727.

67. Chen RJ, Bangsaruntip S, Drouvalakis KA, Kam NWS, Shim M, Li Y, Kim W, Utz PJ, Dai H. Proc Nat Acad Sci USA. 2003;100:4984.

68. Boussaad S, Tao NJ, Zhang R, Hopson T, Nagahara LA. Chem Commun. 2003:1502.

69. Wang J, Musameh M. Anal Chem. 2003;75:2075.

70. Wang J, Musameh M, Lin Y.. J Am Chem Soc. 2003;125:2408.

71. Britto PJ, Santhaman SKV, Ajayan PM. Bioelectrochem Bioelectronics. 1996;41:121.

72. Schindler M, Ahmed I, Kamal J, et al. Biomaterials. 2005;26(28):5624e5631.

73. Zhang S. Nat Biotechnol. 2003;21(10):1171e1178.

74. Khazaei A, Rad MN, Borazjani MK. Int. J. Nanomed. 2010;5:639−645.

75. Dresselhaus MS, Dresselhaus G, Eklund PC. Academic; San Diego: 1996.

76. Pantarotto D, Briand J-P, Prato M, Bianco A. ChemCommun. 2004;16.

77. Kam NWS, Jessop TC, Wender PA, Dai H. J Am Chem Soc. 2004;126:6850.

78. Balavoine F, Schultz P, Richard C, Mallouh V, Ebbesen TW, Mioskowski C. Angew Chem Int Ed. 1999;38:1912.

79. Davis JJ, Green MLH, Hill HAO, Leung YC, Sadler PJ, Sloan J, Xavier AV, Tsang SC. Inorg Chem Acta. 1998;272:261.

80. de Vries JW, Schnichels S, Hurst J, Strudel L, Gruszka A., Kwak M, et al. Biomaterials, 2018;157:98-106.

81. Zuber G, Dauty E, Nothisen M, Belguise P, Behr JP. AdV. Drug DeliVery ReV. 2001;52:245-253.

82. Luo D, Saltzman WM. Nat. Biotechnol. 2000;18:33-37.

83. Bloomfield VA. DNA condensation, Curr. Opin. Struct. Biol. 1996;6:334-341.

84. Blessing T, Remy JS,Behr JP. Proc. Natl. Acad. Sci. U.S.A. 1998;95:1427-1431.

85. Xu Y, Hui SW, Frederik P, Szoka FC. Biophys. J. 1999;77:341-353.

86. Montigny WJ, Houchens CR, Illenye S, Gilbert J, Coonrod E, Chang YC, Heintz NH. Nucleic Acids Res. 2001;29, 1982-1988.

87. Duguid JG, Li C, Shi M, Logan MJ, Alila H, Rolland A, Tomlinson E, Sparrow JT, Smith LC., Biophys. J. 1998;74:2802-2814.

88. Saminathan M, Thomas T, Shirahata A, Pillai CKS, Thomas TJ., Nucleic Acids Res. 2002;30, 3722-3731.

89. Hud NV, Downing KH. Proc. Natl. Acad. Sci. U.S.A. 2001;98:14925-14930.

90. Vijayanathan V, Thomas T, Thomas, TJ. Biochemistry, 2002;41(48):14085-14094.

91. Fang Y, Hoh JH. J. Am. Chem. Soc. 1998;120:8903-8909.

92. Livolant F, Leforestier A. Prog. Polym. Sci. 996;21, 1115-1164.

93. Brewer LR, Corzett M, Balhorn R. Science 1999;286:120-123.

94. Koltover I, Wagner K, Safinya CR. Natl. Acad. Sci. U.S.A. 2000;97:14046-14051.

95. Lai E, van Zanten JH. Biophys. J. 2001;80:864-873.

96. Rouzina I, Bloomfield VA. Biophys. J. 1998;74:3152-3164.

97. Golan R, Pietrasanta LI, Hsieh W, Hansma HG. Biochemistry 1999;38:14069-14076.

98. Post CB, Zimm BH. Biopolymers 1982;21:2123-2137.

99. Zuber G, Dauty E, Nothisen M, Belguise P, Behr JP. AdV. Drug DeliVery ReV. 2001;52:245-253.

100. Luo D, Saltzman WM. Nat. Biotechnol. 2000;18:33-37.

101. Blessing T, Remy JS, Behr JP. Proc. Natl. Acad. Sci. U.S.A. 1998;95:1427-1431.

102. Xu Y, Hui SW, Frederik P, Szoka FC, Biophys. J. 1999;77:341-353.

103. Montigny WJ, Houchens CR, Illenye S, Gilbert J, Coonrod E, Chang YC, Heintz NH. Nucleic Acids Res. 2001;29:1982-1988.

104. Duguid JG, Li C, Shi M, Logan MJ, Alila H, Rolland A, Tomlinson E, Sparrow JT. Smith LC. Biophys. J. 1998;74:2802-2814.

105. Junghans M, Kreuter J, Zimmer A. Biochim. Biophys. Acta 2001;1544:177- 188.

106. Truong-Le VL, Walsh SM, Schweibert E, Mao HQ, Guggino WB, August JT, Leong KW. Arch. Biochem. Biophys. 1999;361:47-56.

107. Liu G, Molas M, Grossmann GA, Pasumarthy M, Perales JC, Cooper MJ, Hanson RW. J. Biol. Chem. 2001;276:34379-34387.

108. Lim YB, Choi YH, Park JS. Journal of the American Chemical Society, 1999;121(24):5633-5639.

109. Dauty E, Remy JS, Blessing T, Behr JP. J. Am. Chem. Soc. 2001;123:9227-9234.

110. Pichon C, LeCam E, Guerin B, Coulaud D, Delain E, Midoux P. Bioconjugate Chem. 2002;13:76-82.

111. Eickbush TH, Moudrianakis EN. Cell 1978;13:295-306.

112. Wilson RW, Bloomfield VA, Biochemistry 1979;18:2192-2196.

113. Allison SA, Herr JC, Schurr JM, Biopolymers 1981;20:469-488.

114. Thomas TJ, Bloomfield VA. Biopolymers 1983;22:1097-1106

115. Vijayanathan V, Thomas T, Thomas TJ. Biochemistry, 2002;41(48):14085-14094.

116. Bo¨ttcher C, Endisch C, Fuhrhop JH, Catterall C, Eaton M. J. Am. Chem. Soc. 1998;120:12-17.

117. Dauty E, Remy JS, Blessing T, Behr JP. J. Am. Chem. Soc. 2001;123: 9227-9234.

118. Wagner E, Zenke M, Cotten M, Beug H, Birnstiel ML. Proc. Natl. Acad. Sci. U.S.A. 1990;87:3410-3414

119. Zhang Q, Chuang KT. Adv Environ Res 2001;5:251–8.

120. Fudouzi H, Xia Y. Adv Mater 2003;15:892–6.

121. Wang X, Summers CJ, Wang ZL Nano Lett 2004;4:423–6.

122. Hosokawa M, Nogi K, Naito M, Yokoyama T. Netherlands: Elsevier; 2007.

123. Rao JP, Geckeler KEProgress in polymer science, 2011;36(7):887-913.

124. Vauthier C, Couvreur PNew York: Marcel Dekker; 2000. p. 13–429.

125. Bae Y, Kataoka KAdv Drug Deliv Rev 2009;61(10):768e84.

126. Peer D, Karp JM, Hong S, Farokhzad OC, Margalit R, Langer R. Nat Nanotechnol 2007;2(12):751e60.

127. Davis ME, Chen Z, Shin DM. Nat Rev Drug Discov 2008;7(9):771e82.

128. Cheng R, Meng F, Deng C, Klok HA, Zhong Z. Biomaterials, 2013;34(14):3647-3657.

129. Torchilin V. Adv Drug Deliv Rev 2011;63(3):131e5.

130. Hrkach J, Von Hoff D, Ali MM, Andrianova E, Auer J, Campbell T, et al. Sci Transl Med 2012;4(128):128ra139.

131. Gong J, Chen MW, Zheng Y, Wang SP, Wang YT. J Control Release 2012;159(3):312e23.

132. Deng C, Jiang YJ, Cheng R, Meng FH, Zhong ZY Nano Today 2012;7(5):467e80.

133. Meng FH, Cheng R, Deng C, Zhong ZY.2012;15(10):436e42.

134. Ganta S, Devalapally H, Shahiwala A, Amiji M. J Control Release 2008;126(3):187e204.

135. Meng FH, Zhong ZY, Feijen J. Biomacromolecules 2009;10(2):197e209.

136. Rapoport N. Prog Polym Sci 2007;32(8e9):962e90.

137. Chen W, Meng FH, Li F, Ji SJ, Zhong ZY. Biomacromolecules 2009;10(7):1727e35.

138. Du JZ, Tang YQ, Lewis AL, Armes SP. J Am Chem Soc 2005;127(51): 17982e3.

139. Henglein A. Chem Rev 1989;89:1861-1873.

140. Schmid G. Chem Rev 1992;92:1709-1727.

141. Alivisatos AP. Science 1996; 271:933-937.

142. Nirmal M, Brus LE. Acc Chem Res 1999;32:407-414.

143. Niemeyer CM. Angew Chem Int Ed Engl 2001;40:4128-4158.

144. Chan WC, Maxwell DJ, Gao X, Bailey RE, Han M, Nie SCurrent opinion in biotechnology, 2002;13(1):40-46.

145. Whaley SR, English DS, Hu EL, Barbara PF, Belcher AM. Nature 2000;405:665-668.

146. Bruchez M Jr, Moronne M, Gin P, Weiss S, Alivisatos AP. Science 1998;281:2013-2015.

147. Chan WCW, Nie SM. Science 1998;281:2016-2018.

148. Mattoussi H, Mauro JM, Goldman ER, Anderson GP, Sundar VC, Mikulec FV, Bawendi MG. J Am Chem Soc 2000;122:12142-12150.

149. Mitchell GP, Mirkin CA, Letsinger RL. J Am Chem Soc 1999;121:8122-8123.

150. Pathak S, Choi SK, Arnheim N, Thompson ME. J Am Chem Soc 2001;123:4103-4104.

151. Chan WC, Nie S. Science, 1998;281(5385):2016-2018.

152. Bailey RE, Smith AM, Nie S. Low-dimensional Systems and Nanostructures, 2004;25(1):1-12.

153. Parak WJ, Gerion D, Zanchet D, Woerz AS, Pellegrino T, Micheel C, et al. Nanotechnology, 2003;14(7):R15.

154. Pathak S, Choi SK, Arnheim N,Thompson ME. Journal of the American Chemical Society, 2001;123(17), 4103-4104.

155. Mitchell GP, Mirkin CA, Letsinger RL. Journal of the American Chemical Society, 1999;121(35):8122-8123.

156. Goldman ER, Anderson GP, Tran PT, Mattoussi H, Charles PT, Mauro JM. Analytical Chemistry, 2002;74(4):841-847.

157. Goldman ER, Balighian ED, Mattoussi H, Kuno MK, Mauro J M, Tran PT, Anderson GP. Journal of the American Chemical Society, 2002;124(22):6378-6382.

158. Clapp AR, Medintz IL, Mauro JM, Fisher BR, Bawendi MG, Mattoussi H. Journal of the American Chemical Society, 2004;126(1):301-310.

159. Goldman ER, Clapp AR, Anderson GP, Uyeda HT, Mauro JM, Medintz IL, Mattoussi H. Analytical Chemistry, 2004;76(3):684-688.

160. Lingerfelt BM, Mattoussi H, Goldman ER, Mauro JM, Anderson GP. Analytical chemistry, 2003;75(16):4043-4049.

161. Tran PT, Anderson GP, Mauro JM, Mattoussi H. Physica status solidi (b), (2002;229(1):427-432..

162. Willard DM, Mutschler T, Yu M, Jung J, Van Orden A. Analytical and bioanalytical chemistry, 2006;384(3):564-571.

163. Willard DM, Carillo LL, Jung J, Van Orden A Nano Letters, 2001;1(9):469-474.

164. Medintz IL, Clapp AR, Mattoussi H, Goldman ER, Fisher B, Mauro JM. Nature materials, 2003;2(9):630.

165. Wargnier R, Baranov AV, Maslov VG, Stsiapura V, Artemyev M, Pluot M, et al. Nano Letters, 2004;4(3):451-457.

166. Wang S, Mamedova N, Kotov NA, Chen W, Studer J.. Nano letters, 2002;2(8):817-822.

167. Han M, Gao X, Su JZ, Nie, S. Nature biotechnology, 2001;19(7):631.

168. Gaponik N, Radtchenko IL, Sukhorukov GB, Weller H, Rogach AL. Advanced materials, 2002;14(12):879-882.

169. Wang D, Rogach AL, Caruso, F. Nano Letters, 2002;2(8):857-861.

170. Xu H, Sha MY, Wong EY, Uphoff J, Xu Y, Treadway JA, et al. Nucleic Acids Research, 2003;31(8):e43-e43.

171. Rosenthal SJ. (Bar-coding biomolecules with fluorescent nanocrystals. 2001.

172. Dubertret B, Skourides P, Norris DJ, Noireaux V, Brivanlou AH, Libchaber A. Science, (2002;298(5599):1759-1762.

173. Rosenthal SJ, Tomlinson I, Adkins EM, Schroeter S, Adams S, Swafford L, Blakely RD. Journal of the American Chemical Society, 2002;124(17):4586-4594.

174. Åkerman ME, Chan WC, Laakkonen P, Bhatia SN, Ruoslahti E. Proceedings of the National Academy of Sciences, (2002;99(20):12617-12621.

175. Wu XY, Liu HJ, Liu JQ, Haley KN, Treadway JA, Larson JP, Ge NF, Peale F, Bruchez MP. Nat. Biotechnol.21 2003;41.

176. Dahan M, Laurence T, Pinaud F, Chemla DS, Alivisatos AP, Sauer M, Weiss S. Optics letters, 2001;26(11):825-827.

177. Jaiswal JK, Mattoussi H, Mauro JM, Simon SM. Nature biotechnology, 2003;21(1):47.

178. Parak WJ, Boudreau R, Le Gros M, Gerion D, Zanchet D, Micheel CM, Larabell C. Advanced Materials, 2002;14(12):882-885.

179. Hanaki KI, Momo A, Oku T, Komoto A, Maenosono S, Yamaguchi Y, Yamamoto K. Biochemical and biophysical research communications, 2003;302(3):496-501.

180. Chan WC, Nie S. Science, 1998;281(5385):2016-2018.

181. Kratz F. Journal of controlled release, (2008;132(3):171-183.

182. Elzoghby AO, Samy WM, Elgindy NA. Journal of controlled release, (2012);157(2):168-182.

183. Kratz F, Fichtner I, Schumarcher P, Roth T, Feibig HH, Unger C. Eur. J. Cancer 1997;33:S175.

184. Rahimnejad M, Jahanshahi M, Najafpour GD. Afr. J. Biotechnol. 2006;5:1918–1923.

185. Patil GV. Biopolymer albumin for diagnosis and in drug delivery, Drug Dev. Res. 2003;58:219–247.

186. Irache JM, Merodio M, Arnedo A, Mini Rev. Med. Chem. 2005;5:293–305.

187. Weber C, Coester C, Kreuter J, Langer K. Int. J. Pharm. 2000;194:91–102.

İletişim ve Çalışma Gönderim e-mail adresi:
insackongre@gmail.com